WARSAW UNIVERSITY
OF TECHNOLOGY

Faculty of Physics

Ph.D. THESIS

Łukasz Kamil Graczykowski, M.Sc. Eng.

Femtoscopic analysis of hadron-hadron correlations in ultrarelativistic collisions of protons and heavy-ions registered by ALICE at the LHC

Supervisor
Professor Adam Kisiel, Ph.D., D.Sc.

Warsaw 2014

Acknowledgments / Podziękowania

Po polsku

Najważniejsze podziękowania chciałbym skierować w języku polskim. Dziękuję mojej Rodzinie, Przyjaciołom i wszystkim znajomym, którzy zawsze mnie wspierali w mojej karierze naukowej. Przede wszystkim chciałbym jednak podziękować moim Rodzicom i Siostrze, zarówno za wsparcie i wszelką pomoc w ciągu tych 4 lat studiów doktoranckich, jak i za wiarę, że to wszystko się uda. Wam dedykuję tę pracę!

In English

Foremost, I would like to express my deepest gratitude to my Supervisor, Prof. Adam Kisiel. His immerse knowledge, constant support, and expert advise were inspiring motivations throughout my studies. I have been extremely lucky to have a supervisor who cared so much about my work, with his immediate answers to my questions, constructive criticism, and patience. My research and this thesis would not have been possible without him. Thank you very much!

Special thanks must go to Prof. Jan Pluta, Head of the Nuclear Physics Division and the Heavy-Ion Reactions Group (HIRG) at the Faculty of Physics, Warsaw University of Technology (WUT). All my scientific activities, especially the 17 months that I spent, in total, at CERN, were possible only because of his personal interest and his ability to secure the necessary financial support. I must say that six years ago it was him, with his great teaching skills and enthusiasm, who convinced me to choose my scientific path and focus on the field of heavy-ion physics.

This thesis, for sure, would not had been possible without Dr. Yiota Foka, who was my supervisor when I first came at CERN in 2009 as an undergraduate student. She was the one who introduced me to the ALICE community, found financial resources which allowed me to stay for so long at CERN, and helped me in the first steps of my scientific activities in the Laboratory. I also owe to her the skills of giving scientific presentations and writing scientific articles and reports, which I have acquired during all these years. Finally, she has put a tremendous work in reading and correcting this thesis; sometimes late at night or while travelling.

I would like to express my big thanks to the ALICE Collaboration. In particular, I am especially indebted to Paolo Giubelino and Jurgen Schukraft, current and former ALICE Spokespersons. Without their hospitality, financial support and the opportunity they gave me, this work would not have been possible. I also thank Federico Carminati, the ALICE Offline Group Leader at the time, for his support, generosity, and stimulating interactions.

This work was performed within the Femtoscopy Physics Analysis Group, therefore special thanks go to the Conveners (Adam Kisiel, Dhevan Gangadharan). In addition, I must mention Michael Weber and Panos Christakoglou, Conveners of the Physics Working Group – Correlations and Fluctuations, as well as the Internal Review Committee of the p–Pb femtoscopy paper – Dariusz Miśkowiec, Andreas Morsch, and Constantin Loizides, for their careful review and detailed comments. I also want to express my sincere gratitude to Prof. Barbara Erazmus, Chair of the ALICE Editorial Board at the time, for physics discussions and her invaluable help.

I would also like to thank my colleagues from the HIRG group. First of all, the other Ph.D. students who are or, at the time, were in ALICE: Maciek Szymański, Ania Zaborowska, Jeremi Niedziela, and Marcin Patecki; for the nice atmosphere when we worked and spent time together at CERN. Then, the other HIRG members: Hania, Kasia, Kasia, Daniel, Daniel, Maja, Martin, Bartek, Tobiasz, Leszek, Rafał, Basia (now in Prague), and all the others which I cannot mention by name; for creating an enjoyable environment at work.

Finally, I would like to thank Małgorzata Janik, with whom I have been working since the very beginning of my journey in ALICE and heavy-ion physics. I can recall many hours of discussing physics, the months that we spent at CERN, as well as a number of travels to scientific conferences around the World. Practically all we have achieved and the knowledge we have acquired, would not have been possible without our two-person team! Thank you very much!

This work has been supported by the Polish National Science Centre under decisions no. DEC-2011/01/B/ST2/03483, DEC-2012/05/N/ST2/02757, DEC-2013/08/M/ST2/00598, and by the European Union in the framework of European Social Fund (Human Capital Operational Programme, Sub-measure 8.2.2 Regional Innovation Strategies). During his Ph.D. studies, the author was a scholar of WUT Center for Advanced Studies and Lubuskie Voivodeship.

Abstract

One of the most powerful methods developed to probe the properties of the Quark-Gluon Plasma (QGP) is the technique of two-particle correlations in momentum space, called *femtoscopy*. Femtoscopy gives the unique possibility to measure the space-time evolution of the system created in particle collisions. It is capable of measuring space scales of the order of femtometers (10^{-15} m; the size of a nucleon), as well as times of the order of 10^{-23} s. In heavy-ion collisions it provides insight into the collective effects exhibited by the created bulk strongly coupled matter.

Intriguing results from the analysis of the p–Pb collisions at the Large Hadron Collider (LHC) suggest that collective properties could also develop in small systems after all. First studies of the p–Pb system, which was initially expected to serve as a control measurement, assuming no formation of a QGP state, show that particularly at the extreme energies at the LHC, more complex physics mechanisms maybe involved, interesting on their own right. Therefore, systematic femtoscopic measurements of pp, p–Pb, and Pb–Pb systems are expected to provide crucial experimental input that can advance our understanding of the QGP state of matter and provide further constraints on its properties and characteristics.

Typically, pion-pion or kaon-kaon correlations are studied in order to determine the source size and its evolution in time. However, the femtoscopic formalism is not restricted to light mesons only. Other particles, in particular baryons, are also studied. For the study of baryon-baryon correlations the femtoscopic formalism can be employed in a novel way allowing us to extract the strong interaction parameters, which are known only for a few of the lightest baryon systems, like proton-proton, proton-neutron, proton-deuteron, etc.

One of the surprising results from Pb–Pb collisions at the LHC are the yields of protons and lambda hyperons, which are lower than predicted by extrapolations from lower energies. It is suggested that one aspect of the strong interaction, the annihilation of different baryon-antibaryon pairs, is responsible for these observations. Femtoscopy can be employed to measure the baryon-antibaryon interactions which then can be used to explain this effect.

This thesis presents the results of two-pion femtoscopy in p–Pb collisions at $\sqrt{s_{\mathrm{NN}}} = 5.02$ TeV and preliminary results of baryon femtoscopy in Pb–Pb collisions at $\sqrt{s_{\mathrm{NN}}} = 2.76$ TeV delivered by the LHC and registered by the ALICE detector.

For the p–Pb system there are, in general, predictions of the source sizes originating from two possible physics mechanisms. The potential existence of a collective phase in high-multiplicity p–Pb collisions is predicted to increase the measured femtoscopic radii by a factor of 1.5–2 with respect to the pp collisions at similar multiplicity. On the other hand, within a Color Glass Condensate (CGC) initial-state model, without a hydrodynamic phase, similar source sizes in both p–Pb and pp collisions are predicted. To verify these scenarios the three-dimensional pion femtoscopic radii were measured for the first time in four multiplicity and seven pair transverse momentum k_{T} ranges. Similarly to A–A and high multiplicity pp collisions, the radii decrease with k_{T} in all cases. They also increase with event multiplicity. At low multiplicity they are comparable to pp values, while at higher multiplicities and low k_{T} they are larger by 10–20%. However, the p–Pb radii do not reach the values observed in A–A collisions at lower energies.

The high multiplicity p–Pb data were compared to predictions from two hydrodynamic models. They provide larger values of the R_{out} and R_{long} parameters; however, the introduction of smaller initial size of the system brings calculations closer to the experimental data. In particular, the R_{side} parameter and the slope of the k_{T} dependence of the radii are in reasonable agreement. Nevertheless, the observed differences of 10–20% between high multiplicity pp and p–Pb collisions do not exclude the CGC scenario.

In Pb–Pb collisions the correlations of protons with lambda hyperons were measured. The correlation functions for different systems (baryon-baryon: $\mathrm{p}\Lambda$, $\overline{\mathrm{p}}\overline{\Lambda}$, as well as baryon-antibaryon: $\mathrm{p}\overline{\Lambda}$, $\overline{\mathrm{p}}\Lambda$) were obtained for five centrality ranges. Baryon-antibaryon correlations were qualitatively compared to theoretical expectations calculated using the Lednicky & Lyuboshitz analytical model with and without the annihilation process. The qualitative comparison revealed the presence of a wide anticorrelation that can be interpreted as a significant contribution of the baryon-antibaryon annihilation process. This result is the starting point for the future measurements of the interaction cross sections in these systems, which will be used to propose an explanation for the baryon yields at the LHC.

Both measurements presented in this thesis, the pion femtoscopy in p–Pb collisions and baryon femtoscopy in Pb–Pb collisions, address different aspects of QGP and contribute to its understanding and characterization. Combined with other measurements, they provide further insight into the processes which occur in strongly coupled matter at extreme energy density.

Streszczenie

Analiza femtoskopowa korelacji hadronów w ultrarelatywistycznych zderzeniach protonów oraz cieżkich jonów zarejestrowanych przez eksperyment ALICE na LHC

Jedną z metod badania plazmy kwarkowo-gluonowej (QGP) jest technika korelacji dwucząstkowych w przestrzeni pędów, zwana *femtosopią*. Femtoskopia stwarza unikalną możliwość pomiarów czasowo-przestrzennej ewolucji źródła powstałego w wyniku zderzeń cząstek przy relatywistycznych energiach. Za jej pomocą jesteśmy w stanie mierzyć rozmiary przestrzene rzędu pojedynczych femtometrów (10^{-15} m; rozmiar nukleonu) oraz czasy rzędu 10^{-23} s. W szczególności, w zderzeniach ciężkich jonów, femtoskopia jest wykorzystywana do badania efektów kolektywnych występujących w silnie związanej materii jądrowej.

Oprócz reakcji typu Pb–Pb, Wielki Zderzacz Hadronów (LHC) dostarczył zderzenia proton-proton oraz proton-ołów. Do tej pory w badaniach QGP służyły one jako eksperyment kontrolny, w którym początkowo nie przewidywano formowania się tego stanu materii. Wyniki najnowszych badań sugerują jednak, że efekty kolektywne, związane z wytworzeniem plazmy kwarkowo-gluonowej, mogą być obecne również w zderzeniach p–Pb o wysokiej krotności. Z uwagi na ten fakt, przeprowadzenie systematycznych pomiarów femtoskopowych zderzeń pp, p–Pb i Pb–Pb, oraz porównanie ze sobą otrzymanych wyników jest szczególnie istotne i może przyczynić się do lepszego opisu właściwości plazmy.

W celu otrzymania rozmiarów i czasu ewolucji powstałego w zderzeniu źródła najczęściej badane są korelacje typu pion-pion oraz kaon-kaon. Formalizm femtoskopowy nie jest jednakże ograniczony tylko do lekkich mezonów. Inne cząstki, w szczególności bariony, również są badane. W korelacjach typu barion-barion formalizm femtoskopowy może zostać wykorzystany w nowatorski sposób, pozwalając na otrzymanie parametrów oddziaływania silnego, które znane są tylko dla kilku typów par lekkich barionów, takich jak proton-proton, proton-neutron, proton-deuteron, itp.

Jednym z zaskakujących wyników pomiarów przeprowadzonych na LHC w zderzeniach Pb–Pb są niższe, niż wynikałoby to z ekstrapolacji z niższych energii, krotności produkowanych

barionów. Prawdopodobnym powodem jest jeden z aspektów oddziaływania silnego, anihilacja par barion-antybarion. Technika femtoskopii zastosowana do pomiarów oddziaływań silnych może zostać wykorzystana w celu weryfikacji tej hipotezy.

Niniejsza rozprawa doktorska przedstawia wyniki badań femtoskopii pionów w zderzeniach p–Pb przy energii w środku masy $\sqrt{s_{\mathrm{NN}}} = 5.02$ TeV oraz wstępne wyniki femtoskopii barionów w zderzeniach Pb–Pb przy energii w środku masy $\sqrt{s_{\mathrm{NN}}} = 2.76$ TeV. Oba rodzaje zderzeń zostały uzyskane w akceleratorze LHC oraz zarejestrowane przez detektor ALICE.

Obecnie istnieją dwa główne rodzaje przewidywań dotyczących rozmiarów źródła w zderzeniach p–Pb, wykorzystujące różne mechanizmy fizyczne. Możliwe występowanie fazy kolektywnej, związanej z formacją QGP, przewiduje promienie większe o czynnik 1.5–2 w zderzeniach p–Pb o wysokiej krotności, w stosunku do promieni zmierzonych w zderzeniach pp o tej samej krotności. Z drugiej strony, model oparty o mechanizm saturacji gluonów, bez fazy hydrodynamicznej, przewiduje rozmiary źródła podobne zarówno w zderzeniach pp jak i p–Pb. W celu odpowiedzi na pytanie, które z powyższych przewidywań jest poprawne, przeprowadzona została trójwymiarowa analiza femtoskopowa pionów dla czterech przedziałów krotności zderzenia oraz siedmiu przedziałów pędu poprzecznego pary k_{T}. Podobnie jak w reakcjach jądro-jądro (A–A) oraz proton-proton o wysokiej krotności, promienie femtoskopowe w tych zderzeniach zmniejszają się k_{T}. Zwiększają się one również wraz z krotnością zderzenia. Dla niskich krotności promienie są porównywalne z wartościami otrzymanymi w zderzeniach pp, podczas gdy dla wysokich krotności i niskich k_{T} są one większe o 10–20%. Rozmiary źródła nigdy jednak nie osiągają wartości otrzymanych w zderzeniach A–A przy niższych energiach.

Dane ze zderzeń p–Pb o wysokiej krotności zostały porównane do przewidywań otrzymanych za pomocą dwóch modeli hydrodynamicznych. Modele te przewidują większe niż w danych eksperymentalnych wartości promieni R_{out} oraz R_{long}; jednakże, wprowadzenie mniejszego rozmiaru początkowego zbliża obliczenia do danych eksperymentalnych. Parametr R_{side} oraz zależność promieni od k_{T} są w dobrej zgodności z danymi. Niemniej jednak, zaobserwowane różnice rzędu 10–20% pomiędzy promieniami otrzymanymi w zderzeniach pp a p–Pb o wysokiej krotności nie wykluczają rozwiązania proponowanego przez model saturacyjny.

W zderzeniach Pb–Pb zmierzone zostały korelacje protonów z hiperonami lambda. Femtoskopowe funkcje korelacyjne dla różnych par barionów (barion-barion: $\mathrm{p}\Lambda$, $\overline{\mathrm{p}}\overline{\Lambda}$ oraz barion-antybarion: $\mathrm{p}\overline{\Lambda}$, $\overline{\mathrm{p}}\Lambda$) zostały otrzymane w pięciu przedziałach krotności zderzenia. Eksperymentalne funkcje korelacyjne barion-antybarion porównane zostały jakościowo do przewidy-

wań teoretycznych otrzymanych z modelu analitycznego, który uwzględnienia proces anihilacji jak i pozwala na wyznaczenie funkcji korelacyjnej bez tego efektu. Porównanie wykazało istnienie znaczącej antykorelacji w danych eksperymentalnych, zgodnej z oczekiwanym procesem anihilacyjnym. Otrzymane wyniki są punktem wyjściowym do dalszych badań mających na celu ilościowe pomiary przekrojów czynnych oddziaływań barionów, które będą mogły zostać wykorzystane do wyjaśnienia zmniejszonych krotności barionów w LHC.

Oba rodzaje pomiarów, zarówno femtoskopia pionów w zderzeniach p–Pb jak i femtoskopia barionów w zderzeniach Pb–Pb, dotyczą różnych aspektów tego samego problemu, jakim jest zrozumienie plazmy kwarkowo-gluonowej. W połączeniu z innymi pomiarami, dają one lepszy wgląd w procesy zachodzące w silnie związanej materii jądrowej w warunkach wielkiej gęstości energii.

Contents

Chapter 1

Introduction

Physics, the most fundamental science, aims to understand and describe the world we live in – from the largest galaxies to the smallest subatomic particles. Over the centuries scientists developed theories and conducted experiments pushing the boundaries of mankind's knowledge further and further. During this evolution of our understanding of the principal laws of Nature, four fundamental interactions have been identified: gravitational, electromagnetic, weak, and strong. Gravitation and electromagnetism act potentially over infinite distance and mediate phenomena that we experience in everyday life. In contrast, the weak and strong forces act only over subatomic distances and do not manifest directly on macroscopic scales. This property makes them difficult to study and is the reason why they were discovered relatively recently, about hundred years ago.

These four fundamental interactions govern the dynamics of fundamental particles – quarks and leptons. However, the strong interaction, as the name indicates, is the strongest attractive force, with a magnitude more than hundred times greater than the electromagnetic force and 10^{37} greater than gravity. It is the strong force which is responsible for binding quarks and gluons in composite particles called hadrons, such as protons and neutrons, in atomic nuclei. The most commonly accepted theory that describes the strong interaction is the quantum chromodynamics (QCD), established in the beginning of 70s' of the last century. Being a precise and mathematically elegant quantum field theory, QCD can describe a very wide spectrum of phenomena observed in the experiment and is the basic tool used today by particle physicists. However, many observed properties of strongly interacting matter still remain open questions and collisions of particles at relativistic energies are studied in order to address them. In such collisions we expect to reproduce in the laboratory conditions similar to the ones prevailing at the very beginning of the Universe. In particular, the aim is to create small droplets of strongly interacting matter which we believe have similar properties as the Universe had shortly after

the Big Bang. Understanding the processes of the creation and evolution of such systems could map out new frontiers of knowledge.

Relativistic collisions of heavy ions require accelerators – powerful machines which are capable to accelerate particles to almost the speed of light. There are several big particle accelerators over the World; the biggest one at present is the Large Hadron Collider (LHC) at the European Organization for Nuclear Research (CERN), close to the city of Geneva in Switzerland. Since the start of its operation, in 2009, the LHC has successfully delivered millions of collisions of protons at center-of-mass energies[1] of $\sqrt{s}$ = 0.9 TeV, $\sqrt{s}$ = 2.36 TeV, $\sqrt{s}$ = 2.76 TeV, $\sqrt{s}$ = 7 TeV, and $\sqrt{s}$ = 8 TeV, as well as Pb–Pb collisions at $\sqrt{s_{\mathrm{NN}}}$ = 2.76 TeV and p–Pb collisions at $\sqrt{s_{\mathrm{NN}}}$ = 5.02 TeV, aiming at a maximum of $\sqrt{s}$ = 14 TeV for pp collisions and $\sqrt{s}$ = 5.52 TeV for Pb–Pb collisions. Four big experiments (ATLAS, CMS, ALICE, LHCb) together with three smaller ones (TOTEM, LHCf, MoEDAL), designed to address the unsolved question of particle physics, are currently operational and have delivered numerous experimental results.

ALICE (A Large Ion Collider Experiment) is optimized to study collisions of lead ions and the properties of the hot and dense strongly interacting system produced in such collisions. In fact, QCD predicts that at extreme conditions of temperature and/or energy density, exceeding certain critical values, normal matter undergoes a phase transition to a deconfined state of quarks and gluons, called Quark-Gluon Plasma (QGP). The creation, observation and characterization of such a state of matter is the main focus of the ALICE experiment.

Scientists working at Super Proton Synchrotron (SPS) at CERN tried to create QGP in the laboratory in 80s and 90s, which was finally announced in the year 2000. Today, the Relativistic Heavy Ion Collider (RHIC) at Brookhaven National Laboratory and the the LHC at CERN collide gold (at RHIC) and lead (at LHC) ions to produce the hottest system ever made by man and further studies are ongoing.

[1] In particle physics the energy, momentum, and angles of a scattering process are usually described by the Mandelstam variables which are invariant under Lorentz transformation. Let us consider collision of two particles with four-momenta p_1 and p_2. In such scenario the Lorentz-invariant variable $s = (p_1 + p_2)^2$ can be defined. In the center-of-mass frame (no net momentum) the four-momenta are expressed as $p_1 = (E_1, \mathbf{p})$, $p_2 = (E_2, -\mathbf{p})$, from which $s = (p_1 + p_2)^2 = (E_1 + E_2)^2 - (\mathbf{p} - \mathbf{p})^2 = (E_1 + E_2)^2$ is obtained. Therefore, the quantity $\sqrt{s}$ represents the total energy available in the center-of-mass frame. In heavy-ion physics, where collisions of heavy atomic nuclei are studied, the collision energy per nucleon pair is denoted as $\sqrt{s_{\mathrm{NN}}}$.

It would be trivial to verify the existence of QGP if we could directly see the quarks and gluons as we do see electrons and nuclei in ordinary plasma. However, the QGP droplet which we believe is formed in an relativistic heavy-ion collision is so small and lives only for such a short glimpse of time that no device exists which would be able to measure its properties directly. Therefore, several indirect observables, called signatures, have been proposed over the years to probe the nature and different stages of the system created in heavy-ion collisions and provide information on its composition and dynamical evolution. Accordingly, several specific techniques have been developed and optimized for the analysis of individual observables.

The creation of a QGP state in a heavy-ion collision is a theoretical prediction and, as all concepts in science, must be very precisely defined and tested. In fact, it is validated against a null hypothesis – a scenario without the formation of the QGP. Therefore, in order to rely on the QGP signatures we must know how they behave in the absence of plasma. In practice, such validation is performed by employing benchmark elementary collisions, where we expect that the volume is too small to form the QGP. To some extent collisions of protons, where the effects originating from particles traversing the plasma are absent, can be used for such benchmarking. Yet, in order to disentangle these effects from the ones coming from particles traversing cold matter, i.e. a nucleus made of protons and neutrons rather than QGP, it was believed that p–A collisions were crucial. When the p–Pb data finally arrived at LHC it turned out that the global picture is not that clear anymore. Their analysis suggests that collective and final-state phenomena could be present in small systems after all[2]. More detailed studies are needed to properly characterize the exact nature of these collisions.

One of the tools developed to probe the Quark-Gluon Plasma is the technique of two-particle correlations in momentum space, called *femtoscopy*. It is capable of measuring the space scales of the order of single femtometers (10^{-15} m; the size of a nucleon), as well as times of the order of 10^{-23} s. In heavy-ion collisions femtoscopy gives the unique possibility to measure the space-time evolution of the system and provides insight into the collective effects exhibited by the bulk strongly interacting matter. Typically, pion-pion or kaon-kaon correlations are studied in order to determine the source sizes and its evolution time. However, the femtoscopic formalism is

[2]The analysis of the very fresh p–Pb data at the LHC is still ongoing. However, some observables which have been attributed only to Pb–Pb collisions and explained by collective effects have been observed also in pp and p–Pb collisions with significant number of produced particles ("high multiplicity" collisions). For more details see Sec. 2.5.

not limited only to light mesons and other particles, in particular baryons, can also be studied. In baryon-baryon correlations the femtoscopic formalism can be employed in a novel way to extract the strong interaction parameters, which is known only for a few lightest baryon systems (like proton-proton, proton-neutron, proton-deuteron, etc.). Strong interaction between pairs of more exotic baryons, containing at least one strange quark, is poorly known or not known at all. Therefore, the femtoscopic formalism can be applied to measure these interactions[3].

In this work we present the results of the two-pion femtoscopy analysis performed in p–Pb collisions registered by ALICE. In general, there are two competing model predictions of the source sizes in this system. The possible existence of a collective phase in high-multiplicity p–Pb collisions is predicted to increase the measured source sizes by a factor of 1.5–2 with respect to the pp collisions at similar multiplicity. In contrast, a Color Glass Condensate (CGC) initial-state model, without a hydrodynamic phase, predicts similar source sizes in both p–Pb and pp collisions. Therefore, femtoscopic measurements in the two systems will lead to crucial experimental constraints on the interpretation of the p–Pb data.

In addition to pion femtoscopy in p–Pb collisions, this thesis also briefly discusses the idea and preliminary results of baryon femtoscopy in Pb–Pb collisions at $\sqrt{s_{\mathrm{NN}}} = 2.76$ TeV. These type of correlations are currently extensively studied in ALICE; however, some preliminary results already have been released and presented at scientific conferences. The work of this thesis also includes the preliminary results of the correlation of (anti-)protons with (anti-)lambdas.

The thesis is organized as follows. In Chapter 2 the general overview of physics in collisions of heavy-ions at relativistic energies is discussed. The LHC and ALICE are described in Chapter 3. Chapter 4 describes the basic theory of two-particle correlations in momentum space and also includes a short overview of previous pion femtoscopy in small systems. The procedure to extract femtoscopic radii and its validation are described in detail in Chapter 5. The p–Pb data sample as well as selection criteria are discussed in Chapter 6. The final results of pion femtoscopy measurements in p–Pb are presented in Chapter 7 and the details of systematic uncertainty estimation are shown in Chapter 8. In addition to pion results, Chapter 9 presents a short highlight of ongoing proton-lambda studies. All results are discussed and conclusions are drawn in Chapter 10.

[3]The only limitations here are the particle identification capabilities of ALICE – some of more exotic baryons cannot be measured in the experiment.

In addition to the regular chapters, the thesis includes three appendices which include supplementary studies. A detailed analysis of non-femtoscopic background in various Monte Carlo models is described in Appendix A. Appendix B presents correlations of unlike-sign pions. Finally, Appendix C briefly discusses the results of angular ($\Delta\eta\Delta\varphi$) correlation of like- and unlike-sign pions.

The material presented in Chapter 5, description and validation of the methodolgy, has been published in Ref. [1], while the content of Chapter 7, the experimental results, is published in Ref. [2]. In addition, the preliminary results of these studies were presented at the Quark Matter 2014 conference [3] and published in the conference proceedings in Ref. [4].

Chapter 2

Heavy-ion physics at relativistic energies

The study of relativistic heavy-ion collisions is a field of physics which lies at the border of the high-energy physics and the nuclear physics. The main focus of the field is the study of collisions of two nuclei occurring at very high energies, which results in the production of up to several thousands particles. The observed physical phenomena that characterize the identity, kinematic properties, and correlations between the produced particles are far beyond the simple superposition of elementary collisions of two nucleons.

It is predicted that at the collision energies achievable by the biggest particle accelerators the produced conditions (extremely high densities and temperatures) are close to the ones which existed few microseconds after the Big Bang. In such conditions hadronic matter is predicted to undergo a phase transition into a deconfined state called the Quark-Gluon Plasma. In other words, by colliding two heavy ions at relativistic energies we are not only studying the properties of matter but we are also recreating the early Universe in the laboratory. Therefore, these studies are of great importance both in physics where we want to understand how the Nature works, but also in cosmology where we try to answer the most fundamental questions about the history of our Universe.

2.1 Standard Model

The *Standard Model* (SM) is a theory which describes the subatomic particles and the interactions between them. It incorporates three of the four main forces that exist in Nature: electromagnetic, weak and strong. However, it is not a complete *theory of everything* because it does not incorporate general relativity – the theory of gravitation. The model is called *standard* because after many years and numerous measurements and validation tests it continues to agree with the experimental results, and is one of the most successful and widely accepted theories in physics. The last missing piece in the model, the Higgs boson, has been finally confirmed experimentally in 2012 at the LHC [5, 6].

The Standard Model introduces quarks and leptons as the most fundamental *constituents of matter*. There are six types of quarks, called *flavors* (and accordingly, six types of antiquarks) divided into three generations. The names of quark flavors are: u – up, d – down (I generation); s – strange, c – charm (II generation); t – top, b - bottom (III generation). Similarly, there are six types of leptons, also divided into three generations: e – electron, ν_e – electron neutrino (I generation); μ – muon, ν_μ – muon neutrino (II generation); τ – tau, ν_τ – tau neutrino (III generation). Due to the so-called *color confinement* phenomenon, described in Sec. 2.2, quarks cannot exist as free particles. The quarks build composite particles which are called *hadrons*. States of two quarks are called *mesons* and states of three quarks are called *baryons*. Larger particles, containing more quarks, are not forbidden by the theory but have not been discovered until the first observation of a four-quark state (tetraquark) called $Z(4430)$ in June 2014 by the LHCb experiment at CERN [7]. On the other hand leptons, which do not interact strongly but only weakly and electromagnetically, do exist as free particles. The best-known example of leptons are negatively charged electrons which interact electromagnetically with the positively charged nuclei and build atoms.

Particles can also be classified according to their spin. Particles with half-integer spin, like quarks and leptons, are called *fermions* – they obey Fermi-Dirac quantum statistics and the Pauli's exclusion principle. The other class represents particles with integer spins, which are called *bosons*. Bosons may be either composite hadrons or elementary particles like photons or gluons. They obey Bose-Einstein quantum statistics and do not obey the Pauli's exclusion principle.

The fundamental interactions between elementary particles are transferred by *force carrier* bosons. The Standard Model predicts the existence of 8 strong force carriers, which are called *gluons*. The weak interaction has 3 carriers called W^+, W^-, and Z^0; the electromagnetic force has 1 carrier which is called *photon*. The last particle in the Standard Model is the Higgs boson which mediates the interaction of massive particles with the Higgs field via the Brout-Englert-Higgs mechanism [8–10]. Its existence has been confirmed in 2012 by the studies performed by ATLAS and CMS exmeriments at the Large Hadon Collider at CERN [5, 6], which resulted in the 2013 Nobel Prize in Physics awarded to François Englert and Peter Higgs.

The properties of elementary particles of the Standard Model (quarks, leptons, and force carrier bosons) are shown in Fig. 2.1.

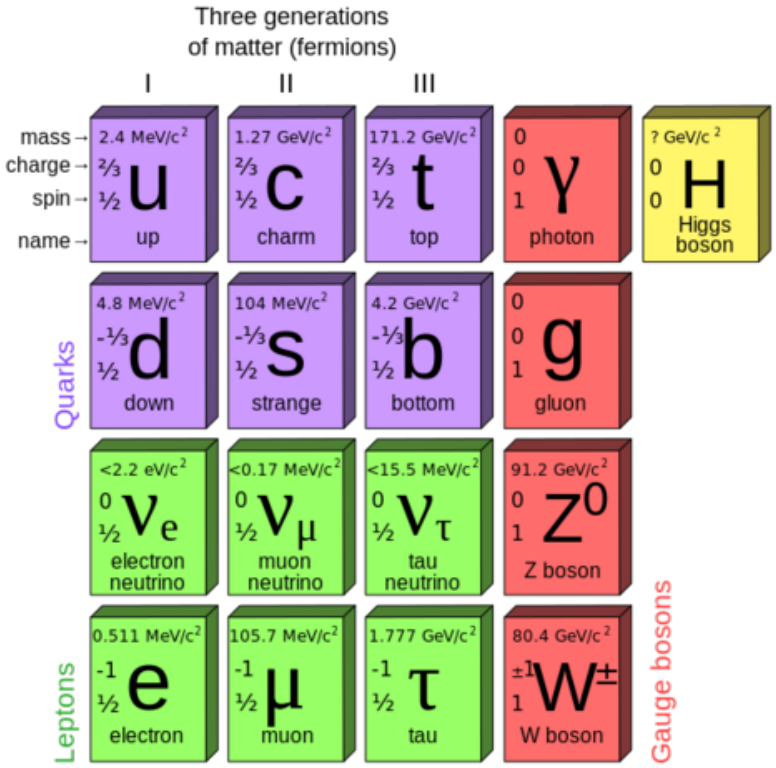

Figure 2.1: Elementary particles of the Standard Model theory. Picture from Ref. [11].

2.2 Quantum chromodynamics

Quantum chromodynamics (QCD) is a quantum field theory, part of the Standard Model, which describes the strong interaction. It was developed in analogy to quantum electrodynamics (QED) – the theory of electromagnetism in which electrically charged particles interact by the exchange of electromagnetic force carriers – photons. The QCD's name refers to *color charge* which is the property of quarks interacting by the exchange of gluons (similarly to electrically charged particles which interact by the exchange of photons). Despite the similarities there are several very important features which differentiate QCD from QED.

Historically, the development of QCD started in 1963 when Murray Gell-Mann and George Zweig, independently, proposed that the structure of hadrons could be explained by the existence of smaller particles from which hadrons are composed [12–14]. At that time the proposal included only three types of quarks – u, d, and s. The idea of color charge comes from the observations of particles like Δ^{++}, Δ^{-} and Ω^{-} which consist of three quarks of the same flavor (uuu, ddd, and sss, respectively). This seems to be in conflict with Pauli's exclusion principle;

therefore, a new quantum number (color) was introduced to differentiate quarks of the same flavor. The color charge was first proposed in 1964 by Greenberg [15] and in 1965 by Han together with Nambu [16]. The existence of quarks was finally confirmed experimentally in 1969 by *deep inelastic scattering* (DIS) experiments of electrons on protons performed at Stanford Linear Accelerator Center (SLAC) and now the quark model is the most widely accepted understanding of the subatomic structure of matter.

The QCD Lagrangian has the following form:

$$\mathcal{L}_{\mathrm{QCD}} = -\frac{1}{4}\sum_{a} F^{a}_{\mu\nu}F^{\mu\nu}_{a} + \sum_{\mathrm{f}}^{N_f} \overline{\Psi}_f \left(i\gamma^{\mu}\partial_{\mu} - g_{\mathrm{s}}\gamma^{\mu}\sum_{a} A^{a}_{\mu}\frac{\lambda^{a}}{2} - m_f \right)\Psi_f, \tag{2.1}$$

where Ψ_f are the quark fields ($f = u,\ d,\ s,\ c,\ b,\ t$ is the quark flavor index), A^{a}_{μ} are the gluon fields ($a = 1, ..., 8$ is the color index), $F^{\mu\nu}_{a}$ is the gluon field strength tensor, m_f are the quark masses, quantity g_{s} is the strong coupling constant (a parameter determining the strength of the interaction), γ^{μ} are the Dirac matrices, and λ^{a} are the Gell-Mann matrices[1]. The theory predicts that the coupling constant is actually not constant, but depends on the momentum transfer Q^2. Therefore, it is usually referred to as *running coupling constant*. This feature is also different from QED where the coupling constant does not change. The running coupling constant $\alpha_{\mathrm{s}} = \alpha_{\mathrm{s}}(Q^2)$ is described by the following equation:

$$\alpha_{\mathrm{s}}(Q^2) = \frac{g^2_{\mathrm{s}}}{4\pi} = \frac{16\pi^2}{(11 - \frac{2}{3}N_f)\ln Q^2/\Lambda^2_{\mathrm{QCD}}}, \tag{2.2}$$

where Λ_{QCD} is the scale parameter and N_f corresponds to the number of light quarks. The generally adopted convention defines the value of α_{s} at the mass of Z^0 boson to be $\alpha_{\mathrm{s}}(m^0_{\mathrm{Z}}) = 0.118 \pm 0.002$. In this case the scale constant $\Lambda_{\mathrm{QCD}} = 217^{+25}_{-23}$ MeV [17, 18]. The summary of measurements of α_{s} is presented in Fig. 2.2.

The quark-quark potential calculated from QCD is shown in Fig. 2.3. From this plot and from Eq. (2.2) we can see that QCD has two peculiar properties which manifest depending on the distance between strongly interacting particles:

- **Confinement** means that the quarks and gluons cannot exist as independent particles. In other words, we can imagine the strong interaction between two quarks as a string

[1]The Gell-Mann matrices, divided by a factor of two, are the generators of the SU(3) group. They satisfy the commutation relations $\left[\frac{\lambda_a}{2}, \frac{\lambda_b}{2}\right] = if_{abc}\frac{\lambda_c}{2}$ which define the Lie algebra of the SU(3) group. For more details see Ref. [17]

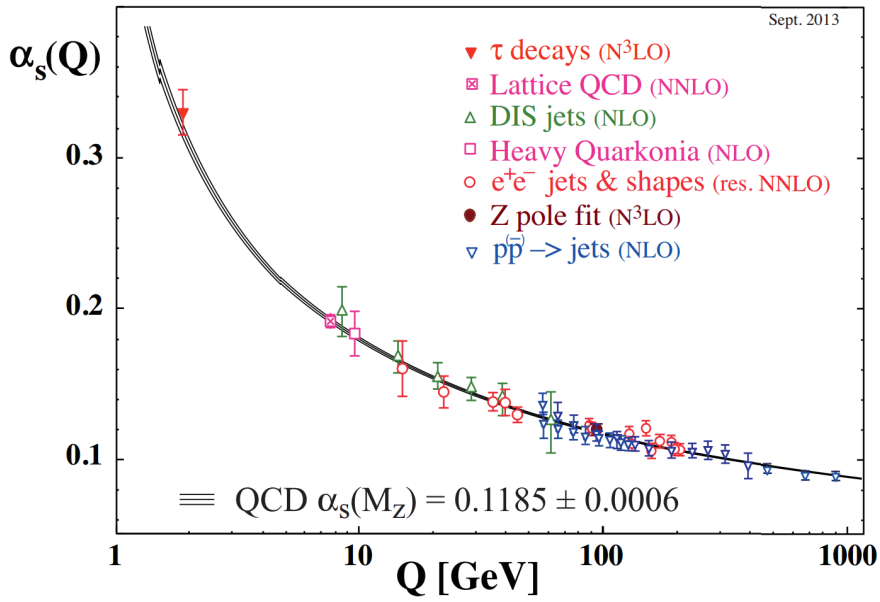

Figure 2.2: Summary of measurements of the strong interaction running coupling constant α_s as a function of the momentum transfer Q. The respective degree of QCD perturbation theory used for the extraction of α_s is indicated in brackets (NLO – next-to-leading order calculations, NNLO – next-to-next-to-leading order calculations, N^{3}NLO – next-to-NNLO calculations). Plot from Ref. [19].

spanned between them. If we try to pull them apart too far, the energy we put in during this process will, at some point, exceed the energy required to produce a quark pair. In this case, the string *breaks* and we are left with two or more pairs of quarks. A schematic picture is shown in Fig. 2.4. This striking feature of QCD is the reason why we cannot observe free quarks like we do observe protons, neutrons, or electrons. However, such description presented here is only qualitative and supported only by numerical calculations. At the moment, due to the complexity of the theory, there is no analytic proof (or analytic approximation) which describes the properties of QCD at large distances.

- **Asymptotic freedom** means that the strong interaction between particles becomes weaker at shorter distances and higher energies. Because of this feature we can make very precise measurements in high-energy experiments since the weaker interaction allows us to apply the perturbation theory calculations to QCD. This phenomenon was discovered in 1974 by David Politzer, Frank Wilczek, and David Gross [20, 21] who received the Nobel Prize in Physics in 2004.

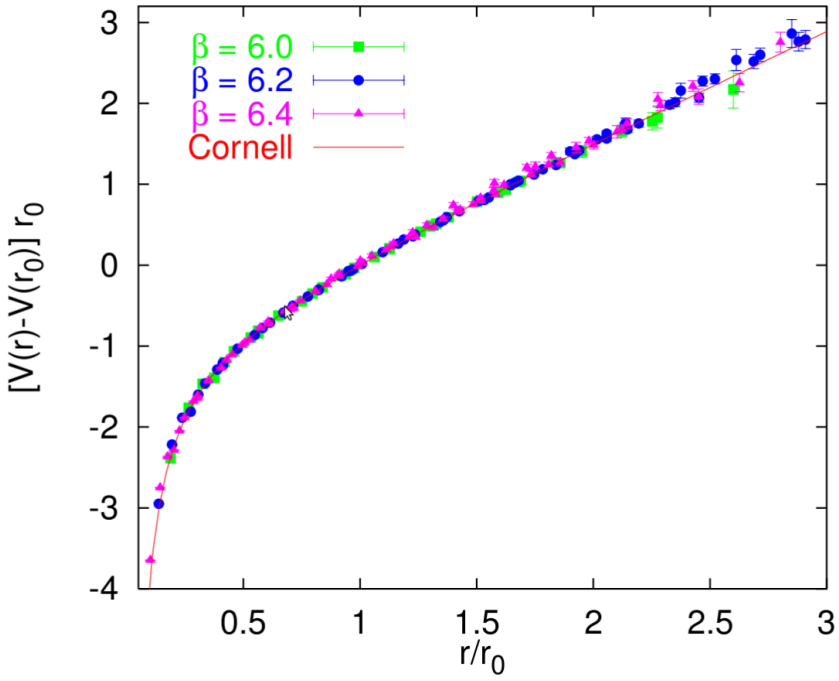

Figure 2.3: The quark-quark potential from lattice QCD calculations (r_0 = 0.5 fm and $V(r_0)$ = 0). Plot from Ref. [22].

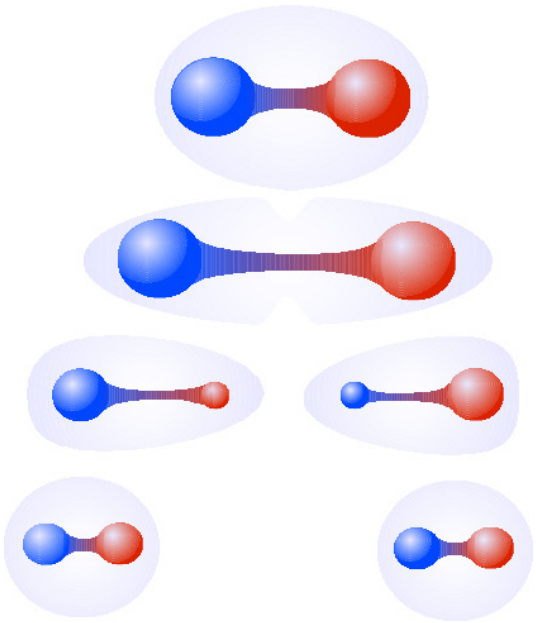

Figure 2.4: String breaking: when quarks are pulled too far apart, new quark-antiquark pairs are produced. Picture from Ref. [23].

From the mathematical point of view QCD is a non-abelian gauge theory (Yang-Mills theory) which is invariant under the SU(3) symmetry group. As it was mentioned before, partons (common name for quarks and gluons) are color-charged. There are three colors (*red, green,*

blue) and, accordingly, three anticolors (*antired, antigreen, antiblue*). The theory says that free particles can only be color neutral (*white*). Mesons are pairs of color-anticolor dublets and baryons are red, green, and blue triplets. Quarks exchange colored gluons and therefore change their color. We do not discriminate 18 quarks but 6, because we treat quark of each mass, charge and any color as one particle. As it has been just mentioned, gluons are color-charged (a gluon carries any combination of color and anticolor; on the other hand, the electromagnetic charge carrier in QED, the photon, is a neutral particle). This property means that gluons not only mediate the strong interaction between quarks (as do photons in QED) but also interact with them and other gluons.

There are several approaches to solve the QCD equations, but generally speaking there are two main ones: applying the perturbation theory (so-called *perturbative QCD*) for large values of Q^2 and not (*non-perturbative QCD*) for small Q^2. These two scenarios are also referred to as *hard* QCD (or hard physics) and *soft* QCD (or soft physics), respectively. In the latter, the numerical calculation techniques are based on the *lattice*. This means, that we perform numerical calculations on discrete space-time points. Phenomenological models are also very helpful in understanding some mechanisms observed in experiments. Figure 2.5 shows the QCD coupling constant α_s as a function of distance which is the variable "inverse" to Q^2. The vertical band represents the intermediate region between "perturbative QCD" at small distances and "strong QCD", usually also called "non-perturbative QCD", at distances close to the nucleon radius.

In recent years another powerful tool has been developed – the so-called AdS/CFT (Anti-de-Sitter / Conformal Field Theory) correspondance (or duality). Some aspects of the Quark-Gluon Plasma can be described in the language of AdS/CFT in terms of black holes in multi-dimensional space [25, 26]. AdS/CFT also predicted that the shear viscosity over entropy ratio for QGP is approximately equal to a universal constant:

$$\frac{\eta}{s} \approx \frac{\hbar}{4\pi k}, \tag{2.3}$$

where $\hbar$ denotes the reduced Planck's constant and k is the Boltzmann's constant. This prediction was confirmed in 2008 by the data from the Relativistic Heavy Ion Collider (RHIC) at Brookhaven National Laboratory (BNL) [27, 28].

The force which binds together hadrons (for example protons and neutrons in the nucleus), called the *nuclear force*, is in some sense a residual strong force. This is similar to the *van*

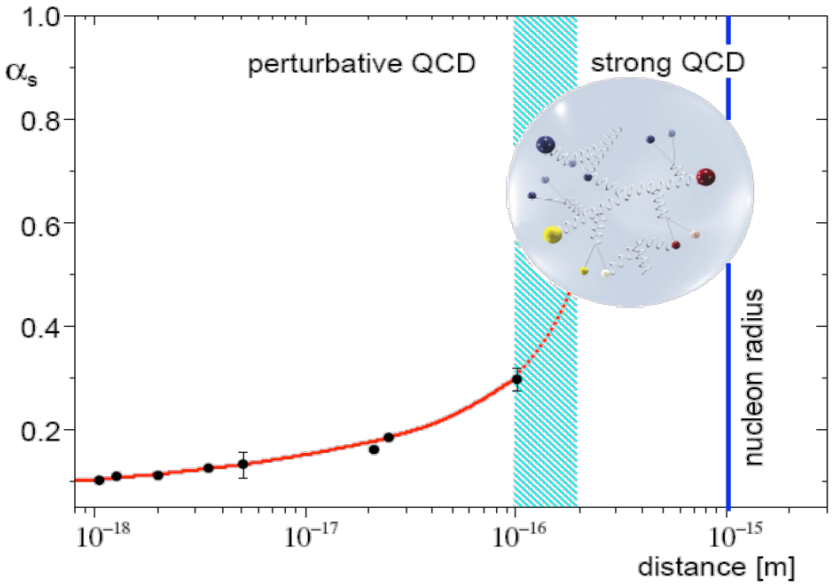

Figure 2.5: QCD coupling constant α_s as a function of distance. Black points correspond to experimental measurements [19]. Plot from Ref. [24].

der Waals force, the basis for chemistry, which is a residual electromagnetic force. We are using phenomenological models describing these forces (nuclear force and van der Waals force) because of the complexity of the systems (nuclei, atoms, or chemical compounds) which make the description with strong or electromagnetic force impossible from the practical point of view. The field of relativistic heavy-ion collisions deals with complex systems of nuclear-hadronic matter similarly to nuclear physics, but it tries to understand such systems from the laws derived from first principles rather than effective models only.

2.3 Quark-Gluon Plasma

2.3.1 Theory

The main consequence of the asymptotic freedom property of QCD is the prediction of the existence of a deconfined state of quarks and gluons, called the *Quark-Gluon Plasma (QGP)*. The QGP is a phase of QCD matter which is predicted to exist at extremely high temperatures and densities. A conceptual sketch showing the creation of QGP by heating and compression is shown in Fig. 2.6.

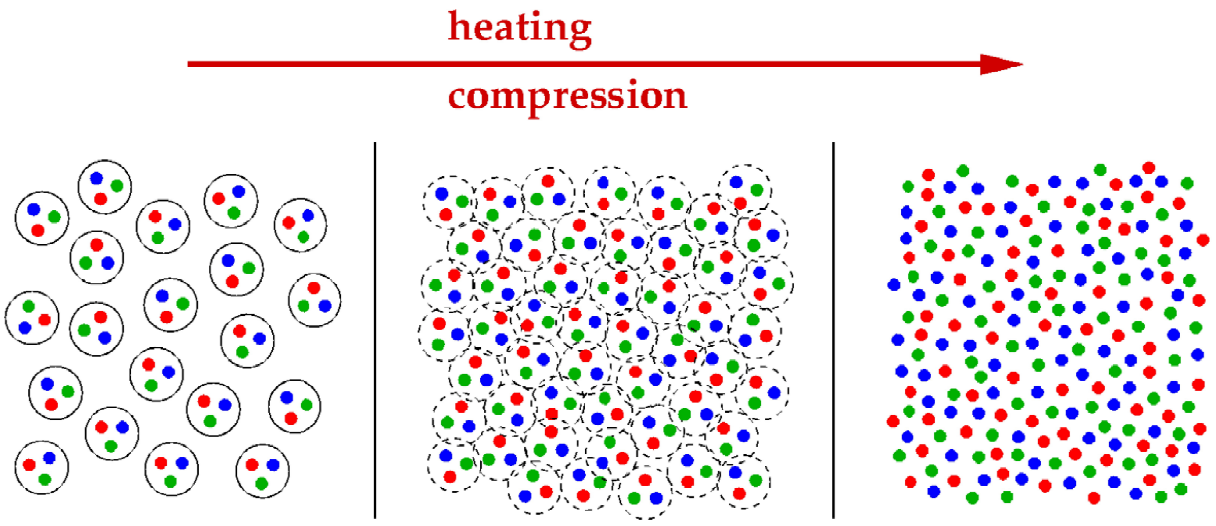

Figure 2.6: Formation of the QGP by heating and compression. Picture from Ref. [29].

The name *plasma* comes from several properties of QGP which are similar to "ordinary" plasma: it is color neutral (like electrically neutral ordinary plasma) and consists of freely-propagating color-charged particles. However, in contrast to ordinary plasma which behaves like a gas, QGP behaves as a nearly perfect liquid.

The signatures of QGP formation can be seen directly from lattice QCD calculations [30]. In order to describe a phase transition to QGP most often a statistical approach is used. It assumes that QGP is in thermal equilibrium as a fluid or gas of quarks and gluons. If the baryon chemical potential[2] is set to zero, the partition functions in relativistic gases are [31]

$$(T \ln Z)_{\mathrm{f}} = \frac{g_{\mathrm{f}V}}{12}\left(\frac{7\pi^2}{30}T^4 + \mu^2 T^2 + \frac{1}{2\pi^2}\mu^4\right), \tag{2.4}$$

for fermions, and

$$(T \ln Z)_{\mathrm{b}} = \frac{g_{\mathrm{b}V\pi^2}}{90}T^4, \tag{2.5}$$

for bosons. Values of g_{f} and g_{b} in Eq. (2.4) and Eq. (2.5) correspond to fermionic and bosonic degrees of freedom, respectively. Assuming the equation of state for ideal gas is given by:

$$\rho = \frac{\epsilon}{3}, \tag{2.6}$$

where ρ is the density (usually corresponding to baryon chemical potential, μ_{B}) and ϵ is the energy density, and assuming that the hadronic phase is composed only of pions, the following

[2] Among the hadrons, mesons have equal amount of matter and antimatter, while baryons are entirely made of one or another. Since our Universe is made of matter (in terms of baryons), therefore baryon chemical potential, μ_{B}, is a measure of the imbalance between matter and antimatter; zero indicates perfect balance.

equations are obtained for the energy densities of hadronic and QGP phases, respectively:

$$\epsilon_{\mathrm{h}}/T^4 = \frac{\pi^2}{4}, \tag{2.7}$$

$$\epsilon_{\mathrm{QGP}}/T^4 = (32 + 21N_{\mathrm{f}})\frac{\pi^2}{60}, \tag{2.8}$$

where N_{f} is the number of flavors. From these relations we can see that in the QGP phase there is a huge increase in the number of degrees of freedom caused by the asymptotically free quarks and gluons. Regardless of the number of flavors it is clear from Eq. (2.7) and Eq. (2.8) that the energy density of the QGP phase is much higher compared to the hadronic phase. The case $N_{\mathrm{f}} = 3$ (taking into account three types of quarks (u,d,s)) is known as the Stefan-Boltzmann limit. It is possible to solve the lattice QCD equations to obtain the behavior of matter near the critical temperature of the phase transition, T_{C}, which is estimated to be around $T_{\mathrm{C}} \approx 160$ MeV with the associated critical energy density $\epsilon_{\mathrm{C}} \approx 1$ GeV/fm^3 [32]. The results of lattice QCD calculations for ϵ/T^4 around T_{C} for zero baryon chemical potential are shown in Fig. 2.7. The

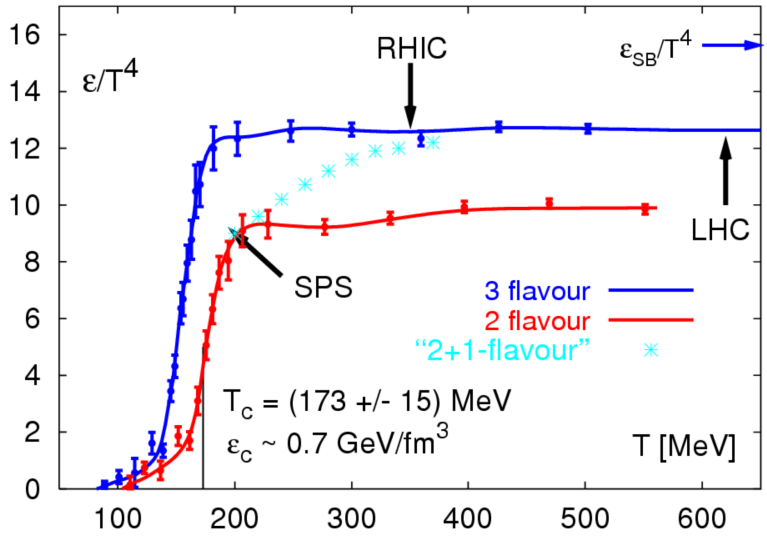

Figure 2.7: Energy density as a function of temperature calculated from lattice QCD for different number of flavors. Plot from Ref. [33].

different colors of the lines show calculations where different numbers of flavors of quarks were taken into account. As we can see, when the temperature reaches the critical temperature T_{C}, the number of degrees of freedom significantly and rapidly increases. This is the signature of the Quark-Gluon Plasma – the number of degrees of freedom in normal hadronic matter, where the quarks and gluons are combined in hadrons, is smaller than in QGP.

The QCD calculations allow us to construct a phase diagram in (μ_B, T) space. The schematic picture of such diagram is shown in Fig. 2.8. As we see from the phase diagram, the QGP state

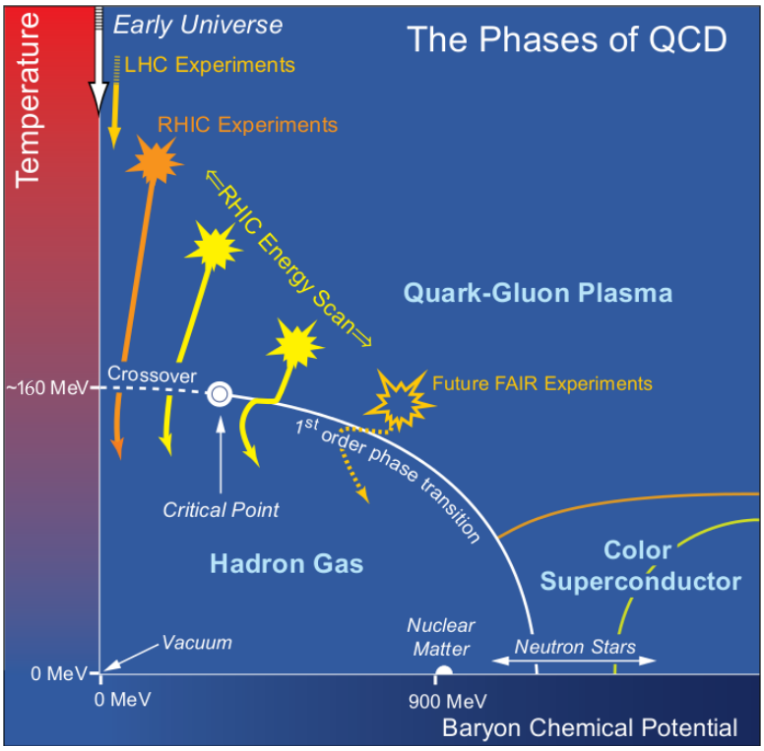

Figure 2.8: Phase diagram of strongly interacting matter. Picture from Ref. [29].

of matter is formed at high temperatures. On the other hand, at low temperatures and high baryon chemical potential a color superconductor is expected to exist. It is expected, that the phase transition between the Quark-Gluon Plasma and the hadronic matter is 1st order at non-vanishing baryon chemical potential μ_b. However, as baryon chemical potential goes towards zero, the phase transition becomes a smooth cross-over. The point where the phase transition changes from the 1st order to the smooth cross-over is called the *critical point*. The details of the structure of the phase diagram and the location of a possible critical point are currently the topics of extensive research by the experiments at RHIC and SPS.

2.3.2 Bjorken scenario

The study of relativistic heavy-ion collisions requires a model of the collision. Over the years several models have been developed (Fermi statistical model [34], Landau model with full stopping [35]), but today the approach proposed by Bjorken [36] is commonly used. It assumes "transparent" nuclei, which penetrate each other and loose a fraction of their energy. This sce-

nario is shown in Fig. 2.9. The following assumptions are made in the Bjorken model:

- **Transparency** The region at mid-rapidity[3] ($y = 0$) is net-baryon free (even though baryons from the interacting nuclei will be shifted from beam rapidity, the mid-rapidity region will be devoid of original baryons).

- **Boost invriance** The particle density (the number of particles per unit of rapidity) as a function of rapidity is constant at the mid-rapidity region.

- **Hydrodynamic phase** Relativistic hydrodynamic calculations can be applied to describe the system.

Boost invariance implies that the longitudinal flow has a form $\beta = z/t$. In turn, all thermodynamic quantities characterizing the central region depend only on the longitudinal proper time $\tau = t/\gamma = t \cdot \sqrt{1-\beta^2} = \sqrt{t^2 - z^2}$ and (x, y) coordinates in the transverse plane. If we ignore the transverse expansion the dependence on transverse coordinates vanishes and the model is reduced to only one dimension z. We can then represent the proper times (various collision stages) as hyperbolas on a space-time diagram (as can be seen in Fig. 2.10).

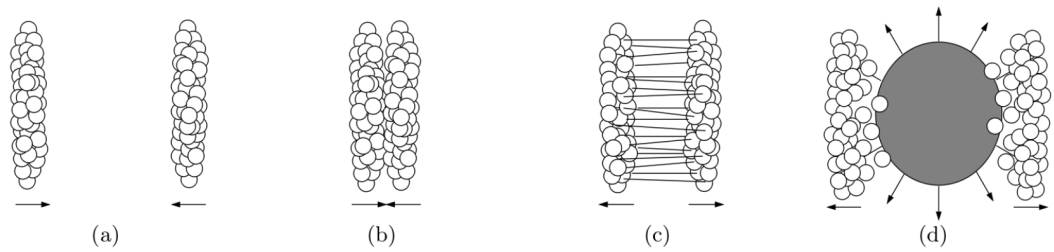

Figure 2.9: The Bjorken model of a heavy-ion collision. Picture from Ref. [29].

We consider now the space-time evolution of the Quark-Gluon Plasma shown in Fig. 2.10. The collision scenario including the QGP formation can be described by several stages: a) before the collision two Lorentz-contracted nuclei move towards each other, b) firstly, after the collision, a non-equilibrium initial state is created, c) then, QGP is formed, d) at the so-called *chemical freeze-out* the phase transition to the hadron gas occurs (the inelastic collision rate becomes smaller than the elastic collision rate – the chemical composition of the system is

[3]Rapidity, defined as $y = \frac{1}{2} \log \frac{E+p_L}{E-p_L}$, where E is the energy and p_L is the momentum along the direction of incident particle, is a measure of motion alternative to velocity. It is used in particle physics because it is additive under Lorentz transformation.

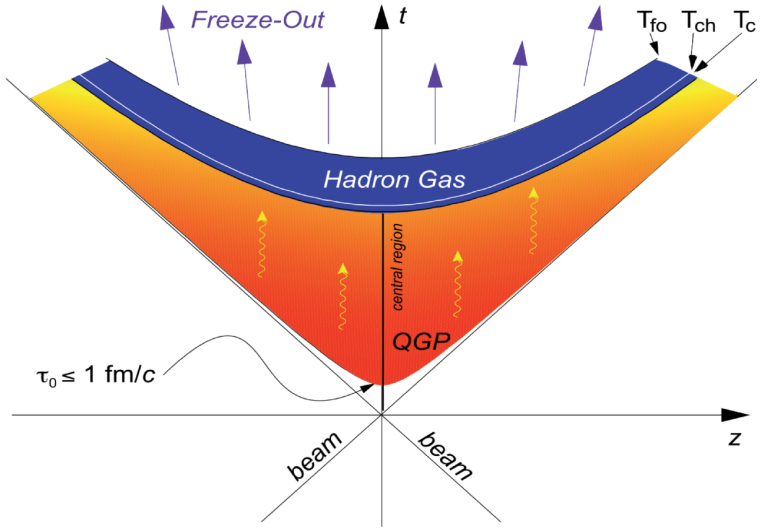

Figure 2.10: Evolution of the system created in a heavy-ion collision assuming formation of QGP. The (z, t) hyperbolas correspond to the boundaries between different phases. Picture from Ref. [37].

fixed from that moment), e) after the so-called *kinetic freeze-out* particles are no longer produced and we have a stream of particles flying to the detectors (elastic collisions stop – the particle momenta are fixed from that moment). This scenario results in three time scales. The first one is the time after the initial state when matter is thought to be thermalized, τ_0, of the order of 1 fm/c. The chemical and kinetic freeze-outs are characterized by respective temperatures T_{ch} and T_{kin}. Although particle abundances and ratios are fixed at chemical freeze-out, at the LHC energies they might be influenced by the rescattering phase (in particular baryon-antibaryon annihilation) at the end of the medium's evolution (for details see Sec. 2.3.6).

2.3.3 QGP at the early Universe

According to our current understanding of cosmology, the birth of the Universe happened around 13.8 billion years ago [38] with a violent "explosion" called the Big Bang (from the mathematical point of view the origin of Big Bang is a space-time singularity). In the first moments after the Big Bang all matter in the Universe was concentrated in a very small volume with extremely high energy density, temperature, and pressure. As time passed the Universe cooled down and went through several stages – one of them, around 1 μs after the Big Bang, being the Quark-Gluon Plasma. The Universe in the QGP stage cooled down to freeze-out to hadrons and leptons. In the next, much longer, stages protons and neutrons were bound in atomic nuclei and later together with electrons, formed neutral atoms, around 300 thousand

years after the Big Bang. In that moment the radiation, called the Cosmic Microwave Background (CMB), was released. CMB is the oldest light in the Universe and its discovery by Arno Penzias and Robert Wilson in 1964 [39] is considered as one of the most important tests of the Big Bang theory. Penzias and Wilson were awarded the Nobel Prize in Physics in 1978.

2.3.4 Initial conditions

2.3.4.1 Glauber model

The initial geometrical properties of the heavy-ion collisions can be calculated by the so-called Glauber model[4]. There are two forms of the model: (1) the "traditional" (optical) Glauber model which employs quantum wave functions [40, 41], and (2) the Monte Carlo Glauber model (GMC) which employs computer simulations [42, 43]. Both approaches require experimental results as input. The two most important are nuclear charge densities and inelastic nucleon–nucleon cross section [44]:

- **Nuclear Charge Densities** The Fermi distribution is usually used for the description of the nuclear charge density:
$$\rho(r) = \rho_0 \frac{1 + w(r/R)^2}{1 + \exp\left(\frac{r-R}{a}\right)}, \tag{2.9}$$
where ρ_0 is the density in the core of the nucleus, R is the radius of the nucleus, a is the "skin depth" of the nucleus, and w is the deviation from a spherical shape of the nucleus.

- **Inealstic Nucleon–Nucleon Cross Section** In a heavy-ion collision we treat the system as individual nucleon–nucleon collisions. For the calculation of such an interaction the corresponding experimental cross section $\sigma_{\text{inel}}^{\text{NN}}$ is needed. These, for different collision energies, are obtained from pp collisions.

Figure 2.11 shows a sketch of a heavy-ion collision, assuming the "traditional" Glauber model, with the most important geometrical quantities. We can see two nuclei, A and B, approaching each other with an impact parameter **b**. The optical Glauber model employs the so-called "optical limit" approximation, where it is assumed that the nucleons from one nucleus see the second nucleus as a smooth object. There are two important quantities which can be calculated knowing the impact parameter and the cross section: the number of collisions

[4]The name comes from Prof. Roy J. Glauber, a 2005 Nobel Prize in Physics Laureate.

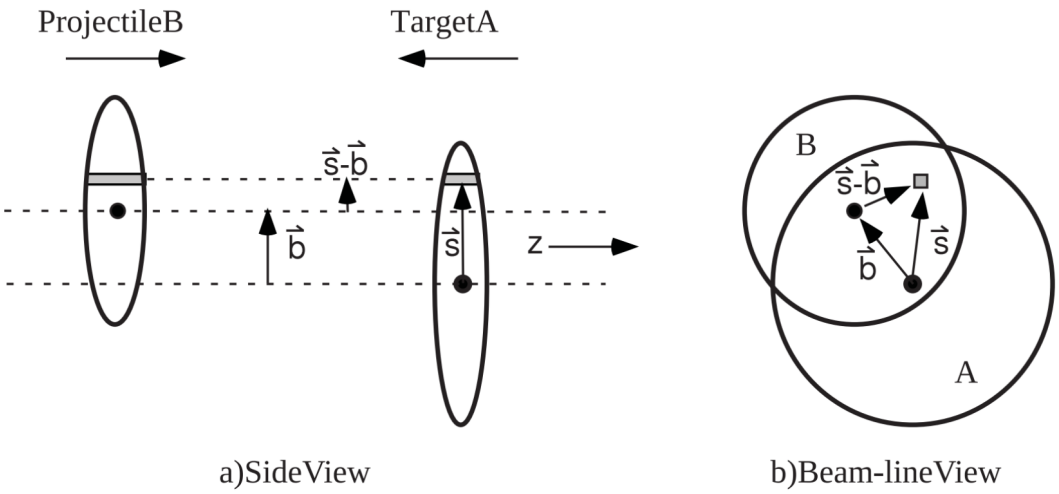

Figure 2.11: Heavy-ion collision seen from the (a) plane parallel to the beam direction and (b) plane perpendicular the beam direction. Picture from Ref. [44].

N_{coll} and number of participants N_{part}. The first one corresponds to the number of individual nucleon–nucleon interactions in A–B collisions, while N_{part} can be understood as the number of nucleons in the overlap region of the two colliding nuclei (the number of nucleons which actually "participate" in the collision). These two quantities relate the properties of the collision with the impact parameter.

A Monte Carlo approach, as shown in Fig. 2.12, is used when we want a more detailed picture. The nucleons of both A and B nuclei are distributed in a three-dimensional coordinate system according to the nuclear density distributions. Random impact parameter b is assigned from the corresponding distribution $\mathrm{d}\sigma/\mathrm{d}b = 2\pi b$ and each process concerning every single nucleon is calculated randomly using the relevant probability distributions. In such scenario the whole collision is evolved and N_{coll} and N_{part} can be calculated.

Unfortunately, neither N_{part} nor N_{coll} can be directly measured by experiments. However, mean values of such quantities can be extracted for classes of measured events (N_{evt}) via a mapping procedure. Typically, a measured distribution is mapped to the corresponding distribution obtained from Glauber calculations. This is done by defining "centrality classes" in both the measured and calculated distributions and then associating the mean values from the same centrality class in the two distributions. The specifics of this mapping procedure differ between experiments as well as between collision systems within a given experiment. An example of such procedure is presented in Fig. 2.13.

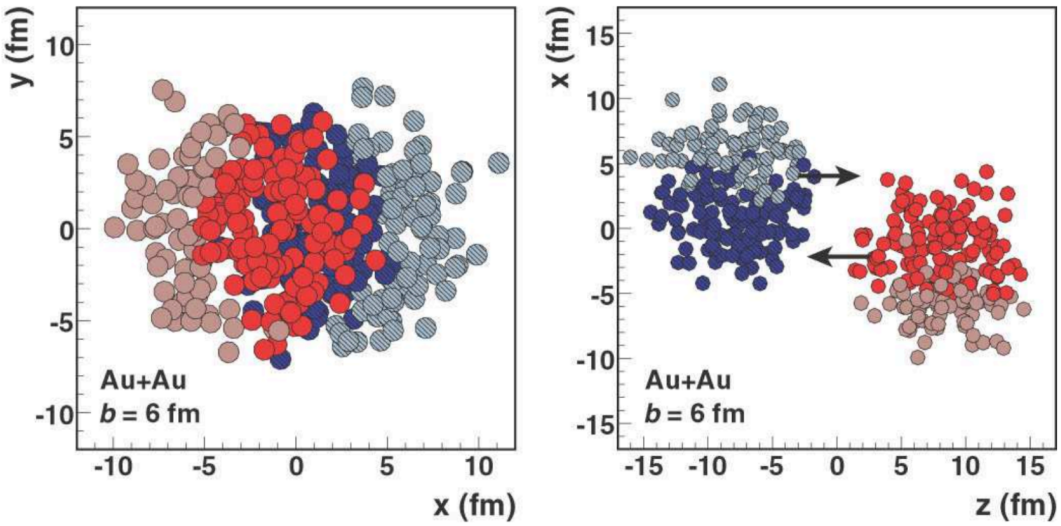

Figure 2.12: Coordinates of the nucleons of Au–Au colliding nuclei at an impact parameter $b = 6$ fm in the Glauber Monte Carlo model. Picture from Ref. [44].

The first event generator which applied the Monte Carlo Glauber model was HIJET [42] and today it is employed by practically all the A–A simulation codes, including HIJING [45], AMPT [46], DPMJET [47], and GLISSANDO [48].

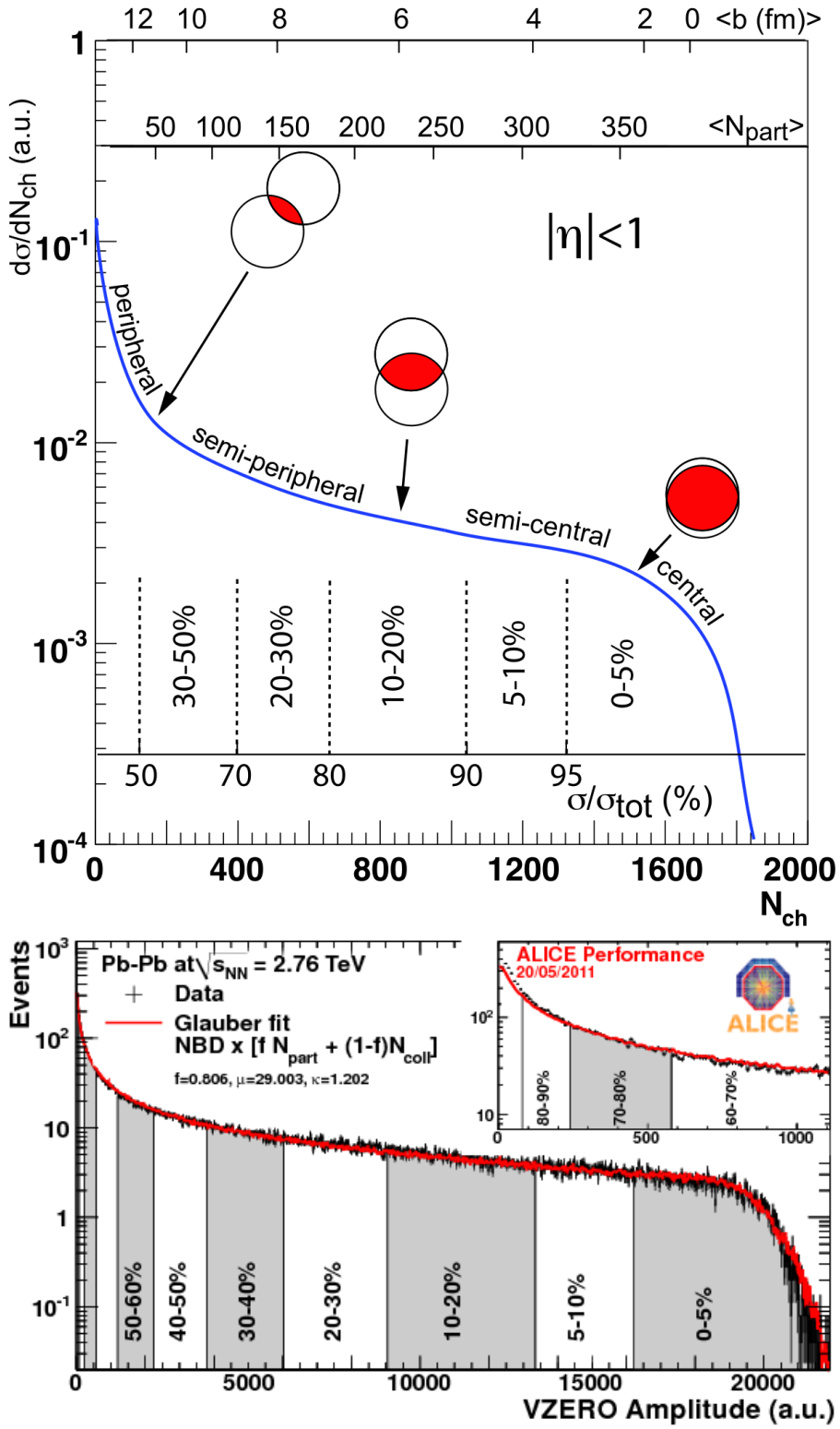

Figure 2.13: Top: A cartoon example of the correlation of the final-state observable N_{ch} with Glauber calculated quantities b and N_{part}. The plotted distribution and various values are illustrative and not actual measurements. Plot from Ref. [44]. Bottom: Measured distribution of the sum of amplitudes in the V0 scintillators from the ALICE experiment. The line shows the fit of the Glauber calculation to the measurement. The centrality classes used in the analysis are indicated in the figure. The inset shows a zoom of the most peripheral region.

2.3.4.2 Color Glass Condensate

Besides the QGP another state of matter, called *Color Glass Condensate* (CGC), is theorized to exist and is anticipated to play an important role in relativistic heavy-ion collisions [49]. The idea of CGC was motivated by the HERA data on the gluon distribution function shown in the left panel of Fig. 2.14. The results show that as the nuclei collide (and eventually form QGP at a later stage), the gluon density rises with the collision energy. These additional gluons must be squeezed together in the Lorentz contracted nuclei. Due to the asymptotic freedom property the strong interaction between them is absent. Therefore, the CGC should be weakly interacting in contrast to the strongly interacting QGP.

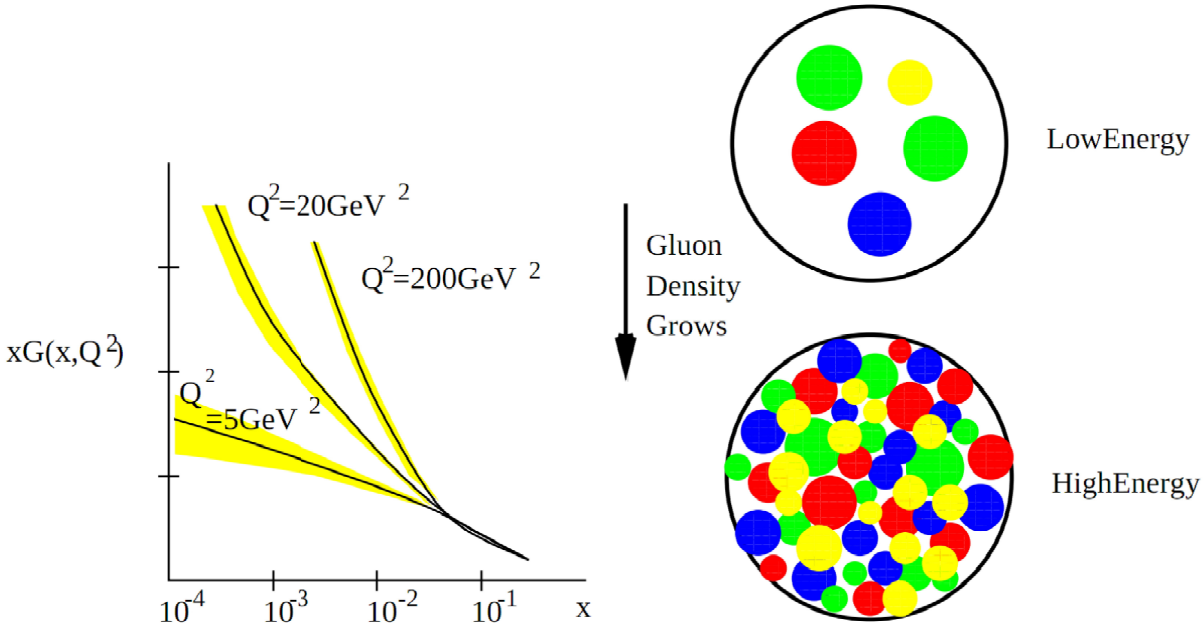

Figure 2.14: Left: Gluon density $xG(x, Q^2)$ as a function of a fraction of longitudinal momentum x for three values of Q^2 from HERA data [50, 51]. Right: Sketch of the increase in gluon density with energy [50].

The weakly coupled dense system is called the Color Glass Condensate for the following reasons:

- **Color** Gluons which form the CGC are colored.
- **Glass** The evolution of the gluons is Lorentz time dilated which is very slow in comparison to the "natural" collision time scales. Such behavior is observed in a glass.

- **Condensate** Due to non-existent strong interaction the quantum mechanical states are multiply occupied. This resembles the Bose-Einstein condensate.

In the CGC there is a critical momentum transfer Q_s^2, called the *saturation scale*. For momentum transfers above this value gluons saturate due to the gluon shadowing process [37]. The saturation scale plays a similar role as the T_C in the QGP – both values define two phases of matter. The difference is that the QGP is strongly coupled while the CGC can be weakly coupled.

The Color Glass Condensate theory can be directly tested at RHIC and LHC in d–A and p–A collisions respectively, where the probability for QGP formation is small. In particular, CGC predicts that the initial system size in p–A collisions should be similar to that observed in pp collisions, at least in the transverse direction [52, 53]. The observation of a larger size in the p–A system with respect to pp would mean that a comparable initial state evolves differently in the two cases, which would be challenging to explain based on CGC arguments alone. Therefore, the results of femtoscopic analysis of p–Pb collisions at LHC, presented in this thesis, may provide important additional constraints on understanding the underlying physics in this system.

2.3.5 Hydrodynamics

The experimental results from heavy-ion collisions at RHIC suggest that the QGP, near the critical temperature, can be described as nearly perfect fluid with the lowest possible viscosity, rather than a gas of free quarks and gluons [54–60]. Therefore, a successful description of the observed collective effects have been achieved using relativistic hydrodynamics (see i.e. Ref. [17, 61–63] for reviews). It is worth to mention that the use of relativistic hydrodynamics in high-energy physics dates back to Landau [35], long before the development of QCD.

We now briefly discuss the concept of a perfect fluid [17]. The ideal fluid is formally defined by the energy-momentum tensor:

$$T^{\mu\nu} = (\epsilon + P)u^\mu u^\nu - Pg^{\mu\nu}, \tag{2.10}$$

where $u^\mu = \gamma(1, \mathbf{v})$ is the four-velocity of a fluid element, $\gamma = (1 - v^2)^{-1/2}$ is the Lorentz factor, $\mathbf{v}$ is the three-velocity, P is the pressure of a fluid element, and $g^{\mu\nu}$ is the metric tensor with $g^{00} = 1$. The energy density ϵ can be treated as a function of the density of baryons n (number

of baryons per fluid element) and entropy density s. The functional dependence of $\epsilon = \epsilon(n, s)$ is called the *equation of state* (EOS). From the conservation laws:

$$\partial_\mu T^{\mu\nu} = 0, \tag{2.11}$$

one can obtain the equations of motion of the ideal fluid.

Modern Monte Carlo models of heavy-ion collisions employ the hydrodynamic description as described above. The main input needed for such calculations are the determination of the QCD phase transition temperature and the form of the equation of state where this transition is included. There is a number of studies aiming to determine both ingredients with the highest precision (see Ref. [64] for recent review).

Recently, after the first p–Pb data from the LHC appeared, the hydrodynamic calculations have been employed in order to verify whether the collective effects are present in such systems. At the moment, current experimental results are still inconclusive and more studies are needed. One of the observables which could lead to the verification of whether collective effects are in fact present in p–Pb is the three-dimensional femtoscopic analysis of identical pions – the analysis which is the scope of this thesis. Therefore, the comparison of Monte Carlo models which assume a hydrodynamic expansion of the system with the experimental results, as shown in Sec. 7.2, is of particular importance.

2.3.6 QGP signatures

The small piece of the Quark-Gluon Plasma produced in a heavy-ion collision is a system which has spatial sizes on the order of a few femtometers (10^{-15} m) and lives for only brief flashes of time (10^{-23} s). No experimental device exists which could measure the properties of such object directly. Therefore, in order to confirm the existence of QGP and understand its properties, we employ various indirect methods which measure the residue signals originating from the QGP state. There is a large variety of such individual probes; however, there is no definite proof. The most important probes are: anisotropic flow (described in Sec. 2.3.6), transverse momentum spectra and yields of identified particles (described in Sec. 2.3.6), emission of direct photons, suppression of J/ψ particle production, jet quenching, enhancement of di-lepton production, strangeness enhancement, and more (for detailed reviews see Refs. [54, 65–67]). The properties of bulk matter can be also obtained from multi-particle correlations (see Sec. 2.5.3); in particular the size and lifetime of the QGP medium can be extracted using the technique of

femtoscopy (two-particle correlations at low relative momenta), which is the scope of this thesis and is described in detail in Chapter 4. The measured source sizes and lifetimes from heavy-ion collisions at several experiments are shown in Fig. 2.15.

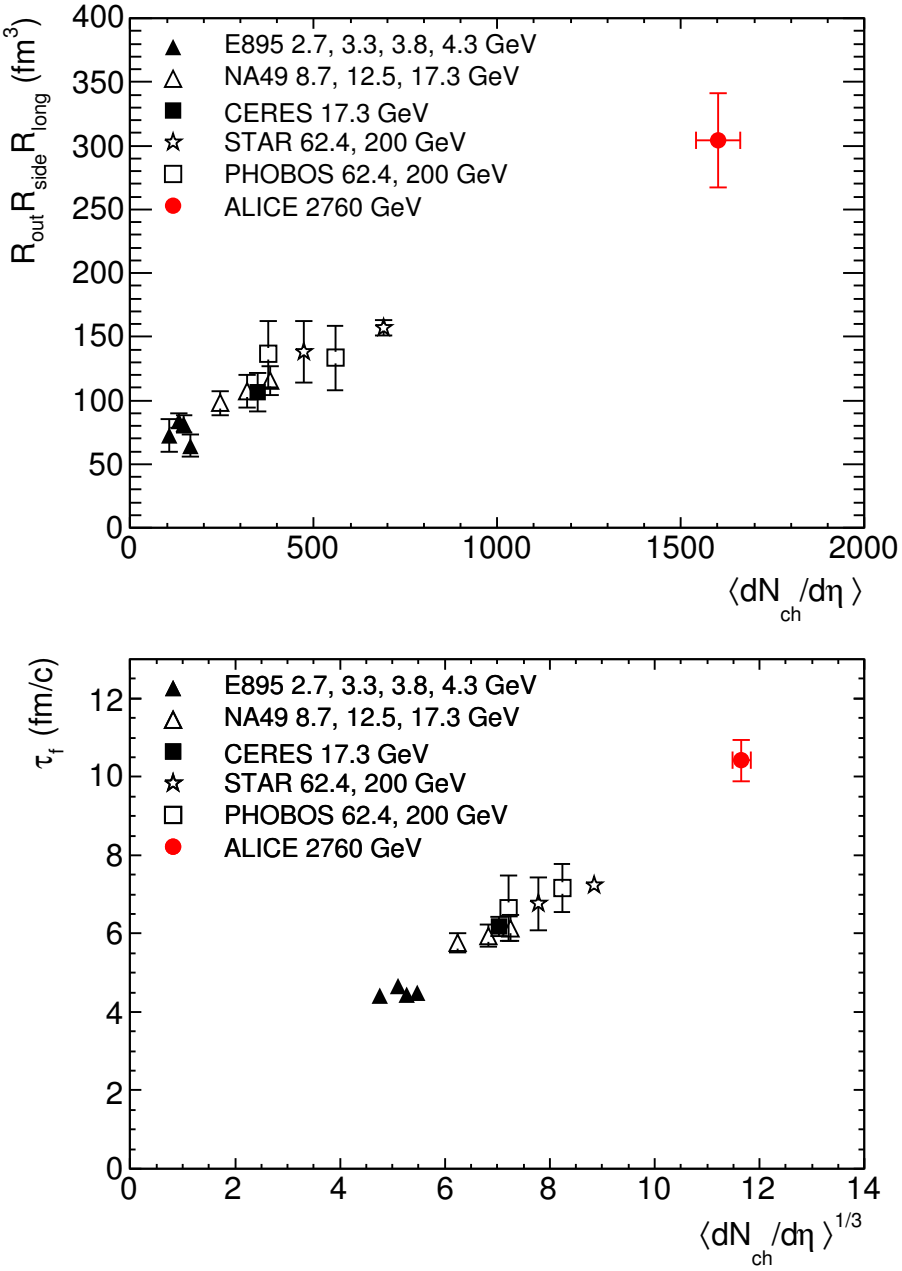

Figure 2.15: World systematics of the source size characteristics as a function of charged particle multiplicity, top: system volume (product of the three pion HBT radii), bottom: the decoupling time extracted from $R_{\mathrm{long}}(k_{\mathrm{T}})$. Plots taken from Ref. [68].

Anisotropic flow

Anisotropic flow, considered as the clearest experimental indication of the collective effects in heavy-ion collisions, is an observable providing information on the transport properties as well as the equation of state of the Quark Gluon Plasma [69–71].

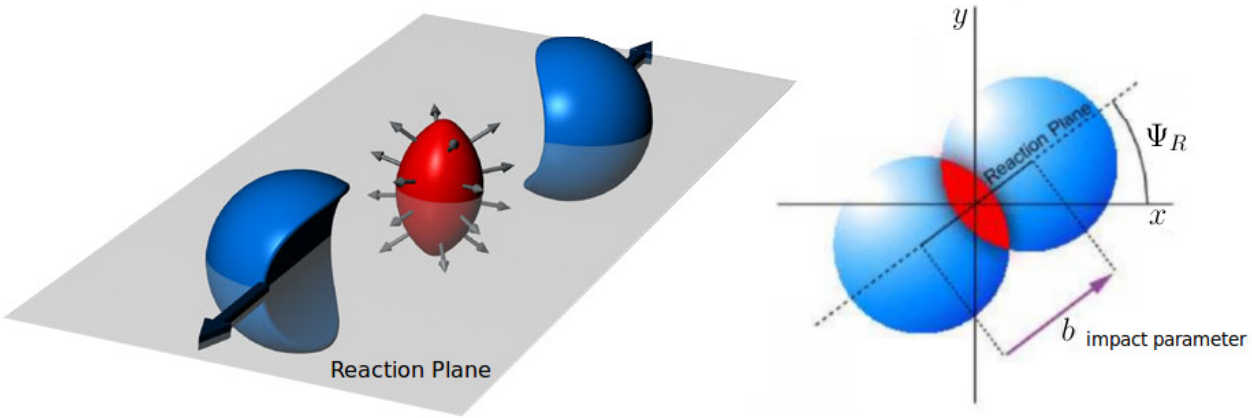

Figure 2.16: Interaction volume created after a non-central heavy-ion collision. The spatial anisotropy with respect to the reaction plane transforms into anisotropy of momentum distribution of the produced particles. Picture from Ref. [69].

Let us focus on non-central collisions (non-zero impact parameter) of two identical spherical nuclei, as shown on the right panel of Fig. 2.16. We can see that the initial overlap zone (particle production region) is asymmetric in the transverse plane (it has an almond-like shape). This spatial asymmetry leads to an anisotropy in particle momentum distributions correlated with the reaction plane (RP). The RP is defined by the impact parameter and the direction of the beam (see left panel of Fig. 2.16). The anisotropic flow is conveniently characterized using a Fourier expansion of the invariant triple differential distributions, which is a periodic even function of azimuthal angle φ:

$$E\frac{\mathrm{d}^3N}{\mathrm{d}^3\mathrm{p}} = \frac{\mathrm{d}N}{\mathrm{d}y p_\mathrm{T}\mathrm{d}p_\mathrm{T}\mathrm{d}\varphi} = \frac{\mathrm{d}N}{\mathrm{d}y p_\mathrm{T}\mathrm{d}p_\mathrm{T}}\frac{1}{2\pi}\left[1 + 2\sum_{n=1}^{\infty} v_n \cos\left(n(\varphi - \Psi_{\mathrm{RP}})\right)\right], \tag{2.12}$$

where E is the energy of the particle, p the momentum, p_T the transverse momentum[5], y is the rapidity, and Ψ_{RP} the reaction plane angle. The Fourier coefficients v_n are referred to as

[5]In high-energy physics the momentum of a particle is usually decomposed into a longitudinal part, p_L, fraction of momentum along the beam axis, and a transverse part defined as $p_\mathrm{T} = \sqrt{p_x^2 + p_y^2}$, where (x, y) is the transverse (perpendicular to the beam axis) plane.

harmonics of the flow and are given by the equation:

$$v_n = \langle \cos\left(n(\varphi - \Psi_{\mathrm{RP}})\right) \rangle \,, \tag{2.13}$$

where the angular brackets denote an average over the particles, summed over all events. The coefficients v_1 and v_2 are known as directed and elliptic flow, respectively.

Figure 2.17 shows the evolution of the interaction volume (the contours represent the energy density profiles). Plots from left to right show how the system evolves from an almond shaped region into an almost symmetric object, while the hot and dense matter cools down.

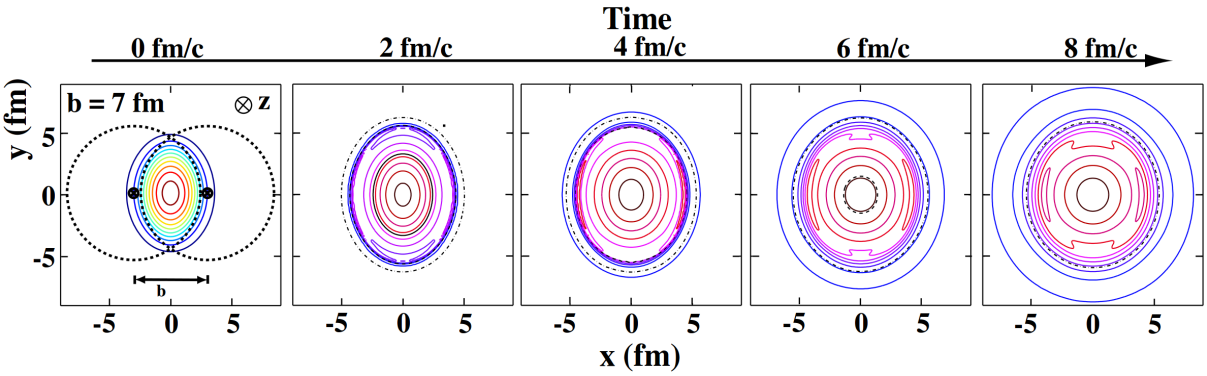

Figure 2.17: The dependence of the energy density profile created in a non-central heavy-ion collision. Plots from Ref. [72].

The discussion presented above assumes that the overlap region has an almond shape. However, the most recent theoretical developments and experimental results suggest that this picture in reality is more complicated [73]. The physicists started to focus on higher order ($n > 2$) components of anisotropic flow. In Fig. 2.18 the overlap region from recent lattice QCD calculations is presented and we can clearly see that the shape of the interaction volume is more complicated than the simple almond shape picture, which leads to non-negligible values of higher components. The result of v_n studies from the LHC experiments are shown in Fig. 2.19. They clearly show that higher order flow components cannot be neglected while describing the bulk properties of the system created in heavy-ion collisions., but the dominant contribution is still v_2.

Moreover, the experiments at RHIC have shown that the elliptic flow, v_2, scales with the number of constituent quarks of a particle in the intermediate p_{T} region [76–80], as shown in Fig. 2.20. The important conclusion which arises from this scaling is that the collective motion is developed before the final-state hadrons are created [81–84], and affects the deconfined

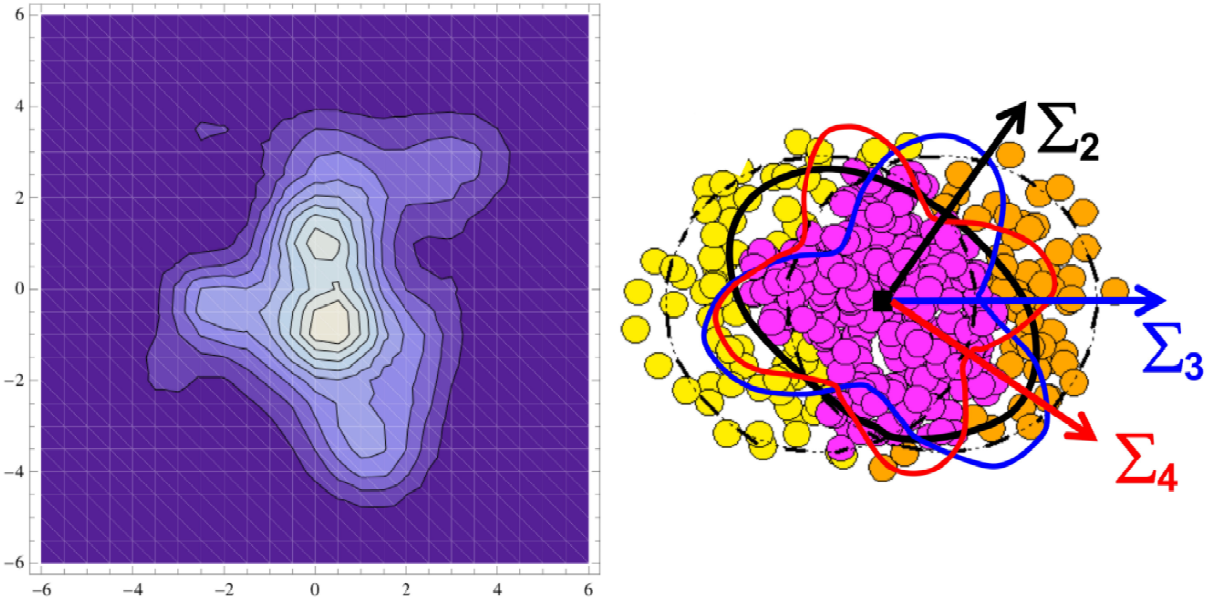

Figure 2.18: Left: The overlap region from lattice QCD calculations showing a much more complicated picture than an ideal almond shape [74]. Right: Artistic impression of the second, third, and fourth transverse flow components [75].

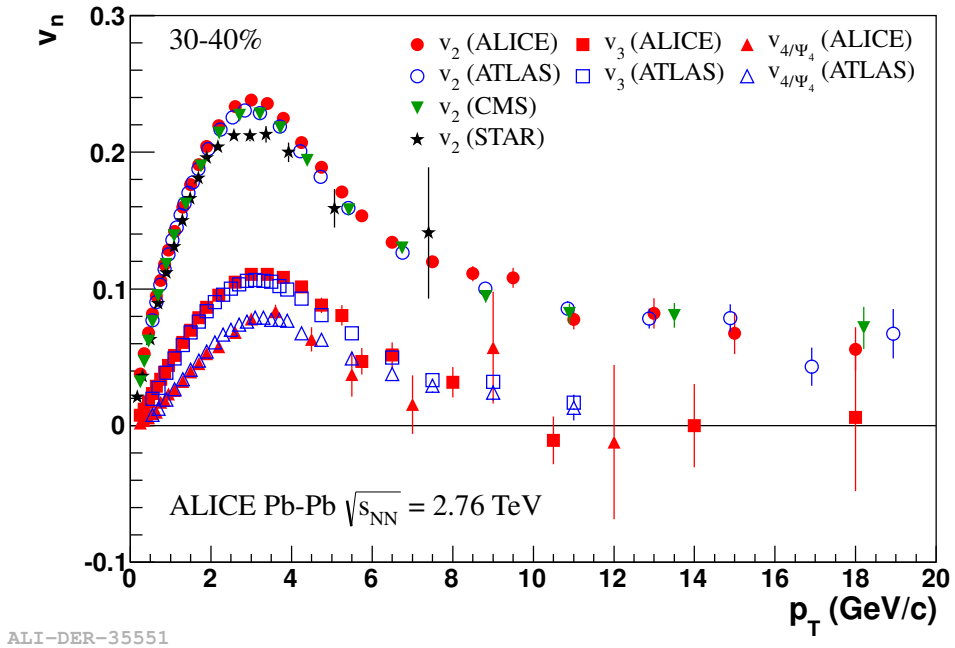

Figure 2.19: Transverse flow components (v_2, v_3, v_4) from the LHC experiments as a function of transverse momentum p_T for 30-40% centrality in ALICE.

partons. This was one of the strongest arguments for the observation of the QGP at RHIC. However, at the LHC, where the collision energies are much higher, the experimental data, as shown in Fig. 2.21, indicate that the scaling is only approximate [85].

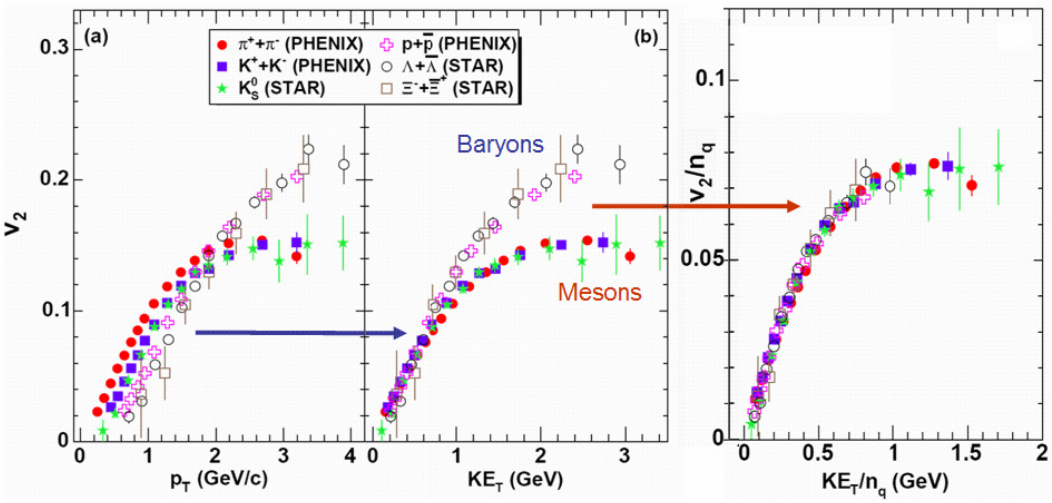

Figure 2.20: The v_2 parameter scaling with the number of quarks for $\pi^{\pm}$, $K^{\pm}$, K^0_s, p+$\overline{p}$, and Λ+$\overline{\Lambda}$ from RHIC experiments. Plots from Ref. [86].

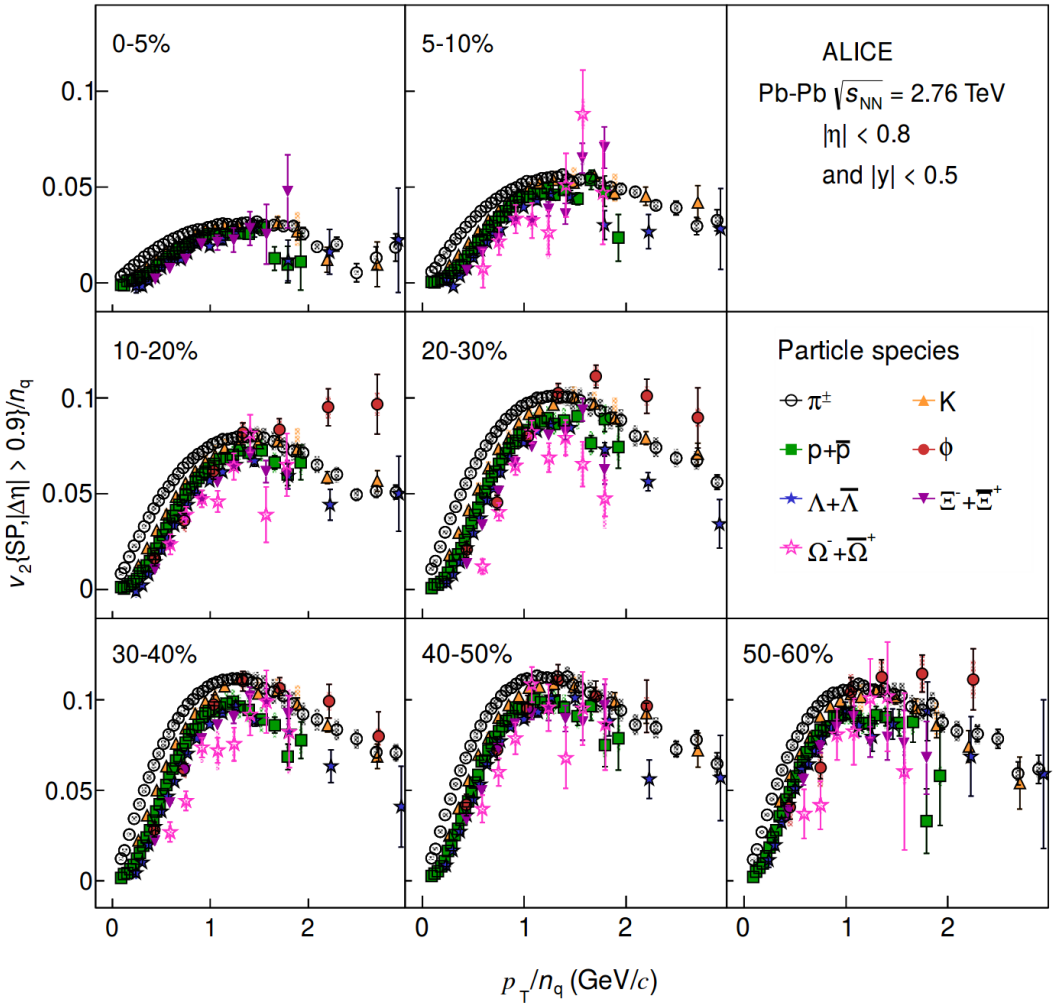

Figure 2.21: The p_T/n_q dependence of v_2/n_q for $\pi^{\pm}$, K, p+$\overline{p}$, ϕ, Λ+$\overline{\Lambda}$, Ξ^-+$\overline{\Xi}^+$ and Ω^-+$\overline{\Omega}^+$ for Pb–Pb collisions in various centrality intervals at $\sqrt{s_{NN}}$ = 2.76 TeV from ALICE. Plots from Ref. [85]

Particle spectra and yields

Thermal and collective properties of the Quark Gluon Plasma can be studied with the transverse momentum distributions (also referred to as p_{T} spectra) and yields of identified particles. The particle abundances measured at RHIC were described by thermal models, which generally are governed by the chemical freeze-out temperature, T_{ch}, and the baryon chemical potential, μ_{B}. The expectations from thermal models are consistent with the particle yields measurements in collisions of heavy ions at RHIC, SPS, and AGS: [87–90]. Since the interactions in the hadronic phase practically do not influence the relative abundances [91, 92], the T_{ch} temperature can be linked to the temperature of the phase transition [93]. The transverse momentum distributions describe the conditions at the "kinetic freeze-out" (the moment when the elastic collisions stop and particle momenta are fixed) and allow to extract its respective temperature T_{kin} [94]. They also allow to extract the information about the radial flow – collective transverse expansion [95, 96]. The predictions based on hydrodynamic and thermal models were also formulated for the LHC [88, 97].

The p_{T} distributions, for combined negative and positive particles, measured by ALICE are shown in Fig. 2.22 [98]. They are compared to results obtained at RHIC in Au–Au collisions at $\sqrt{s_{\mathrm{NN}}} = 200$ GeV [99, 100] as well as to three hydrodynamic models. We can observe a significant change of the distributions while changing the energy from RHIC to LHC. In the range $p_{\mathrm{T}} < 1.5$ GeV/c the viscous hydrodynamic model called VISH2+1 [101] agrees with the pion and kaon distributions. However it misses the protons (both in shape and absolute abundance). This model assumes that the yields are thermal at $T_{\mathrm{ch}} = 165$ MeV. The deviations seen for protons may come from the lack of description of the hadronic phase in VISH2+1. The HKM model [102, 103], in general similar with VISH2+1, agrees with data better; however, it injects the particles after hydrodynamic phase into a hadronic cascade model (UrQMD [104, 105]), which further transports them until final decoupling. The non-negligible hadronic phase results in additional radial flow, which comes mostly due to elastic interactions, and also affects particle ratios due to inelastic interactions. This result means that at the LHC these interactions (especially the baryon-antibaryon annihilation) in the hadronic phase are not longer negligible and must be taken into account in the description of particle yields [103, 106]. The third model shown in Fig. 2.22 is Kraków model [107, 108]. It assumes viscosity at the phase transition and therefore provides additional non-equilibrium corrections which change the effective T_{ch}, and

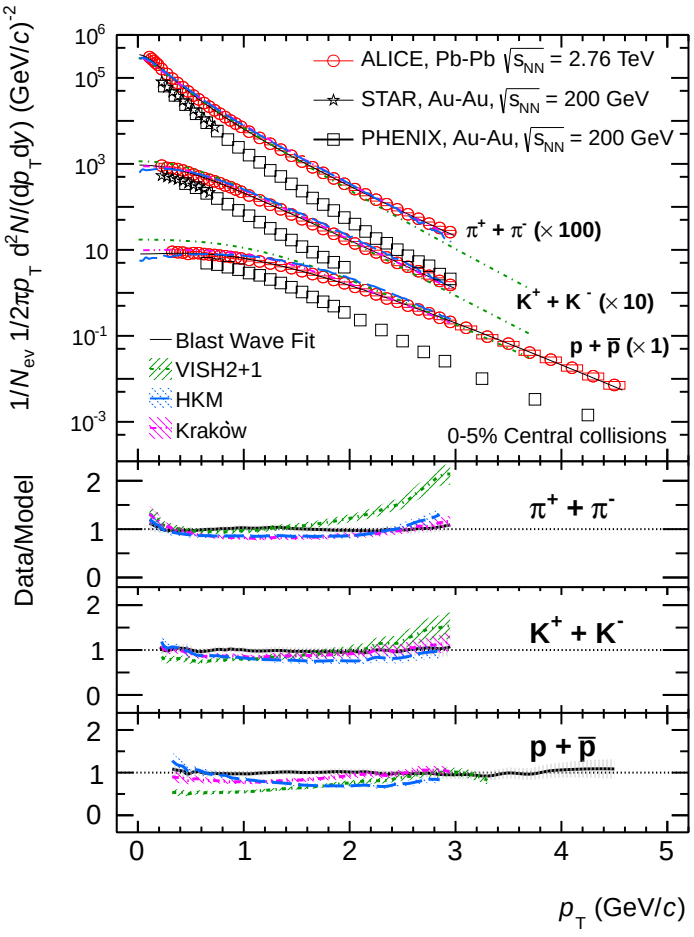

Figure 2.22: Transverse momentum distributions of the sum of positive and negative particles from ALICE (box: systematic errors; statistical uncertainties smaller than the symbol for most data points), fitted individually with a blast wave function, compared to RHIC data and hydrodynamic models. Plot from Ref. [98].

therefore lead to a good agreement with the data.

It is therefore very important to verify the hypothesis of baryon-antibaryon annihilation playing an important role in the description of particle yields. We stress that UrQMD relies only on theoretical assumptions about the annihilation cross-sections since no measurements for most of the baryon-antibaryons systems are available (see Sec. 4.7 for details). The femtoscopic measurements of such pairs can provide this information and are an important ingredient in understanding the last stages of heavy-ion collisions at LHC. The preliminary results of one of such systems, correlations of protons (antiprotons) with antilambda (lambda) hyperons, are shown in Chapter 9.

2.4 pp and p–A collisions as reference for heavy-ion physics

The QGP probes need to be very precisely defined and tested. This validations require benchmark processes with elementary systems, where the QGP is not formed and therefore the final-state phenomena (such as collective behavior of QCD matter) are absent. To some extent such benchmarking can be performed using proton-proton (pp) collisions, where both initial and final-state medium effects are absent. However, proton-nucleus collisions are crucial for completeness because of the presence of the initial-state effects and absence of final-state ones [109].

Comparisons of small (i.e. pp) and big (heavy-ion) systems were not straightforward in the past. The results were obtained from different experiments, which had different acceptance, kinematic ranges to select particles of interest and even different definitions of the key observables (i.e. multiplicity). All these aspects made apples-to-apples comparisons between elementary and heavy-ion systems very difficult, if not impossible.

Today, all the heavy-ion dedicated experiments at relativistic energies at LHC, RHIC, and SPS, study elementary collisions as well. When exactly the same detector, with comparable experimental conditions, is employed, the comparison of the results is significantly simplified and undesired detector biases are reduced.

This collision picture (A–A: initial- and final-state medium effects, p/d–A: initial-state medium effects, pp: no initial- and final-state medium effects) was widely established until the year 2013, when the first p–Pb data from LHC arrived. Detailed analysis of high-multiplicity p–Pb collisions at LHC as well as d–Au at RHIC revealed that many observables do exhibit apparent final-state signatures which can be described by collective motion of matter. The most important results of p–Pb run at the LHC are discussed in Sec. 2.5.

2.5 Highlights of p–Pb results at the LHC

Since large part of this thesis is devoted to the analysis of the p–Pb data, this section presents selected results from the p–Pb run at the LHC, focusing on particle production, spectra of identified particles, multi-particle correlations, and nuclear modification factor. Most of the results presented below were obtained with the ALICE detector, which is described in detail in Chapter 3.

2.5.1 Charged-particle pseudorapidity density

The effects which are present in the initial-state are expected to influence the production of particles in p–Pb collisions. The implementation of these processes differ between various Monte Carlo Models, thus resulting in different predictions of the charged-particle pseudorapidity density. Therefore, the measurements of particle production in p–Pb collisions can constrain the models and expand our understanding of p–Pb collisions.

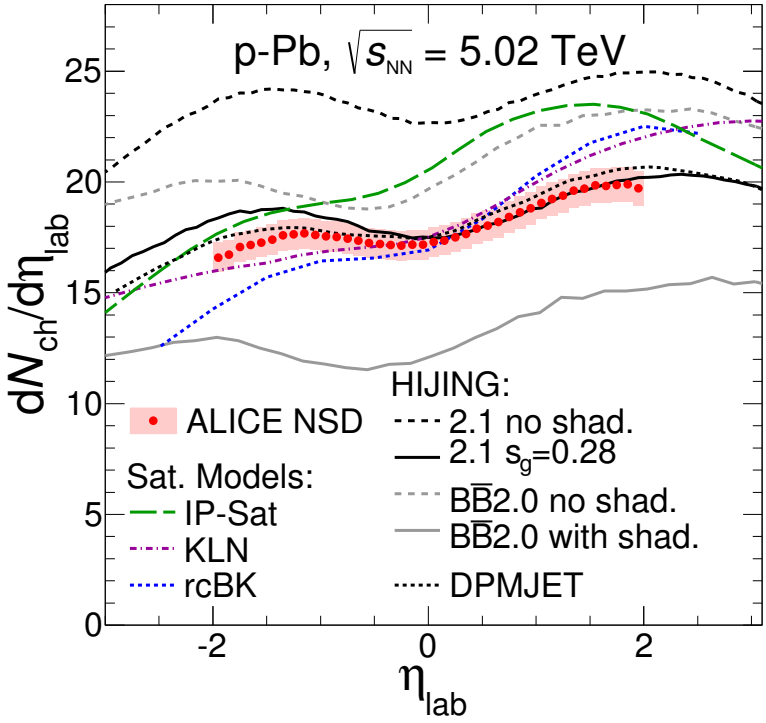

Figure 2.23: Pseudorapidity density of charged particles measured in the laboratory system (η_{lab}) for non-single diffractive p–Pb collisions at $\sqrt{s_{\mathrm{NN}}}$ = 5.02 TeV compared to model predictions. Plot from Ref. [110].

Figure 2.23 shows the $\mathrm{d}N_{\mathrm{ch}}/\mathrm{d}\eta_{\mathrm{lab}}$ distribution measured by ALICE in p–Pb collisions at $\sqrt{s_{\mathrm{NN}}}$ = 5.02 TeV. One can observe a clear forward-backward asymmetry between the proton and lead hemisphere. The experimental results are compared to various Monte Carlo models [111–115] describing similar measurements in other collision systems. The models which include the so-called shadowing mechanism [115] or saturation mechanism [111, 112], approximately agree with the measured $\mathrm{d}N_{\mathrm{ch}}/\mathrm{d}\eta_{\mathrm{lab}}$ value. In particular, HIJING 2.1 model [115], which has been tuned to describe the RHIC data [116, 117], describes the ALICE pseudorapidity distribution pretty well.

The results of charged-particle pseudorapidity density measurements performed by ALICE are presented in Ref. [110].

2.5.2 Identified particle spectra

More information about p–Pb collision is expected to be obtained from the measurements of identified particle spectra. The transverse momentum p_{T} spectra of pions, kaons, and protons (π^+/π^-, K^+/K^-, and p/$\bar{\mathrm{p}}$) were measured by CMS [118] and ALICE [119].

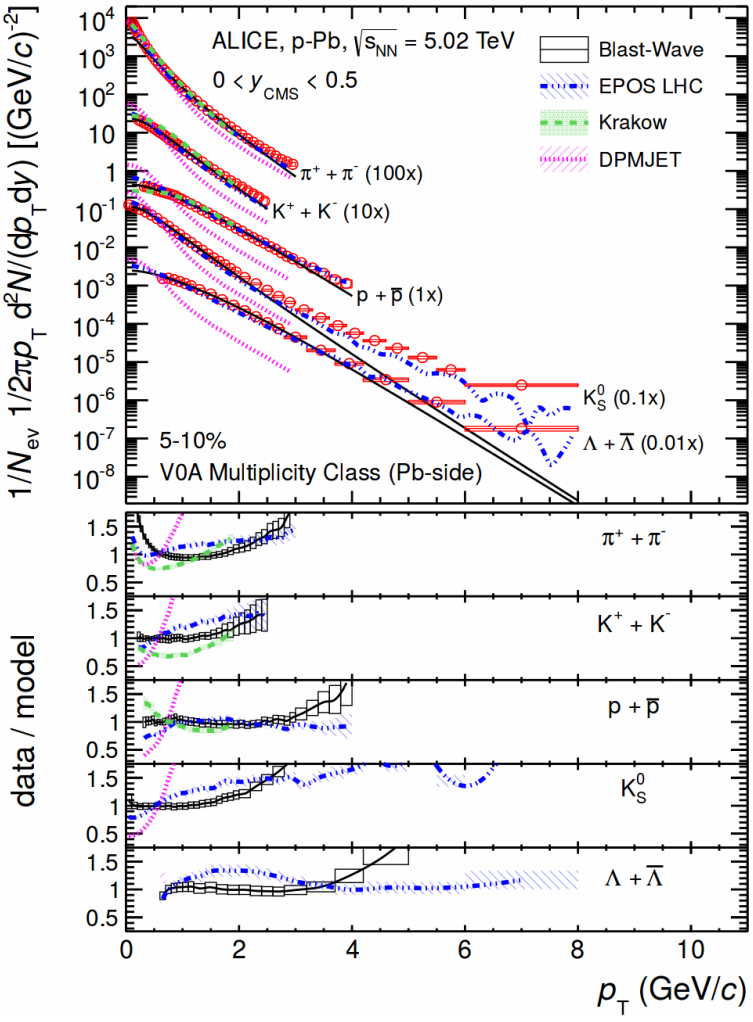

Figure 2.24: Transverse momentum distributions of identified charged hadrons (pions, kaons, protons) from ALICE. Measured values are plotted together with predictions from EPOS LHC 1.99 v3400 [120], Kraków [121], and DPMJET [47] models. Plot from Ref. [119].

Results obtained with the ALICE detector are presented in Fig. 2.24 and compared to several models. One can see that DPMJET overpredicts the data for all particles for p_{T} lower than

around $0.5 - 0.7$ GeV/c. For higher momenta it underpredicts the data. On the other hand, for high transverse momenta (above 1 and 1.5 GeV/c, respectively), the shapes of the spectra of pions and kaons. For lower momenta the inclusion of effects present in the hadronic state may be needed in order to describe the data. The Kraków model agrees with the data for pions and kaons for transverse momenta below 1 GeV/c, where hydrodynamic description is expected work. The differences which are seen for pions and kaons at higher momenta may be explained in a hydrodynamic framework as due to the onset of a non-thermal component. We observe around 20% agreement between EPOS model and data for pions and protons over the full transverse momentum range. However, kaons and lambdas exhibit larger differences. The p_{T} spectra shapes of protons are quite well reproduced by both Kraków and EPOS models. Finally, when the final-state effects are switched off in EPOS, significantly more differences between the model and data are observed [120].

2.5.3 Multi-particle correlations

The angular correlation analysis in $(\Delta\eta, \Delta\varphi)$ space (where $\Delta\eta = \eta_1 - \eta_2$ is the pseudorapidity difference and $\Delta\varphi = \varphi_1 - \varphi_2$ is the azimuthal angle difference between two particles) provides important information for the characterization of the underlying mechanism of particle production in both elementary and heavy-ion collisions. For instance, in pp collisions the correlation at $(\Delta\eta \approx 0, \Delta\varphi \approx 0)$, known as the "near-side" peak, and at $\Delta\varphi \approx \pi$, known as the "away-side" ridge, originate from particle production related to jets [122, 123]. On the other hand, in A–A collisions additional long-range structures emerge along $\Delta\eta$ on the near- and away-side. The shape of these structures is typically quantified by Fourier coefficients v_n which are related to the geometry and density fluctuations of the colliding nuclei in hydrodynamic models [124]. Unexpectedly, it has been observed that at high multiplicity pp collisions at $\sqrt{s} = 7$ TeV a similar long-range $(2 < |\Delta\eta| < 4)$ structure, called "the Ridge"[6], emerges on the near-side [130]. The origin of the ridge has been connected to the effects present either in the initial-state (such as gluon saturation and color connections forming along the longitudinal direction) or in the final-state effects (such as parton-induced interactions, and collective effects [127]). A similar ridge structure, with the strength of the correlation stronger than in collisions of protons, is observed

[6]Capital letter used deliberately. Due to the notoriety of this effect in the recent years, referring to "the ridge" without further explanation is usually a relation to this particular structure [125–129].

also in p–Pb collisions at $\sqrt{s_{\mathrm{NN}}}$ = 5.02 TeV [131]. Subsequent measurements [132, 133] show that in addition to the near-side ridge there is also similar ridge on the away-side, what can been seen in Fig. 2.25. Similar long-range structures have been found also in high-multiplicity d–Au collisions at $\sqrt{s_{\mathrm{NN}}}$ = 200 GeV at RHIC [134].

The p_{T} dependence of the extracted v_2 and v_3 coefficients from two-particle correlations is found to be similar to that measured in Pb–Pb collisions, as can be seen in Fig. 2.26. The differences between the two systems become visible for $v_2\{4\}$, which is obtained by extracting the four-particle correlations using the cumulants method [135]. The integrated $v_2\{4\}$, as well as $v_2\{2\}$, are smaller than in Pb–Pb collisions at the same multiplicity. This is presented in Fig. 2.27.

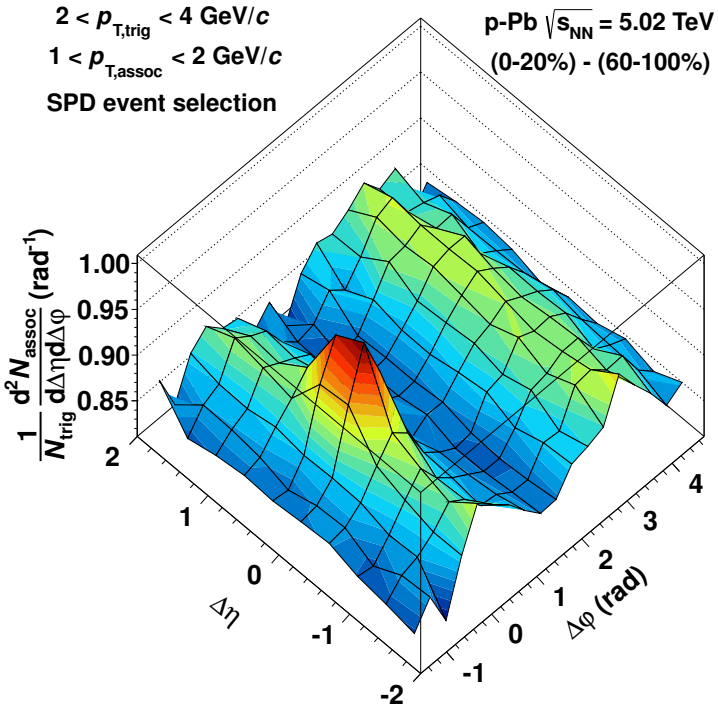

Figure 2.25: The angular correlations in $\Delta\varphi$ and $\Delta\eta$ for pairs of charged particles in p–Pb collisions at $\sqrt{s_{\mathrm{NN}}}$ = 5.02 TeV from ALICE for the 0–20% event class, after subtraction of the yield obtained in the corresponding 60–100% event class. Plots from Ref. [132].

The results of angular correlations in p–Pb collisions basically have two different interpretations: in the first scenario they can be described by a quantum interference between rapidity-separated gluons enhanced by gluon saturation in the Color Glass Condensate framework [52, 138], while in the second scenario they can be described in the hydrodynamic framework, where similarly as in heavy-ion collisions, they originate from the strong final-state inter-

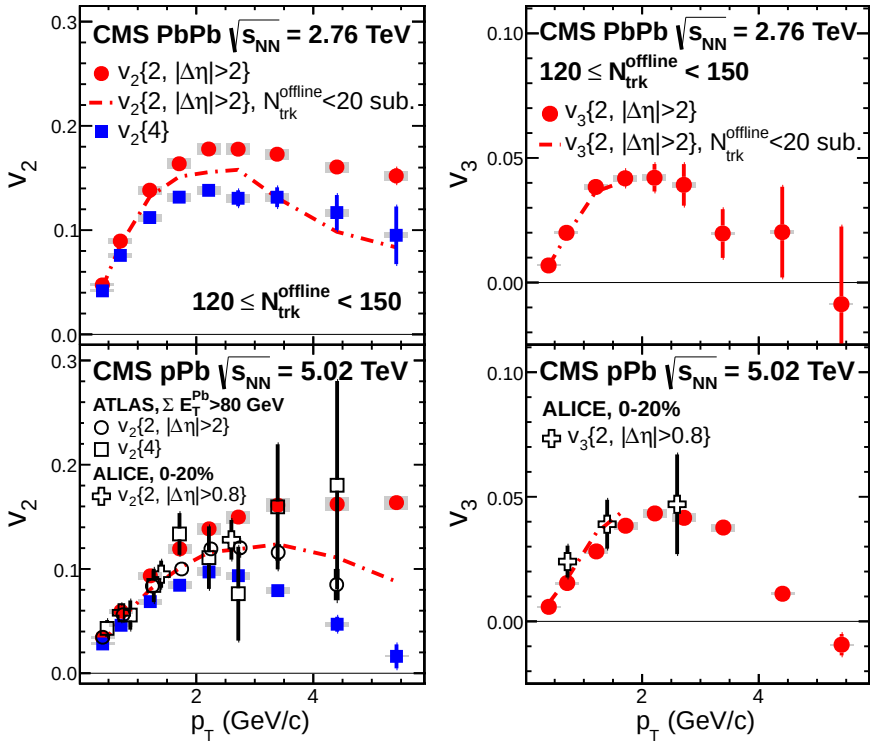

Figure 2.26: The p_{T} differential v_2 (left panels) and v_3 (right panels) distributions in Pb–Pb collisions at $\sqrt{s_{\mathrm{NN}}}$ = 2.76 TeV (top panels) and p–Pb collisions at $\sqrt{s_{\mathrm{NN}}}$ = 5.02 TeV (bottom panels) for similar multiplicity interval. The results of CMS (full points) are from Ref. [136], of ALICE (hollow crosses) are from Ref. [132], and of ATLAS (hollow circles and squares) are from Ref. [133] and Ref. [137].

actions and collective motion [139–141]. However, only the hydrodynamic models are currently able to reproduce the v_3 result. Therefore, it is argued that the rare nucleon density fluctuations cause the observed effects [142]. We can also observe that the $v_2\{4\}$ and $v_3\{2\}$ in p–Pb and Pb–Pb, at fixed multiplicity, are similar to each other. This is interpreted as the collective response to the fluctuations of clusters [143]. However, the applicability of hydrodynamic models to systems like p–Pb (or high multiplicity pp) is not straightforward, most of all because of their significant dependence on the fluctuations in the initial-state as well as necessity of applying too large viscous corrections, which may be unreliable [53].

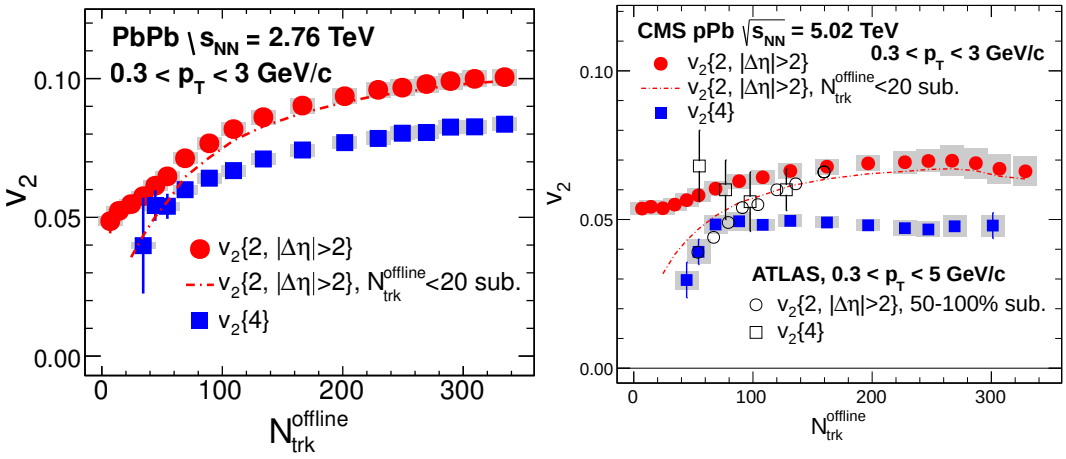

Figure 2.27: Integrated $v_2\{2, |\Delta\eta| > 2\}$, $v_2\{2, \text{sub}\}$ and $v_2\{4\}$ values as a function of number of tracks N_{trk} in Pb–Pb collisions at $\sqrt{s_{\text{NN}}} = 2.76$ TeV (left panel) and in p–Pb collisions at $\sqrt{s_{\text{NN}}} = 5.02$ TeV (right panel). Plots from Ref. [136]

2.6 Monte Carlo models of high-energy particle collisions

All the effects and phenomena describing high-energy, elementary or heavy-ion, collisions arise from experimental observables based on the detection of hundreds of particles which are being produced. This is a very complex environment and the only possibility to test our understanding of the underlying physics mechanisms is to simulate such collisions in great detail, from the two approaching particles accelerated to the highest energies to the final-state products which can be seen by the detectors. For this purpose the so-called *event generators* have been developed. They are sophisticated computer programs which incorporate the known physics as well as phenomenological approaches where no theoretical solutions exist, aiming to produce events which could be directly comparable to the experimental ones. All the event generators share an extensive use of random number generators, hence the name Monte Carlo (MC). The MC selection of some input variables for the generation process ensures the randomness of the final event. This allows us to generate hundreds of thousands of events and perform statistical analysis as it is done in the real experiment. We may say that a generated event is a product of our current understanding and implementation of known physics as seen by the ideal detector.

Event generators serve several important purposes. The main applications include planning of new analysis strategies (the generated events give an idea of what should be expected), designing of a new experiment/detector (they can be used to optimize the detector performance) or

corrections for detector acceptance and inefficiencies (generated events, together with software responsible for simulating the detector response, can be used to eliminate or correct for undesired detector effects in the experimental data so the "true" physics message can be extracted). They also allow a convenient comparison between experimental data and the underlying theory. These are only few out of many more applications of Monte Carlo event generators.

In this thesis the Monte Carlo models are used for the description of unwanted particle correlations which blur the femtoscopic signal as well as for comparisons with the final result in order to understand the underlying physics. The non-femtoscopic correlations are described by PYTHIA 6.4 [144], Perugia-0 tune [145] and EPOS 3.076 [146, 147], which are elementary event generators. The final results are compared with model predictions employing hydrodynamic evolution of the system [148, 149].

Chapter 3

A Large Ion Collider Experiment

3.1 Large Hadron Collider

The *Large Hadron Collider* (LHC) [150] is a particle accelerator built and operated by the European Organization for Nuclear Research (CERN). LHC is a circular collider where two beams of particles are accelerated in opposite directions and brought to collide head-on. The accelerator is designed to collide protons and lead ions at energies up to $\sqrt{s}$ = 14 TeV and $\sqrt{s_{\mathrm{NN}}}$ = 5.52 TeV, respectively; however, these energies have not yet been reached.

LHC is located in an underground tunnel of 27 km circumference, about 50–100 meters below surface, at the French-Swiss border, just a few kilometers from the center of Geneva. It is the result of almost 25 years of planning and construction by a collaboration of around 10,000 scientists and engineers from all over the world. The machine was fully completed in 2008 and started its operation in the summer of that year. However, on 19th September 2008 during the commissioning phase, a massive magnet quench took place which caused an extensive leakage of liquid helium, used for the cooling of the superconducting magnets, as well as major damage to some parts of the LHC. For the next year repair and upgrade works were carried on in order to prevent similar incidents in the future. Finally, the machine successfully delivered the first pp collisions at $\sqrt{s}$ = 900 GeV on 23rd November 2009. Since that time the LHC has been operating without any major problems and delivered hundreds of millions of collisions with maximum energies of $\sqrt{s}$ = 8 TeV for pp, and $\sqrt{s_{\mathrm{NN}}}$ = 2.76 TeV for Pb–Pb. Although not initially planned, LHC was able to deliver asymmetric collisions of protons and lead ions at collision energy of $\sqrt{s_{\mathrm{NN}}}$ = 5.02 TeV. After the successful p–Pb run in the beginning of 2013 the machine was shut down for a scheduled period of almost 2 years for planned repairs and upgrades. The restart with higher energies is expected in the beginning of 2015.

A schematic view of LHC together with the full CERN accelerator complex is shown in Fig. 3.1. A number of smaller accelerators are used as intermediate steps before the beam is injected to the LHC. In addition, they have their own and successful physics programs.

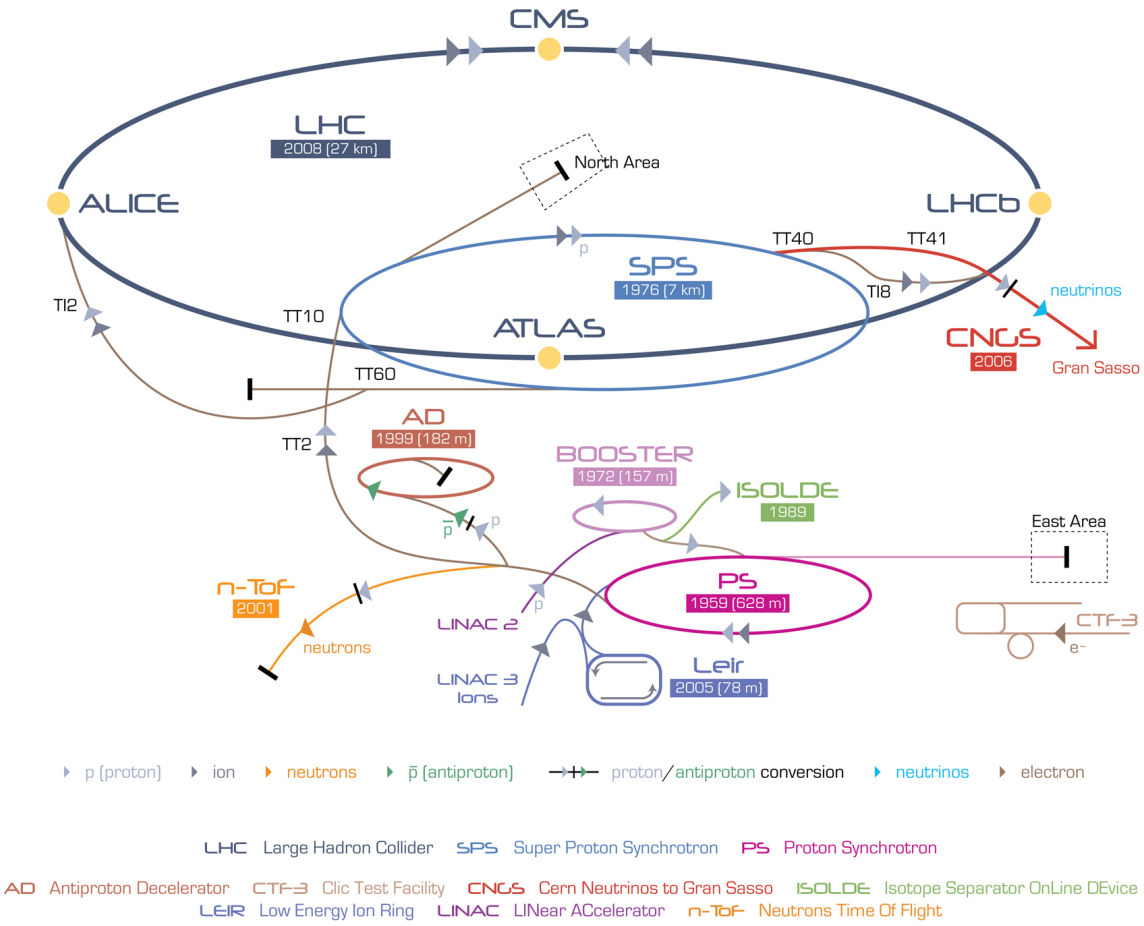

Figure 3.1: CERN accelerator complex. Picture from Ref. [151].

3.2 ALICE experiment

A Large Ion Collider Experiment (ALICE) [152] is one of the four large experiments at the LHC. The first proposal of the detector was created in 1993 [153] and approved for construction later in 1997. Generally speaking, ALICE is optimized to study all aspects of heavy-ion collisions delivered by the accelerator; however the proton-proton collisions are measured and studied as well. The main scientific goal of ALICE is to measure and characterize the properties of the Quark Gluon Plasma, which could lead to new discoveries at the highest collision energies achieved at the LHC. This section briefly describes the ALICE subdetector systems, focusing especially on those which have been used in the analysis presented in this thesis.

We stress that the content of this section has been published by the author in the conference proceedings available in Ref. [154], which itself is based on the official and detailed description of ALICE available in Ref. [152].

3.2.1 Experimental setup

The ALICE detector is located at Intersection Point 2 of the LHC in a French town of Saint Genis-Pouilly, about 40 m below the ground level. It is 16 m high, 16 m wide, 26 m long, and weights approximately 10,000 tons. It came as a result of two decades of design and construction performed by a collaboration which currently includes over 1,200 scientists and engineers from more than 120 institutes in more than 30 different countries.

There are 18 different detection systems used in the experiment. Each one of them is constructed using dedicated technology, with its own design constraints, and generally serves for different purposes. What makes ALICE unique from other high-energy physics experiments is tracking and particle identification (PID), which can be performed over a large momentum range: from a few MeV/c up to 100 GeV/c. This capabilities allow to study both *soft* and *hard* physics effects. Moreover, ALICE was designed in the way that the acceptance is large enough to study the particle ratios, p_{T} spectra, as well as Bose-Einstein correlations. In order to fully exploit the Pb–Pb collision at the highest energies, the experiment was constructed assuming the possibility measure and track up to 8,000 charged particles per unit rapidity. The layout of the ALICE experiment, with all detector systems, is shown in Fig. 3.2.

3.2.1.1 Inner Tracking System

The *Inner Tracking System* (ITS) [156] is the subdetector closest to the interaction point. The basic functions of ITS are the determination of the primary vertex (the point where the beams cross and collisions occur) and of the secondary vertices (the points where the unstable heavy particles decay), with a precision on the order of few tens of micrometers, necessary for the reconstruction of short-lived charm and hyperon particles. In addition, it is used for PID of low-momentum particles and improvements of the momentum and angle measurements of the main tracking detector – the Time Projection Chamber.

The ITS comprises six layers of high-precision silicon detectors, with double-sided silicon strips (SSD – Silicon Strip Detector) in the outer two layers, silicon drift detectors (SDD) in

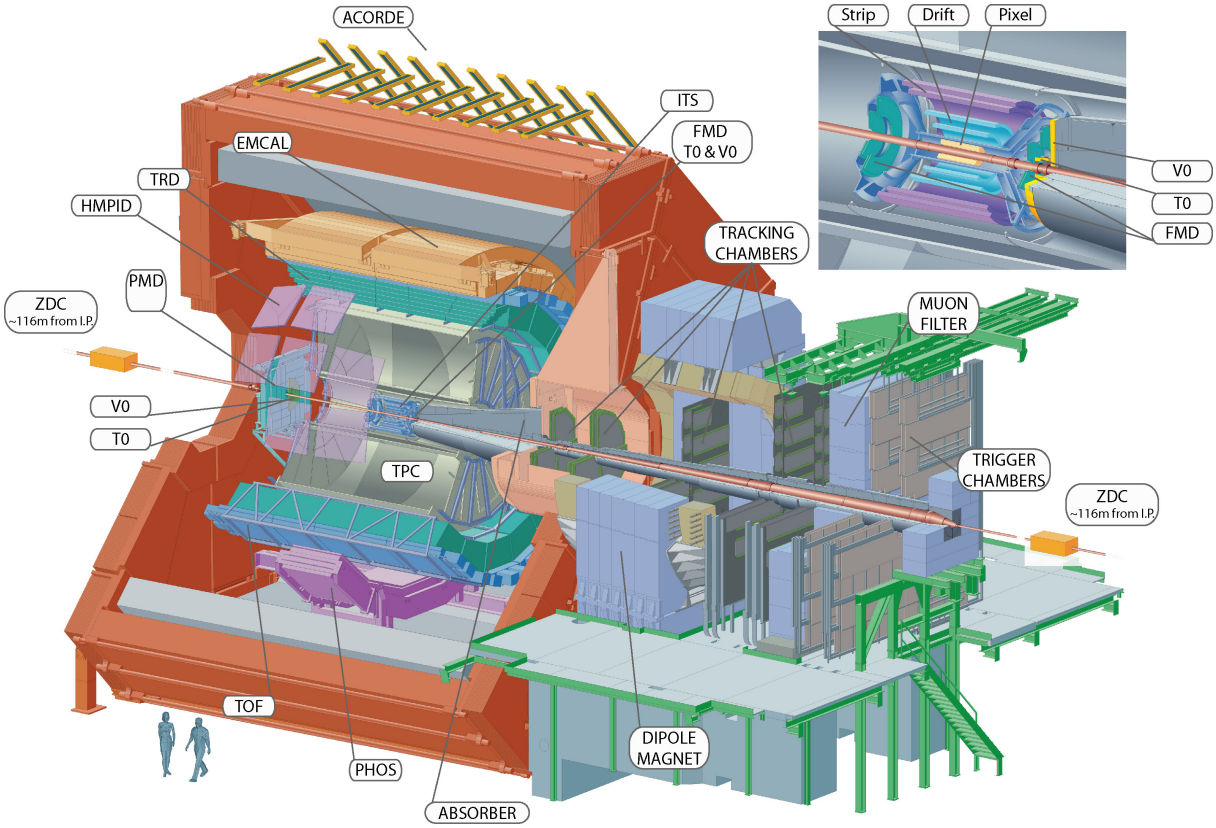

Figure 3.2: The ALICE experiment at LHC. Picture from Ref. [155].

the middle two layers and silicon pixels (SPD) in the two inner layers. The collision point is surrounded by the detector layers which measure the properties of the emerging particles, such as their trajectories and energy loss. The ITS recognizes particles containing heavy quarks by identifying the secondary vertices (points at which they decay). The detector layout is shown in Fig. 3.3 [156].

Silicon Pixel Detector

The two innermost layers, called *Silicon Pixel Detector* (SPD) [156], are based on hybrid silicon pixels which consist of silicon detector diodes. All detector elements were carefully optimized to minimize the material budget, achieving a radiation length of at most 1.1% X_0 per layer. Unlike the rest of the detectors in the main barrel the first SPD layer has a larger acceptance $|\eta| < 1.95$, this is so that in combination with the Forward Multiplicity Detector charged particle multiplicities can be provided over the full rapidity range.

The SPD is fundamental in determining the quality of the vertexing capability of ALICE (determination of the position of the primary vertex). It was designed to operate in a region

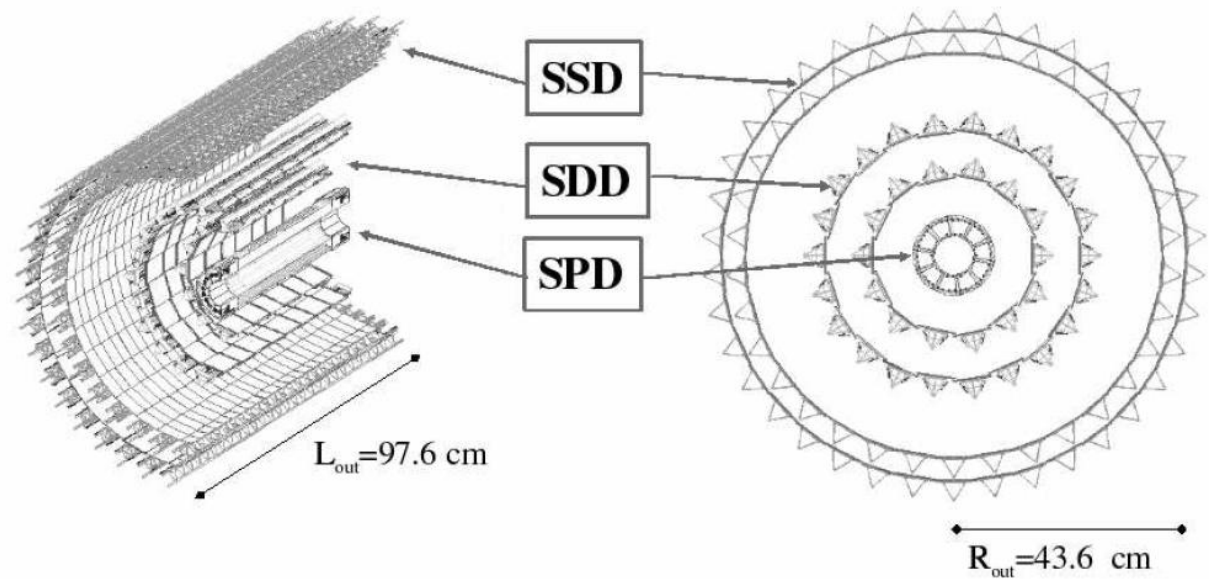

Figure 3.3: Layout of the Inner Tracking System. Picture from Ref. [157].

where the track density was expected to exceed 50 tracks/cm^2. This made it necessary to use a detector of high precision and granularity. In addition, the detector was required to operate in a relatively high-radiation environment. The SPD is very thin allowing minimal energy to be deposited in it and it is also able to withstand large radiation doses, since it is so near to the interaction point.

The spatial resolution of the SPD is 50 μm in the (r, φ) plane for particles with $p_{\mathrm{T}} >$ 1.3 GeV/c.

Silicon Drift Detector

The two middle layers of ITS are called *Silicon Drift Detector* (SDD) [156]. When a charged particle passes through the silicon, it excites electrons and leaves a trail of them which are attracted towards the n^+ type semiconductor, as in Fig. 3.4. The detector gives high precision position information and also provides the energy loss per unit path dE/dx information for PID. However, the downsides of the SDD are long readout time and sensitivity to temperature changes, down to about 0.1 K; so, efficient cooling systems and heat shields have been put in place for the SSD and SPD.

Modules of the SDD provide an average spatial resolution of 35 mm in the (r, φ) plane and 25 mm in the z direction.

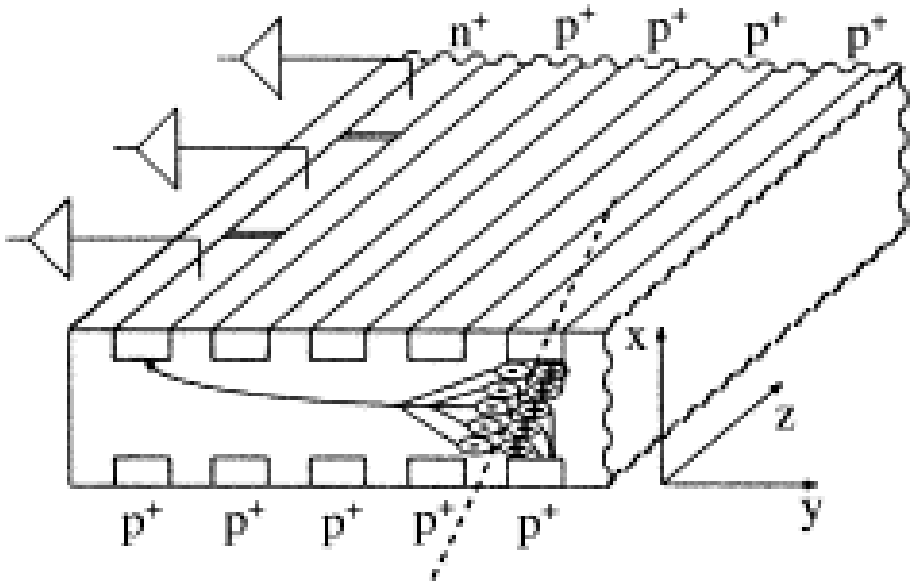

Figure 3.4: The Silicon Drift Detector operation.

Silicon Strip Detector

The two outermost layers are called *Silicon Strip Detector* (SSD) [156]. These are double sided detectors with silicon micro-strips located at radii of 38 and 43 cm respectively, covering $|\eta| < 0.9$. Strips are arranged under a small stereoscopic angle, which allows two-dimensional measurements of the track position together with an energy-loss measurement for the particle identification.

The importance of the SSD is in the connection of tracks from the TPC to the ITS. It also provides $\mathrm{d}E/\mathrm{d}x$ measurement to help identify low-momentum particles.

The spatial resolution of the SSD is 20 mm in the (r, φ) plane and 830 mm in the z direction.

3.2.1.2 Time Projection Chamber

The main tracking device in the ALICE experiment is the *Time Projection Chamber* (TPC) [158]. It is located between radii of 0.85 m and 2.5 m (sensitive volume) and has a length of 5 m. It provides information about charged particles (their momenta, positions of vertices and particle identification). Figure 3.5 shows a schematic picture of the TPC. It is a gas detector with a volume of 90 m^3, filled with a Ne-CO_2-N_2 gas mixture. A drift field of 100 kV stretches between the central electrode (which is located at $z = 0$) and the two readout planes at $z = 2.5$ m and $z = -2.5$ m.

The readout of the signal is performed by 570132 pads of 3 different sizes which form the

cathode of the Multi-Wire Proportional Chambers (MWPC) located at the TPC end caps. The end caps are segmented into 18 trapezoidal sectors. These sectors are divided radially in two chambers with varying pad sizes, optimized for the radial dependence of track density. Pads are organized in 159 rows radially.

The TPC is able to track particles in the pseudorapidity range of $|\eta| < 0.9$ for full radial length and up to $|\eta| < 1.5$ for 1/3 radial length. Particles with transverse momenta p_{T} from about 200 MeV/c (at nominal magnetic field of 0.5 T) up to 100 GeV/c can be measured. The momentum resolution of the tracks is better than 2.5% for tracks with a momentum below 4 GeV/c. The TPC allows up to 8,000 tracks per unit of rapidity in one collision event to be reconstructed and identified.

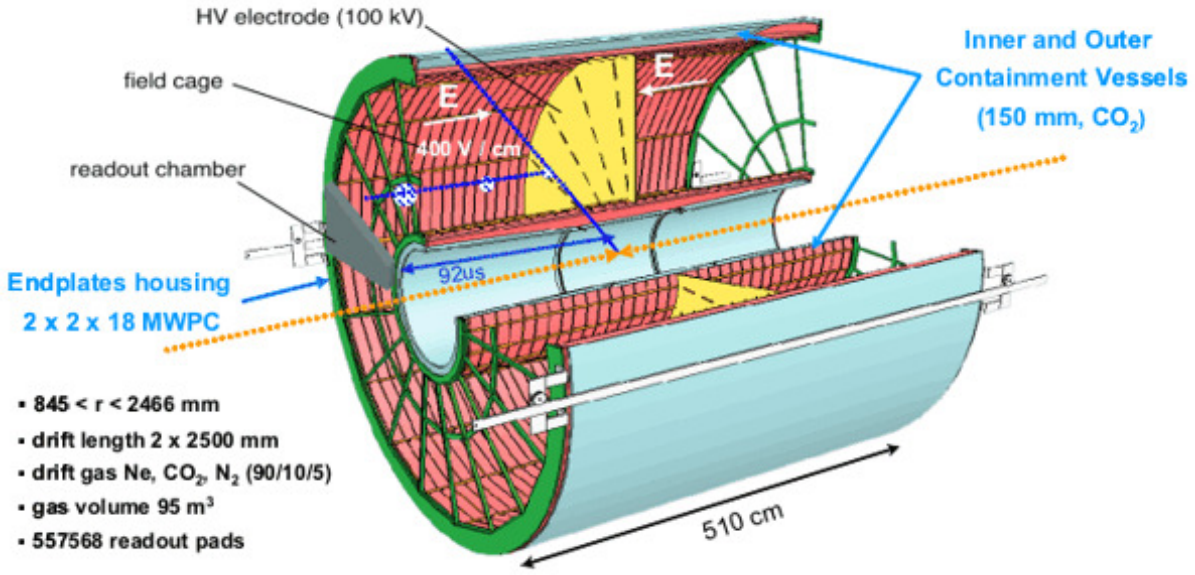

Figure 3.5: The Time Projection Chamber layout [155].

3.2.1.3 Transition Radiation Detector

The main task of the Transition Radiation Detector (TRD) [159] is to distinguish electrons from pions. The detector is located at radii from 2.9 m to 3.7 m. It is segmented into 18 sectors, each one consisting of six layers. It was added to the ALICE setup at a later stage, because simulations of first ALICE designs had shown a poor ability to identify electrons and pions. Their improved detection allows to provide better measurements of J/ψ production through its di-electron decay channel. The TRD combined with the ITS and TPC improves the accuracy of

particle tracking. Its resolution in the (r, φ) plane is 600 μm for high multiplicity events.

The detector measures the transition radiation which is produced when a charged relativistic particle passes through two media with different dielectric constants. The radiator is the innermost layer of the TRD and it consist of a foam. The charged particle (i.e. electron) passes through it and since the dielectric constant alternates between the foam and the air this will produce a transition radiation X-Ray (if the momentum of a particle is big enough - in the case of an electron $p_{\mathrm{T}} > 1$ GeV/c). This radiation is then absorbed in a drift chamber module, which contains a gas of Xe$-CO_2$ in a 85/15 ratio in a strong electric field. When the charged particle enters that region, the ionization trail is produced. The electrons coming from the ionization drift outwards towards the outer part of the chamber and are amplified, as in Fig. 3.6. The readout of these electrons is done by the pads on the outside and then they are analysed by the Front-End Electronic on top of the chamber. The TRD differentiates between pions and electrons, because when the electron or pion passes through the drift chamber the ionisation produced by each of them is different.

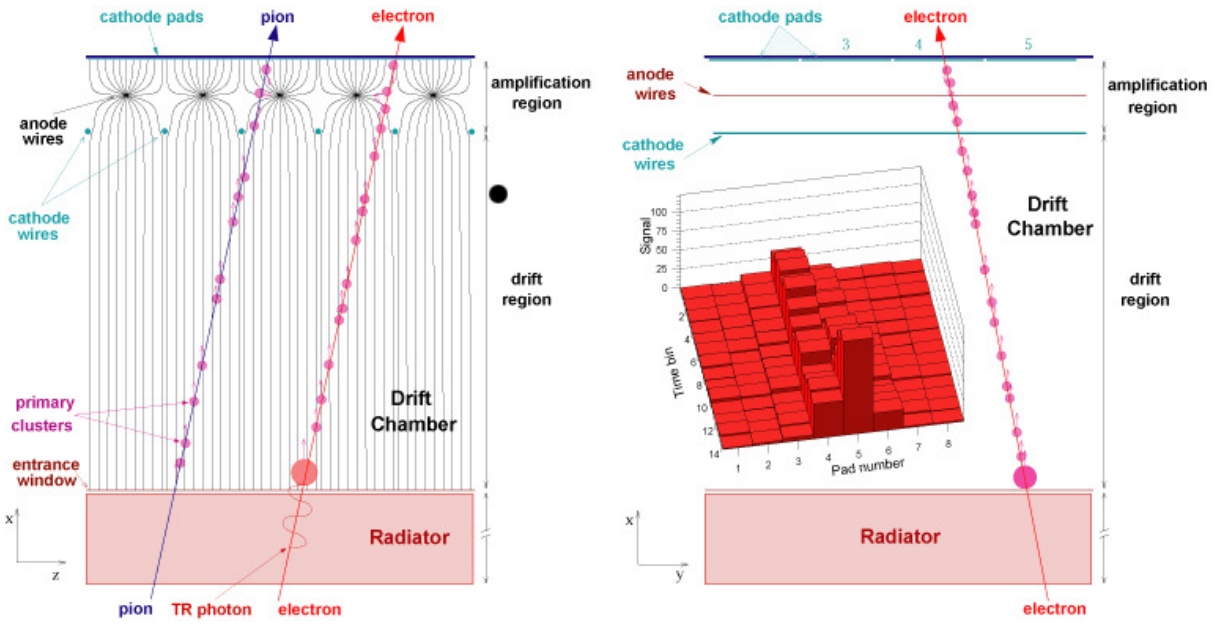

Figure 3.6: The Transition Radiation Detector drift chambers with a pion and high energy electron producing transition radiation.

3.2.1.4 Time-Of-Flight Detector

The *Time-Of-Flight Detector* (TOF) [160], at 3.7 m from the beam line, covers a cylindrical surface of polar acceptance from 45 to 135 degrees and has a full azimuthal coverage in φ angle.

It uses MRPC (Multigap Resistive Plate Chamber) strips. The TOF modules are arranged in a similar scheme to the ones of the TRD.

The main task of TOF is to improve particle identification. It is capable of identifying charged particles (pions, kaons, protons), in the intermediate momentum range (0.2−2.5 GeV/c) and in polar angle range $|\theta - 90°| < 45°$ i.e. in roughly the same range in pseudorapidity as the TPC, by measuring the time between the collision and the arrival of the particles in the TOF.

3.2.1.5 V0 detector

The V0 detector (also referred to as *VZERO*) [161] is a pair of forward scintillator arrays located on each side, A ($\eta > 0$) and C ($\eta < 0$), of the interaction point. They are called V0A and V0C, respectively. The detector records the amplitude as well as the arrival time of signals produced by charged particles. It also serves as the main interaction trigger.

V0C and V0A are located 90 cm and 340 cm from the TPC center on opposite sides of ALICE, respectively. They consist of four rings covering pseudorapidity ranges of $-3.7 < \eta < -1.7$ for V0C and $2.8 < \eta < 5.1$ for V0A. Eeach ring covers the full azimuth and is segmented into 8 sectors which are read independently.

3.3 ALICE software environment

3.3.1 ROOT

The ROOT system [162, 163], being developed at CERN since 1995 [164], is a cross-platform framework created for storage and analysis of petabytes of data in an efficient way. ROOT is written in object-oriented C++ language and contains tools for advanced statistical analysis (classes for multi-dimensional histogramming, fitting, minimization, etc.), visualization (classes for 2D and 3D graphics with an OpenGL interface), a rich set of container classes, remote database access (i.e. for GRID connection), and a C++ interpreter called CINT which allows to execute simple C++ scripts.

Nowadays ROOT is the most commonly used tool within the high-energy physics community around the World (by both theoretical and experimental physicists), but has also gained users from other fields of science.

3.3.2 AliRoot

AliRoot [165] is the name of ALICE offline framework for simulation, reconstruction and analysis. It uses the ROOT system as a foundation for ALICE-specific framework and applications. It is therefore a complete environment needed to handle and analyze data recorded by ALICE experiment. AliRoot contains full representation of ALICE detector geometry as well as full simulation and reconstruction environment. It also includes full reconstruction chain and the analysis code.

It is worth to mention that the output of the simulation process has similar format as the data stream from Data Acquisition System (DAQ) [166]. This feature has several important advantages. It allows to check the influence of detector itself (the geometry, electronics response, and reconstruction process) on the reconstructed data – we know what is the difference between pure simulation data and fully reconstructed data. This is essential for testing the analysis software as well as for comparison with the Monte Carlo models developed by the theorists.

AliRoot, except for large existing libraries, such as GEANT 3 [167], GEANT 4 [168], FLUKA [169], JETSET [170], and some remaining legacy code, is fully based on the Object-Oriented programming paradigm and is written in C++.

3.3.3 GRID

One of the big challenges for the LHC experiments is the very large data volume which needs to be stored and analyzed. It is not possible for a single university or research institute to provide sufficient computing power and storage for the data coming from LHC. Only ALICE experiment, since its start of operation in 2009, has already delivered almost 27 PB of raw data as of August 2014. Moreover, the storage requirements must include backup copies, space for users and results of their analyses. This is far beyond what any single computing facility can provide. The solution for these challenges is the *GRID computing* concept and ALICE realization of it is called ALICE GRID Environment, or simply AliEn [171].

The idea of the GRID computing extends the concept of World Wide Web (WWW) – it is not only sharing of information but also sharing of computing power and data. The participating institutes connect their computing centers to the GRID network and the data registered by the experiment is distributed to all of them, according to their computing and storage capabilities. The end-user (a physicist performing the analysis) does not care where the data is – one specifies

the type of data which has to be analyzed and provides the analysis code (this process is called *job submission*). The rest is handled by GRID which looks up the data and books the computing power in the computing centers connected to the GRID. Here another advantage of the GRID system manifests – full parallelization of the analysis. Each particle collision is by definition a separate process from the statistical point of view – there is no physics law which connects two collisions. Therefore, exactly the same analysis code can be split and executed on many machines in different computing centers on different sets of data (these are called *subjobs*) and produce the results in exactly the same format. When the job ends `AliEn` can merge the results from different subjobs and save the final file which is then accessible to the user. From the user perspective it can happen that a physicist submits his/her job from Warsaw which will be then analyzed in the USA on data requested from South Africa and the final result will be stored in Japan.

Figure 3.7 shows the ALICE GRID online monitoring tool, called MonALISA [172], with the location of computing centers connected to the ALICE GRID network around the World.

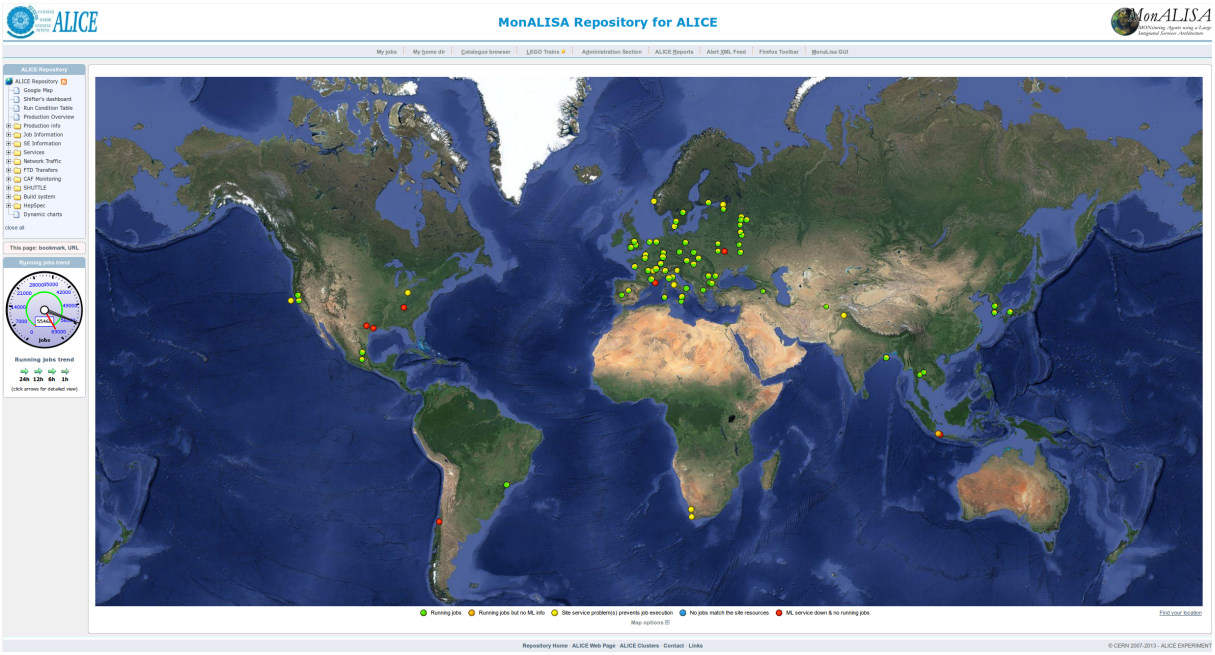

Figure 3.7: MonALISA – ALICE GRID monitoring webpage [172]. Dots on the map show locations of computing centers around the World which are connected to the ALICE GRID and are used to store and analyze ALICE data. Different colors correspond to the actual operational status.

3.3.4 AliFemto

The analysis was performed using the `AliFemto` package which is a part of the `AliRoot` framework of the experiment [173]. It is based largely on the `StHbt` framework, used since 1999 in the STAR experiment at RHIC. `StHbt`, itself, was developed by femtoscopy experts from earlier heavy ion experiments at the AGS and SPS; as such, it distills the generic features of any femtoscopic analysis. `AliRoot` is provided without any restrictions by the CERN Git repository system and is accessible under this link [174]. The `AliFemto` package is accessible in the `AliRoot` directory: `$ALICE_ROOT/src/PWGCF/FEMTOSCOPY`.

Several developments of `AliFemto` were needed to perform the analysis presented in this thesis. In the case of p–Pb studies, modifications were required in order to read the new data as well as additional selection criteria, specific for this collision system (i.e. pile-up rejection procedure and different multiplicity estimators; for details see Chapter 6), had to be introduced by the author. In the case of the correlations of protons and lambda hyperons in Pb–Pb collisions, a completely new part of `AliFemto` was implemented. Lambda is a heavy unstable particle which is registered in the experiment by the detection of its decay products. For this purpose dedicated algorithms are employed (for details see Chapter 9). Since `AliFemto` had not been used for the analysis of such particles before, a new set of interface classes which use these algorithms and allow to provide different selection criteria were developed by the author.

Chapter 4

Two-particle correlations at low relative momentum

The technique of two-particle correlations in momentum space, called *femtoscopy*, is used to measure sizes of the order of a single nucleon. Femtoscopy uses the momentum distribution of particle pairs to calculate the space-time characteristics of the emitting source.

4.1 Hanbury-Brown Twiss effect

Historically, the technique is based on the correlation measurements developed in astronomy. In 1954 astronomer Robert Hanbury-Brown and mathematician Richard Twiss [175, 176] proposed a method of measuring the angular sizes of stars by studying the intensity of electromagnetic waves emitted from a stellar source and registered by two detectors on Earth (such a device is called an intensity interferometer). The intensity interferometry is known today as *Hanbury-Brown Twiss effect*, or shortly HBT.

The underlying principle of HBT interferometry is the following. The amplitude of the electromagnetic waves registered by the two detectors located at points $\mathbf{x}_3$ and $\mathbf{x}_4$ is a superposition of waves emitted from points $\mathbf{x}_1$ and $\mathbf{x}_2$ in a stellar source. Detectors measure amplitudes of signals as a function of the distance between them $d = |\mathbf{x}_3 - \mathbf{x}_4|$. From the correlation between both signals, one can calculate the momentum characteristics of the source and the angular size of the star can be derived. Figure 4.1 presents a sketch of the general principle of the intensity interferometry.

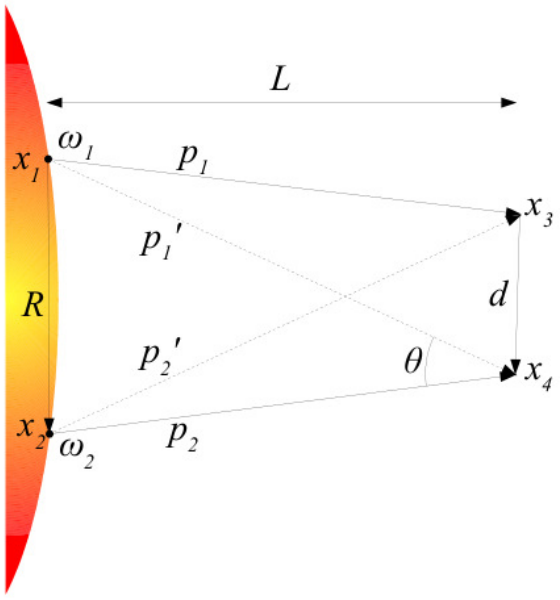

Figure 4.1: Hanbury-Brown Twiss interferometry in astronomy. Picture from Ref. [177].

4.2 Intensity interferometry in particle collisions

The interferometry method used in particle collisions is similar to the classic HBT, but it is not the same. In femtoscopy one measures the momenta distributions of particles registered in the detectors and from this information one can obtain the space-time characteristics of the sources. The idea of intensity interferometry in particle collisions is shown in Fig. 4.2.

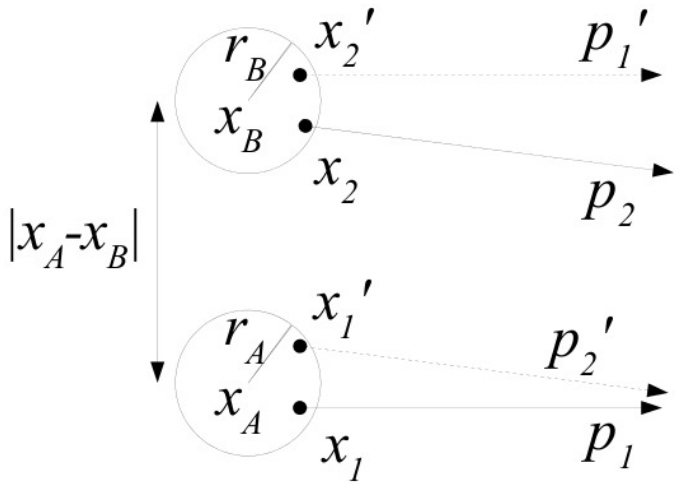

Figure 4.2: Hanbury-Brown Twiss interferometry in particle collisions. Picture from Ref. [177].

Generally speaking, "classic" HBT measures correlations in space (relative separation of detectors) to determine the widths of the momentum distribution of the star which can be con-

verted to angular size. Femtoscopy measures correlations in relative momentum to obtain the information about the size of the emitting region in space [178–180].

Two particles are emitted from points $\mathbf{x}_1$ and $\mathbf{x}_2$ of the two emitting sources. We can treat them as two incoherent waves. Usually we assume that the sizes of the emission regions are small (this is one aspect of the so-called *smoothness approximation*). This means also that:

$$\mathbf{x}_1 \approx \mathbf{x}_1^{'} \approx \mathbf{x}_\mathrm{a}, \qquad \mathbf{x}_2 \approx \mathbf{x}_2^{'} \approx \mathbf{x}_\mathrm{b}. \tag{4.1}$$

We can introduce $\mathbf{x}$, which is the distance between emitting sources:

$$\mathbf{x} = \mathbf{x}_1 - \mathbf{x}_2 \approx \mathbf{x}_\mathrm{a} - \mathbf{x}_\mathrm{b}. \tag{4.2}$$

If we now consider that particles are identical (for example identical pions) two scenarios must be studied. The first scenario is that a particle with momentum $\mathbf{p}_1$ is emitted from point $\mathbf{x}_1$ and a particle with momentum $\mathbf{p}_2$ from point $\mathbf{x}_2$. The second possible scenario is symmetric – a particle with momentum $\mathbf{p}_1$ is emitted from point $\mathbf{x}_2$ and a particle with momentum $\mathbf{p}_2$ is emitted from point $\mathbf{x}_1$. The wave function of the pair is a linear combination of both scenarios (both have the same probability). Therefore, the pair wave function has the following form:

$$\Psi_{12} = \frac{1}{\sqrt{2}}\left(e^{i\mathbf{p}_1\mathbf{x}_1 + i\mathbf{p}_2\mathbf{x}_2} \pm e^{i\mathbf{p}_1\mathbf{x}_2 + i\mathbf{p}_2\mathbf{x}_1}\right). \tag{4.3}$$

This is well-known in quantum mechanics where the wave function of the pair must be symmetrized ("+" sign in Eq. (4.3)) for bosons which obey the Bose-Einstein statistics, and anti-symmetrized ("−" sign in Eq. (4.3)) for fermions due to the Pauli's exclusion principle, as they obey the Fermi-Dirac statistics.

In the following sections we will describe how this purely quantum effect can be employed to measure the size.

4.2.1 Correlation function definition

The correlation function for two particles, of type "1" and type "2" (which in general may be non-identical), is defined as the inclusive two-particle distribution $P_{12}(\mathbf{p}_1, \mathbf{p}_2)$ divided by the product of the inclusive single-particle distributions $P_1(\mathbf{p}_1)$ and $P_2(\mathbf{p}_2)$[1]:

$$C(\mathbf{p}_1, \mathbf{p}_2) = \frac{P_{12}(\mathbf{p}_1, \mathbf{p}_2)}{P_1(\mathbf{p}_1)P_2(\mathbf{p}_2)}. \tag{4.4}$$

[1]We note that the expression given by Eq. (4.4) is general and also applicable to all two-particle correlations, not just femtoscopic ones.

We can interpret the distribution $P_{12}(\mathbf{p}_1, \mathbf{p}_2)$ as a conditional probability to observe a particle with momentum $\mathbf{p}_1$ if a particle with momentum $\mathbf{p}_2$ is observed as well, and distributions $P_1(\mathbf{p}_1)$ and $P_2(\mathbf{p}_2)$ as probabilities of observing particles with momenta $\mathbf{p}_1$ and $\mathbf{p}_2$, respectively.

Following Ref. [181], we can also define the correlation function in terms of single- and two-particle emission functions (also referred to as source functions), $S_1(x_1, \mathbf{p}_1)$, $S_2(x_2, \mathbf{p}_2)$, and $S_{12}(x_1, \mathbf{p}_1, x_2, \mathbf{p}_2)$, respectively. This definition is used in models. The emission function S_1 (or S_2) is interpreted as probability of emission of a particle of type "1" (or "2") from a space-point x_1 (or x_2) with momentum $\mathbf{p}_1$ (or $\mathbf{p}_2$), while S_{12} is interpreted as probability of emission of a pair of particles of type "1" and type "2" from space-points x_1 and x_2, with momenta $\mathbf{p}_1$ and $\mathbf{p}_2$. Substitution of S_1 for P_1, S_2 for P_2, and S_{12} for P_{12} in Eq. (4.4) will lead to a multi-dimensional object; so, further assumptions reducing the number of dimensions are needed. In general, one assumes that the emission process is independent from the interaction of two particles in the final state. In this case the correlation function yields the following form:

$$C(\mathbf{p}_1, \mathbf{p}_2) = \frac{\int \mathrm{d}^4x_1 \mathrm{d}^4x_2 S_{12}(x_1, \mathbf{p}_1, x_2, \mathbf{p}_2) \, |\Psi_{12}|^2}{\int \mathrm{d}^4x_1 S_1(x_1, \mathbf{p}_1) \int \mathrm{d}^4x_2 S_2(x_2, \mathbf{p}_2)}, \tag{4.5}$$

where S_{12} includes all two-particle correlations, excluding the ones coming from final-state interactions (FSI)[2].

There are additional simplifications which can be made. We can consider identical particles ($S_1 \equiv S_2 \equiv S$) and a static emission function (no dependence on time). In that case the formula for the correlation function becomes:

$$C(\mathbf{p}_1, \mathbf{p}_2) = \frac{\int \mathrm{d}^3x_1 \mathrm{d}^3x_2 S_{12}(\mathbf{x}_1, \mathbf{p}_1, \mathbf{x}_2, \mathbf{p}_2) \, |\Psi_{12}|^2}{\int \mathrm{d}^3x_1 S(\mathbf{x}_1, \mathbf{p}_1) \int \mathrm{d}^3x_2 S(\mathbf{x}_2, \mathbf{p}_2)}. \tag{4.6}$$

4.2.2 Correlations of identical pions

This section focuses on two identical bosons correlations. Such correlations were first observed by G. Goldhaber, S. Goldhaber, W. Lee, and A. Pais [182] for identical pion pairs ($\pi^+\pi^+$, $\pi^-\pi^-$). They noticed that there is an increase of probability of registering pairs at small emission angles compared to the probability of registering non-identical pairs of pions ($\pi^+\pi^-$). They interpreted this effect as the Bose-Einstein correlation. The theory was finalized in 1975 by Kopylov and Podgoretsky [179]. This method, following Ref. [17] and Ref. [181], is introduced below.

[2]Final state interactions, called shortly FSI, is the common name for all two- and many-body interactions that occur between particles after the hadronization process.

The effect of the Bose-Einstein quantum statistics on the correlation function is discussed using a simple model with symmetrization of the pion wave function. The correlation function has been defined in Eq.(4.6). We can introduce the relative momentum of the pair:

$$\mathbf{q} = \mathbf{p}_1 - \mathbf{p}_2, \tag{4.7}$$

and the momentum of the center of mass:

$$\mathbf{k} = \frac{1}{2}(\mathbf{p}_1 + \mathbf{p}_2). \tag{4.8}$$

We can rewrite the wave function of the pair from Eq (4.3) using these variables:

$$\Psi_{12} = \frac{1}{\sqrt{2}} e^{i\mathbf{k}(\mathbf{x}_1+\mathbf{x}_2)} \left(e^{i\mathbf{q}(\mathbf{x}_1-\mathbf{x}_2)/2} + e^{-i\mathbf{q}(\mathbf{x}_1-\mathbf{x}_2)/2} \right). \tag{4.9}$$

Then, the correlation function becomes:

$$C(\mathbf{k},\mathbf{q}) = \frac{\int \mathrm{d}^3x_1 \mathrm{d}^3x_2 S_{12}(\mathbf{x}_1,\mathbf{p}_1,\mathbf{x}_2,\mathbf{p}_2) \left[1 + \frac{1}{2} \left(e^{i\mathbf{q}(\mathbf{x}_1-\mathbf{x}_2)} + e^{-i\mathbf{q}(\mathbf{x}_1-\mathbf{x}_2)} \right) \right]}{\int \mathrm{d}^3x_1 S(\mathbf{x}_1, \mathbf{k} + \frac{1}{2}\mathbf{q}) \int \mathrm{d}^3x_2 S(\mathbf{x}_2, \mathbf{k} - \frac{1}{2}\mathbf{q})}. \tag{4.10}$$

The *smoothness approximation* assumes that the dependence on $\mathbf{q}$ in the denominator is weak, therefore we can write:

$$S\left(\mathbf{x}_1, \mathbf{k} + \frac{1}{2}\mathbf{q}\right) \approx S(\mathbf{x}_1, \mathbf{k}) \qquad \text{and} \qquad S\left(\mathbf{x}_2, \mathbf{k} - \frac{1}{2}\mathbf{q}\right) \approx S(\mathbf{x}_2, \mathbf{k}), \tag{4.11}$$

which yields the following form of the correlation function:

$$C(\mathbf{k},\mathbf{q}) = \frac{\int \mathrm{d}^3x S_{12}(\mathbf{x}_1,\mathbf{p}_1,\mathbf{x}_2,\mathbf{p}_2) \left[1 + \frac{1}{2} \left(e^{i\mathbf{q}\mathbf{x}} + e^{-i\mathbf{q}\mathbf{x}} \right) \right]}{\left[\int d^3x S(x,\mathbf{k}) \right]^2}. \tag{4.12}$$

From the Eq. (4.12) it can be seen that the correlation function is the Fourier transform of the emission function.

In models usually only the single-particle emission functions are provided. In that case we assume that the emission process of each particle is independent and S_{12} can be constructed via a convolution of single-particle emission functions:

$$S_{12}(\mathbf{x},\mathbf{k}) = \int \mathrm{d}^3 S(\mathbf{x}_1,\mathbf{k}) S(\mathbf{x}_1 - \mathbf{x},\mathbf{k}). \tag{4.13}$$

If we further assume that the single-particle emission functions are described by a Gaussian, the convolution of two identical Gaussians is also a Gaussian with the standard deviation σ

multiplied by $\sqrt{2}$, while its Fourier transform has a width decreased by the same factor. In this approximation the following form of the correlation function is valid:

$$C(\mathbf{k}, \mathbf{q}) = 1 + \frac{\left[\int \mathrm{d}^3 x e^{i\mathbf{q}\mathbf{x}} S(\mathbf{x}, \mathbf{k})\right]^2}{\left[\int d^3 x S(x, \mathbf{k})\right]^2}. \tag{4.14}$$

For very small values of $\mathbf{q}$, the correlation function approaches 2, for large values it is close to 1.

Equation (4.14) is often used in simplified model calculations, because it only involves the integral over single-particle emission source. Therefore, the calculation can often be performed analytically. However, in the realistic case where S is not a Gaussian, this formula is only approximate and the exact form from Eq. (4.10) is more accurate. It can be employed in models which provide the two-particle emission function [183]. The hydrodynamic predictions of the femtoscopic radii in p–Pb system [148], discussed in Chapter 7, used this formula.

4.3 LCMS coordinate system

In high-energy collisions, femtoscopic analyses are usually carried out in a coordinate system defined in such a way that the vector $\mathbf{k}$ has only two non-zero components:

$$\mathbf{k} = (k_\mathrm{T}, 0, k_\mathrm{L}), \tag{4.15}$$

where $k_\mathrm{T} = |\mathbf{p}_{\mathrm{T},1} + \mathbf{p}_{\mathrm{T},2}|/2$ is the pair transverse momentum and $k_\mathrm{L} = |\mathbf{p}_{\mathrm{L},1} + \mathbf{p}_{\mathrm{L},2}|/2$ is the pair longitudinal momentum. In addition, usually the coordinate system is longitudinally co-moving (LCMS), defined in a frame where the pair longitudinal momentum vanishes $\mathbf{p}_{\mathrm{L},1} = -\mathbf{p}_{\mathrm{L},2}$. Figure 4.3 shows the construction of the LCMS coordinate system.

The axes are defined separately for each pair, using the so-called *out*, *side*, *long* parametrization. The longitudinal (or *long*) direction is parallel to the beam; the outwards (or *out*) direction is parallel to the pair transverse momentum k_T; the sidewards (or *side*) direction is perpendicular to *out* and *long*.

4.4 Correlation function parametrizations

In order to extract the source sizes from the experimental data we have to perform the integration in Eq. (4.10) or Eq. (4.14) to obtain the exact formula of the correlation function, which

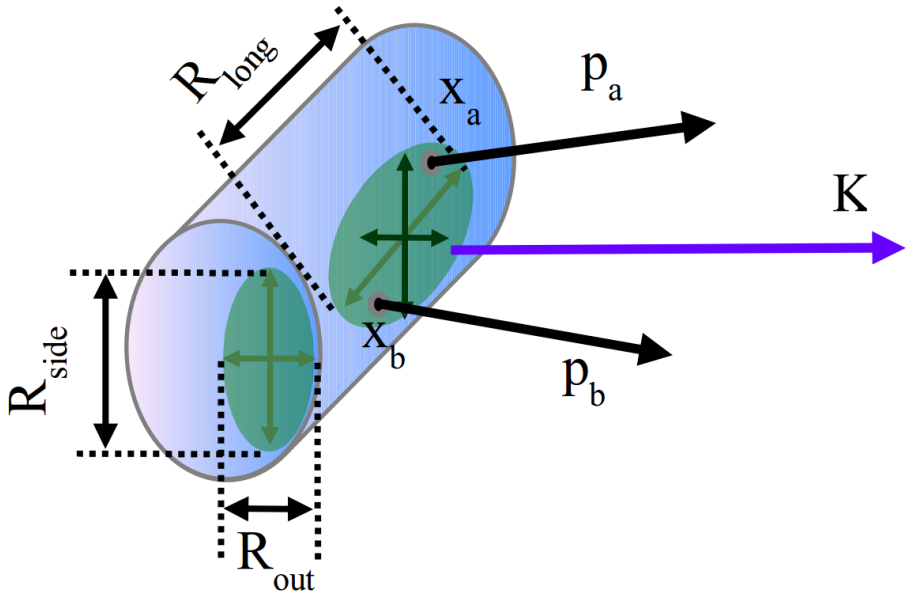

Figure 4.3: Definition of the Longitudinal Co-Moving System.

then could be used in the fitting procedure. In order to do this we must know the two-pion wave function Ψ_{12} and postulate the functional form of the emission function $S(\mathbf{x}, \mathbf{k})$. Usually the following further assumptions about S are made: (1) the dependence on the longitudinal component of $\mathbf{k}$ is neglected, (2) the dependence on the transverse component of $\mathbf{k}$ is analyzed via the so-called k_{T} binning[3], (3) the emission function has a Gaussian shape in LCMS [184]. These assumptions lead to the following form of S, which was used in heavy-ion collisions at RHIC [185–191] and at the LHC [68]:

$$S(\mathbf{x}) \approx \exp\left(-\frac{x_{\mathrm{out}}^2}{4R_{\mathrm{out}}^{\mathrm{G}\ 2}} - \frac{x_{\mathrm{side}}^2}{4R_{\mathrm{side}}^{\mathrm{G}\ 2}} - \frac{x_{\mathrm{long}}^2}{4R_{\mathrm{long}}^{\mathrm{G}\ 2}}\right). \tag{4.16}$$

The $R_{\mathrm{out}}^{\mathrm{G}}$, $R_{\mathrm{side}}^{\mathrm{G}}$ and $R_{\mathrm{long}}^{\mathrm{G}}$ parameters, corresponding to widths of the correlation function, describe the single-particle source sizes in the LCMS in the *out*, *side*, and *long* directions, respectively. They are also commonly referred to as "HBT radii"[4].

In pp collisions, apart from commonly used Gaussian emission function, also other forms are used, i.e. exponential and Lorentzian. The ALICE experiment has found that Lorentzian parametrization in the *out* and *long* directions and Gaussian parametrization in the *side* direction

[3] We assume that S is independent of $\mathbf{k}$ inside each of the k_{T} ranges.

[4] It has been shown in Ref. [192] that in reality the HBT radii measure the sizes of the region of homogeneity, i.e. the region from which correlated pairs are emitted. Therefore, the radii are also commonly referred to as "homogeneity lengths".

fit the data best [193–195]:

$$S(\mathbf{x}) \approx \frac{1}{x_{\text{out}}^2 + {R_{\text{out}}^{\text{E}}}^2} \exp\left(-\frac{x_{\text{side}}^2}{4{R_{\text{side}}^{\text{G}}}^2}\right) \frac{1}{x_{\text{long}}^2 + {R_{\text{long}}^{\text{E}}}^2}. \tag{4.17}$$

The corresponding source sizes in *out* and *long* are $R_{\text{out}}^{\text{E}}$ and $R_{\text{long}}^{\text{E}}$, while for the *side* direction the size parameter $R_{\text{side}}^{\text{G}}$ is the same as in the Gaussian case.

The Gaussian source provides a common approximation, for any collision system and across experiments, of the source size and can be used to compare to other experimental results, especially the ones coming from A–A collisions, where the source is well described by a Gaussian.

The simplified pair wave function for identical bosons, Ψ_{12}, has been already introduced in Eq. (4.9). However, charged pions also interact via the Coulomb and strong interactions. In order to introduce these two components, let us first discuss the general case. In such scenario we consider two non-identical particles with the interaction[5] given by:

$$\Psi_{-\mathbf{k}^*}^{(+)}(\mathbf{r}^*, \mathbf{k}^*) = \sqrt{A_{\text{C}}(\eta)} \frac{1}{\sqrt{2}} \left[e^{-i\mathbf{k}^*\mathbf{r}^*} F(-i\eta, 1, i\zeta^+) + f_{\text{C}}(\mathbf{k}^*) \frac{\tilde{G}(\rho, \eta)}{\mathbf{r}^*} \right], \tag{4.18}$$

where A_{C} is the Gamow factor, $\zeta^{\pm} = k^* r^* (1 \pm \cos\theta^*)$, $\eta = 1/(k^* a_{\text{C}})$, F is the confluent hypergeometric function, and $\tilde{G}$ is the combination of the regular and singular S-wave Coulomb functions. θ^* is the angle between the pair relative momentum $k^* = |\mathbf{k}^*| = q/2$ and relative position $r^* = |\mathbf{r}^*|$ in the Pair Rest Frame (PRF), while a_{C} is the Bohr radius of the pair. The component f_{C} is the strong scattering amplitude, modified by the Coulomb interaction. For like-sign pion pairs the contribution of the strong interaction is small for the expected source sizes (a few fm) [197], and is usually neglected. In addition, formula in Eq. (4.18) must be properly symmetrized. The pair wave function then becomes [197]:

$$\Psi_{-\mathbf{k}^*}^{(+)}(\mathbf{r}^*, \mathbf{k}^*) = \sqrt{A_{\text{C}}(\eta)} \frac{1}{\sqrt{2}} \left[e^{-i\mathbf{k}^*\mathbf{r}^*} F(-i\eta, 1, i\zeta^+) + e^{i\mathbf{k}^*\mathbf{r}^*} F(-i\eta, 1, i\zeta^-) \right]. \tag{4.19}$$

The remaining Ψ is a convolution of the Coulomb interaction and wave-function symmetrization. It is further approximated by factorizing the Coulomb part out and integrating

[5] More precisely, it is the Bethe-Salpeter amplitude for the pair, corresponding to the solution of the quantum scattering problem taken with the inverse time direction. We also factorize the wave function into a part describing the motion of the pair as a whole (a function of the pair total momentum and "average" emission point) and a component describing the interaction itself – dependent on the pair relative momentum $\mathbf{k}^*$ and separation $\mathbf{r}^*$ in PRF. The first component produces only an additional phase, which does not influence the modulus of the wave function. Because in our study we are only interested in the modulus, we can neglect this component [196].

it separately, applying the procedure known as Bowler-Sinyukov fitting [198, 199]. This procedure was used previously for large source sizes such as the ones observed in the analysis of Pb–Pb data [68] as well as small source sizes observed in pp collisions [193]. In this approximation the integration of Eq. (4.14) with S given by Eq. (4.16) yields the following form for the correlation function:

$$C_{\mathrm{f}}(\mathbf{q}) = (1-\lambda) + \lambda K_{\mathrm{C}}\left[1 + \exp(-{R^{\mathrm{G}}_{\mathrm{out}}}^2 q^2_{\mathrm{out}} - {R^{\mathrm{G}}_{\mathrm{side}}}^2 q^2_{\mathrm{side}} - {R^{\mathrm{G}}_{\mathrm{long}}}^2 q^2_{\mathrm{long}})\right]. \tag{4.20}$$

The K_{C} function is the Coulomb part of the two-pion wave-function integrated over the spherical Gaussian source with a fixed radius. Equation (4.20) gives a Gaussian shape in all directions[6], therefore we call it a Gaussian or a GGG form of the correlation function. Similarly for the shape given by Eq. (4.17) the correlation function is:

$$C_{\mathrm{f}}(\mathbf{q}) = (1-\lambda) + \lambda K_{\mathrm{C}}\left[1 + \exp\left(-\sqrt{{R^{\mathrm{E}}_{\mathrm{out}}}^2 q^2_{\mathrm{out}}} - {R^{\mathrm{G}}_{\mathrm{side}}}^2 q^2_{\mathrm{side}} - \sqrt{{R^{\mathrm{E}}_{\mathrm{long}}}^2 q^2_{\mathrm{long}}}\right)\right]. \tag{4.21}$$

It has an "exponential" shape in *out* and *long* and a Gaussian shape in *side*. Therefore we will call it an exponential-Gaussian-exponential or an EGE form of the correlation function.

The formulas given by Eq. (4.20) and Eq. (4.21) can be than fitted to the experimental correlation functions to extract parameters of R, the HBT radii. This is the essence of the femtoscopic measurement.

4.5 Spherical harmonics representation

The correlation function given by the Eq. (4.20) or Eq. (4.21) can be conveniently represented in spherical harmonics (SH) [200–202] in addition to the traditionally-used Cartesian coordinates. Moments of the spherical harmonic decomposition of the correlation function are given by:

$$C^m_l(q) = \frac{1}{\sqrt{4\pi}} \int \mathrm{d}\varphi \mathrm{d}(\cos\theta) C(\mathbf{q}) Y^{m*}_l(\theta,\varphi), \tag{4.22}$$

where θ and φ are the spherical angles, $Y^{m*}_l(\theta,\varphi) = (-1)^m Y^{-m}_l(\theta,\varphi)$ are conjugate spherical harmonic functions ($Y^m_l(\theta,\varphi)$ are the spherical harmonics), l is a natural number, and m is an integer $-l \leq m \leq l$.

[6]The source sizes in each direction can be different, therefore, the three-dimensional shape of the correlation function is in general an ellipsoid in LCMS.

The components of the three-vector $\mathbf{q}$ in the LCMS frame are then $q_{\text{long}} = |\mathbf{q}|\cos\theta$, $q_{\text{out}} = |\mathbf{q}|\sin\theta\cos\varphi$, and $q_{\text{side}} = |\mathbf{q}|\sin\theta\sin\varphi$. In the case of collider experiments and correlations of identical particles, the following components vanish: (1) all imaginary components, (2) odd l components, (3) odd m components for even l. The first three non-vanishing components (C_0^0, C_2^0, and C_2^2) capture essentially all the three-dimensional structure of the correlation effect:

- the C_0^0 angle-averaged component describes the general shape of the correlation (the width of the peak near $q = 0$ is inversely proportional to the overall size of the system),
- the C_2^0 component is the correlation weighed with the $\cos^2(\theta)$ (it differs from 0 if the longitudinal and transverse sizes of the source differ),
- the C_2^2 component is the correlation weighed with the $\cos^2(\varphi)$ (it differs from 0 if the size in the outwards direction differs from the size in the sidewards direction).

The full correlation function $C(\mathbf{q})$ constructed from the spherical harmonic components has therefore the following form:

$$C(\mathbf{q}) = \sqrt{4\pi}\sum_{l,m} C_l^m(q)Y_l^m(\varphi,\theta). \tag{4.23}$$

The complete formalism of the calculation of the femtoscopic correlation function in spherical harmonics can be found in Ref. [200].

4.6 Femtoscopy in small systems

The motivation as well as the historical overview of pion femtoscopy measurements have been discussed in details in Refs. [193, 203, 204]. In this section we present a short overview.

As it was discussed in Sec. 4.2.2, two-pion correlations at low relative momenta were first shown to be sensitive to the spatial scale of the emitting source in $\mathrm{p\overline{p}}$ collisions around 50 years ago [182]. Since then, they have been studied in e^+e^- [205], hadron- and lepton-hadron [206], as well as heavy-ion collisions [207]. To some extent, Bose-Einstein correlations were initially of interest only as a source of systematic uncertainty in the determination of the W boson mass [208]. However, in heavy-ion collisions, two-particle femtoscopy has been developed into a precision tool to probe the dynamically-generated geometry structure of the emitting system. In particular, a sharp phase transition between the color-deconfined and confined states

was precluded by the observation of short timescales. In addition, femtoscopic measurement contributed to the study of bulk collective flow phenomena, which have shown that a strongly self-interacting system was created in the collision [209, 210].

In heavy-ion collisions a wide variety of aspects is understood, see e.g. Ref. [207] for details. The spatial scales grow naturally with the multiplicity of the event. Strong hydrodynamical collective flow in the longitudinal and transverse directions is revealed by dynamical dependencies of femtoscopic scales (decrease of pair HBT radii with increasing pair transverse momentum k_T or transverse mass of the pair $m_T = \sqrt{m^2 + k_T^2}$). However, overviews [203, 205, 206] of femtoscopic measurements in hadron- and lepton-induced collisions reveal surprisingly similar systematics, i.e. a similar m_T scaling is observed in small systems, as presented in Fig. 4.4. Whether or not these effects arise from the same physics is still an open question.

Table 4.1 and Table 4.2 present a collection of pion femtoscopy measurements performed over the years by various experiments in small systems and in a broad range of collision energies.

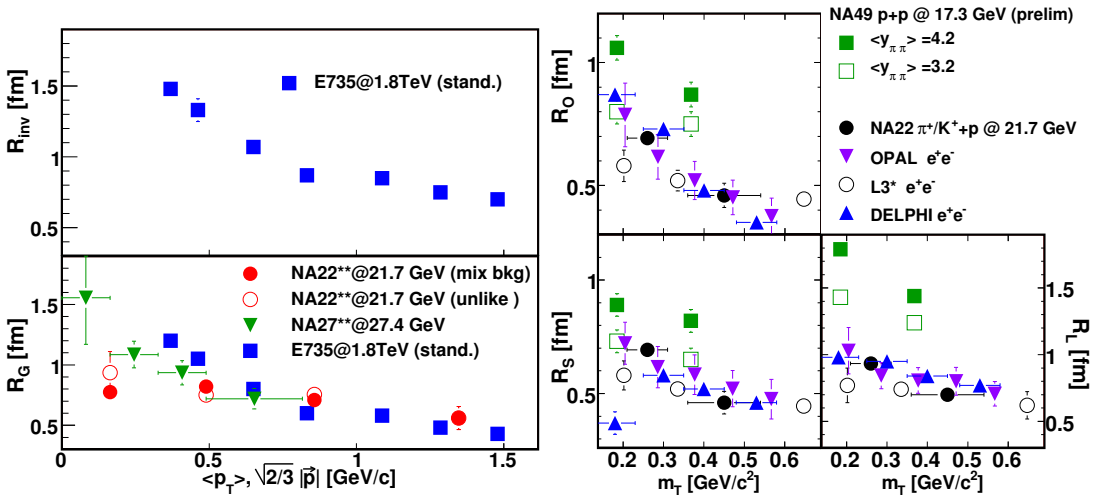

Figure 4.4: The transverse momentum p_T dependence of R_{inv} (left panel) and transverse mass m_T dependence of the 3D HBT radii (right panel) from elementary particle collisions. Data from NA22 [211], NA49 preliminary [212], OPAL [213], L3 [214], and DELPHI [215].

Table 4.1: Collection of published experimental studies of two-particle correlations in small systems. Part I: pp, $p\overline{p}$, and p/d–A systems. Table taken from Ref. [203] and updated with the most recent measurements.

System	Energy (GeV)	Facility	Experiment	Refs.
pp	1.9	LEAR	CPLEAR	[216, 217]
	1.9	CERN	ABBCCLVW	[218]
	7.2	AGS	E766	[219]
	17	SPS	NA49	[212]
	26	SPS	NA23	[220]
	27.4	SPS	NA27	[221]
	31-62	ISR	AFS	[222–224]
	44,62	ISR	ABCDHW	[225]
	200	SPS	NA5	[226]
	200	RHIC	STAR	[227]
	200	RHIC	PHENIX	[228]
	900,2360,7000	LHC	CMS	[229, 230]
	900,7000	LHC	ALICE	[193, 231]
$p\overline{p}$	53	ISR	AFS	[232]
	200	SPS	NA5	[226]
	200-900	SPS	UA1	[233]
	1800	Tevatron	E735	[234]
p/d–A	200	RHIC	STAR	[235]
	200	RHIC	PHENIX	[236]
	5020	LHC	ALICE	[237]

Table 4.2: Collection of published experimental studies of two-particle correlations in small systems. Part II: hp, e^+e^-, e^+p, μp, α–α, μN, and νN systems. N here stands for nucleon. Table taken from Ref. [203] and updated with the most recent measurements.

System	Energy (GeV)	Facility	Experiment	Refs.
hp	5.6	CERN	ABBCCLVW	[218]
	21.7	SPS	EHS/NA22	[211, 238]
e^+e^-	3-7,29	SLAC	Mark-II	[239]
	10	CESR	CLEO	[240]
	29	SLAC	TPC	[241]
	29-37	DESY-PETRA	TASSO	[242, 243]
	58	TRISTAN	AMY	[244]
	91	LEP	OPAL	[213, 214, 245–248]
	91	LEP	L3	[214]
	91	LEP	DELPHI	[215, 249–252]
	91	LEP	ALEPH	[253–256]
e^+p	300	HERA	ZEUS	[257, 258]
	300	HERA	H1	[259]
μp	23	CERN	EMC-NA9	[260]
α–α	126	ISR	AFS	[222–224, 232]
μN	30	Tevatron	E665	[261]
νN	>10		BBNC	[262]

Pion femtoscopy in pp collisions

The first direct comparison of femtoscopy in heavy-ion and proton-proton collisions in the same apparatus was possible at RHIC. Essentially identical multiplicity and momentum dependence of the femtoscopic radii was reported for the two systems [263]. However, the multiplicities at which the femtoscopic measurement in pp collisions at RHIC was performed were still significantly smaller than those of even the most peripheral Au–Au collisions. Two-pion correlations measurements for both pp and Pb–Pb collisions at comparable multiplicites were possible for the first time at the LHC and reported in Ref. [193]. The observed correlations at the LHC may be influenced by jets [264], while other studies suggest that a system behaving collectively may be created [265, 266].

In addition, ALICE measurements for central Pb–Pb collisions [68] and for pp collisions at $\sqrt{s}$ = 0.9 and 7 TeV [193, 231] have been compared to results from heavy-ion collisions at lower energies, as can be seen in Fig. 4.5. Two clear trends were found: (i) The A–A data scale approximately linearly with the cube root of the final state multiplicity density at midrapidity $\langle \mathrm{d}N_{\mathrm{ch}}/\mathrm{d}\eta \rangle^{1/3}$ for all three radii separately [207]. For pp collisions, the radii scale linearly as well, however the slope and radius intercept of the scaling line are clearly different than in A–A. (ii) A significant, universal decrease of the radii with pair momentum has been observed in A–A collisions, while the analogous trend in pp depends on the considered direction (*out*, *side*, or *long*) and event multiplicity. A similar transverse momentum dependence of the radii was observed for the asymmetric d–Au collision system at RHIC [235, 236].

Pion femtoscopy in p–Pb collisions

The A–A pion femtoscopy results are interpreted in the hydrodynamic framework as a signature of collective radial flow. Models including this effect are able to reproduce the ALICE data for central collisions [103, 269]. The pp data cannot be described in the same framework and it is speculated that additional effects, related to the uncertainty principle, may play a role in such small systems [149]. In p–A collisions, hydrodynamic models which assume the creation of a hot and dense system expanding hydrodynamically predict system sizes higher than those observed in pp, and comparable to those observed in lower-energy A–A collisions at the same multiplicity [148, 149].

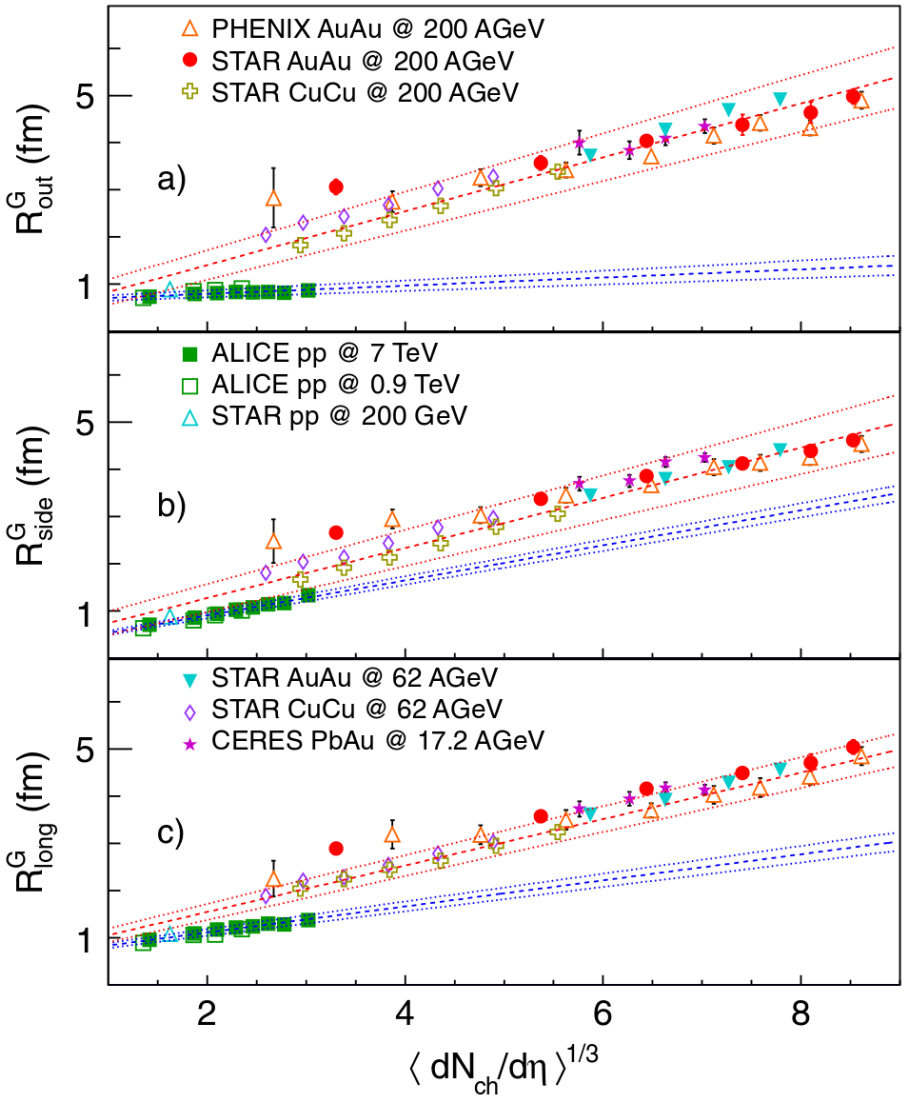

Figure 4.5: HBT radii as a function of cube root of the charged particle pseudorapidity density $\langle \mathrm{d}N_{\mathrm{ch}}/\mathrm{d}\eta \rangle^{1/3}$ for pp data from ALICE compared to (heavy-)ion collisions at RHIC [188, 267] and SPS [268]. All results are for $\langle k_{\mathrm{T}} \rangle = 0.4$ GeV/c, except for the values from the PHENIX experiment, which are for $\langle k_{\mathrm{T}} \rangle = 0.45$ GeV/c. Dashed lines show linear fits, performed separately to pp and heavy-ion data; dotted lines show the uncertainty of the fit. Plot from Ref. [193].

Alternatively, a model based on the gluon saturation formalism predicts that the initial system size in p–A collisions should be similar to that observed in pp collisions, at least in the transverse direction [52, 53]. In this scenario both systems are treated in the same manner in the Color Glass Condensate model; so, their subsequent evolution should lead to comparable femtoscopic sizes at freeze-out. Ref. [270] suggests that there is a (small) Yang-Mills evolution in addition. The observation of a larger size in the p–A system with respect to pp would mean

that a comparable initial state evolves differently in the two cases, which would be challenging to explain based on CGC arguments alone. The d–Au results from RHIC suggest that hydrodynamic evolution may be present in such a system. ALICE has performed a one-dimensional three-pion cumulant analysis in pp, p–Pb and Pb–Pb collisions at the LHC [237] and the results are shown in Fig. 4.6. The femtoscopy parameters of the p–Pb system were found to be between the values extracted for the smaller and larger system, but closer to the pp value. This leaves room for different interpretations. The three-dimensional pion femtoscopic radii as a function multiplicity and pair transverse momentum from p–Pb collisions at the LHC, which are reported in Chapter 7, provide important additional constraints on the validity of both approaches.

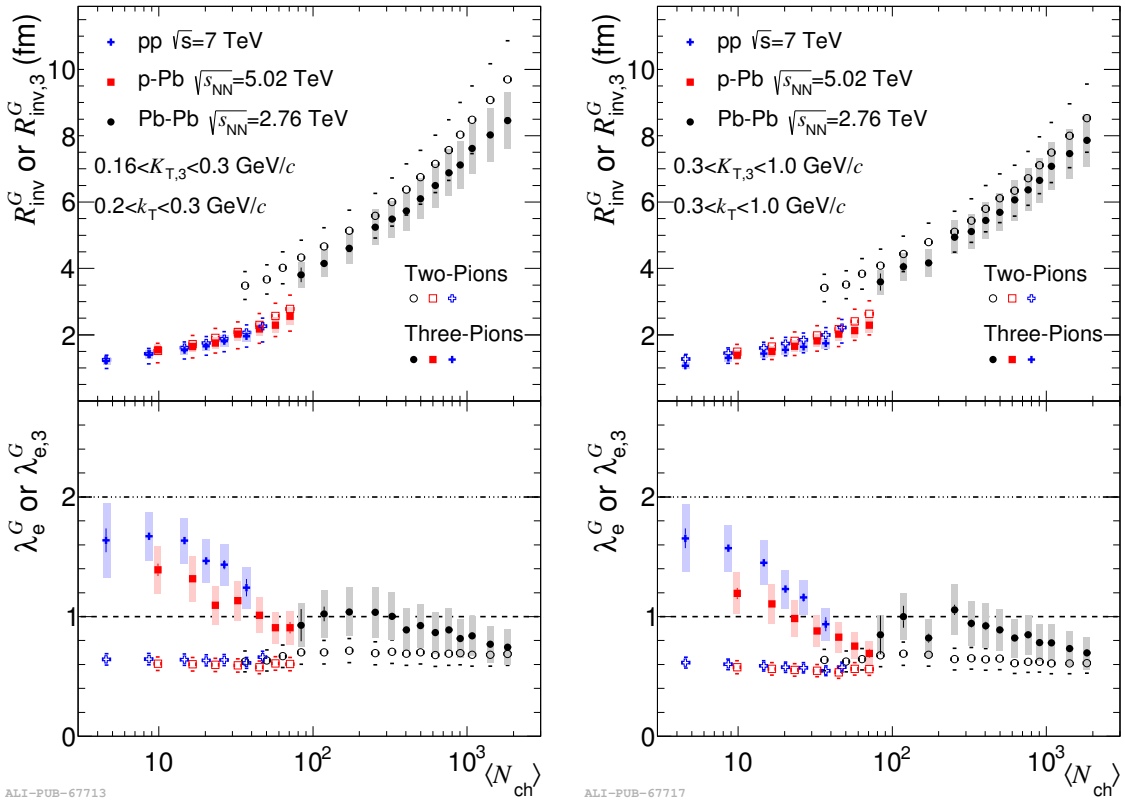

Figure 4.6: Two- and three-pion Gaussian radii from ALICE as a function of N_{ch} in pp, p–Pb and Pb–Pb collision systems for low and high pair transverse momentum ranges. Plots from Ref. [237].

4.7 Beyond the system size – baryon femtoscopy

Typical femtoscopic measurements are performed for light mesons such as pions (which are the scope of this thesis) or kaons. However, the femtoscopic formalism is not restricted only to the light particles. One of the current extensively studied subject, which goes far beyond the standard calculation of the system size, is the femtoscopy of different types of baryons.

Baryons are important for several reasons. First of all, the system size can be measured to cross-check the pion and kaon results and find whether there are any trends between meson and baryon systems, i.e. approximate scaling of femtoscopic radii with transverse mass of the pair m_{T} is predicted by hydrodynamic models. However, in addition to those goals which are typical for traditional femtoscopic measurements, baryon femtoscopy has the potential to influence also other fields of physics and deepen our understanding of the basics of QCD. Up to this moment we were using the general form of the correlation function, Eq. (4.6), for the calculation of the parameters of the source function S and fixing the two-particle interaction Ψ. In the case of baryons it is the Ψ, the two-baryon strong interaction, which is of main interest. It happens that parameters of most of the interactions between heavy baryons are very poorly known or not known at all. We can then apply the femtoscopic formalism to measure the parameters of Ψ. These interactions are important not only in particle physics but also in astrophysics, where they play a significant role in the models describing the neutron stars.

In this section we briefly introduce the concept of baryon femtoscopy measurements and a method to extract the strong interaction potential parameters for different baryon pairs.

4.7.1 Current understanding

As it was mentioned, one of the main problems in QCD is the unknown strong interaction between two baryons [271, 272]. There are dedicated experiments [273–275] aiming to study such processes and significant amount of data already exists [276]. Baryon-antibaryon systems, where the matter-antimatter annihilation process is present are of particular interest. Baryon-antibaryon annihilation was studied in great detail theoretically [277–280] and measured with good precision [276]. However, the measurements were performed only for $\mathrm{p\overline{p}}$, $\mathrm{p\overline{n}}$, and $\mathrm{\overline{p}d}$ systems. The theoretical guidance of what should be expected for other baryon-antibaryon pairs is also limited. UrQMD [105], the standard hadronic rescattering code used in heavy-ion

collision modelling, assumes that any baryon-antibaryon interaction has the same parameters as the $\mathrm{p\bar{p}}$ system, expressed either as a function of relative momentum or pair energy at the center of mass.

4.7.2 Measuring two-baryon interactions

The idea of measuring unknown baryon-baryon interaction potentials is the following. At first, we perform the analysis of those systems where the interaction is known, such as proton-proton, and extract the system size. In the second step, assuming no significant changes of the femtoscopic radii between different baryon systems with similar m_{T}, we move to other baryons and fix the system size. This means that in Eq. (4.6) the source function S is fixed and the parameters of Ψ are the ones which are kept free. If the described procedure succeeds, the parameters of the strong interaction in a considered baryon system will be obtained.

4.7.3 Lednicky & Lyuboshitz analytical model

The procedure described in Sec. 4.7.2 requires assumptions for the two-baryon interaction. From the general form of Ψ given by Eq. (4.18), in the case when particles interact only with the strong FSI, we obtain:

$$\Psi^{s(+)}_{-\mathbf{k}^*}(\mathbf{r}^*, \mathbf{k}^*) = e^{i\mathbf{k}^*\mathbf{r}^*} + f^s(k^*)\frac{e^{ik^*r^*}}{r^*}, \tag{4.24}$$

where $f^s(k^*) = \left(\frac{1}{f_0^s} + \frac{1}{2}d_0^s k^{*2} - ik^*\right)$, f_0^s is the scattering length, d_0^s is the effective radius, and s iterates over different spin states (singlet, triplet). The complex f_0^s and d_0^s are the main variables of interest, since they can used to calculate the interaction cross section:

$$\sigma = 4\pi|f(k^*)|^2. \tag{4.25}$$

We focus here on the baryon-antibaryon case. For these systems the parametrization of Ψ, called the Lednicky & Lyuboshitz analytical model, is provided in Ref. [281]. In the model the following form of the correlation function is derived:

$$C(\mathbf{k}^*) = 1 + \sum_s \rho_s \left[\frac{1}{2}\left|\frac{f^s(k^*)}{R}\right|^2\left(1 - \frac{d_0^s}{2\sqrt{\pi}R}\right) + \frac{2\Re f^s(k^*)}{\sqrt{\pi}R}F_1(2k^*R) - \frac{\Im f^s(k^*)}{R}F_2(2k^*R)\right], \tag{4.26}$$

where $F_1(z) = \int_0^z \mathrm{d}x e^(x^2 - z^2)/z$, $F_2(z) = (1 - e^z)/z$, and ρ_s corresponds to pair spin fractions. Summation over spin orientations is neglected[7], $f^{\mathrm{signlet}}(k^*) = f^{\mathrm{triplet}}(k^*) = f(k^*)$, and the effective

[7] It is not possible to measure the spin dependence in the current experiments.

radius is usually set to, $d_0 = 0$. Parameter R corresponds to the size of the spherically symmetric source in PRF:

$$S(\mathbf{r}^*) = \exp\left(-\frac{r^{*2}}{4R^2}\right). \tag{4.27}$$

The imaginary part of the scattering length in Eq. (4.26) accounts for the baryon-antibaryon annihilation process. The correlation functions calculated from the Lednicky & Lyuboshitz model with non-zero and zero imaginary components of the scattering lengths are shown in Fig. 4.7 and Fig. 4.8, resepectively. When the imaginary part of the scattering length is set to zero, the anticorrelation width is limited to about 100 MeV. On the other hand, when we take into account the annihilation by introducing a non-zero imaginary component, a wide (few hundreds of MeV in k^*) anticorrelation appears. The observation of a similar structure in the experimental data would be an evidence for the presence of significant annihilation process between baryons in nature.

The current status and the preliminary results of the analysis of femtoscopic correlations of protons with antilambdas in ALICE are presented in Chapter 9.

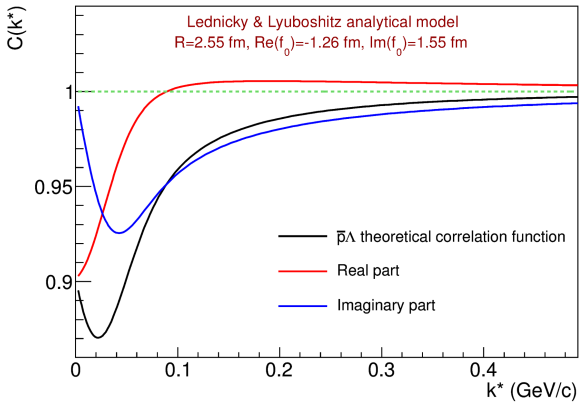

Figure 4.7: The correlation function derived from the Lednicky & Lyuboshitz analytical model with the non-zero imaginary component of the scattering length, which implies that annihilation is taken into account. A clear wide anticorrelation extending up to hundreds of MeV in k^* is observed.

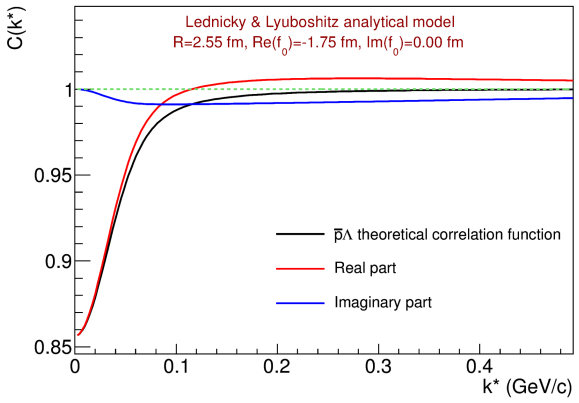

Figure 4.8: The correlation function derived from the Lednicky & Lyuboshitz analytical model with the imaginary component of the scattering length set to 0, which implies that annihilation is switched off. The anticorrelation effect is limited in k^*.

Chapter 5

Non-femtoscopic correlations and fitting procedure

This chapter introduces additional correlation sources (other than quantum statistics and final-state interactions) that are manifested in the femtoscopic correlation functions measured by experiments, especially in small systems like pp or p–A. These correlations are not part of the "standard" femtoscopic formalism but must be accounted for in order to extract reliable experimental results. Therefore, a robust fitting procedure must include in some way also these type of correlations

These "non-femtoscopic" correlations have been extensively studied using EPOS 3.076 Monte Carlo model [146, 147], which includes such additional correlations as well as allows to extract the femtoscopic information. In this chapter we propose a robust method which allows to take them into account in the procedure of extracting the femtoscopic radii.

We stress that all the studies, figures, and results presented in this chapter have been published in Ref. [1]. This publication have been prepared primarily by the author of this thesis, in collaboration with the supervisor and other co-authors. We also note that the text of this chapter, with slight modifications, is taken from the above reference.

5.1 Non-femtoscopic correlations

In the ideal case, as introduced in Chapter 4, the femtoscopic correlation rests on a flat baseline, reflecting the lack of other two-particle correlations. Such scenario is indeed realized for example for heavy-ion collisions, where all other correlations are either small or have a q scale vastly different than the femtoscopic effect. This is not the case for collisions in small systems, where a relatively small number of particles is produced. Measurements done by various exper-

iments [193, 203, 229–231, 235–237, 263] show that significant additional correlation sources are contributing to the two particle correlation function. We will later collectively refer to such effects as non-femtoscopic background, to differentiate it from the femtoscopic signal, which we are primarily interested in extracting. These correlations have a magnitude and width in q comparable to the femtoscopic signal, and therefore the two cannot be easily disentangled. The sources of such correlations are, among others, the energy-momentum conservation and the "mini-jet" phenomena [193].

Two main approaches have been taken by experiments to deal with the non-femtoscopic correlations, both relying on the modelling of the background by Monte Carlo (MC) models. The first is to construct a "double-ratio", where the experimental correlation function is divided by a corresponding one from the MC calculation. This technique relies on the fact that the particle production process in MC does not take into account the Bose-Einstein enhancement, but it does include other sources of correlation. The application of the "double-ratio" technique should be equivalent to "dividing out" the non-femtoscopic effects and leave a pure Bose-Einstein signal. The second technique is to parametrize the background in MC calculation and then use it as an additional term in the fitting function applied to the experimental correlation function. We note that both approaches are, in perfect conditions (small size of q bins in the correlation function, large statistics both for data and MC, etc.), mathematically equivalent. However, the method with the additional term in the fitting function offers greater flexibility, which is needed for this work.

In this chapter we perform a methodological verification of the procedures used to account for the non-femtoscopic background. Using the EPOS 3.076 model [146, 147], we calculate the three-dimensional correlation functions in the LCMS frame [282, 283], where the pair momentum along the beam vanishes. The correlation functions are calculated with (1) pure Bose-Einstein signal, (2) with the background effects only, and (3) with both correlation sources combined. We extract the source size from the "pure" correlations functions, and compare them with the ones extracted from the "full" calculation, where the background is constrained using the "only background" calculation. We propose several methods to parametrize the background. We estimate the systematic uncertainty coming from their application and discuss their validity and stability. We conclude by selecting the method which is most reliable and introduces the smallest uncertainty in the procedure. This procedure is employed in the analysis of collision data in Chapter 7.

5.2 Monte Carlo simulations

5.2.1 Choice of model

In order to perform the calculations planned for this work, a Monte Carlo event generator able to perform a calculation for a small system, such as p–Pb (including realistic modelling of minimum-bias collisions with "mini-jet" effects), is required. The model must also provide, for each particle, information crucial for femtoscopy, such as freeze-out coordinates. The EPOS ver. 3.076 [146, 147] was chosen and run with the parameters corresponding to the p–Pb collisions at $\sqrt{s_{\mathrm{NN}}}$ = 5.02 TeV, the same as p–Pb run at the LHC which is analyzed in this thesis. The model is based on the Regge formalism and includes fragmentation of partons scattered with moderate energy which are usually associated with the mini-jet phenomena. As such, it produces significant non-femtoscopic correlations, which are in qualitative agreement with the trends observed in data (see Chapter 7). The minimum-bias sample of events was generated, containing all information about the produced particles, including their freeze-out coordinates.

5.2.2 Calculation of the correlation functions

To perform the calculation of the correlation function according to Eq. (4.6) with particles produced by the event generator, a Monte Carlo procedure must be applied. First, all charged pions from the EPOS event are combined into pairs. A distribution B is created where each pair is filled with the weight of 1.0, at a corresponding relative momentum q. The second distribution W is created, where the pair is inserted in the same manner, but with the weight calculated according to Eq. (4.19). To construct the third distribution, two pions in the pair are taken from different EPOS events in a so-called “mixing” technique and pairs are inserted with weight 1.0 in the distribution M. Three distinct correlation functions can then be created, each containing a specific set of information. All of them are needed for the study presented in this work. The function $C_{\mathrm{QS}} = W/B$ is mathematically equivalent to the Monte Carlo integration of Eq. (4.5). It contains only the "pure" Quantum Statistics + FSI signal. The correlation function $C_{\mathrm{B}} = B/M$ contains all the event-wide correlations which are present in the EPOS simulation, including the ones which contribute to the non-femtoscopic effect, but it does not include the QS+FSI correlation. Therefore, it represents the "background" in our study. The third histogram $C_{\mathrm{F}} = W/M$ represents the "full" correlation, including both the effects of the QS+FSI, as well as

all other correlations contained in the model. The C_{F} most closely resembles an experimental correlation function.

Moreover, since all the distributions are calculated in three dimensions in LCMS, following the approach of the experiments [193, 263], we employ a spherical harmonic decomposition of the measured correlation functions, as described in Sec. 4.5.

All the correlation functions have been calculated for seven ranges of pair transverse momentum k_{T}, which were exactly the same as in the analysis of experimental data. The k_{T} intervals are introduced in Sec. 6.4.1. An example of all three correlation functions, calculated for two (low and high) k_{T} ranges are shown in Fig. 5.1.

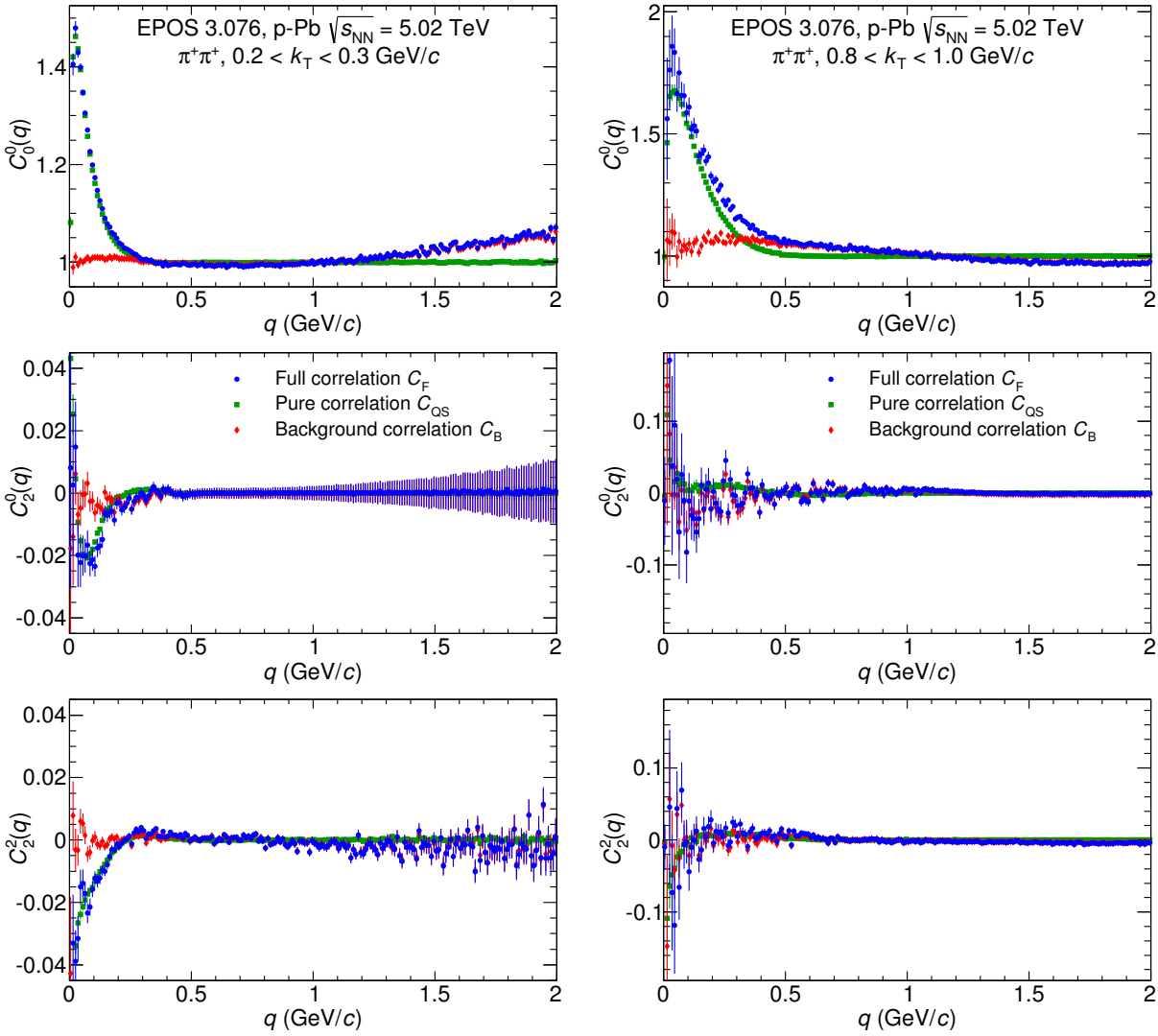

Figure 5.1: First three non-vanishing components of the SH representation of the $\pi^+\pi^+$ correlation functions from EPOS model for $0.2 < k_{\mathrm{T}} < 0.3$ GeV/c (left plot) and $0.8 < k_{\mathrm{T}} < 1.0$ GeV/c (right plot).

5.2.3 Extracting the femtoscopic information

With the three correlation functions calculated we proceed to treat them with an experimentalist's recipe. We use the Gaussian and EGE forms of correlation function derived in Sec. 4.4 and employ a fitting procedure to extract the femtoscopic radii. Equations (4.20) and (4.21) for the Gaussian and EGE forms, respectively, are fitted directly to the calculated correlation functions C_{QS} to extract the "true" femtoscopic radii. We use both fitting functions in order to see if a particular shape of the femtoscopic effect influences the background estimation procedure.

In the presence of additional non-femtoscopic correlations, the forms given by Eq. (4.20) or Eq. (4.21) will produce unreliable results. Those effects must be taken into account with additional factors in the fitting equation. Following the discussion in Sec. 5.2.2 such factor should be multiplicative with the QS+FSI effect. A modified fitting function for the Gaussian and the EGE fit case is then

$$C_{\mathrm{f}}(\mathbf{q}) = NC_{\mathrm{qs}}(\mathbf{q})\Omega(\mathbf{q}), \tag{5.1}$$

where N is the normalization factor and Ω term contains the "non-femtoscopic" effects. Obviously, the exact form of Ω is not known. Ω will also naturally introduce new fitting parameters. The main purpose of this chapter is to propose a recipe to obtain a form for Ω. We will then apply this procedure to our model calculation and try to extract the "realistic" femtoscopic radii by fitting Eq. (5.1) to the calculated C_{F}. By comparing these "realistic" radii with the "true" ones obtained from the fit of C_{QS} we will be able to judge the correctness of the procedure to extract Ω as well as the correctness of the fitting process itself. We will also estimate the theoretical systematic uncertainty coming from the presence of the background.

5.2.4 Characterizing the background

In order to propose a function for the Ω term needed in Eq. (5.1) and accounting for the non-femtoscopic effects in the fitting procedure, we need to calculate C_{B} that contains only non-femtoscopic correlations. Examples of the C_{B} calculated for selected pair k_{T} ranges are shown in Fig. 5.1. The background at low k_{T} is flat at low q, where the femtoscopic effect is most prominent. It shows a rise at $q > 1.0$ GeV/c due to the momentum conservation in mini-jet mechanism, however this behavior is not relevant for the femtoscopic analysis. At large k_{T} there is a significant correlation, wide in q, approximately Gaussian in shape, with prominent

contribution to the low q, where the femtoscopic effect is located. Its three-dimensional shape is reflected in the (2,0) and (2,2) SH components. They differ from zero, but not strongly, indicating that the shape is approximately spherically symmetric in LCMS.

Fixing the background with the MC calculation introduces a model dependence in the analysis. Therefore we propose several options for the parametrization of C_{B}, with varying degree of such model dependence. We propose that the background has a Gaussian shape:

$$\Omega_0^0(q) = 1 + a_0^0 \exp\left(-\frac{q^2}{2(\sigma_0^0)^2}\right), \tag{5.2}$$

where a_0^0 is a free parameter describing the magnitude of the correlation and σ_0^0 is another free parameter describing its width. In the first scenario, with minimal model dependence, we only fix σ_0^0, separately for each k_{T} range, from the fit to the C_{B}. In the second scenario, we fix both the σ_0^0, as well as a_0^0 for each k_{T} range. In the third scenario we also account for the full three-dimensional shape of the background, with the parametrization of the (2,0) and (2,2) components of the background:

$$\Omega_2^0(q) = a_2^0 \exp\left(-\frac{q^2}{2(\sigma_2^0)^2}\right) + \beta_2^0, \tag{5.3}$$

$$\Omega_2^2(q) = a_2^2 \exp\left(-\frac{q^2}{2(\sigma_2^2)^2}\right) + \gamma_2^2 q + \beta_2^2, \tag{5.4}$$

where a_2^0, σ_2^0, a_2^2, σ_2^2, γ_2^2, β_2^0, and β_2^2 are free parameters of the fit to C_{B}. All of them but β_2^0 and β_2^2, which are kept free, are then fixed in the fitting of the full correlation function. The overall fitting formula is therefore of the following form:

$$C_{\mathrm{f}}(\mathbf{q}) = N \cdot C_{\mathrm{qs}}(\mathbf{q}) \cdot \left[\Omega_0^0(q) \cdot Y_0^0(\theta,\varphi) + \Omega_2^0(q) \cdot Y_2^0(\theta,\varphi) + \Omega_2^2(q) \cdot Y_2^2(\theta,\varphi)\right], \tag{5.5}$$

where $Y_0^0(\theta,\varphi)$, $Y_2^0(\theta,\varphi)$, and $Y_2^2(\theta,\varphi)$ are the corresponding spherical harmonics.

We stress that this particular functional form has been derived for this particular EPOS MC calculation and is by no means a universal one. Each time such analysis is performed, a new functional form should be proposed, corresponding to the particular background shape observed in data or MC calculation. Nevertheless, the three scenarios proposed represent three rather general cases of background characterization. Scenario 1 (also referred to as "Background 1") corresponds to only constraining the background shape in q, scenario 2 (also referred to as "Background 2") corresponds to constraining also the background magnitude, while scenario 3 (also referred to as "Background 3") corresponds to fixing the full three-dimensional shape and magnitude of the background.

5.3 Fitting the pure correlation

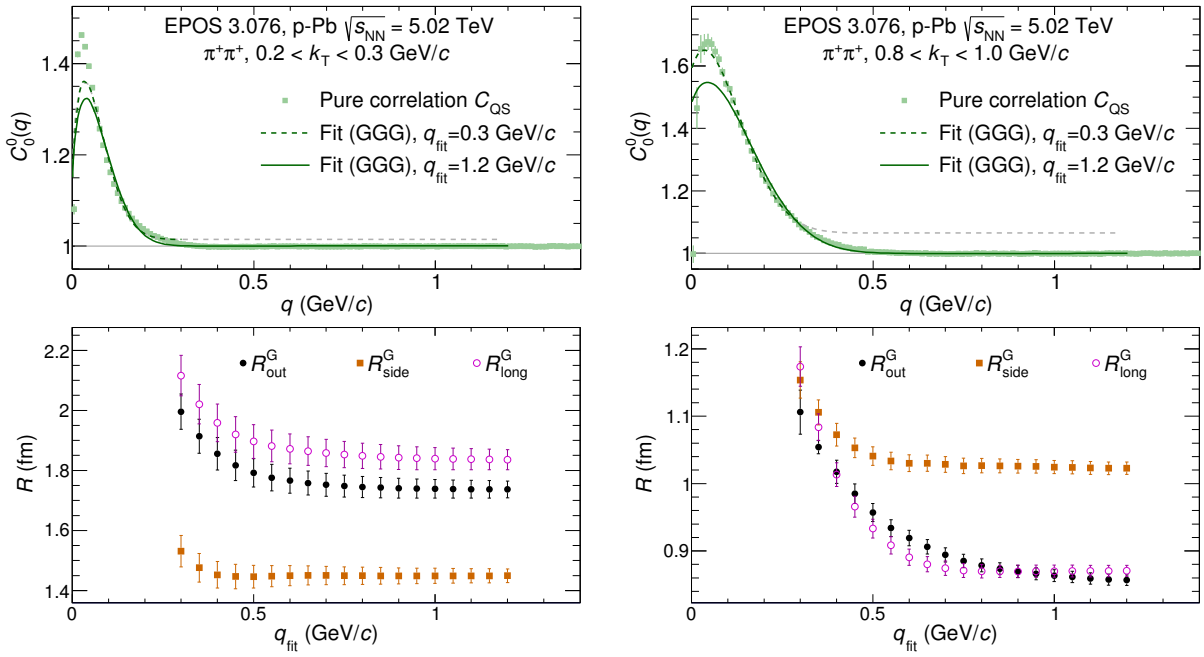

Figure 5.2: C_0^0 component of the SH representation of pure femtoscopic effect C_{QS} for low and high k_T ranges (upper panels). Extracted Gaussian femtoscopic radii as a function of maximum fit range in q for low and high k_T (lower panels). Dashed and solid lines correspond fo fits with maximum fit range q_{fit} = 0.3 GeV/c and q_{fit} = 1.2 GeV/c, respectively.

The pure correlation function C_{QS} is fitted with formulas given in Eqs. (4.20) and (4.21) to obtain the reference radii. The values of the fit naturally depend on the range in q in which the fit is performed, which is shown in Figs. 5.2 and 5.3. An expected behavior is seen: when the fitting range is not wide enough, a dependence of the fit parameters on the fitting range is observed. Also for a narrow fitting range the procedure is not able to correctly constrain the normalization of the correlation function. Both effects are quite pronounced for the Gaussian fits, but they are also present, to a smaller degree, when a more appropriate shape of the correlation peak, the EGE, is used. Only when the fit range maximum is larger than the width of the femtoscopic effect: around 0.6 GeV/c for the low k_T and 0.8 GeV/c for the high k_T, the radii values stabilize and do not change further with increase of the fit range maximum. At the same time the normalization is also properly constrained.

In Fig. 5.4 a full dependence for radii in all directions and in all k_T is shown for both functional forms, normalized to the value obtained for the maximum fitting range q_{fit} = 1.2 GeV/c.

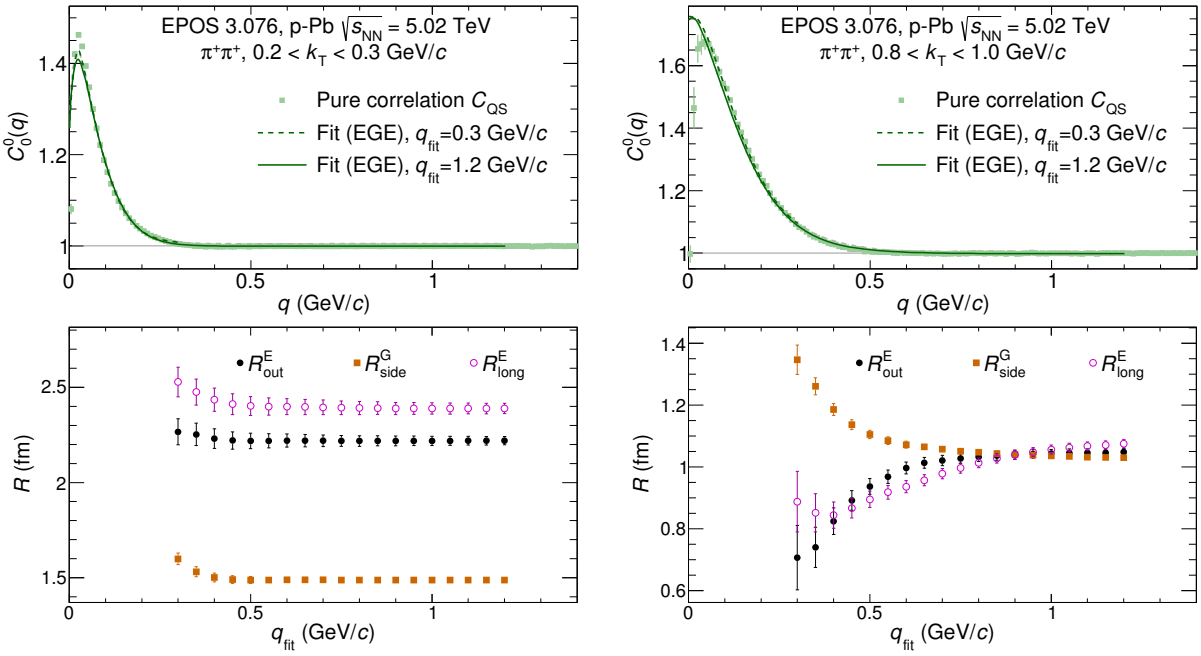

Figure 5.3: C_0^0 component of the SH representation of pure femtoscopic effect C_{QS} for low and high k_T ranges (upper panels). Extracted EGE femtoscopic radii as a function of maximum fit range in q for low and high k_T (lower panels). Dashed and solid lines correspond fo fits with maximum fit range q_{fit} = 0.3 GeV/c and q_{fit} = 1.2 GeV/c, respectively.

All radii, for all k_T, all directions, and both functional forms, reach a stable value if a sufficiently wide fitting range q_{fit} is selected. However, values for large k_T stabilize for q_{fit} larger by even a factor of 2 than at lower k_T. This is expected, since the width of the effect grows with k_T (femtoscopic size becomes smaller). In other words, selecting a fixed fitting range for all k_T which is too narrow may introduce an artificial k_T dependence into the fitted radii. Also a narrow fitting range can result in the radii being either lower or higher than the stable value, depending on k_T and the functional form being fitted. Incorrect fitting range selection may result in systematic deviations of up to 30%. We use a value of the maximum fitting range of 1.0 GeV/c, which is enough to obtain stable fitting results for all directions, all k_T, and both functional forms of the fit.

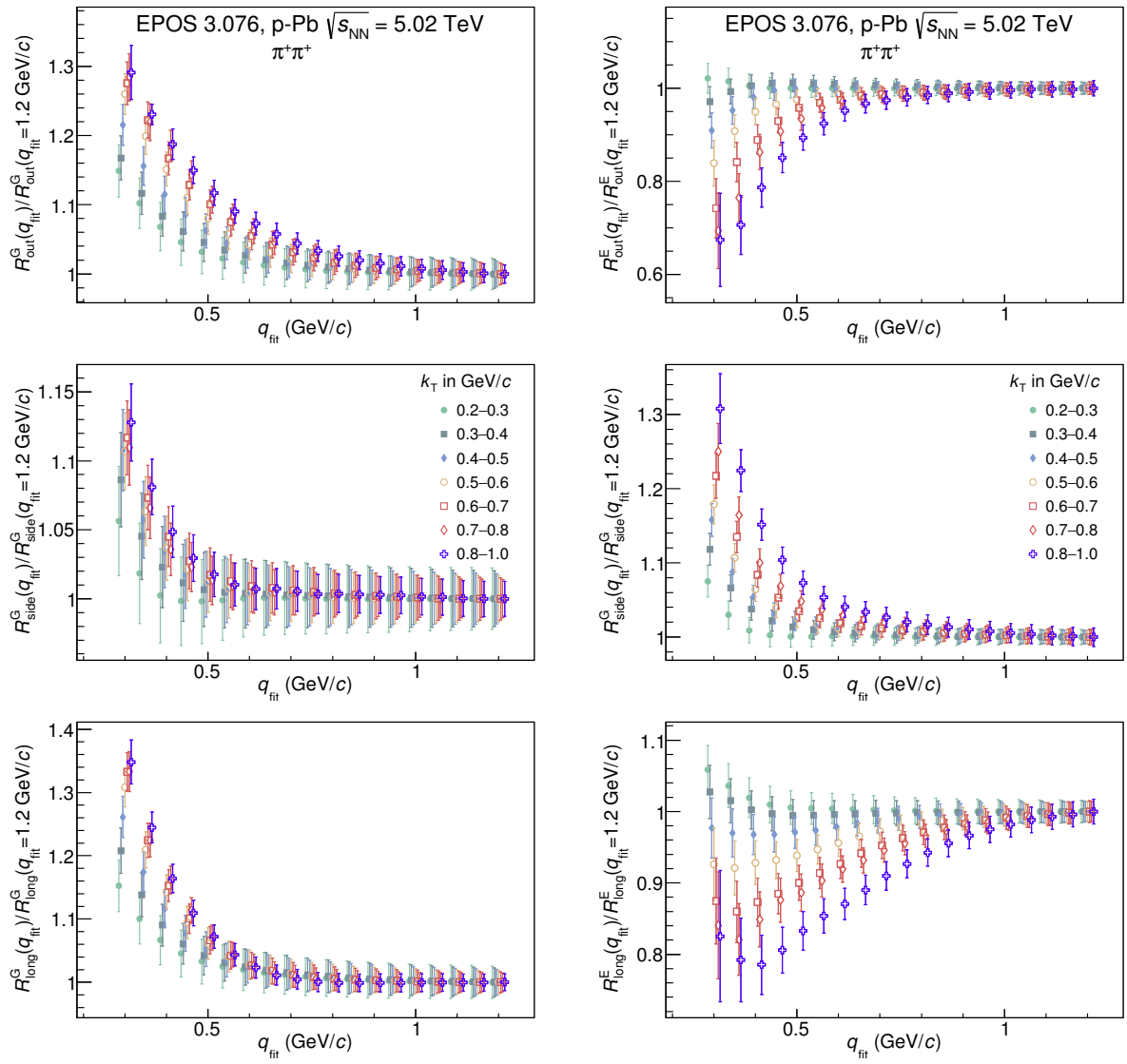

Figure 5.4: Dependence of the fitted radii on the maximum fitting range value q_{fit}, normalized to the value for the maximum fitting range of $q_{\text{fit}} = 1.2$ GeV/c, in the out (upper panels), side (middle panels), and long (lower panels) directions, for all k_{T} ranges. The Gaussian fit is shown in the left panels, the EGE in the right panels. Values for different k_{T} ranges are slightly shifted in q_{fit} for visibility.

5.4 Fitting the full correlation

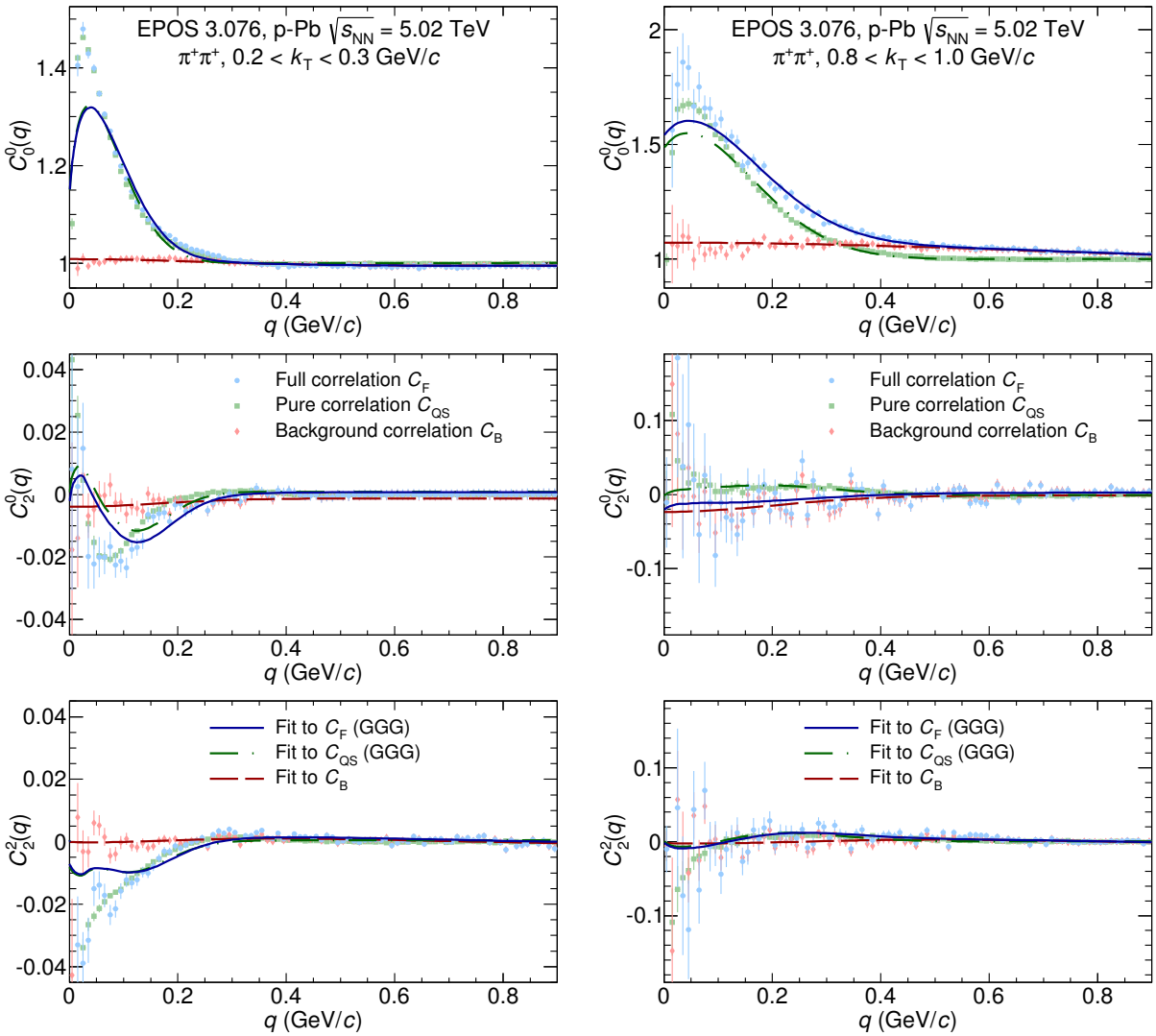

Figure 5.5: First three non-vanishing components of the SH representation of the $\pi^+\pi^+$ correlation functions from EPOS model for $0.2 < k_T < 0.3$ GeV/c (left plot) and $0.8 < k_T < 1.0$ GeV/c (right plot). Lines correspond to the GGG fit with maximum fitting range $q_{fit} = 1.0$ GeV/c.

We have performed reference fits to all pure correlation functions C_{QS} for all k_T with the two functional forms. We also proposed three scenarios for the background characterization, which vary in the number of free parameters and the level of Monte Carlo model dependence that they introduce. We now proceed to fit the full correlation function C_F, which include both the effects of femtoscopic correlations, as well as other event-wide sources. It is now necessary to apply the full fitting formula from Eq. (5.1) with the Ω factor constrained with the procedure described in Sec. 5.2.4. Examples of the fits (with maximum fitting range $q_{fit} = 1.0$ GeV/c)

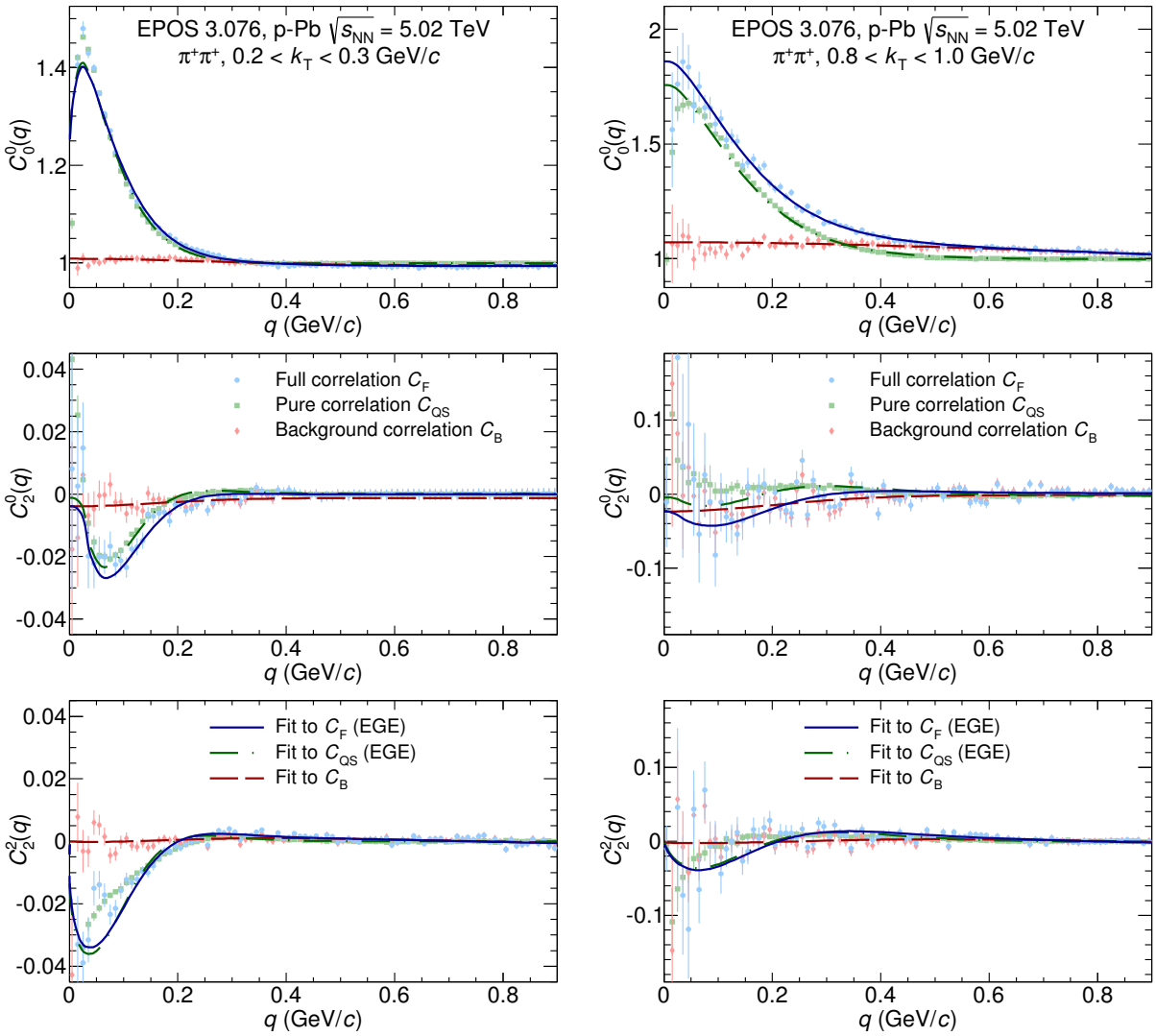

Figure 5.6: First three non-vanishing components of the SH representation of the $\pi^+\pi^+$ correlation functions from EPOS model for $0.2 < k_T < 0.3$ GeV/c (left plot) and $0.8 < k_T < 1.0$ GeV/c (right plot). Lines correspond to the EGE fit with maximum fitting range $q_{fit} = 1.0$ GeV/c.

are shown in Fig. 5.5 for the Gaussian functional form and in Fig. 5.6 for the EGE fit. The background fit, drawn as red dashed lines in both figures, corresponds to scenario 3, i.e. the full three-dimensional function. It is relatively small for the low k_T, although even there some deviation from 1.0 in (0,0) and from 0 in the (2,0) components can be seen. The deviations for the high k_T range are more pronounced. It is also apparent that the Gaussian fit, while able to capture the general trend of the correlation, is not describing the behavior of the correlation function at low q. This is fully consistent with experimental observation of non-Gaussian shape of correlation in small system. At the same time the EGE fit works much better in this range, again in agreement with experimental observations. Also the non-trivial behavior of the (2,0)

and (2,2) components at low q is better captured by the EGE fit.

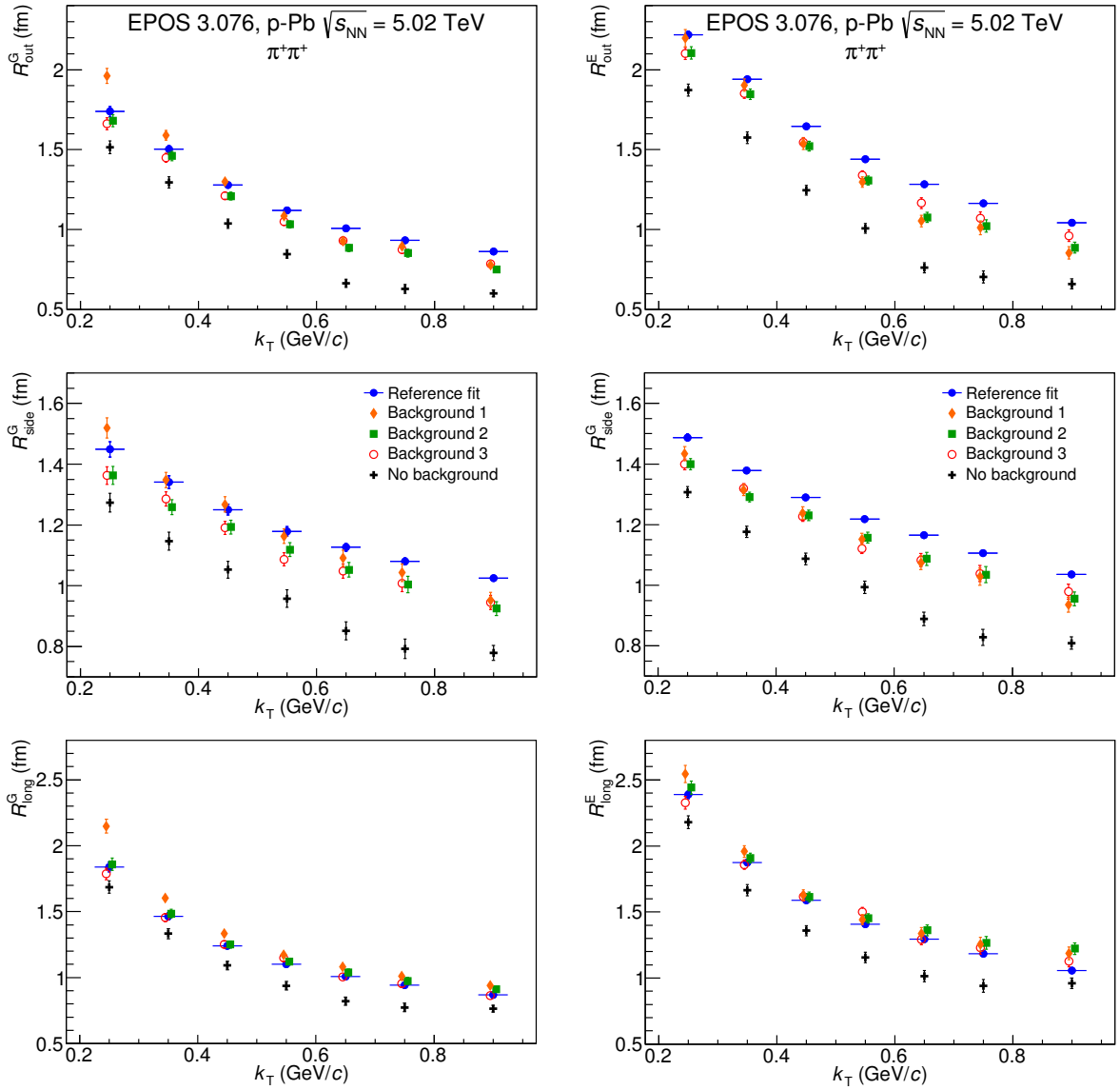

Figure 5.7: Extracted femtoscopic radii. "Reference fit" is performed to pure correlation C_{QS}. "Background 1": first scenario, with minimal MC dependence (magnitude as free parameter), "Background 2": second scenario, with both magnitude and shape fixed, "Background 3": full three-dimensional shape of the background fixed. "No background": fit to C_F is performed with the Ω factor set to 1.0. All fits are performed with maximum fitting range q_{fit} = 1.0 GeV/c. Points for the same k_T range for various versions of the fit are slightly shifted in k_T for visibility.

The final radii coming from all the fits are shown in Fig. 5.7. All three background scenarios are shown, in addition the fit to C_F was performed with no background treatment (Ω in Eq. (5.1) set to 1.0). Let us focus first on the extreme case of not accounting for background at all. The radii are then always strongly underpredicted with respect to the reference, with

differences reaching 30%. Such fits are clearly not acceptable in the low multiplicity environment, where significant additional correlation sources are present. All the other scenarios do take the background into account and, as a consequence, they much more closely resemble the reference values. The Gaussian fit with the magnitude of the background free shows relatively large differences. In addition the slope of the k_{T} dependence is visibly altered – the radii in the transverse directions are higher than the reference at low k_{T} and lower at high k_{T}. The same fit behaves much better for the EGE case. Nevertheless, it seems that trying to constrain the background magnitude with the data itself (leaving the magnitude free in the fit) can potentially dangerously alter the results, unless we precisely control the functional form of the femtoscopic effect. At the moment such form is not known for real collisions, especially in the very fresh p–Pb data at the LHC. Therefore, using a fit with unconstrained background magnitude is also discouraged. That leaves the last two options, where both the magnitude and the shape of the background are constrained based on the Monte Carlo procedure. They both produce comparable agreement with the reference sample, with the full three-dimensional background giving a slightly better agreement, as should be expected. However, it should be noted that EPOS model produces a relatively spherically symmetric shape of the correlation function, which may not be the case for experimental data. For a Gaussian fit the radii deviate downwards by 4-8% for the *out* direction, downward by 6-8% for the *side* direction and no more than 3% in the *long* direction. For the EGE fit the agreement is very similar. Therefore we have shown that in order to account for the non-femtoscopic effects in the small systems, one needs to first constrain the shape and the magnitude of the background with a Monte Carlo simulation. The remaining systematic uncertainty of the method is then 3-8%.

Chapter 6

Data analysis

6.1 Data sample and event selection

The p–Pb collisions at the LHC have been delivered in a short low-luminosity run in September 2012 and a longer high-luminosity run in the beginning of 2013. The energies of the beams were 4 TeV for protons and 82×4 TeV for Pb ions. In this configuration the collision energy was $\sqrt{s_{\mathrm{NN}}} = 5.02$ TeV in the nucleon–nucleon center-of-mass system, shifted in rapidity relative to the laboratory system by $\Delta y = 0.465$ in the direction of the proton beam. About 80 million p–Pb collisions from 2013 have been analyzed for the studies presented in this thesis. In addition, a detailed description of non-femtoscopic correlations required the analysis of the corresponding Monte Carlo data samples. The MC data which were used for this purpose are EPOS 3.076 [146, 147] p–Pb collisions at $\sqrt{s_{\mathrm{NN}}} = 5.02$ TeV (approximately 11 million events) and PYTHIA 6.4 [144], tune Perugia-0 [284], pp collisions at $\sqrt{s} = 7$ TeV (approximately 172 million events).

The main triggering detector was the V0, consisting of two arrays of 32 scintillator counters, installed on each side of the interaction point, covering $2.8 < \eta < 5.1$ (V0A) and $-3.7 < \eta < -1.7$ (V0C) (for description see Sec.3.2.1.5). The minimum-bias trigger required a signal in both V0A and V0C detectors which is consistent with the collision occurring at the center of the ALICE detector. Additionally, specific selection criteria to remove pile-up collisions[1] were applied.

[1] Pile-up is an effect when two or more collisions coincide in a single bunch crossing (so practically at the same time). Tracks from these additional collisions may obscure the results of the analysis, hence special algorithms and selection criteria have been developed in order to find and remove most of such events.

The collision vertex position[2] was determined with the tracks reconstructed in the ITS and TPC as described in Chapter 3. An event was selected if the vertex position along the beam direction was within 10 cm of the detector's center. This ensures a uniform acceptance in η.

6.1.1 Definition and selection of multiplicity

In order to study the influence of nuclear effects in the p–Pb system it is necessary to analyze experimental observables as a function of centrality of the collision. In A–A systems the centrality is usually determined by relating the intervals of measured multiplicity distributions to the number of nucleon–nucleon collisions N_{coll} defined by the Glauber model (for details see Sec. 2.3.4.1). However, in the p–Pb collision system, the correlation between multiplicity and N_{coll} is much weaker than in A–A and the dynamical biases introduced by the multiplicity estimation can strongly affect the experimental results [285]. Therefore, the p–Pb results are reported either for minimum-bias sample or as a function of event multiplicity. In the case of the analysis reported in this thesis the p–Pb events recorded by ALICE were grouped in multiplicity classes (0–20%, 20–40%, 40–60%, and 60–90%) defined as fractions of the analyzed sample sorted by decreasing signal from the V0A detector. These multiplicity intervals are characterized by the mean charged-particle multiplicity density $\langle \mathrm{d}N_{\mathrm{ch}}/\mathrm{d}\eta \rangle$ at midrapidity. Table 6.1 shows the multiplicity class definitions and the corresponding mean charged-particle multiplicity densities averaged over $|\eta| < 0.5$ and obtained using the method presented in Ref. [110]. In Fig. 6.1 the multiplicity distribution in the V0A detector with multiplicity binning (more granular than used in this analysis) is presented.

6.2 Track selection criteria

Charged track reconstruction was performed using the Time Projection Chamber (TPC) (for details see Sec. 3.2.1.2) and the Inner Tracking System (ITS) (for details see Sec. 3.2.1.1). The information from the ITS was used for tracking and primary particle selection. Details on the combined efficiency and acceptance of the track reconstruction in the central pseudorapidity range $|\eta| < 1.2$ are given in Ref. [132]. The momentum of each track was determined from its

[2]The spatial coordinates of the particle collision registered by the experiment are commonly referred to as the emphprimary or *collision* vertex. They are usually measured with respect to the center of the main tracking detector; in the case of ALICE it is the TPC.

Table 6.1: Definition of the multiplicity classes as fractions of the analyzed event sample and their corresponding $\langle \mathrm{d}N_{\mathrm{ch}}/\mathrm{d}\eta(|\eta| < 0.5, p_{\mathrm{T}} > 0)\rangle$. The given uncertainties are systematic as the statistical uncertainties are negligible.

Event class	$\langle \mathrm{d}N_{\mathrm{ch}}/\mathrm{d}\eta\rangle_{\lvert\eta\rvert<0.5}$ $p_{\mathrm{T}} > 0$ GeV/c
60–90%	8.2 ± 0.3
40–60%	16.1 ± 0.4
20–40%	23.2 ± 0.5
0–20%	35.5 ± 0.8

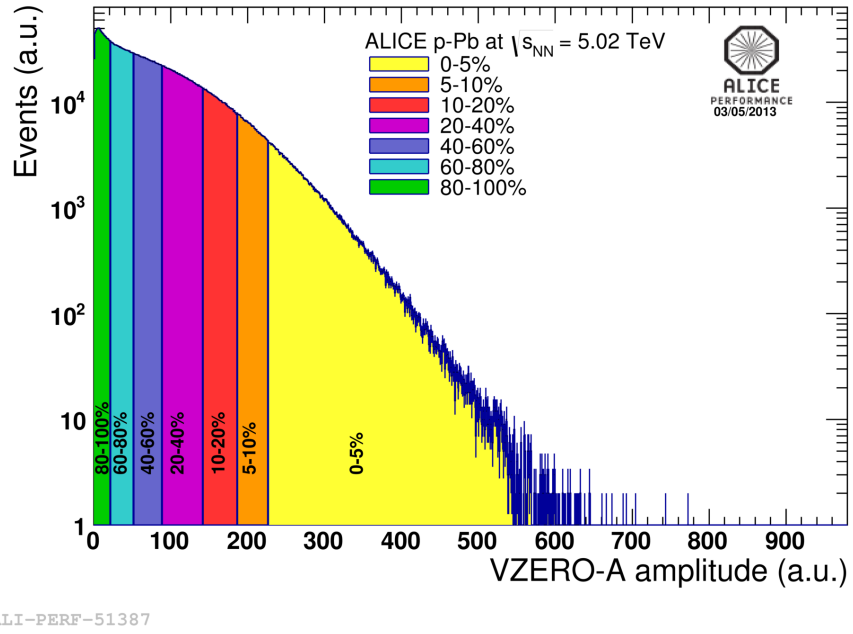

Figure 6.1: Multiplicity distribution in the V0A detector from p–Pb collisions with multiplicity classes in colors (thinner ranges than used for this analysis).

curvature in the uniform magnetic field of 0.5 T oriented along the beam axis, provided by the solenoidal ALICE magnet (also referred to as the L3 magnet).

Track reconstruction in the ALICE central barrel proceeds in three steps using Kalman algorithm [157]. The first step starts from the outer radius of the TPC where the track candidates (called seeds) are found. The seeds are the starting points for the fitting algorithm towards the TPC inner radius. After this process, ITS takes over. It tries to prolong the track as close as possible to the primary vertex. The second step is tracking from the primary vertex to the outer

limit of the TPC. The third step is to refit the track again to the primary vertex, first for TPC (which is called *TPC refit*), then for ITS (which is called *ITS refit*). Dedicated flags provide information if the refit was successful. In this analysis both TPC and ITS refit were required. Additionally, each track was required to have at least one hit in the SPD detector.

A TPC track segment is reconstructed from space points (clusters), maximum one per padrow, as the track propagates radially outwards through the TPC. Each track was required to be composed of at least 50 such clusters. The quality of the fit χ^2 was required to be better than 4 per cluster (each cluster has two degrees of freedom). Tracks that show a kink topology in the TPC were rejected. To ensure that only primary-particle tracks were selected, the distance of closest approach (DCA) of the track to the primary vertex was required to be smaller than 2.0 cm in the longitudinal direction and $0.0105 + 0.0350 \cdot p_{\mathrm{T}}^{-1.1}$ cm, with p_{T} in GeV/c, in the transverse direction. The kinematic range of particles selected for this analysis was $0.12 < p_{\mathrm{T}} < 4.0$ GeV/c and $|\eta| < 0.8$.

Figure 6.2 presents single particle distributions of transverse momentum p_{T}, azimuthal angle φ, position of the vertex along the beam, and DCA distributions along the beam and in the transverse plane.

6.3 Particle identification

The TPC and TOF detectors were used for identification of primary pions. In the TPC particle identification (PID) is based on measurement of energy loss per unit path length, $\mathrm{d}E/\mathrm{d}x$, which is parametrized by the Bethe-Bloch formula:

$$\left\langle \frac{\mathrm{d}E}{\mathrm{d}x} \right\rangle = \frac{C_1}{\beta^2} \left[\ln\left(C_2 \beta^2 \gamma^2\right) - \beta^2 + C_3 \right], \tag{6.1}$$

where C_1, C_2, and C_3 are the detector parameters, $\beta = v/c$ is the particle velocity, and γ is the Lorentz factor. In TOF the measured particle velocity β has the following parametrization:

$$\beta = \frac{1}{\sqrt{\frac{m}{p}^2 + 1}} = \frac{L}{tc}, \tag{6.2}$$

where m is the particle mass, p is the momentum, L is the corresponding track length, and t is the TOF measured time. For both the TPC and TOF the measured signal for each reconstructed particle was compared with the one expected for a pion. Figure 6.3 shows energy loss $\mathrm{d}E/\mathrm{d}x$ (left panel) and TOF signal β (right panel), as a function of particle momentum.

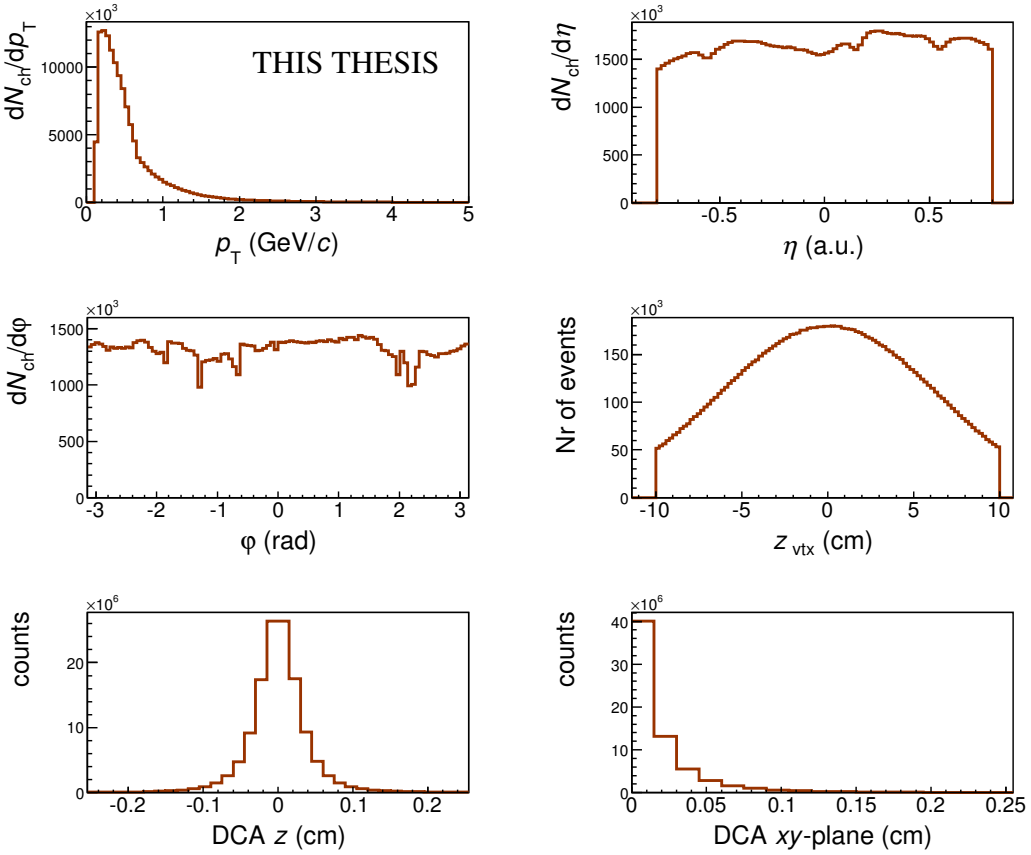

Figure 6.2: Single particle distribution plots and for distance of closest approach (bottom row) in z direction (left panel) and in xy plane (right panel) for analyzed data. Top row: $\mathrm{d}N_{\mathrm{ch}}/\mathrm{d}p_{\mathrm{T}}$ (left panel) and $\mathrm{d}N_{\mathrm{ch}}/\mathrm{d}\eta$ (right panel) distributions, middle row: $\mathrm{d}N_{\mathrm{ch}}/\mathrm{d}\varphi$ distribution (left panel) and position of the vertex along the beam axis with respect to the center of the TPC (right panel), bottom row: distance of closest approach (DCA) distributions along the beam axis (left panel) and in the transverse plane (right panel).

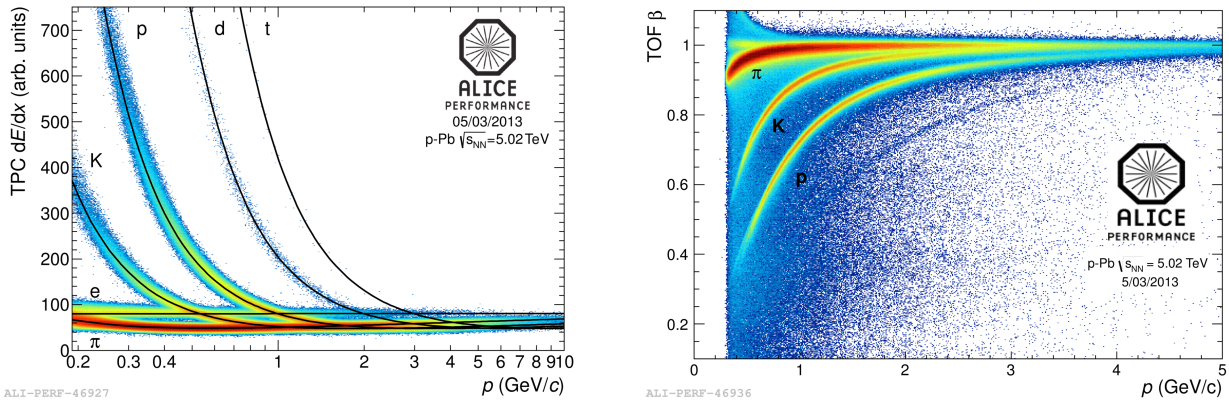

Figure 6.3: Energy loss in the TPC (left plot) and TOF particle velocity β (right plot) as a function of particle momentum. Lines in the TPC energy loss plot correspond to Bethe-Bloch parametrization.

Particle identification was based on the *number of sigmas*, or shortly nσ, method, where sigma σ, is the standard deviation from the Bethe-Bloch curve or the time-of-flight deviation from the expected time for pions respectively. Only those particles are accepted which fall within certain maximum number n of standard deviations from the Bethe-Bloch or particle velocity β curves in the TPC and TOF, respectively. Figure 6.4 shows the nσ distribution for pions in TPC and TOF. The allowed deviations for both detectors, depending on the momentum of the particle, are listed below:

- $|n_{\sigma,\mathrm{TPC}}| < 3$ for tracks without TOF signal for momenta less than 0.5 GeV/c;
- $|n_{\sigma,\mathrm{TPC}}| < 2$ for tracks without TOF signal for momenta in range $(0.5, 0.65)$ GeV/c;
- $|n_{\sigma,\mathrm{TPC}}| < 3$ and $|n_{\sigma,\mathrm{TOF}}| < 3$ for tracks with TOF signal for momenta less than 0.65 GeV/c;
- tracks without TOF signal for momenta higher than 0.65 GeV/c were rejected;
- $|n_{\sigma,\mathrm{TPC}}| < 5$ and $|n_{\sigma,\mathrm{TOF}}| < 3$ for tracks for momenta in range $(0.65, 1.5)$ GeV/c;
- $|n_{\sigma,\mathrm{TPC}}| < 5$ and $|n_{\sigma,\mathrm{TOF}}| < 2$ for tracks for momenta higher than 1.5 GeV/c.

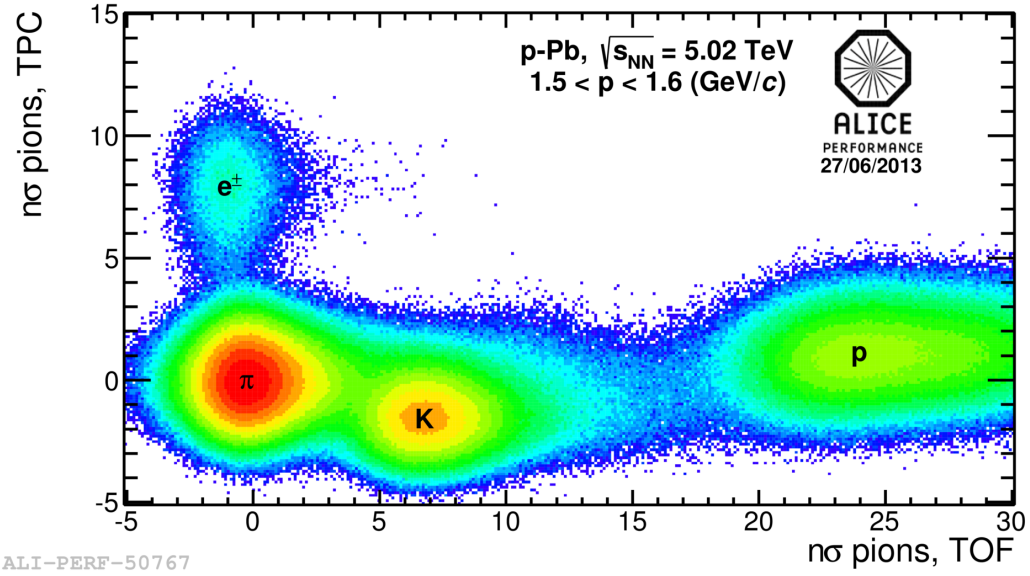

Figure 6.4: Number of sigmas distribution for TPC and TOF for p–Pb collisions in ALICE. Plot is made assuming pion mass.

The selection criteria were optimized to obtain a high purity sample while maximizing efficiency, especially in the regions where the expected signal for other particles (electrons and kaons for the TPC, kaons for TOF) approaches the pion value. The purity of the pion sample was above 98%. The TOF and TPC signals for the pion sample (after the PID selection) are shown in Fig. 6.5.

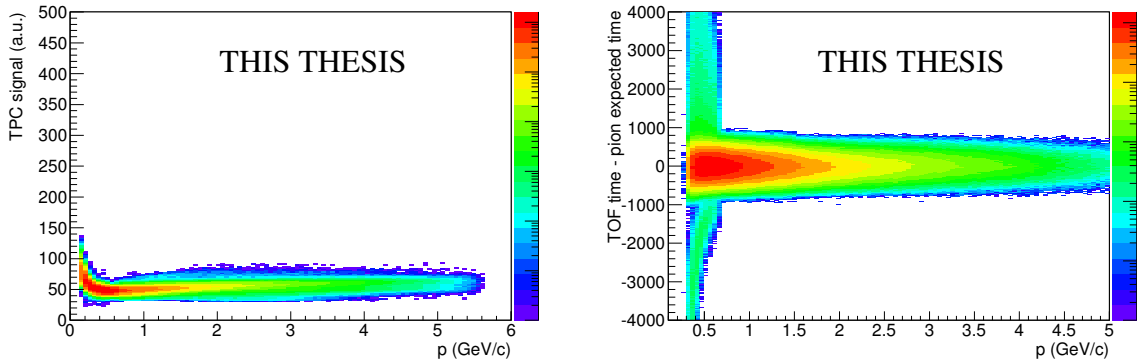

Figure 6.5: Energy loss of the pion sample in the TPC (left plot) and difference between TOF measured time and pion expected time (right plot) for the p–Pb collisions 0-10% multiplicity class measured in ALICE.

6.4 Pair-level selection criteria

6.4.1 Pair transverse momentum selection

As it has been mentioned in Sec. 4.6, the decrease of HBT radii with increasing pair transverse momentum k_{T} is interpreted as a manifestation of a strong collective flow in the A–A system. Therefore, presence of such behavior in p–Pb collisions would be an important indication of the existence of the collective effects in this system. Hence, the analysis was performed in seven ranges of pair transverse momentum, as shown in Table 6.2.

Table 6.2: Pair transverse momentum k_{T} ranges.

Range	k_{T} (GeV/c)
1	0.2–0.3
2	0.3–0.4
3	0.4–0.5
4	0.5–0.6
5	0.6–0.7
6	0.7–0.8
7	0.8–1.0

6.4.2 Split and merged tracks rejection

The accepted particles from each event were combined in pairs. The two-particle detector acceptance effects of *track splitting* (one track is mistakenly reconstructed as two) and *track merging* (two tracks are reconstructed as one or not at all) were taken into account and corrected for with the procedure described below (the same procedure was used in the analysis of pp data in Ref. [193]).

There are three steps to remove track splitting and merging. In the first step, the requirement that the track is simultaneously reconstructed in the TPC and ITS decreases splitting significantly. In the second step, we apply a two-track selection called *share fraction*. Each cluster in the TPC is flagged as "shared" if it is used in the reconstruction of more than one track. The split tracks tend to produce pairs which share most of their clusters; therefore, we removed pairs that share more than 5% of their TPC clusters. In the third step, called *share quality*, we look for configurations where a single track is split in two segments in the TPC, e.g. by the TPC central membrane or a TPC sector boundary. Such segments should be correctly connected in the tracking procedure to form a single track if the detector calibration is perfect. However, in a few rare cases this does not happen and a split track can occur. Such pairs would consist of two tracks that have a relatively small number of TPC clusters and they would rarely both have a cluster in the same TPC pad row. Therefore, we count, for each pair, the number of times that both tracks have a separate (non-shared) cluster in a TPC pad row. Pairs for which this number is low are removed.

The effect of the two-particle detector acceptance in small systems, such as p–Pb, is expected to be small.

6.5 Experimental correlation function

The correlation function $C(\mathbf{q})$ was defined experimentally as:

$$C(\mathbf{q}) = \frac{A(\mathbf{q})}{B(\mathbf{q})}, \tag{6.3}$$

where $\mathbf{q}$ is the momentum difference evaluated in the LCMS system, as described in Sec. 4.3. In the analysis, the signal distribution A was composed of pairs of particles from the same event. In order to remove trivial correlations coming from limited detector acceptance, the signal distribution should be divided by the background distribution B composed of physically uncorrelated

particles. The most commonly used technique to calculate the background is "event mixing", with the two particles coming from two different events for which the vertex positions in beam direction agree within 2 cm and the multiplicities differ by no more than 1/4 of the width of the given event class. In order to improve the statistics of the background calculation, each event was mixed with 10 such events. Finally, the correlation function was normalized to the number of entries in numerator and denominator.

6.6 Monte Carlo data

Table 6.3: Complete list of Monte Carlo models used for the studies of the non-femtoscopic background. The models marked in bold describe the non-femtoscopic part of the correlation function in terms of shape and magnitude.

Model	System	Energy (TeV)	`AliRoot` interface	Reconstructed data
AMPT [46]	p–Pb	5.02	✓	
HIJING [45]	p–Pb	5.02	✓	✓
DPMJET [47]	p–Pb	5.02	✓	✓
THERMINATOR 2 [286]	p–Pb	5.02		
EPOS 3.076 [147]	**p–Pb**	**5.02**		
PYTHIA 6.4 [144] Perugia-2011 [145]	p–Pb	5.02	✓	✓
PYTHIA 6.4 [144] **Perugia-0** [145]	**pp**	**7**	✓	✓
PYTHIA 6.4 [144] Z2	pp	7	✓	
PYTHIA 8.1 [287] 4C [288]	pp	7	✓	

In Chapter 5 we showed that Monte Carlo models are crucial for the description of the non-femtoscopic background observed in experimental data. Hence, several event generators were studied at various stages of this analysis, such as AMPT [46], HIJING [45], DPMJET [47], THERMINATOR 2 [286] (with 3+1 viscous hydrodynamics and local charge conservation [140]), EPOS 3.076 [147], and various tunes of PYTHIA 6.4 [144] and PYTHIA 8.1 for both p–Pb and pp collisions at similar multiplicity. All of them are collected in Table 6.3, which also shows whether the reconstructed data was available for a given model and if the model was

implemented in the AliRoot framework. The ones marked in bold (EPOS 3.076 and PYTHIA 6.4 Perugia-0) were used in Chapter 7 in the procedure of the determination of the femtoscopic radii from the p–Pb collision data, the final result of this thesis. Detailed studies of all other Monte Carlo generators are shown in Appendix A.

The analysis of Monte Carlo data must resemble the analysis of experimental data as much as possible, hence similar selection criteria should be applied. In most cases this can be assured by employing a full simulation of the detector response, as in the experimental data. However, such procedure is possible only for those MC models where the interface classes to read events generated by them exist in AliRoot[3]. If such interface does not exist, we can not apply the ALICE reconstruction chain and only the generator-level information is available. In these cases the selection criteria must be defined very carefully in order to be compared to collision data[4].

The most important event selection, needed reliably compare MC models with collision data, is multiplicity. This section will present the procedure of finding multiplicity intervals in EPOS and PYTHIA models which correspond to V0A event classes from the analysis of the collision data.

6.6.1 Multiplicity selection in EPOS

EPOS 3.076 [146, 147] is one of the MC models which lack the interface in AliRoot. The multiplicity ranges were defined employing the following procedure:

1. The ALICE results on pseudorapidity density $\mathrm{d}N_{\mathrm{ch}}/\mathrm{d}\eta$ distribution from p–Pb collisions at $\sqrt{s_{\mathrm{NN}}}$ = 5.02 TeV from Ref. [110] were taken as a reference. They are shown in Fig. 2.23.

[3]The MC reconstruction process is performed on the Grid and is managed centrally by the ALICE Physics Board. Some of datasets from Monte Carlo models were not reconstructed since the reconstruction process had not finished at the time of performing the analysis or upon the decision of the Physics Board.

[4]Datasets generated with Monte Carlo models using the AliRoot framework have a common ALICE output format and no additional software is required to read them. Therefore, practically the same programs can be used for the analysis of both simulated and reconstructed data, which significantly reduces problems with definition of selection criteria. If the model is not embedded in AliRoot, than a careful study of the content of the produced output file is required and additional software to read the generated events needs to be developed.

2. Pseudorapidity density $\mathrm{d}N_{\mathrm{ch}}/\mathrm{d}\eta$ distribution was be calculated from EPOS model (selecting pions, kaons, protons, electrons, and corresponding antiparticles; excluding weak decay products), without applying any selection of multiplicity.

3. Both $\langle \mathrm{d}N_{\mathrm{ch}}/\mathrm{d}\eta \rangle$ distributions, from ALICE and EPOS, were compared. The shapes of both distributions were found similar; hence, we divideded ALICE distribution by EPOS distribution in order to obtain a constant dependence on η (see right panel of Fig. 6.6). We defined the *scaling factor s* as a value of a fit of constant function to this distribution.

4. When s was obtained, the multiplicity intervals in EPOS could be determined by dividing the ALICE $\langle \mathrm{d}N_{\mathrm{ch}}/\mathrm{d}\eta \rangle$ for a given multiplicity class by EPOS $\langle \mathrm{d}N_{\mathrm{ch}}/\mathrm{d}\eta \rangle$ calculated for a considered EPOS multiplicity range.

   (a) The procedure should begin with the 0–20% V0A multiplicity class. We set no upper limit on N_{ch} interval in EPOS and varied the lower limit.

   (b) For each range with different lower limit we calculated mean $\langle \mathrm{d}N_{\mathrm{ch}}/\mathrm{d}\eta \rangle$. Then, we could plot the ratio of $\langle \mathrm{d}N_{\mathrm{ch}}/\mathrm{d}\eta \rangle$ from ALICE for 0–20% multiplicity class (see Table 6.1) to the ones obtained for different lower limits (as shown in Fig. 6.7).

   (c) To find the proper lower limit of N_{ch} corresponding to 20% V0A multiplicity, we fitted this dependence with a linear function. The proper lower limit of the multiplicity range for EPOS is represented as N_{ch} of the intersection of linear fit with the constant line corresponding to s, as shown in Fig. 6.7. In this way the EPOS multiplicity interval corresponding to ALICE 0– 20% V0A multiplicity class was found.

5. Once the highest multiplicity range was found, we could repeat the procedure for lower V0A multiplicity classes (i.e. for 20–40% V0A multiplicity class we fixed the upper limit of the EPOS range to the one obtained as the lower limit in previous step, therefore we had to vary the lower limit again to find EPOS N_{ch} corresponding to 40% V0A multiplicity), and so on.

All the EPOS multiplicity intervals, corresponding to V0A multiplicity classes, which were found with the procedure described above, are shown in Table 6.4.

Table 6.4: Multiplicity ranges from EPOS corresponding to ALICE V0A multiplicity classes.

ALICE V0A event class	EPOS multiplicity range
0-20%	$N_{\mathrm{ch}} > 97$
20-40%	$73 < N_{\mathrm{ch}} < 97$
40-60%	$43 < N_{\mathrm{ch}} < 73$
60-90%	$N_{\mathrm{ch}} < 43$

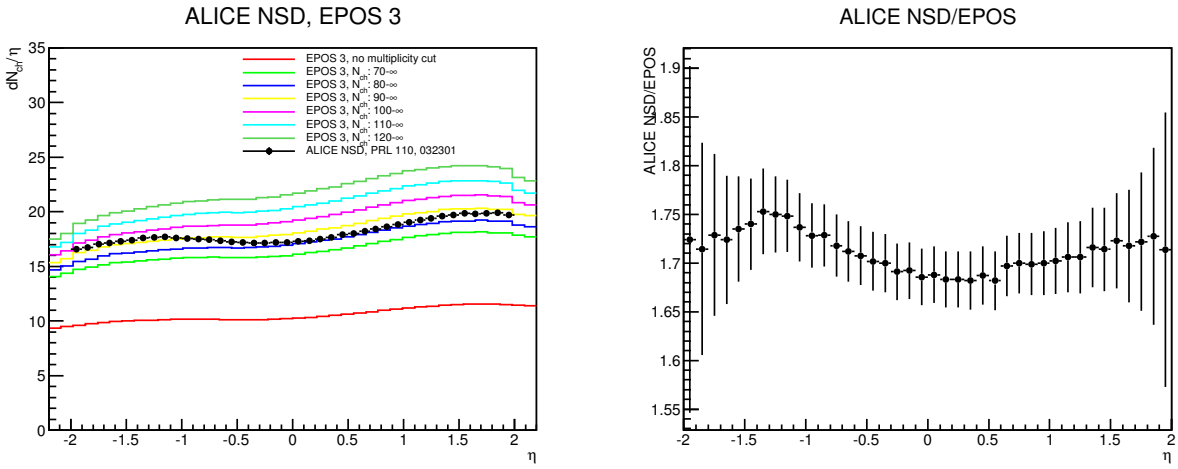

Figure 6.6: Left plot: $\mathrm{d}N_{\mathrm{ch}}/\mathrm{d}\eta$ distributions from ALICE data from Ref. [110] (black points) and from EPOS 3 model (without multiplicity selection – red line, with different lower limits of N_{ch} – other colors). Right plot: Division of ALICE and EPOS 3.076 $\mathrm{d}N_{\mathrm{ch}}/\mathrm{d}\eta$ without multiplicity selection. The constant fit to this distribution yields the scaling factor $s = 1.67$.

6.6.2 Multiplicity selection in PYTHIA Perugia-0

The second model used in the analysis of collision data was PYTHIA Perugia-0, used for the studies of pp collisions at $\sqrt{s} = 7$ TeV (see Fig. 6.8). For the p–Pb collision studies we calculated correlation functions from PYTHIA using exactly the same selection criteria and employing exactly the same multiplicity determination as in the pp analysis. However, in that system the amount of data accumulated by the experiment was much higher than in p–Pb and allowed to introduce more granular multiplicity binning. Hence, in order to correctly use these calculations in p–Pb we compared the $\langle \mathrm{d}N_{\mathrm{ch}}/\mathrm{d}\eta \rangle$ values from V0A multiplicity classes in p–Pb to the ones in pp and chose the most similar multiplicity ranges. Table 6.5 presents all the multiplicity intervals from the pp analysis and the corresponding V0A multiplicity classes from

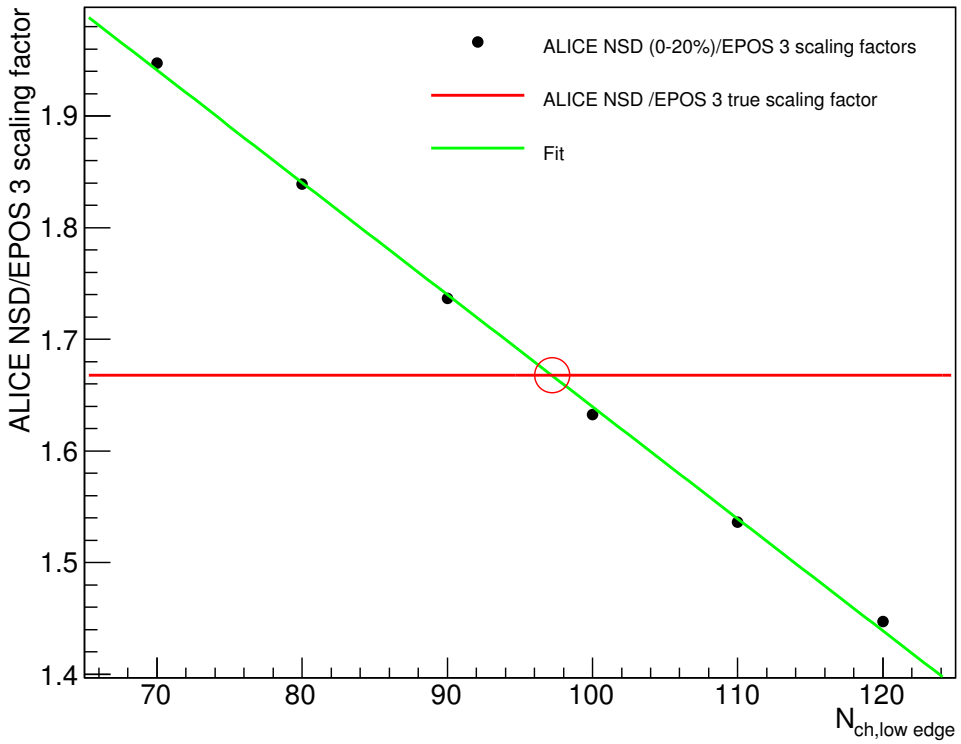

Figure 6.7: Ratios of $\mathrm{d}N_{\mathrm{ch}}/\mathrm{d}\eta$ distributions from ALICE over EPOS for different values of lower edge of multiplicity interval (black points), linear fit (green line), and the scaling factor s (constant red line). The intersection point between the scaling factor and the fit is marked as red circle.

p–Pb data. We must note, however, that for higher multiplicity intervals the $\langle \mathrm{d}N_{\mathrm{ch}}/\mathrm{d}\eta \rangle$ values for PYTHIA are lower than the corresponding ones for collision data. Though, as presented in Fig. 7.7 and described in Chapter 7, the non-femtoscopic background in PYTHIA in C_0^0 component is slightly higher than in data; so, the lower values of $\langle \mathrm{d}N_{\mathrm{ch}}/\mathrm{d}\eta \rangle$ for PYTHIA are not undesirable.

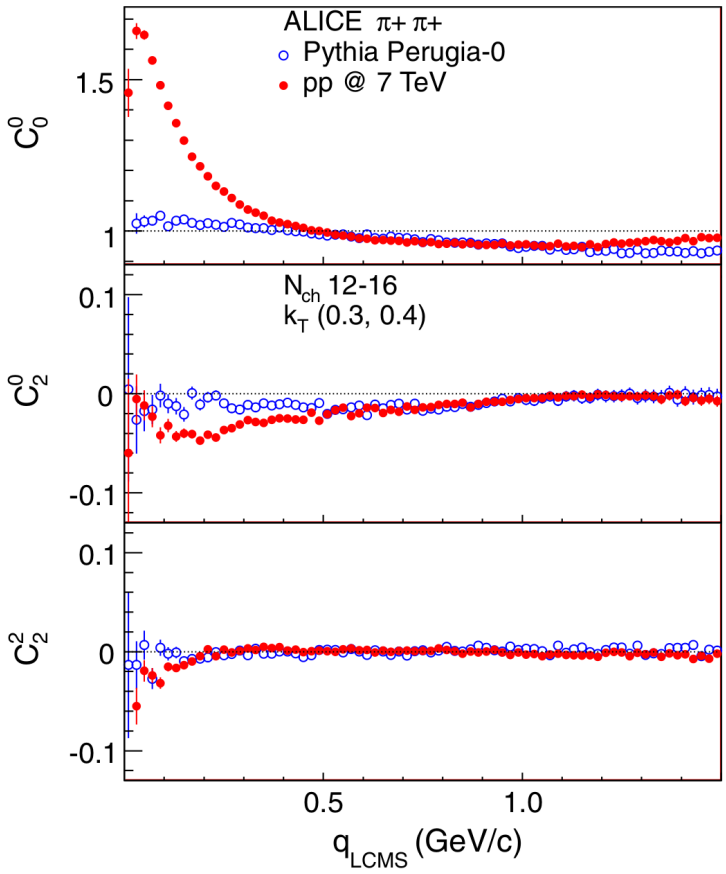

Figure 6.8: First three non-vanishing components of the SH representation of the $\pi^+\pi^+$ correlation functions for events with $12 \leq N_{ch} \leq 16$, pairs with $0.3 < k_T < 0.4$ GeV/c. Open symbols are PYTHIA MC simulations (Perugia-0 tune), closed symbols represent the ALICE data from pp collisions $\sqrt{s} = 7$ TeV collisions. Plot from Ref. [193].

Table 6.5: Multiplicity ranges used in pp analysis [193] corresponding to ALICE V0A multiplicity classes in p–Pb.

PYTHIA multiplicity range	$\langle dN_{ch}/d\eta \rangle$	ALICE V0A event class in p–Pb
1–11	2.8	
12–16	6.6	
17–22	9.2	60-90%, $\langle dN_{ch}/d\eta \rangle = 8.2$
23–28	12.0	
29–34	14.9	
35–41	17.9	40-60%, $\langle dN_{ch}/d\eta \rangle = 16.1$
42–51	21.4	20-40%, $\langle dN_{ch}/d\eta \rangle = 23.2$
52–151	27.6	0-20%, $\langle dN_{ch}/d\eta \rangle = 35.5$

Chapter 7

Results of pion femtoscopy in p–Pb collisions

This chapter presents the results of the three-dimensional pion femtoscopic analysis of p–Pb data at $\sqrt{s_{\rm NN}}$ = 5.02 TeV recorded by ALICE. In Sec. 7.1 the correlation functions for multiplicity and pair transverse momentum ranges are shown. Section 7.1.2 introduces the non-femtoscopic correlations. Finally, the results of the fits, femtosopic radii, and comparison of them to Monte Carlo predictions and femtoscopic data from other experiments and systems, are shown in Sec. 7.1.3.

We note that the content of this chapter (the results and text), with slight modifications in the text, were published in [2]. In addition, the preliminary results were presented a the Quark Matter 2014 conference [3] and published in the conference proceedings in Ref. [4].

7.1 Correlation function analysis

7.1.1 Multiplicity and pair transverse momentum dependence

In Fig. 7.1 three correlation functions are shown, projected over 80 MeV/c - wide slices along the $q_{\rm out}$, $q_{\rm side}$ and $q_{\rm long}$ axes. An enhancement at low relative momentum is seen in all projections. The width of this correlation peak grows with decreasing multiplicity and with increasing $k_{\rm T}$. The femtoscopic effect is expected to disappear at large $q = |\mathbf{q}|$, with the correlation function approaching unity. We observe, especially for large $k_{\rm T}$ and small multiplicities, that the correlation function is not flat in this region and has different values in different projections[1]. The cause may be from non-femtoscopic correlations, which are presumably also affecting the

[1] We note that the overall normalization of the correlation function is a single value for the full three-dimensional object and cannot be independently tuned in all projections.

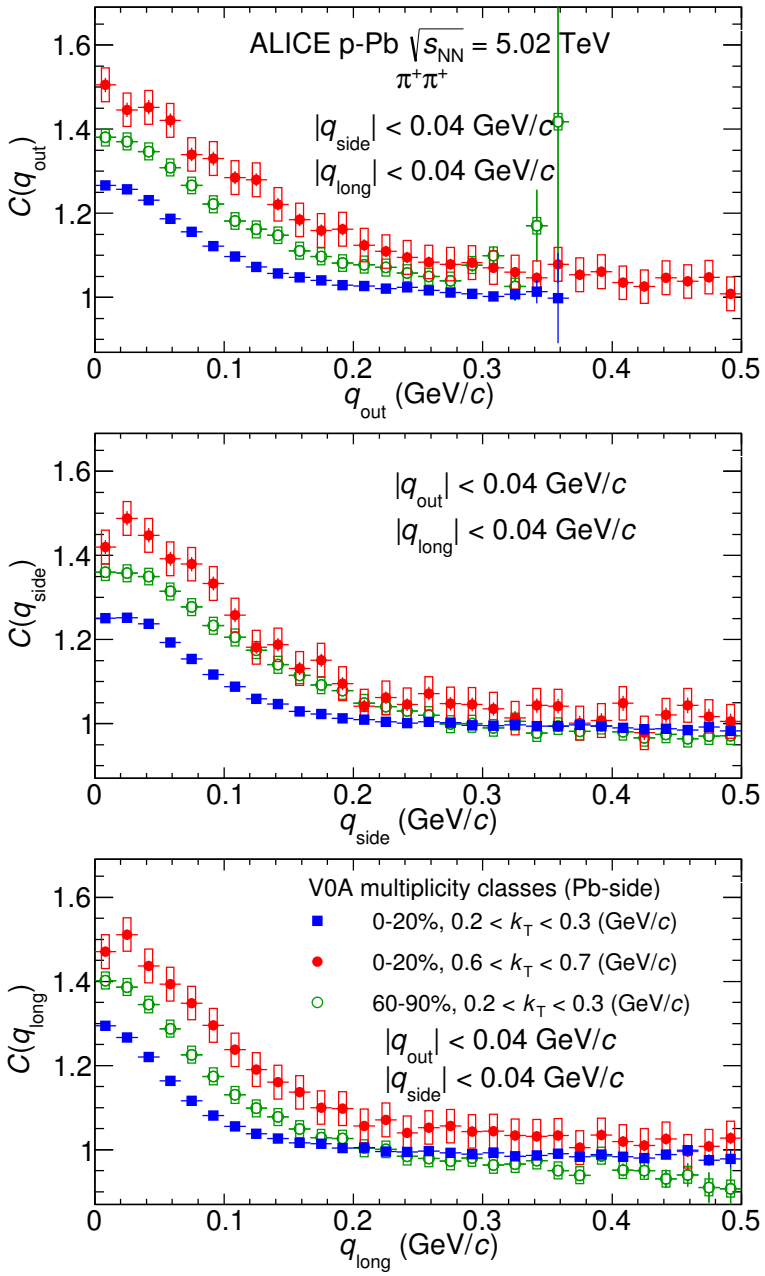

Figure 7.1: Projections of the three-dimensional $\pi^+\pi^+$ correlation functions for three selected multiplicity and k_T ranges along the *out* (top), *side* (middle), and *long* (bottom) axes. The other components are integrated over the four bins closest to zero in their respective q directions.

shape of the correlation function in the femtoscopic (low q) region. This issue is a major source of systematic uncertainty on the extracted radii and is discussed in detail in Sec. 7.1.2 and Sec. 7.1.3.

Figure 7.2 shows the first three non-vanishing components of the spherical harmonics representation corresponding to the correlation functions shown in Fig. 7.1. In the $(0, 0)$ component

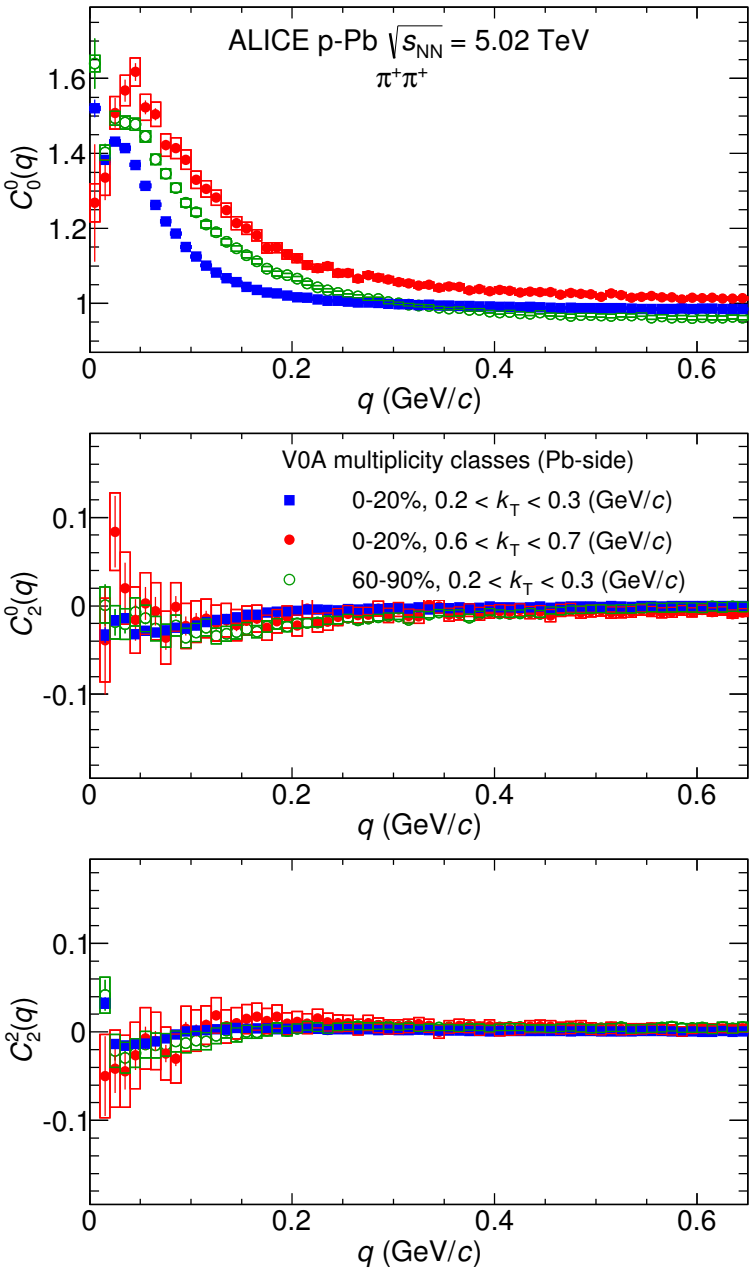

Figure 7.2: First three non-vanishing components of the SH representation of the $\pi^+\pi^+$ correlation functions for three multiplicity and k_T ranges, $l = 0$, $m = 0$ (top), $l = 2$, $m = 0$ (middle), and $l = 2$, $m = 2$ (bottom).

the enhancement at low-q is clearly visible, decreasing (increasing) in width with multiplicity (k_T). The other two components, $(2, 0)$ and $(2, 2)$, show a non-trivial correlation structure, indicating that the source shape is not exactly spherical in the LCMS frame. These structures are located in the same range in q as the enhancement in the $(0, 0)$ component, which suggests that they are femtoscopic in nature.

Exclusion of 90–100% multiplicity range

In order to investigate the behavior of the non-femtoscopic structures at low multiplicity collisions a more detailed analysis has been performed. Figure 7.3 presents the $(0, 0)$ component of the correlation function in SH representation for the 10% wide multiplicity ranges from 50% to 100%. We can clearly see that the lowest multiplicity range, 90–100%, is significantly different from the others (much stronger non-femtoscpic structure). Furthemore, we divided the 90–100% range into two smaller multiplicity classes, 90–95% and 95–100%, shown in Fig. 7.4. The difference between those ranges is only slight (in comparison to significant difference between 80–90% and 90–100% classes). Therefore, since we do not fully understand these effects and, in addition, we do not focus on low multiplicity collisions in this analysis, the 90–100% multiplicity range was excluded from further studies. However, we note that more detailed investigation of low multiplicity collisions is needed in order to understand the observed differences.

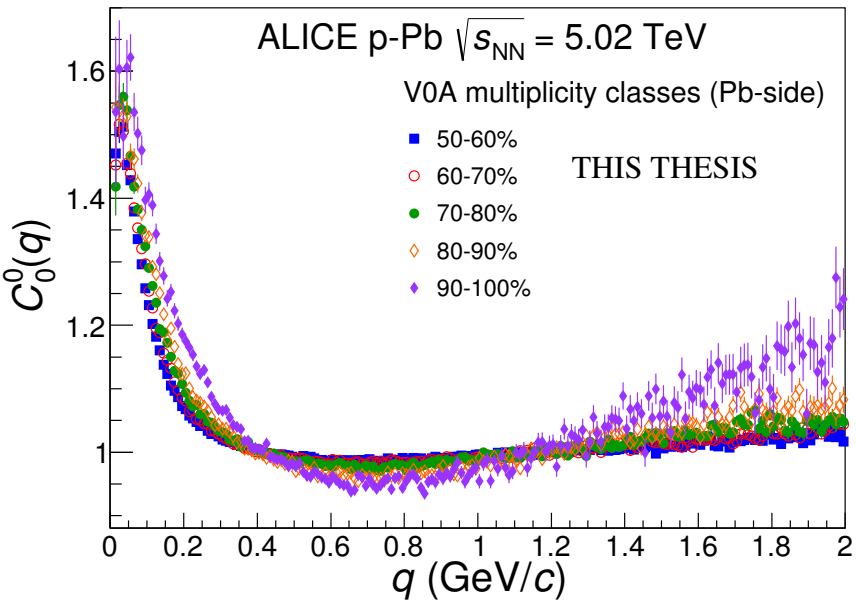

Figure 7.3: The C_0^0 component of the correlation functions for multiplicity ranges 50 – 60%, 60 – 70%, 70 – 80%, 80 – 90%, and 90 – 100%. The non-femtoscopic background is most prominent for the 90 – 100% multiplicity range.

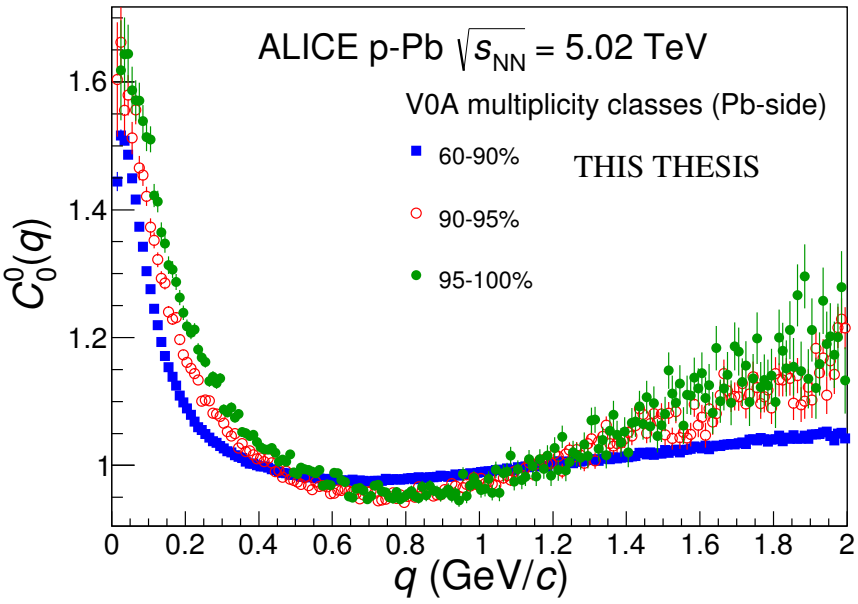

Figure 7.4: The C_0^0 component of the correlation functions for multiplicity ranges 60 – 90%, 90 – 95%, 95 – 100%. The correlation function for multiplicity ranges 90 – 95% and 95 – 100% are clearly different. Those ranges were excluded from the analysis for further studies.

7.1.2 Non-femtoscopic structures

As mentioned in the discussion of Fig. 7.1 and Fig. 7.2, a significant non-femtoscopic correlation is observed in a range in q that is much larger than the characteristic width of the femtoscopic effect. In Fig. 7.5 and Fig. 7.6 we show the correlation in the SH representation up to 2.0 GeV/c in q. A significant slope is seen in the $(0, 0)$ component and a deviation from zero in the $(2, 0)$ component up to approximately 1 GeV/c can be seen for the lowest multiplicity and large k_{T} . Similar correlations have been observed by ALICE in pp collisions [193]. They were interpreted, based on Monte-Carlo model simulations, to be a manifestation of "mini-jets," the collimated fragmentation of partons scattered with modest momentum transfer. The lowest multiplicities observed in p–Pb collisions are comparable to those in pp collisions at $\sqrt{s} = 7$ TeV. Therefore a similar interpretation of the non-femtoscopic correlations here is natural. Similar structures have been observed in d–Au collisions by STAR [235]. One of the specific advantages of the three-pion cumulant analysis [237] is that the influence of such multi-particle correlations is significantly reduced there.

In this analysis the procedure introduced by us in Chapter 5 and published in Ref. [1] was employed to account for non-femtoscopic correlations. It requires a Monte Carlo event gener-

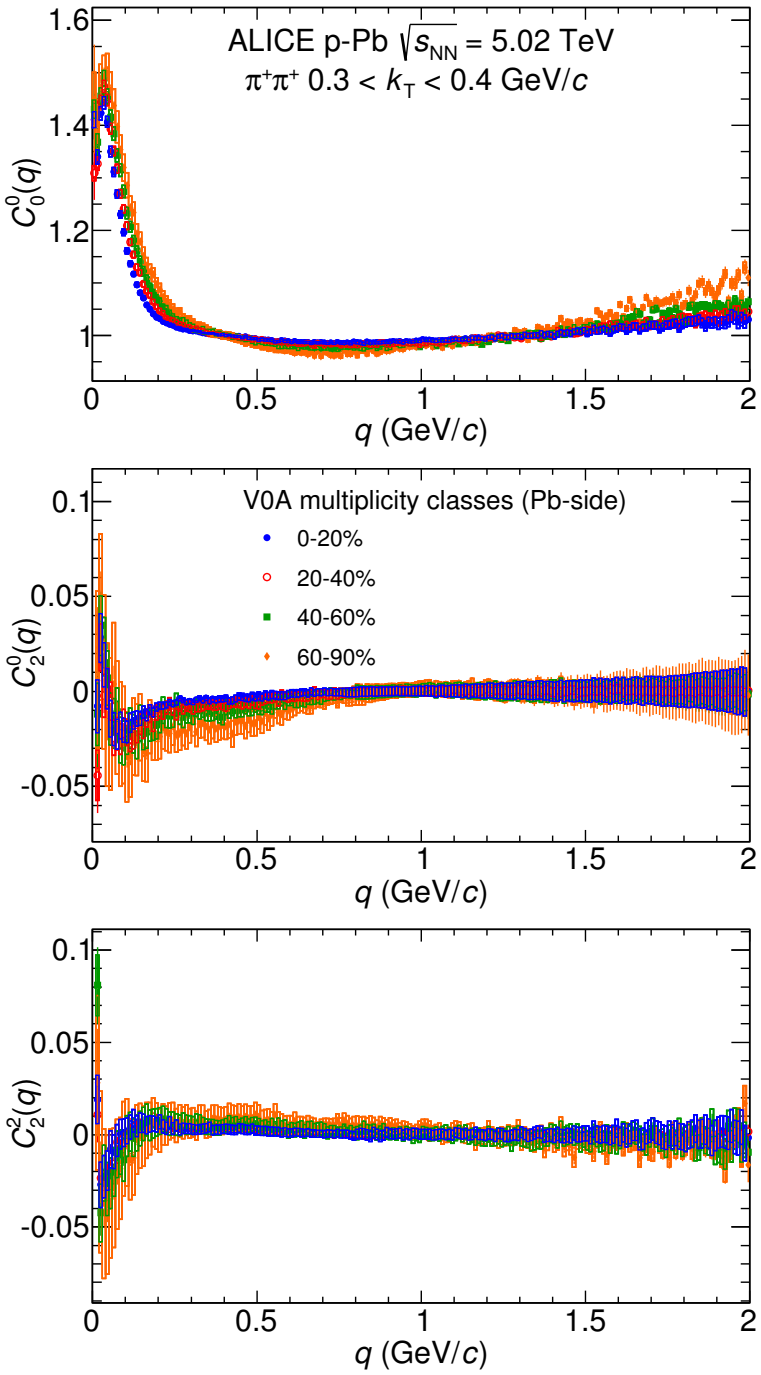

Figure 7.5: Dependence of the SH components of the correlation function on event multiplicity in a broad relative momentum range.

ator which describes the shape of these additional correlations. Several models were studied and all of them are collected Table 6.3. In all cases the Monte Carlo correlation functions exhibit significant structures similar to the long-range effects observed in data, which is another argument for their non-femtoscopic origin. However, quantitative differences in the magnitude

and shape of these structures when compared to those observed in data are seen for AMPT, HIJING, DPMJET, and THERMINATOR 2. These models are therefore unsuitable for precise characterization of the background, which is needed for the fitting procedure (for details see Appendix A). The only models that qualitatively describe the features of the background (enhancement at low q, growing with k_{T}, and falling with multiplicity) are EPOS 3.076 and PYTHIA 6.4, Perugia-0 tune, which was also used in the pp analysis [193]. We note that EPOS 3.076 events contain only generated particles while the ones from PYTHIA are full simulation including detector response. The comparison with data is shown in Fig. 7.7. The behavior of the correlation is well reproduced above 0.5 GeV/c in q, where non-femtoscopic correlations are expected to dominate. At low q, below 0.3 GeV/c the data and models diverge, which is expected, as the femtoscopic correlations are not included in the model calculation. EPOS reproduces the $(0,0)$ component well, PYTHIA is slightly higher than data. For the $(2,0)$ and $(2,2)$, which describe the 3D shape of the non-femto correlations, PYTHIA is more similar to data. Overall, for like-sign pairs, both models are reasonable approximations of the non-femtoscopic background. We use the correlation functions calculated from these two models to fix the background parameters in the fitting procedure, as described in Chapter 5.

Similarly to pp analysis [193], the unlike-sign pairs have also been studied. We found that PYTHIA, for all k_{T} ranges, is slightly higher than data in the $(0,0)$ component and similar to data in the $(2,0)$ and $(2,2)$ components. EPOS was found to reasonably describe the unlike-sign pairs for low k_{T} ranges and is below data in the $(0,0)$ component for the higher k_{T} ranges. For details of unlike-sign correlations see Appendix B

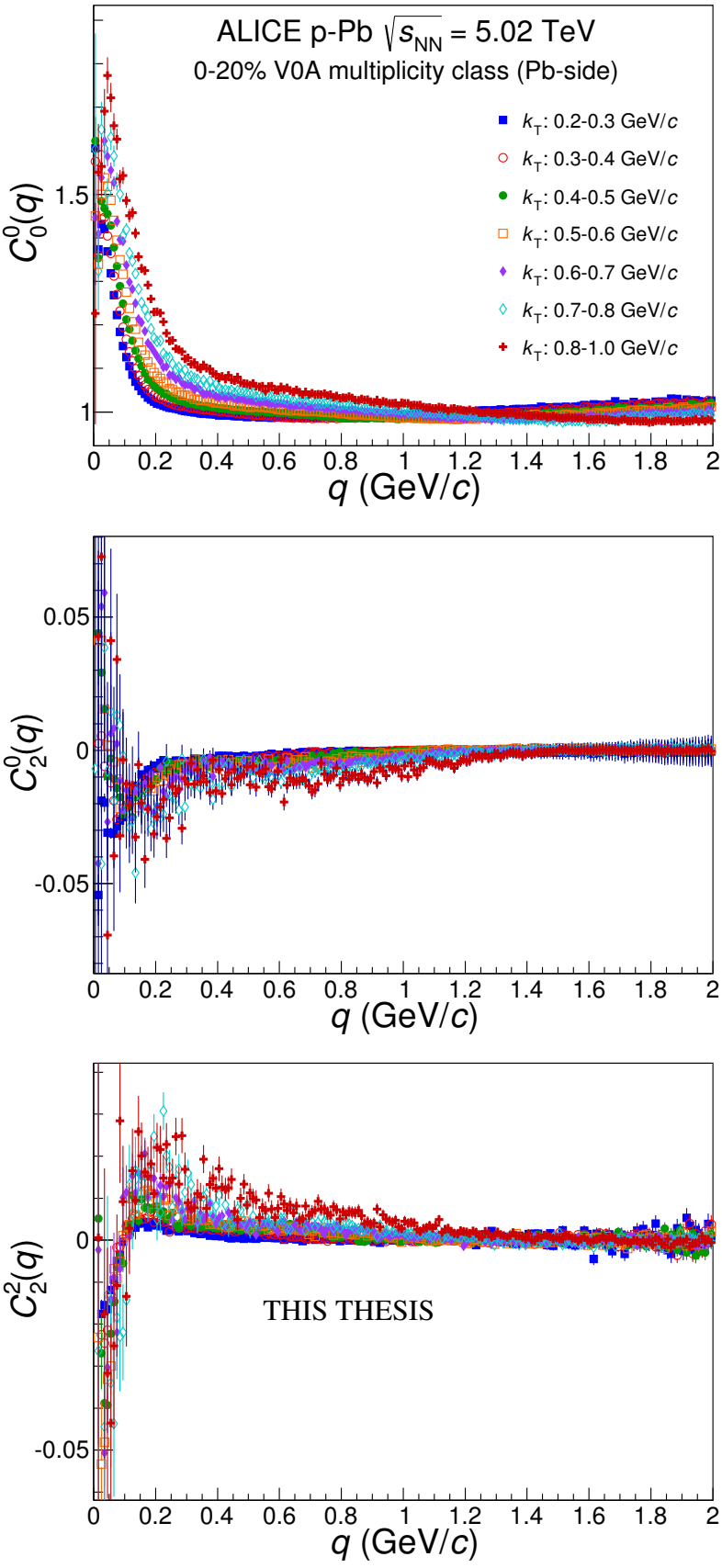

Figure 7.6: Dependence of the SH components of the correlation function on pair transverse momentum k_T the 0–20% centrality class in a broad relative momentum range.

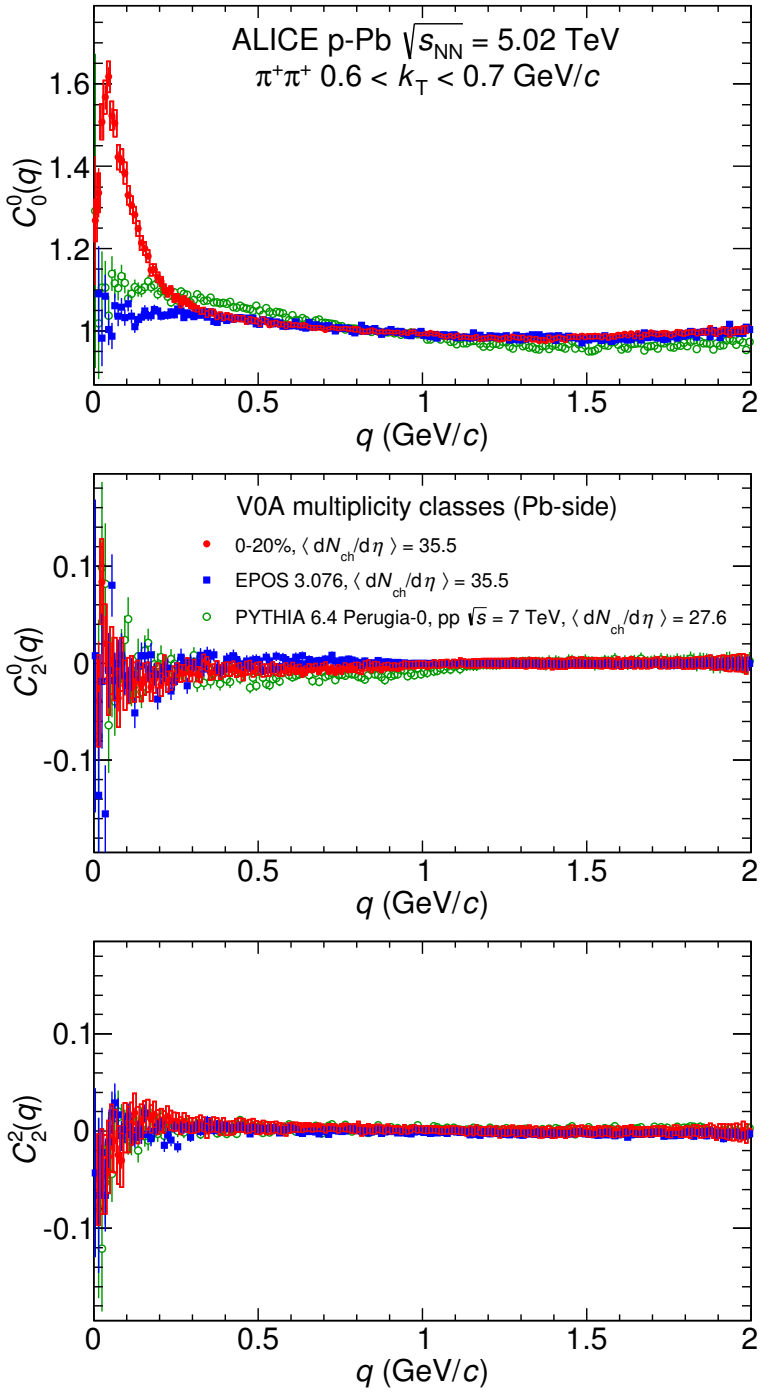

Figure 7.7: First three non-vanishing components of the SH representation of the $\pi^+\pi^+$ correlation functions for a selected multiplicity and k_T range, compared to a calculation from EPOS 3.076 (generator level only) and PYTHIA 6.4 Perugia-0 tune for pp at $\sqrt{s}$ = 7 TeV (full simulation with detector response).

7.1.3 Fitting the correlation functions

Fitting of the correlation functions was performed using the Gaussian and EGE parametrizations of the correlation function as described in Sec. 4.4 by Eq. (4.20) and Eq. (4.21) for the Gaussian and EGE fits, respectively. Additionally, the non-femtoscopic correlations have been accounted for by employing the procedure introduced in Chapter 5. The overall fit formula is therefore given by Eq. (5.5).

The fit is performed with the log-likelihood method in three dimensions for the Cartesian representation, normally resulting in several thousand degrees of freedom. The Gaussian fit reproduces the overall width of the femtoscopic correlation in all cases. The background component describes the behavior of the correlation at large q, but also extends to 0 in q.

A corresponding fit is also performed for the SH representation of the correlation, which is shown in Fig. 7.8. The formula from Eq. (4.20) or Eq. (4.21) (for the Gaussian fit or the EGE fit, respectively) is numerically integrated on a $\varphi - \theta$ sphere for each q bin, with proper $Y_l^m(\theta, \varphi)$ weights, to produce the three components of the SH decomposition.

Statistical uncertainties on each component as well as the covariance matrix between them are taken into account in this simultaneous fits to the three histograms. The results are shown in Fig. 7.8. The fit describes the general direction-averaged width of the correlation function, shown in the upper panel. The background component Ω describes the behavior at large q but also contributes to the description of the correlation at low q. The shape in three-dimensional space, captured by the $(2, 0)$ and $(2, 2)$ components, is also a combination of the femtoscopic and non-femtoscopic correlations.

Overall the Gaussian fit describes the width of the correlation but the data at low q are not perfectly reproduced, which can be attributed to the limitations of the Bowler-Sinyukov formula as well as to the non-Gaussian, long-range tails which are possibly present in the source. Some deviations from the pure Gaussian shape can also be seen for the *long* direction for the higher multiplicity.

The exponential-Gaussian-exponential fit (Eq. (4.21)) better reproduces the correlation peak in the (0,0) component, as shown in Fig. 7.9. The (2,0) and (2,2) components show similar quality of the fit. The χ^2 values for both fits are comparable.

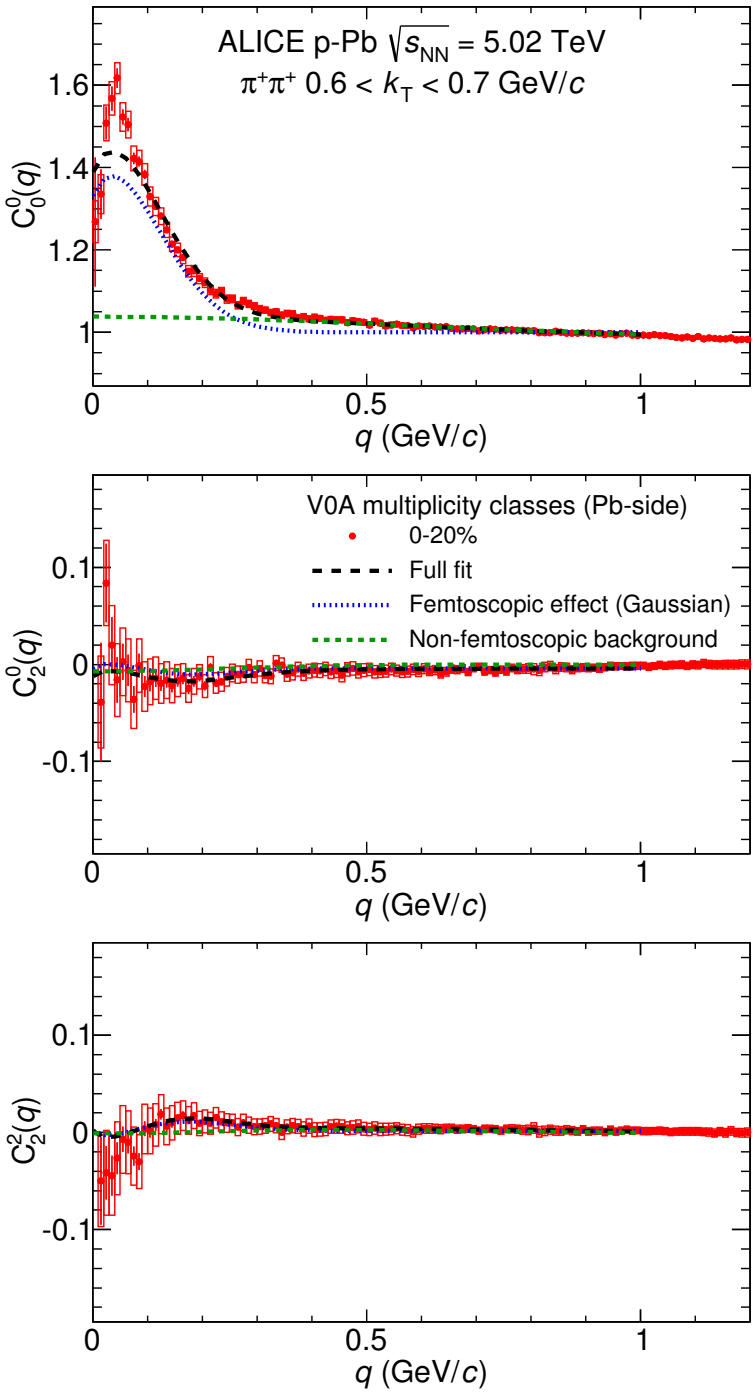

Figure 7.8: First three non-vanishing components of the SH representation of the $\pi^+\pi^+$ correlation function for 0–20% multiplicity class and $0.6 < k_T < 0.7$ GeV/c pair transverse momentum range, $l = 0$, $m = 0$ (top), $l = 2$, $m = 0$ (middle), and $l = 2$, $m = 2$ (bottom). The lines show the corresponding components of the Gaussian fit.

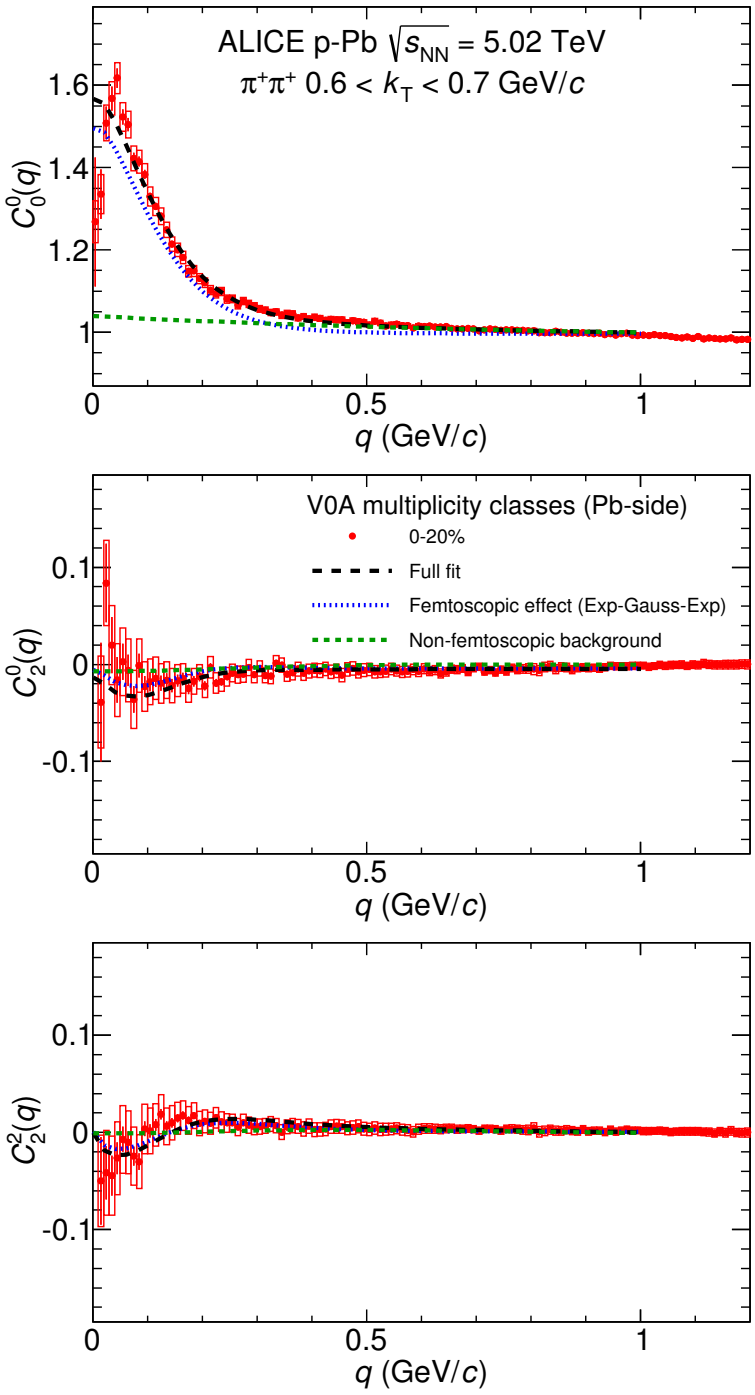

Figure 7.9: First three non-vanishing components of the SH representation of the $\pi^+\pi^+$ correlation function for 0–20% multiplicity class and $0.6 < k_T < 0.7$ GeV/c pair transverse momentum range, $l = 0$, $m = 0$ (top), $l = 2$, $m = 0$ (middle), and $l = 2$, $m = 2$ (bottom). The lines show the corresponding components of the exponential-Gaussian-exponential fit (EGE).

7.2 Results of the fitting

7.2.1 Three-dimensional radii

The fitting procedure resulted in 26 sets of femtoscopic radii, for each combination of multiplicity and k_T range. They are shown in Fig. 7.10. The radii in all directions are in the range of 0.6 to 2.4 fm. The radii universally decrease with k_T. The slope of this decrease is similar for all multiplicities in the *out* and *long* directions, and is visibly increasing with multiplicity in the *side* direction. The radii grow with event multiplicity. The plot also shows data from pp collisions at $\sqrt{s} = 7$ TeV [193] at the highest multiplicity measured by ALICE, which is slightly higher than the multiplicity measured for the 20-40% V0A signal range in the p–Pb analysis. At small k_T the pp radii are lower by 10% (for *side*) to 20% (for *out*) when compared with p–Pb radii at the same $\langle \mathrm{d}N_{\mathrm{ch}}/\mathrm{d}\eta \rangle^{1/3}$. At high k_T the difference in radius grows for R_{out}, while for R_{long} the radii for both systems become comparable. The distinct decrease of radii with k_T is observed both in pp and p–Pb.

The correlation strength λ grows with k_T from 0.44 to 0.58 for the highest multiplicity collisions. It is also higher for low multiplicity collisions, with up to 0.1 difference between highest multiplicity and lowest multiplicity collisions. A non-constant λ parameter as a function of k_T is an indication of a non-Gaussian shape of the correlation function. The correlation functions are normalized to the ratio of the number of pairs in the signal and background histograms. The positive correlation at low q must then be compensated by normalization parameter N, which is in the range of 0.9–1.0. The χ^2/ndf for the three-dimensional fit is on the order of 1.2.

The background parameters show an increasing magnitude of the background with increasing k_T and decreasing multiplicity, which is consistent with qualitative expectations for the "mini-jet" effect. The shape of the background is not spherical, giving finite contributions to the $(2, 0)$ and $(2, 2)$ components. The constant shift in these components is only significant for the $(2, 0)$ component in lower multiplicities.

The corresponding fit results for the EGE fit are shown in Fig. 7.11. In the *side* direction the radii are consistent between the two versions of the fit. The radii in *out* and *long* are not Gaussian widths in this case and cannot be directly compared to previous fits. However, all the trends are qualitatively the same in both cases: radii grow with event multiplicity and fall with pair transverse momentum. The values are 10% (for *side* and *long*) to 20% (for *out*) higher than

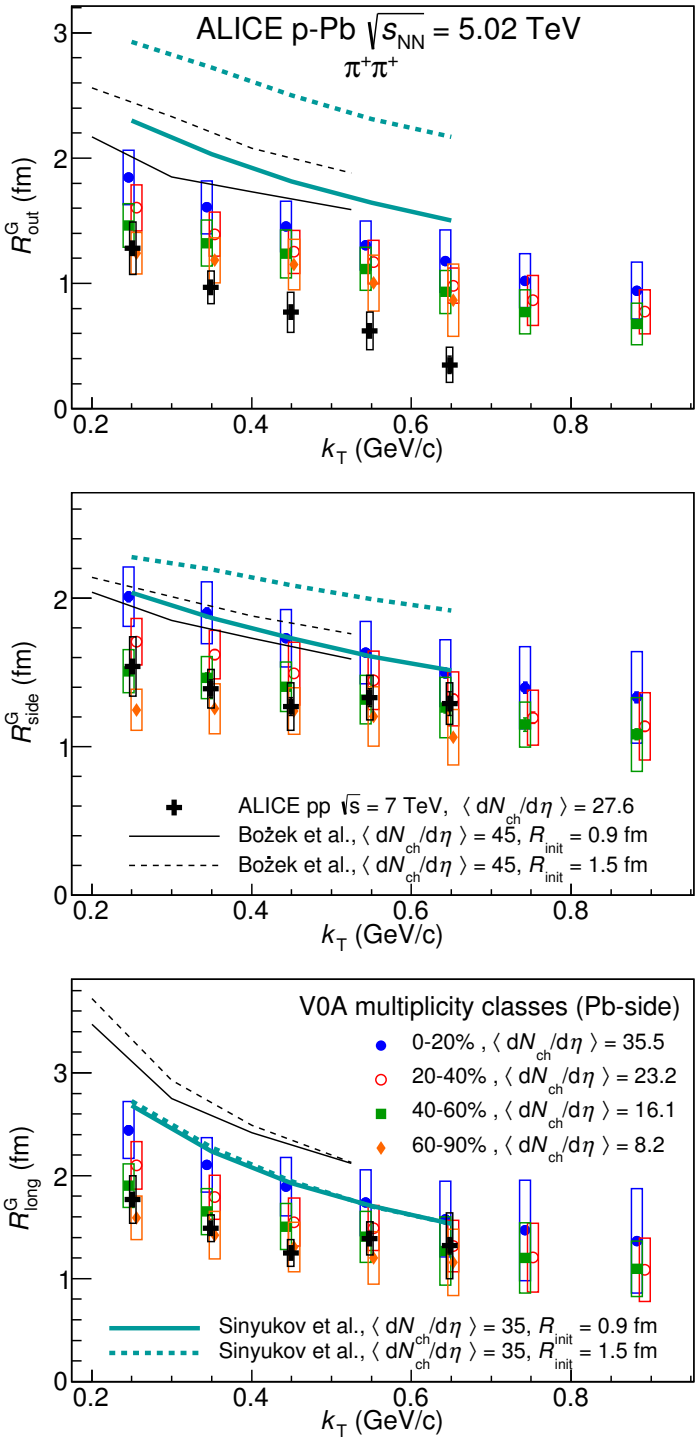

Figure 7.10: Femtoscopic radii (GGG fit) as a function of the pair transverse momentum k_T for four multiplicity classes. For comparison, radii from high-multiplicity pp collisions [231] and four predictions for p–Pb [148, 149] are shown as crosses and lines, respectively. Top panel shows R^G_{out}, middle panel shows R^G_{side}, bottom panel shows R^G_{long}. The points for multiplicity classes 20-40% and 40-60% have been slightly shifted in k_T for visibility.

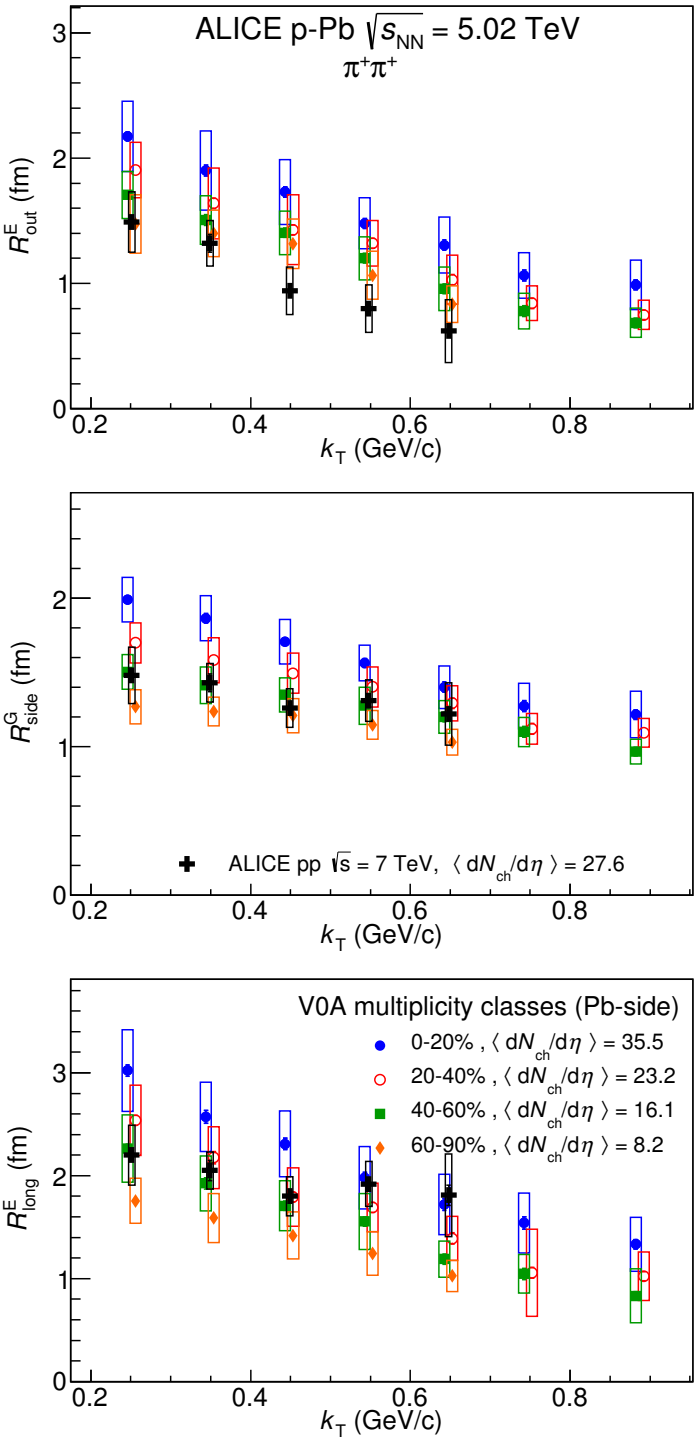

Figure 7.11: Femtoscopic radii (EGE fit) as a function of the pair transverse momentum k_T for four multiplicity classes. For comparison, radii from high-multiplicity pp collisions are shown as crosses and lines, respectively. Top panel shows R^E_{out}, middle panel shows R^G_{side}, bottom panel shows R^E_{long}. The points for multiplicity classes 20-40% and 40-60% have been slightly shifted in k_T for visibility.

those measured in pp collisions at similar event multiplicity [193]. The λ parameter for the EGE is significantly higher than in the Gaussian case, on the order of 0.7 for the SH fits, and growing from 0.7 at low k_{T} to approximately 0.9 at the highest k_{T} for the Cartesian fit. This is expected, as the EGE fit describes the shape of the correlation much better at low q and therefore better accounts for the non-Gaussian tails in the source function.

7.2.2 Model comparisons

Hydrodynamic model calculations for p–Pb collisions by Bożek [148] and Sinyukov [149], shown as lines in Fig. 7.10, assume the existence of a collectively expanding system. Both models employ two initial transverse size assumptions: $R_{\mathrm{init}} = 1.5$ fm and $R_{\mathrm{init}} = 0.9$ fm, which correspond to two different scenarios of the energy deposition in the wounded nucleon model [148]. The resulting charged particle densities $\langle \mathrm{d}N_{\mathrm{ch}}/\mathrm{d}\eta \rangle$ of 45 [148] and 35 [149], respectively, were comparable with the ALICE 0–20% multiplicity class. The calculations for R_{out} are higher than the measured radii. In particular, scenarios with large initial size strongly overpredict the radii. The scenarios with lower initial size are closer to the data. For R_{side} the calculations are in good agreement, both in magnitude and in the slope of the k_{T} dependence, with the data in the highest multiplicity class. Only the Sinuykov calculation for large initial size lies above the data. For R_{long}, calculations by Bożek overshoot the measurement by at least 30% for the most central data, while those by Sinyukov are only slightly higher. Again, the slope of the k_{T} dependence is comparable. The comparison shows that the calculation with large initial size is disfavored by data. Calculations with lower initial size are closer to the experimental results, but are still overpredicting the overall magnitude of the radii by 10–30%. Further refinement of the initial conditions may bring the models into better agreement with the collision data. Interestingly, the slope of the k_{T} dependence, which is usually interpreted as a signature of collectivity, is very similar for collision and Monte Carlo data in all directions, which suggests that the system dynamics might be correctly modelled by hydrodynamics.

Also in the collision data the source shape is distinctly non-Gaussian. Further studies would require examination of the source shape in p–Pb collision models and see if similar deviations from a Gaussian form are observed.

The CGC approach has provided a qualitative statement on the size of the system in p–Pb collisions, suggesting that it is similar to that in pp collisions [53, 270]. The measured radii,

at high multiplicity and low k_{T}, are 10–20% larger than those observed at similar multiplicity in pp data. For lower multiplicities the differences are smaller. These differences are well accommodated in CGC calculations. Also the evolution of the slope of the k_{T} dependence is similar between pp and p–Pb collisions in the *side* direction. Another similarity is the distinctly non-Gaussian shape of the source, which in pp and p–Pb is better described by an exponential-Gaussian-exponential form. In summary, it appears that data in p–Pb collisions still exhibit strong similarities to results from pp collisions. However, some deviations, which make the p–Pb more similar to A–A data, are also observed, especially at high multiplicity.

7.2.3 Comparison to the world systematics

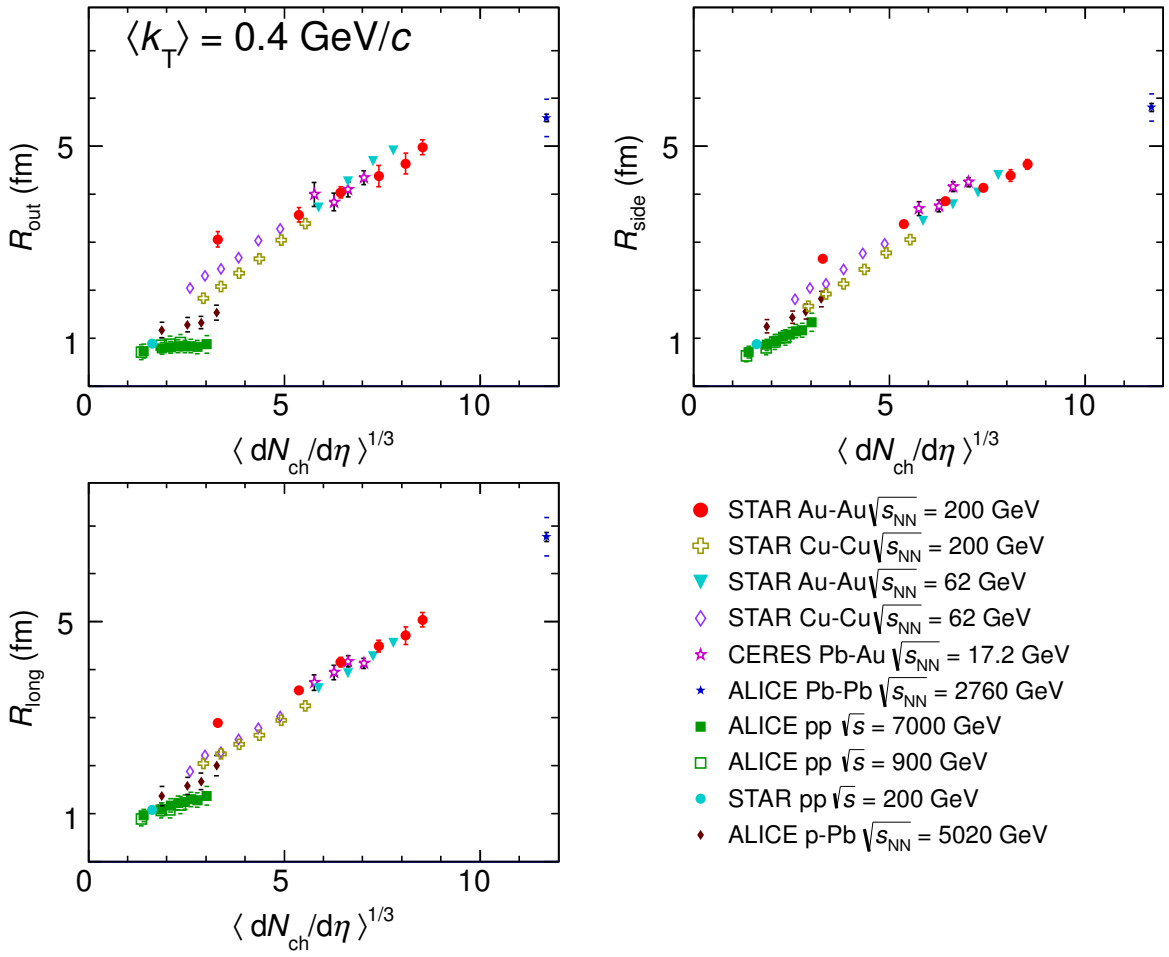

Figure 7.12: Comparison of femtoscopic radii (Gaussian), as a function of the measured charged-particle multiplicity, for various collision systems and collision energies.

In Fig. 7.12 the results from this analysis of the p–Pb data from the LHC (brown diamonds) are compared to the world heavy-ion data, including results obtained at lower collision energies, as well as to results from proton-proton collisions from ALICE and STAR. It has been observed [207] that the three-dimensional femtoscopic radii scale roughly with the cube root of the measured charged particle multiplicity not only for a single energy and collision system, but also across many collision energies and initial system sizes.

The pp and A–A datasets show significantly different scaling, although both are linear in $\langle \mathrm{d}N_{\mathrm{ch}}/\mathrm{d}\eta \rangle^{1/3}$. The p–Pb radii agree with those in pp collisions at low multiplicity. With increasing multiplicity, the radii for the two systems start to diverge. An analysis of one-dimensional averaged radii in pp, p–Pb and Pb–Pb collisions using the three-pion cumulant correlations technique reveals that the multiplicity scaling for p–Pb lies between pp and Pb–Pb trends [237], which is consistent with results presented here. On the other hand the deviation of the correlation shape from Gaussian is similar to that observed for pp collisions, and unlike the shapes observed in A–A data.

7.2.4 Comparison to two- and three-pion 1D results

Usually, two-pion Bose-Einstein correlations are used to extract the characteristic radius of the source. However, higher-order correlations (three-pion, four-pion, etc.) can be used as well; see i.e. Refs. [237, 289, 290] for details. In particular, higher-order cumulants, from which all lower order correlations are removed, contain a larger quantum statistics signal and decreased non-femtoscopic correlations. In ALICE, the one-dimensional two- and three-pion cumulant femtoscopic analysis has been performed for all available collision systems (pp, p–Pb, and Pb–Pb). All the details, results, and conclusions from these studies can be found in Ref. [237][2].

The comparison of 1D and 3D results presented in this thesis is not straightforward. There are two main differences: (1) the 1D analysis was performed in intervals of multiplicity which was defined by the reconstructed number of charged pions while in 3D the results were obtained in V0A multiplicity classes; (2) the 1D analysis was performed in the Pair Rest Frame while the 3D in LCMS and there is no analytic formula to transform 3D radii in LCMS to 1D radius in PRF. In addition, the one-dimensional results were calculated only in two (low and high)

[2]Since the author did not participate in the 1D pion femtoscopic analysis in ALICE, for the details of these studies we refer the Reader to the corresponding article [237].

intervals of pair transverse momentum. The strategy was therefore to transform the radii from multiplicity ranges from 1D analysis to V0A multiplicity classes and calculate 1D radii from 3D analysis. The following paragraphs present the details of this approach.

In order to address (1), the multiplicity bins in the 1D analysis have been merged according to weighted average of radii in different ranges, where the weight is the fraction of the pion sample in a given multiplicity interval (the fractions are given in Ref. [237]).

In order to address (2), a Monte Carlo procedure was used to calculate 1D radii from 3D results. The input for the procedure are the values of $R^{\mathrm{G}}_{\mathrm{out}}$, $R^{\mathrm{G}}_{\mathrm{side}}$, $R^{\mathrm{G}}_{\mathrm{long}}$, and a Lorentz factor γ. Then, we iteratively generate random numbers r_{out}, r_{side}, r_{long} according to Gaussian distributions with mean 0 and RMS of the given input radii ($R^{\mathrm{G}}_{\mathrm{out}} \cdot \gamma$, $R^{\mathrm{G}}_{\mathrm{side}}$, $R^{\mathrm{G}}_{\mathrm{long}}$), respectively. For each set of r_{out}, r_{side}, r_{long} we then calculate r_{inv} and create a distribution of this value. We fit r_{inv} distribution with the Gaussian function and the extracted width is the corresponding 1-dimensional radius R_{inv}. We also calculate R_{inv} from an approximate formula:

$$R_{\mathrm{inv}} \approx \frac{1}{3}\sqrt{\left({R^{\mathrm{G}}_{\mathrm{out}}}^{2} \cdot \gamma^{x} + {R^{\mathrm{G}}_{\mathrm{side}}}^{2} + {R^{\mathrm{G}}_{\mathrm{long}}}^{2}\right)}, \tag{7.1}$$

with various powers x (1.0, 2.0, and 0.5) of γ. The difference between them and the Monte Carlo method is reflected in the systematic uncertainty of the 1D radii.

The comparison of one-dimensional radii from both analyses, after performing the procedure described above, is presented in Fig. 7.13 for the low k_{T} range and all V0A multiplicity classes. The results are compatible with each other within the systematic uncertainties.

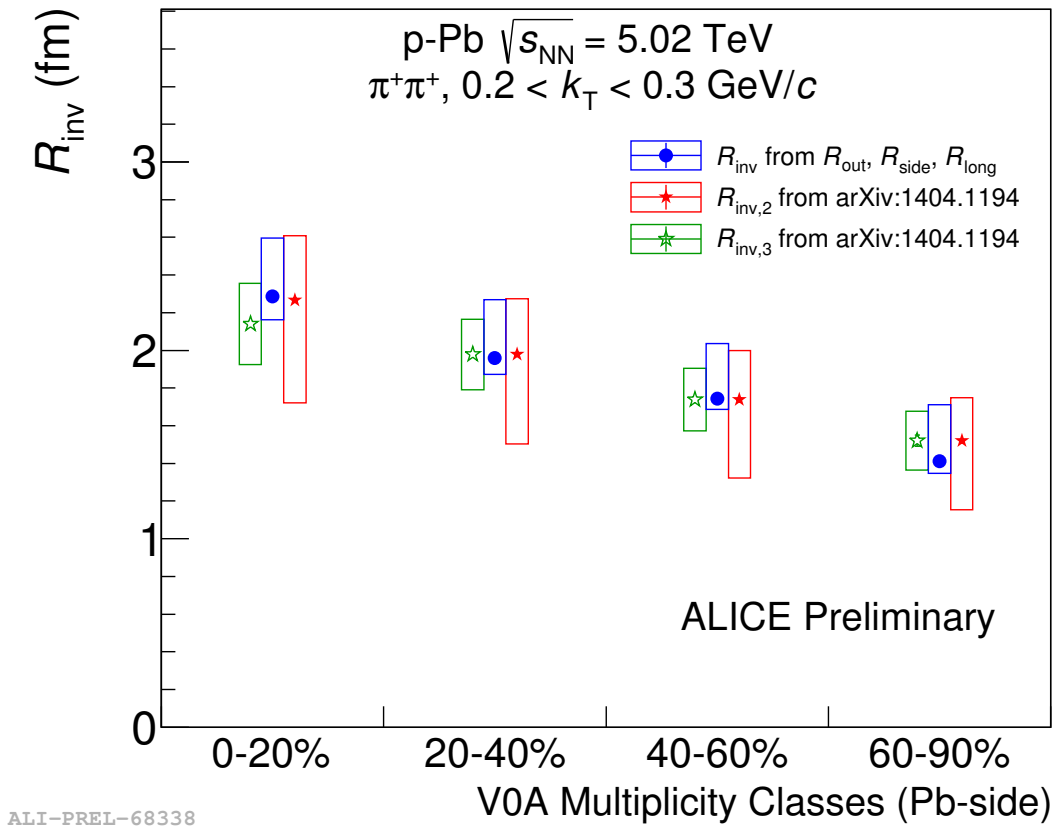

Figure 7.13: Comparison of one-dimensional femtoscopic radii from two- and three-pion from 1D [237] and from 3D analysis.

Chapter 8

Systematic uncertainties

The analysis was performed on several independent data samples recorded under slightly different data-taking conditions. They have been checked for statistical consistency at the level of the correlation function, and the results shown are statistical averages of them. Moreover, the analysis was performed separately for positively and negatively charged pions. For the practically zero-net-baryon-density system produced at the LHC they are expected to give consistent values. Both datasets are also statistically consistent at the correlation function level. In this analysis the Coulomb part of the wave function was integrated over the spherical Gaussian source with a radius fixed to 2 cm. Variation of this value is a source of systematic uncertainty.

Table 8.1: List of contributions to the systematic uncertainty of the extracted femtoscopic radii – GGG fits.

Uncertainty source	$R^{\mathrm{G}}_{\mathrm{out}}$ (%)	$R^{\mathrm{G}}_{\mathrm{side}}$ (%)	R^{G}_{long} (%)
CF representation & Background parametrization	5–32	4–22	4–35
Fit-range dependence	10	8	10
$\pi^{+}\pi^{+}$ versus $\pi^{-}\pi^{-}$	3	3	3
Momentum resolution correction	3	3	3
Two-track selection variation	< 1	< 1	< 1
Coulomb correction	< 1	< 1	< 1
Total correlated	12–34	9–24	11–36
Total	12–34	11–24	12–36

The main contributions to the systematic uncertainty are given in Table 8.1 for GGG radii and in Table 8.2 for EGE radii. Two alternative representations (Cartesian and spherical harmonics) of the correlation function were used. In addition, the same functional form for both of

Table 8.2: List of contributions to the systematic uncertainty of the extracted femtoscopic radii – EGE fits.

Uncertainty source	R^{E}_{out} (%)	$R^{\mathrm{G}}_{\mathrm{side}}$ (%)	$R^{\mathrm{E}}_{\mathrm{long}}$ (%)
CF representation & Background parametrization	4–18	3–14	8–20
Fit-range dependence	10	6	10
$\pi^{+}\pi^{+}$ vs. $\pi^{-}\pi^{-}$	3	3	3
Momentum resolution correction	3	3	3
Two-track selection variation	< 1	< 1	< 1
Coulomb correction	< 1	< 1	< 1
Total correlated	11–21	7–16	13–23
Total	12–21	8–16	14–23

them was used for the fitting procedure. However, the implementation of the fitting procedure is quite different: log-likelihood versus regular χ^2 fit, 3D Cartesian histogram versus three 1D histograms, fitting range as 3D cube in $q_{\mathrm{out}}, q_{\mathrm{side}}, q_{\mathrm{long}}$ or a 3D sphere with constant q radius among others. Therefore the fits to the two representations may react in a systematically different way to the variation of the fitting procedure (fit ranges, Bowler-Sinyukov approximation, etc.).

The fitting procedure requires the knowledge of the non-femtoscopic background shape and magnitude. Two models were used to estimate it, EPOS 3.076 [147] and PYTHIA Perugia-0 [144, 145], as described in Sec. 7.1.2. In addition, the shape of the correlation function is not ideally described by a Gaussian form. The EGE form is better, but still not exactly accurate. As a result the fit values depend on the fitting range q_{fit} used in the procedure of the radius extraction. We have performed fits with q_{fit} from 0.3 GeV/c, up to 1.1 GeV/c. Detailed studies of the fit range have been performed with EPOS model and are described in Chapter 5 as well as published in Ref. [1].

Figures 8.1 and 8.2 present the k_{T} dependence of the fit parameters (femtoscopic radii, correlation strengths λ, normalization factor, and the quality of the fit χ^2/ndf) from the Gaussian and EGE fits, respectively. The fits were performed to the correlation functions for the 20–40% multiplicity class, in two representations with two distinct background parametrizations. Similar results were obtained for all multiplicity classes. The final values of the radii, shown in

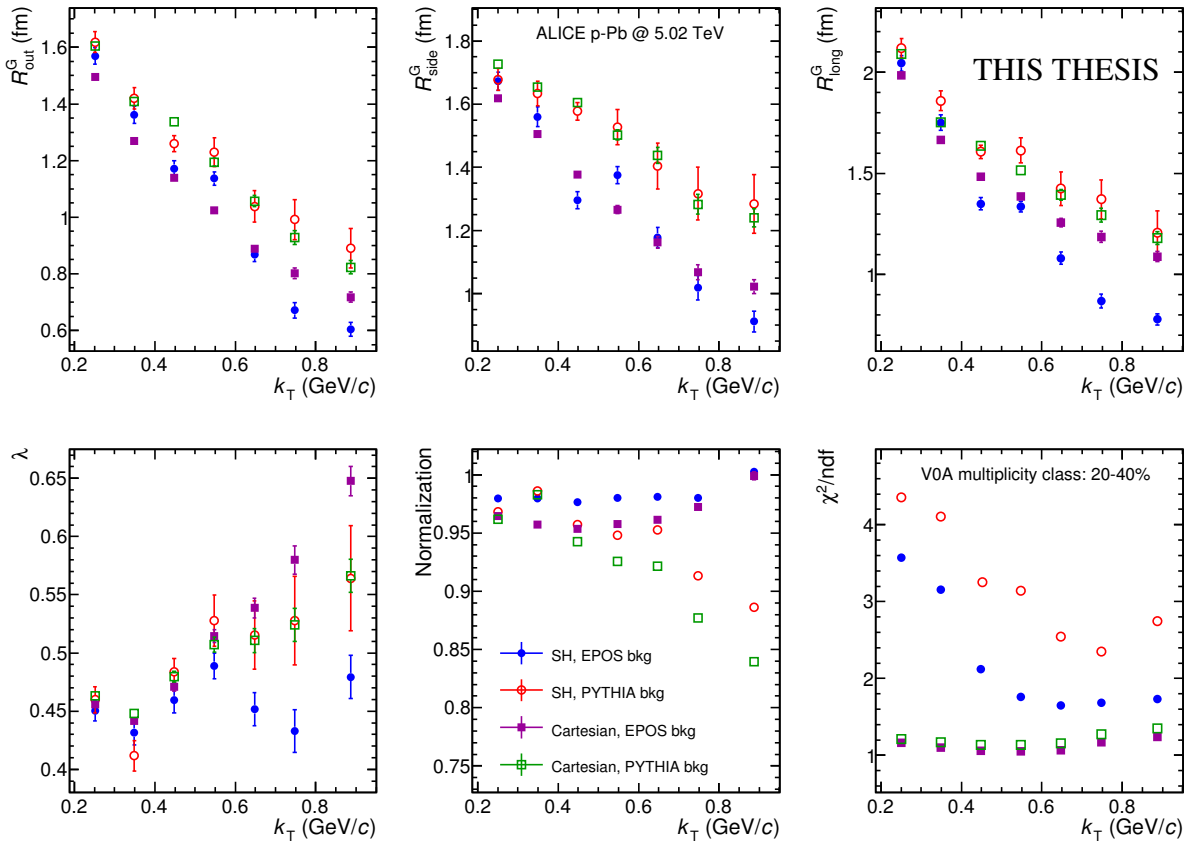

Figure 8.1: The k_T dependence of the fit parameters from the GGG fits to the correlation functions for 20–40% multiplicity class, in spherical harmonics (SH) and Cartesian representations, with EPOS and PYTHIA non-femtoscopic background parametrizations.

Fig. 7.10 and Fig. 7.10, are calculated as the statistical average of them.

The three effects mentioned above are the main sources of the systematic uncertainty on the radii. The background parametrization and the correlation function representation effects lead to systematic uncertainties less than 10% at low k_T and up to 35% for large k_T and low multiplicities. In particular, the radius could not be reliably extracted for the two highest k_T ranges in the lowest multiplicity range; so, these two sets of radii are not shown. Moreover, radii obtained with the background parametrization from PYTHIA are always larger than the ones obtained with the EPOS parametrization. These uncertainties are correlated between k_T ranges. Similarly, the radii from the narrow fit range are always on average 10% higher than the ones from the wide fit range. This also gives a correlated contribution to the systematic uncertainty. The final radii are calculated as an average of four sets of radii – the two representations with both EPOS and PYTHIA background parametrization. They are symmetric and equal to the

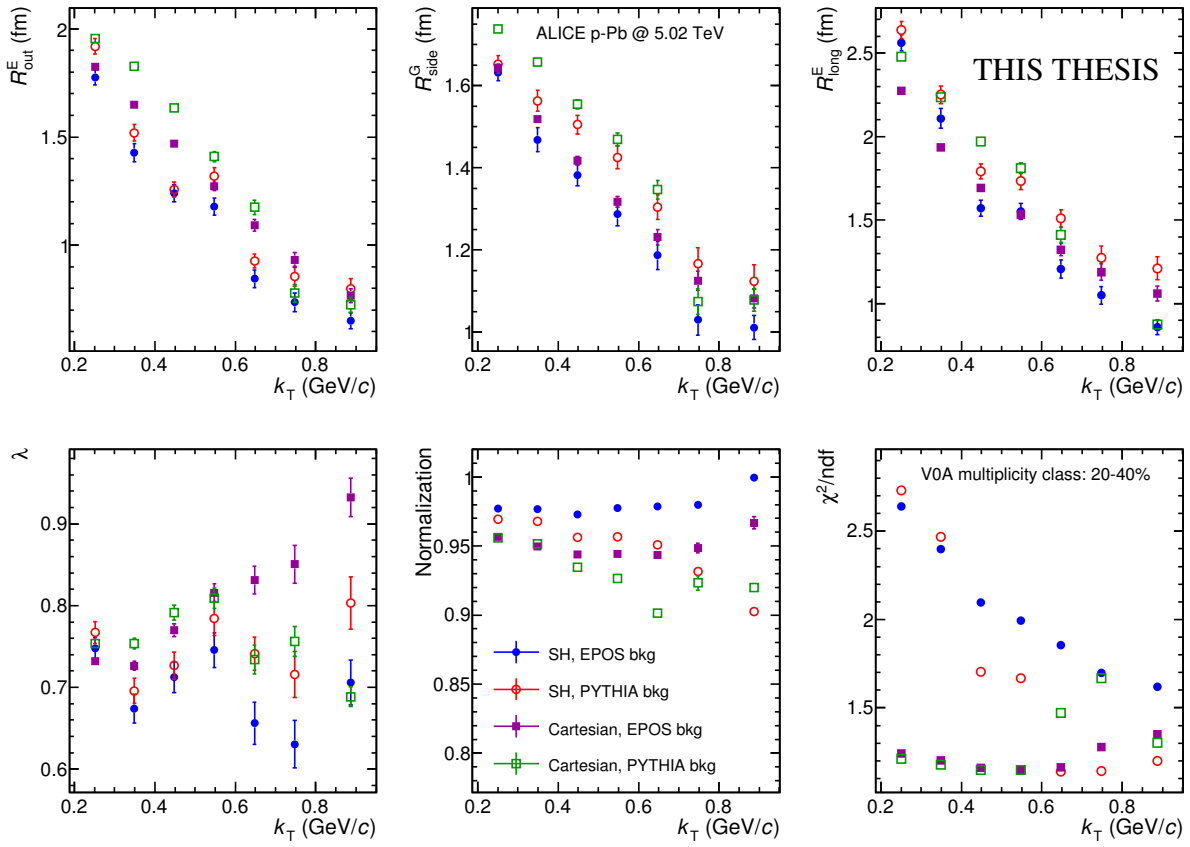

Figure 8.2: The k_T dependence of the fit parameters from the EGE fits to the correlation functions for 20–40% multiplicity class, in spherical harmonics (SH) and Cartesian representations, with EPOS and PYTHIA non-femtoscopic background parametrizations.

largest difference between the radius and one of the four sets of radii.

The effect of the momentum resolution on the correlation function was studied using a Monte Carlo simulations. For low p_T tracks, below 1 GeV/c, the momentum resolution in the TPC is below 1%. Smearing of the single particle momenta makes the correlation peak smaller and wider. It was estimated that this effect changes the reconstructed radius by 2% for a system size of 2 fm and 3% for a size of 3 fm. Therefore, the 3% correlated contribution from momentum resolution is always added to the final systematic uncertainty estimation.

Smaller sources of systematic uncertainties include those originating from the difference between positively and negatively charged pion pairs (around 3%) and from the Coulomb factor (less than 1%). All the uncertainties are added in quadrature.

Chapter 9

Preliminary results of proton-lambda femtoscopy in Pb–Pb collisions

One of the ongoing femtoscopic studies in ALICE is the analysis of correlations between different types of baryons in Pb–Pb collisions at $\sqrt{s_{\mathrm{NN}}} = 2.76$ TeV. The motivation, which is the measurements of unknown strong interaction cross sections, as well as the principles of this analysis have been discussed in detail in Sec. 4.7. The author of this thesis focuses on one specific part of this analysis, which are the correlations of protons with lambda hyperons. The preliminary results of these studies are presented in this chapter.

9.1 Data analysis

9.1.1 Data sample and event selection

The data used for this analysis come from the Pb–Pb collisions delivered by the LHC at the collision energy of $\sqrt{s_{\mathrm{NN}}} = 2.76$ TeV, which were recorded by the ALICE detector in December 2010. About 40 million events have been analyzed for the presented studies.

Events with the collision vertex position within ±10 cm from the center of the TPC, measured along the beam axis, were selected. The centrality was determined using the the signal from the V0 detector and employing the Glauber model [291]. Details of the centrality determination procedure in heavy-ion collisions are described in Sec. 2.3.4.1.

9.1.2 Proton selection

The selection criteria for primary (anti-)protons (track selection as well as particle identification details) have been adapted from the two-proton femtoscopy analysis in Pb–Pb collisions in ALICE. For details see Ref. [292] and Ref. [293].

9.1.3 Lambda selection

Neutral strange particles decaying due to the weak interaction, like the Λ hyperon, can not be measured directly in the experiment. However, they live long enough (i.e. the mean lifetime of a Λ particle is $\tau \approx 2.6 \cdot 10^{-10}$ s) to travel the distance of the order of centimeters from the interaction point before they decay. The search for such particles is thus based on the identification of their decay products, which originate from a common *secondary vertex* and create a characteristic geometrical pattern, called V^0. These decay particles, referred to as daughters, are then bent in opposite directions by the magnetic field provided by the ALICE solenoid, giving a characteristic "V" shape[1].

The identification procedure of such particles is based on a dedicated algorithm, called the V^0 *finder*. The algorithm searches for the V^0 patterns of tracks in an event and reconstructs secondary vertices. In the case of a Λ ($\overline{\Lambda}$) particle, the decay products are π^- (π^+) and p ($\overline{\text{p}}$). The example V^0 pattern of a Λ decay is presented in Fig. 9.1. Other weakly decaying particles, such as K^0_S, exhibit similar topologies.

In order to identify a secondary vertex as a potential Λ ($\overline{\Lambda}$) particle, the following selection criteria for the V^0 and its daughters were applied:

- V^0 was required to have exactly two daughters of different charges,
- V^0 was required to have $|\eta| < 0.8$,
- distance of closest approach (DCA) of the V^0 to the primary vertex had to be less than 1 cm,
- cosine of pointing angle θ (the angle between the particle momentum associated with the V^0 and a vector connecting the primary vertex and the secondary vertex; see Fig. 9.1 for details) had to be be greater than 0.998,
- daughter tracks were required to have at least 80 clusters in the TPC,
- maximum χ^2 per TPC cluster for daughter tracks was set to 4.0,
- daughter protons (antiprotons) were required to have $p_{\text{T}} > 0.5$ (0.3) GeV/c, and the daughter pions (both signs) were required to have $p_{\text{T}} > 0.16$ GeV/c,
- all daughter tracks were required to be within the pseudorapidity range $|\eta| < 0.8$,

[1]Note that the V^0 name is similar to the one of the ALICE sub-detectors, the V0, described in Sec. 3.2.1.5. However, in this case the meaning is different and V^0 refers to the specific weak decay pattern.

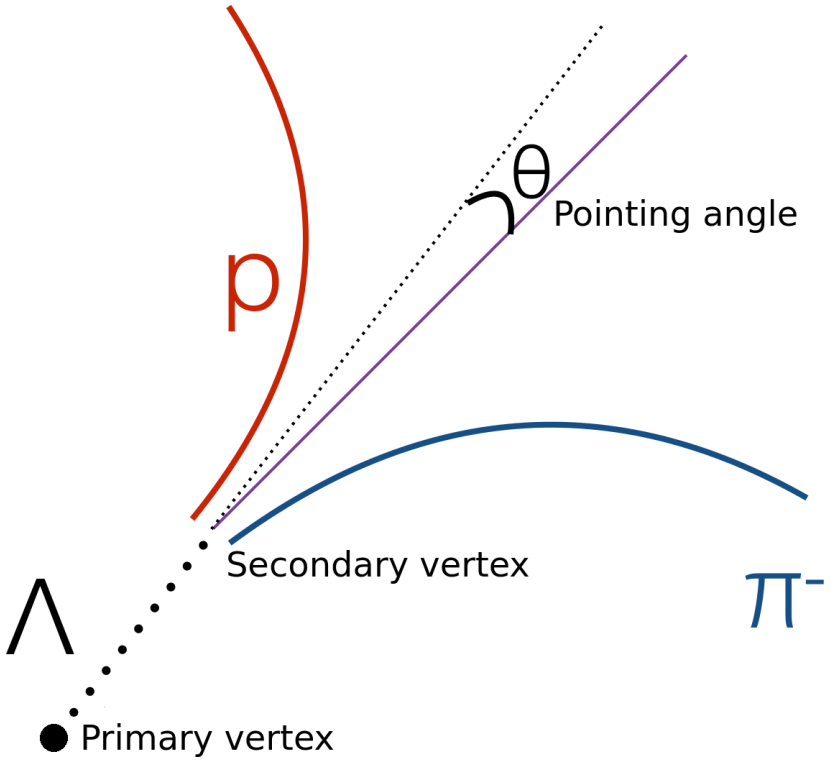

Figure 9.1: The V^0 pattern of a Λ decay showing the primary vertex, secondary vertex, pointing angle, and the decay products (p in red and π^-in blue). Similar topology is observed for other neutral strange particles which decay due to the weak interaction, such as K^0_S.

- daughter tracks, to ensure that they are not primary, were required to have their distance of closest approach (DCA) to the primary vertex greater than 0.4 cm,
- TPC and TOF detectors were used for the particle identification: for pion daughter candidates (both signs) only the TPC was used and particles were required to fall within $|n_{\sigma,\mathrm{TPC}}| < 3$; for proton (antiproton) daughters the PID selection criteria were the following:
  - $|n_{\sigma,\mathrm{TPC}}| < 3$ for tracks with momenta less than 0.8 GeV/c,
  - $|n_{\sigma,\mathrm{TPC}}| < 3$ for momenta higher than 0.8 GeV/c for tracks without the TOF signal,
  - $|n_{\sigma,\mathrm{TPC}}| < 3$ and $|n_{\sigma,\mathrm{TOF}}| < 3$ for momenta higher than 0.8 GeV/c if TOF signal available,
- for both Λ and $\overline{\Lambda}$ particles, the reconstructed invariant mass was required to fall within $1.1127 < m_{\mathrm{inv}} < 1.1187$ GeV/c^2.

The invariant mass distribution of Λ candidates, after applying the selection criteria described above, is shown in Fig. 9.2. The peak corresponds to Λ particles and the baseline is the "background", originating i.e. from random combinations of primary pions and protons which only seem to come from the same secondary vertex or that have been misidentified. The vertical lines correspond to the considered invariant mass range and the red line is the 4th order polynomial fit to the background distribution. The purity of the Λ sample was estimated to be $\approx 92\%$.

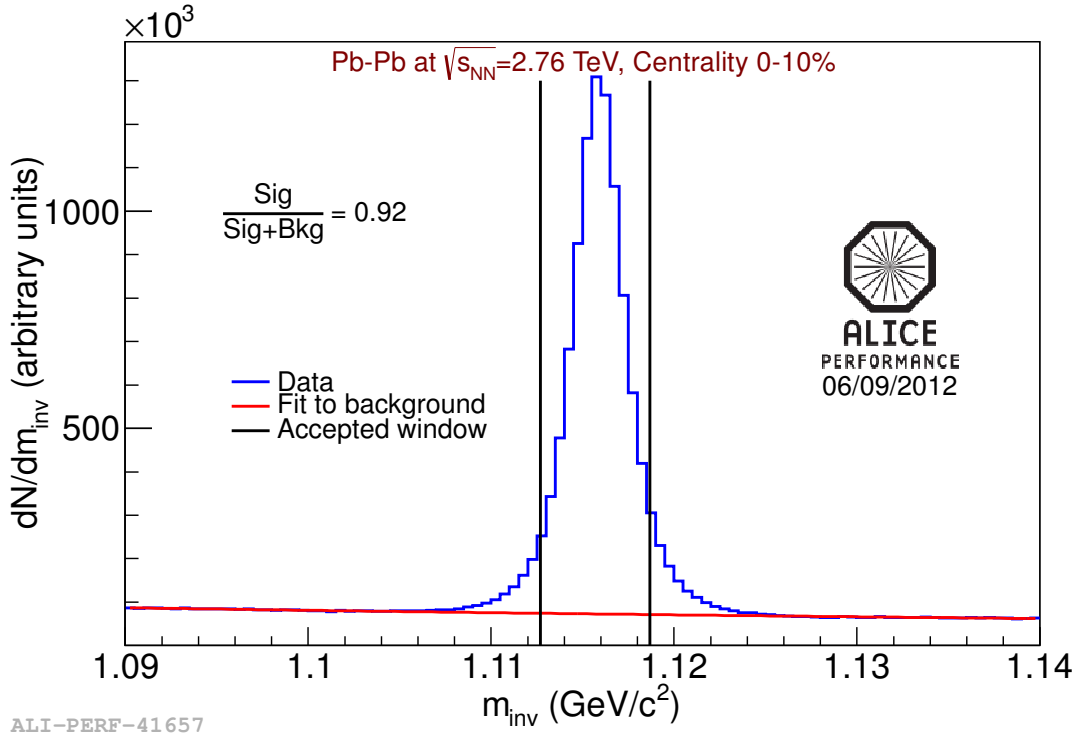

Figure 9.2: The invariant mass distribution of Λ candidates. The black vertical lines show the accepted invariant mass window of $1.1127 < m_{\text{inv}} < 1.1187$ GeV/c^2 and the red line represents the 4th order polynomial fit to the background.

9.1.4 Pair-level selection criteria

The accepted particles from each event were combined in pairs and the correlation functions were calculated according to Eq. (6.3). Figure 9.3 shows the pΛ correlation function as a function of $k^* = q/2$ for the 0–10% centrality range, after applying the single-track selection criteria only. A significant peak around $k^* = 0.05$ GeV/c, not expected in the pure pΛ correlations, is clearly visible. There are two possible explanations of the origin of this effect, which do not

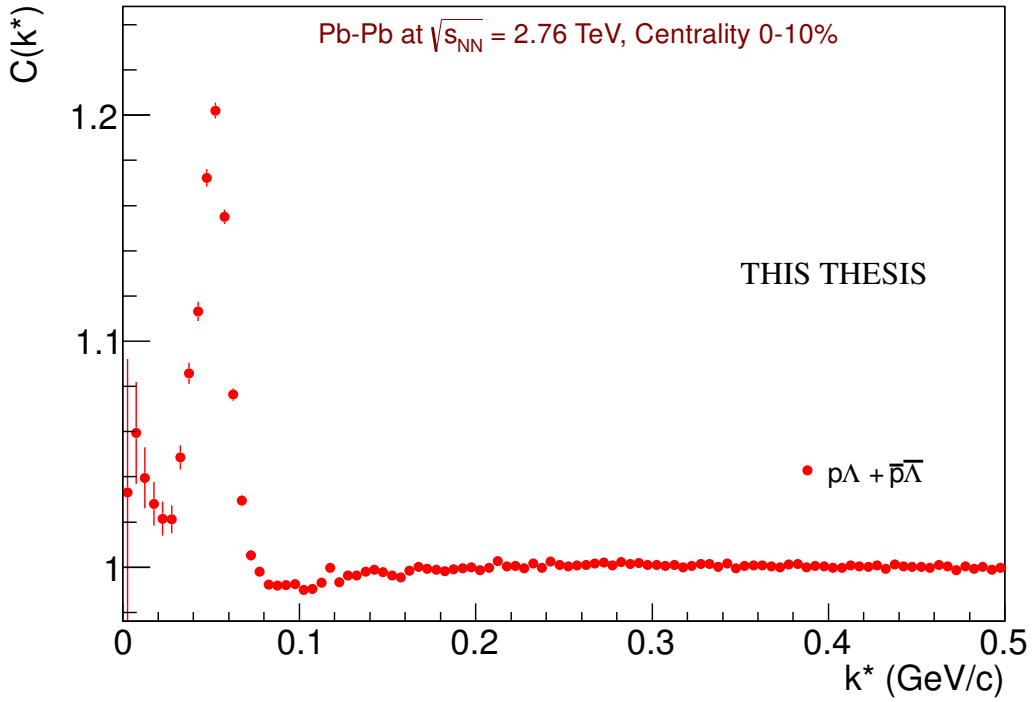

Figure 9.3: The combined $p\Lambda+\overline{p}\overline{\Lambda}$ correlation function for the most central collisions ($0-10\%$ centrality range). The peak at $k^* = 0.05$ GeV/c due to splitting and residual correlations is visible.

exclude each other: the so-called proton-proton *residual correlation* and splitting of primary proton tracks. In addition, merging of primary tracks and the ones associated with the V^0 can also be present in the analyzed correlations. In order to account for all these effects a dedicated study was performed.

Removing the merging effect

In order to remove the effect of track merging in the analyzed correlations, the average separation distance in the TPC between primary p ($\overline{p}$) and same-sign Λ ($\overline{\Lambda}$) daughters, was calculated. Figure 9.4 shows the ratio of the same event pairs over mixed event pairs as a function of the average distance between a primary proton and a positive pion ($\overline{\Lambda}$ daughter) in the study of $p\overline{\Lambda}$ correlations. The merging effect, manifested as anticorrelation appearing below $\approx$ 11 cm, is clearly visible. Therefore, only those pairs with the average separation larger than 11 cm were accepted.

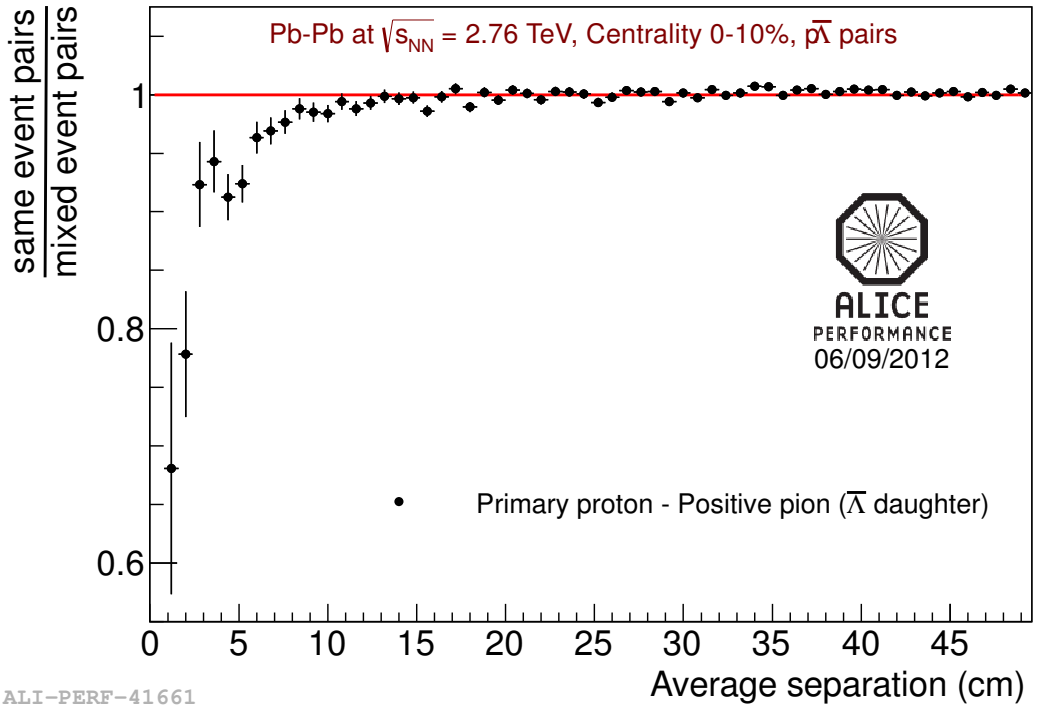

Figure 9.4: The correlation function (ratio of the same event pairs over mixed event pairs) as a function of the average separation distance in the TPC between the primary protons and the positive pions reconstructed as $\overline{\Lambda}$ daughters. The anticorrelation observed for the low values of average separation distance originates from the merging effect.

Table 9.1: List of possible residual correlation sources contributing to the pΛ (and $\overline{\text{p}\Lambda}$) system. The fractions correspond to addmixture of these pairs in the measured pΛ ($\overline{\text{p}\Lambda}$) correlation. Table from Ref. [294].

Pair	Fraction	Decay momentum (MeV/c)
pΛ	15%	0
ΛΛ	10%	101
$\Sigma^+\Lambda$	3%	189
$\text{p}\Sigma^0$	11%	74
$\Lambda\Sigma^0$	7%	101, 74
$\Sigma^+\Sigma^0$	2%	189, 74
$\text{p}\Xi^0$	9%	135
$\Lambda\Xi^0$	5%	101, 135
$\Sigma^+\Xi^0$	2%	189, 135
pp	7%	101

Residual correlations

From the experimental point of view, not all of the V^0s, reconstructed by the dedicated algorithms, correspond to real neutral strange particles. In fact, even after applying the strict selection criteria introduced in Sec. 9.1.3, some of the wrongly reconstructed V^0s remain. These artifacts lead to the admixture of direct protons (antiprotons) in the Λ ($\overline{\Lambda}$) sample, yielding the primary proton *residual correlation* contributing to the measured pΛ correlation function. Other possible sources of residual correlations are protons which are identified as primary but in practice come from decays of heavier baryons, such as Λ and Σ^+. The same mechanism applies to Λ hyperons, which can originate from Σ^0 or Ξ^0 decays.

In fact, the residual correlations are not limited to baryons only; they are present essentially in all systems. For example in the case of two-pion correlations, the possible residual correlation originates from muons decaying into pion pairs. Neveretheless, the admixture of these non-primordial pions is practically negligible. In the case of baryons there are, however, many sources of non-primary particles which significantly affect the measurements. In the pΛ (and $\overline{\text{p}\Lambda}$) systems the possible sources of residual correlations were estimated by the STAR experiment [294] and are presented in Table 9.1.

The potential primary proton residual correlation in the experimental pΛ correlation function can be manifested as a significant correlation peak around $k^* \approx 0.05$ GeV/c visible in Fig. 9.3. In order to test this assumption the following procedure was employed.

First, we calculated the theoretical pp correlation function using the `CorrFit` [295] tool. However, the pΛ and pp correlation functions are calculated in different reference frames. The latter is calculated as a function of k^*_{pp}, which is defined as the relative momentum between the two protons, while the pΛ correlation function is calculated as a function of $k^*_{\mathrm{p\Lambda}}$, defined as the relative momentum between a primary proton and a lambda. Therefore, in order to compare the two correlation functions, one needs to apply a dedicated transformation procedure of the pp correlation function from k^*_{pp} frame to $k^*_{\mathrm{p\Lambda}}$. This transformation requires calculation of the Λ decay kinematics, which was obtained from the THERMINATOR 2 model [286]. This decay kinematics, shown in Fig. 9.5, is represented as a two-dimensional correlation matrix $T(k^*_{\mathrm{pp}}, k^*_{\mathrm{p\Lambda}})$. The transformation is then defined as a weighted average: for each value of $k^*_{\mathrm{p\Lambda}}$, $C_{\mathrm{pp}}(k^*_{\mathrm{p\Lambda}})$ is determined as a sum over all k^*_{pp} values of $C_{\mathrm{pp}}(k^*_{\mathrm{pp}})$ scaled by factors taken from a two-dimensional transformation matrix $T(k^*_{\mathrm{pp}}, k^*_{\mathrm{p\Lambda}})$. This leads to the following transformation formula:

$$C_{\mathrm{pp}}(k^*_{\mathrm{p\Lambda}}) = \sum_{k^*_{\mathrm{pp}}} C_{\mathrm{pp}}(k^*_{\mathrm{pp}}) T(k^*_{\mathrm{pp}}, k^*_{\mathrm{p\Lambda}}). \tag{9.1}$$

We note that Eq. (9.1) assumes normalization of the transformation matrix:

$$\sum_{k^*_{\mathrm{pp}}} T(k^*_{\mathrm{pp}}, k^*_{\mathrm{p\Lambda}}) = 1. \tag{9.2}$$

The result of the transformation is shown in Fig. 9.6. The theoretical pp correlation function is plotted as a function k^*_{pp} (red full symbols) and, after the transformation procedure, as a function of $k^*_{\mathrm{p\Lambda}}$ (green open symbols). One should notice that the peak around 0.02 GeV/c in k^*_{pp} transforms into the peak around 0.05 GeV/c in $k^*_{\mathrm{p\Lambda}}$. This calculation is consistent with the experimental result shown in Fig. 9.3.

The procedure was then applied to the experimental data by removing the proton pairs with $k^*_{\mathrm{pp}} < 0.04$ GeV/c, which includes the whole correlation peak in the pp correlation function. We note that this procedure also removes the split tracks, which by construction have close relative momenta. We can clearly see in Fig. 9.7 that the peak around 0.05 GeV/c in $k^*_{\mathrm{p\Lambda}}$, which was present in Fig. 9.3, is removed and a clear enhancement at low k^* is visible.

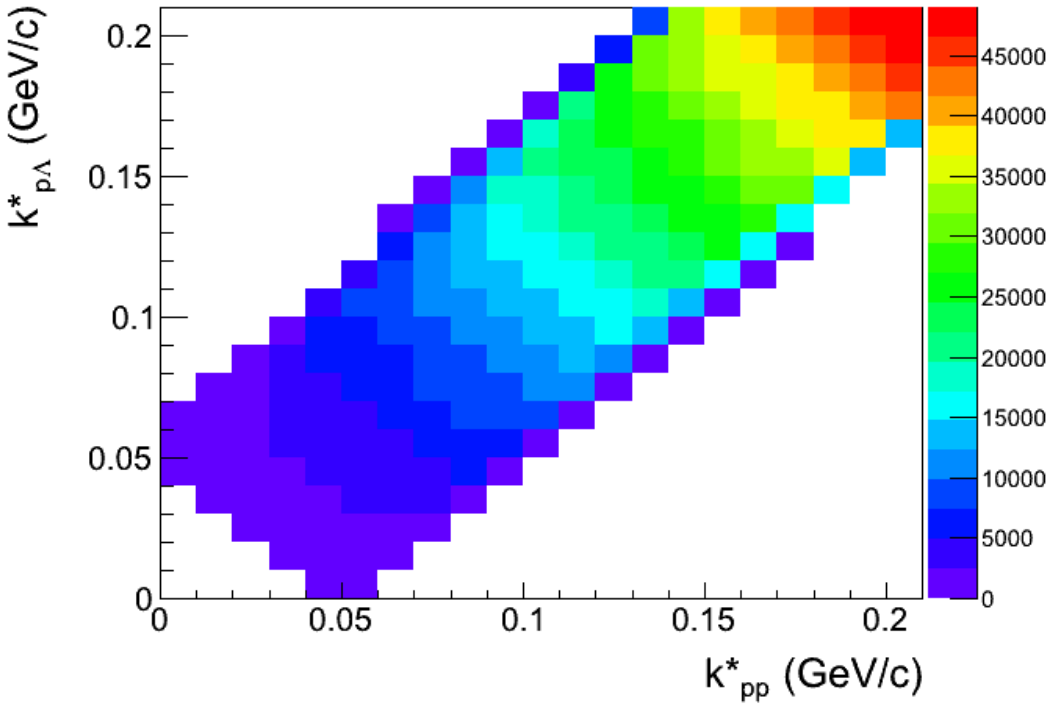

Figure 9.5: The Λ kinematics decay matrix $T(k^*_{\mathrm{pp}}, k^*_{\mathrm{p\Lambda}})$ calculated using the THERMINATOR 2 model.

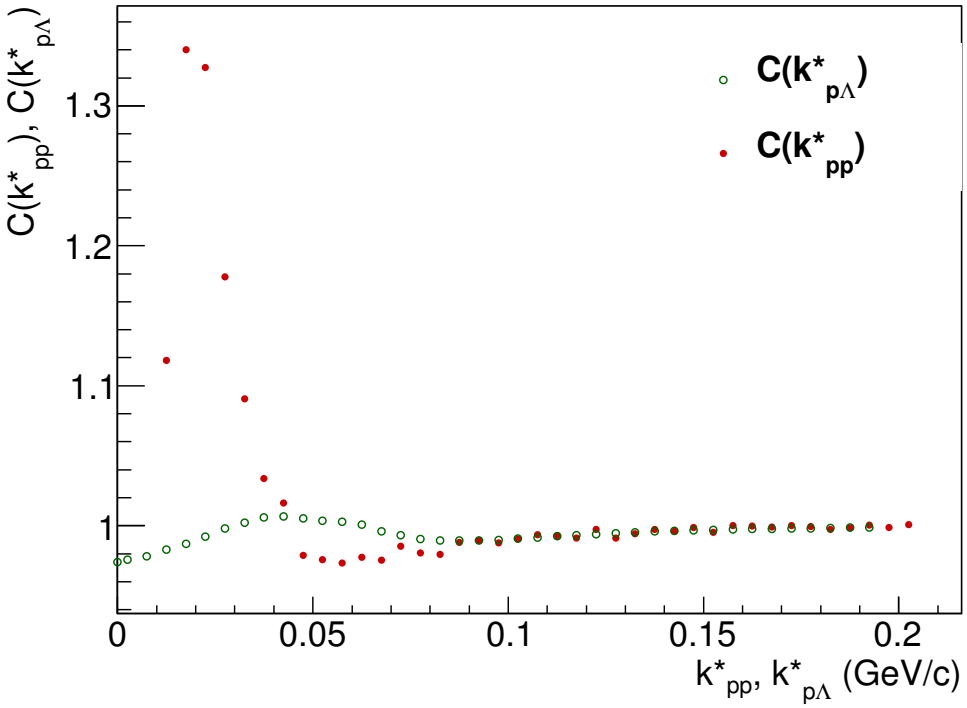

Figure 9.6: The pp theoretical correlation function from CorrFit as a function of k^*_{pp} (red full points) and $k^*_{\mathrm{p\Lambda}}$ (green open symbols).

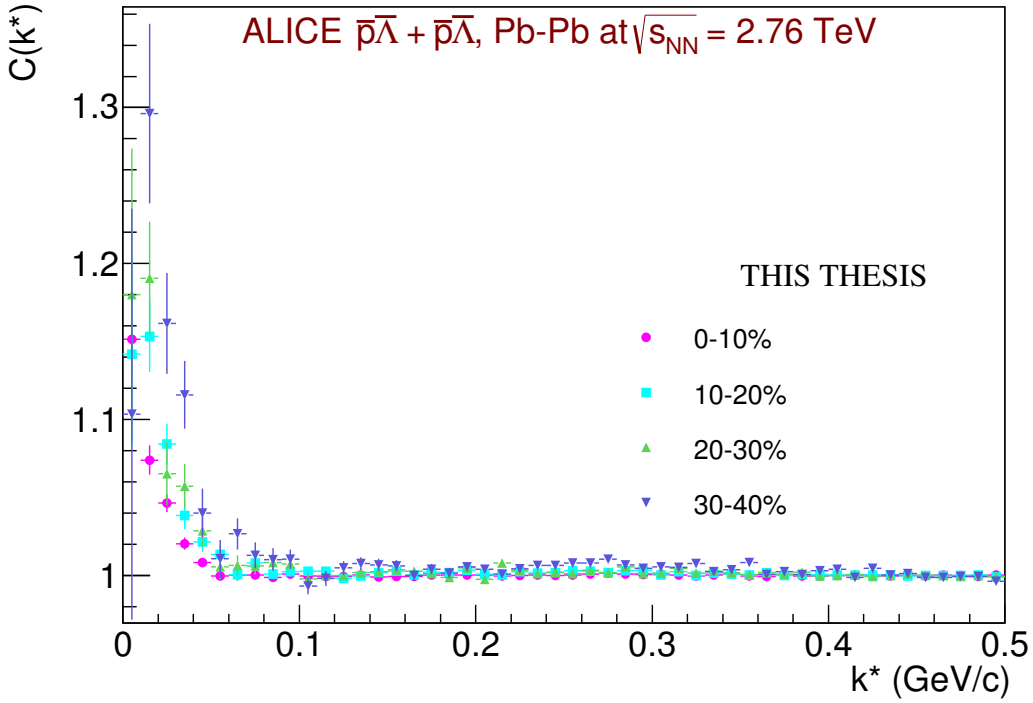

Figure 9.7: The combined pΛ+$\bar{p}\bar{\Lambda}$ correlation functions for centralities 0–10%, 10–20%, 20–30%, and 30–40%.

9.2 Results

The combined pΛ+$\bar{p}\bar{\Lambda}$ and p$\bar{\Lambda}$+$\bar{p}$Λ correlation functions from Pb–Pb collisions at $\sqrt{s_{\mathrm{NN}}}$ = 2.76 TeV for different centrality classes are shown in Fig. 9.7 and Fig. 9.8, respectively. The correlation (anticorrelation) effect observed for low relative momenta exhibits a clear dependence on event centrality for both baryon-baryon and baryon-antibaryon systems, suggesting the increase of the system size with increasing centrality.

Moreover, the p$\bar{\Lambda}$+$\bar{p}$Λ correlations show also another anticorrelation effect, visible for large values of k^* and increasing with decreasing event centrality. Surprisingly, it is not observed for the pΛ+$\bar{p}\bar{\Lambda}$ case, where the flat dependence of the correlation function for large values of k^* is observed for all centrality ranges.

Comparison with Lednicky & Lyuboshitz model

The results for combined p$\bar{\Lambda}$+$\bar{p}$Λ pairs are shown in Fig. 9.8. Recalling the Ledicky & Lyuboshitz analytical model, introduced in Sec. 4.7.3, one can qualitatively compare the experimen-

tal correlation functions from Fig. 9.8 with the theoretical expectation presented in Fig. 4.7. A wide anticorrelation structure, corresponding to the significant baryon-antibaryon annihilation process, is observed in the experimental data for all centrality classes.

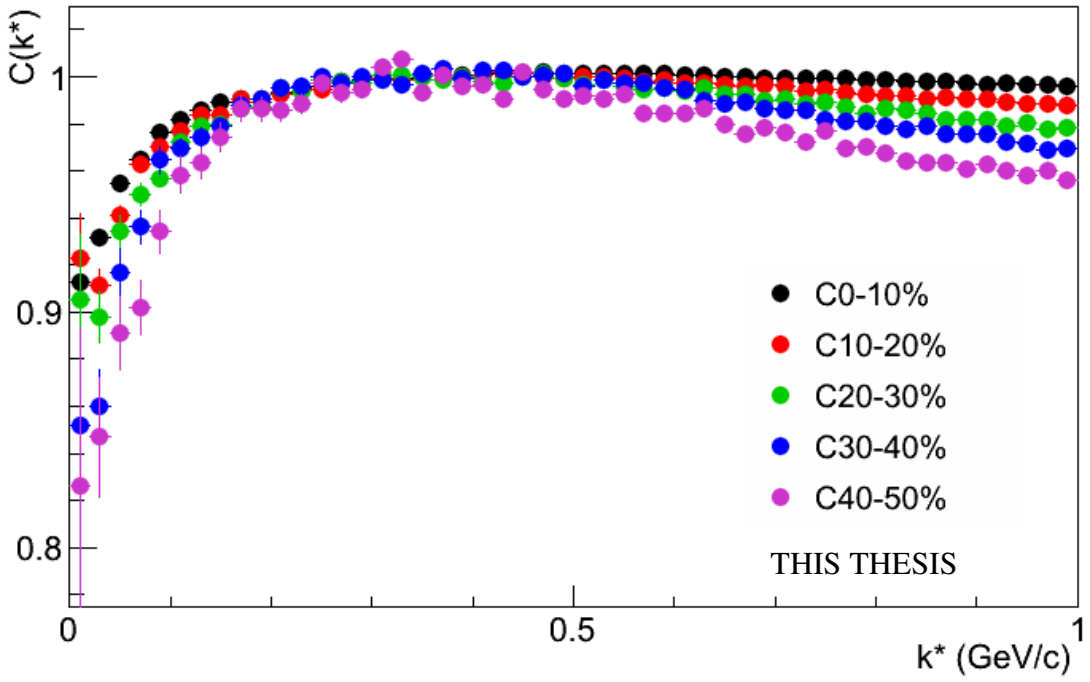

Figure 9.8: The combined $p\overline{\Lambda}+\overline{p}\Lambda$ correlation functions for centralities 0–10%, 10–20%, 20–30%, 30–40%, and 40–50%.

We note that the plots shown in Fig. 9.7 and Fig. 9.8 are still in the early stage of the analysis. However, the data points for the highest centrality range were approved by the ALICE Collaboration as the official ALICE Preliminary results and showed on number of scientific conferences. The approved plots for the 0–10% centrality range are presented in Fig. 9.9 and Fig. 9.10.

Comparison with STAR data

The femtoscopic analysis of $p\overline{\Lambda}$ ($\overline{p}\Lambda$) correlations was performed also by the STAR experiment at RHIC [294] in Au–Au collisions at $\sqrt{s_{\mathrm{NN}}}$ = 200 GeV for the 0–10% centrality range. The comparison between the two experiments is not straightforward since the STAR correlation functions were corrected for purity and contamination. However, this correction procedure does not account for residual correlations. Therefore, in order to plot together the ALICE correlation function and the one from STAR one must remove the purity corrections from the STAR data by

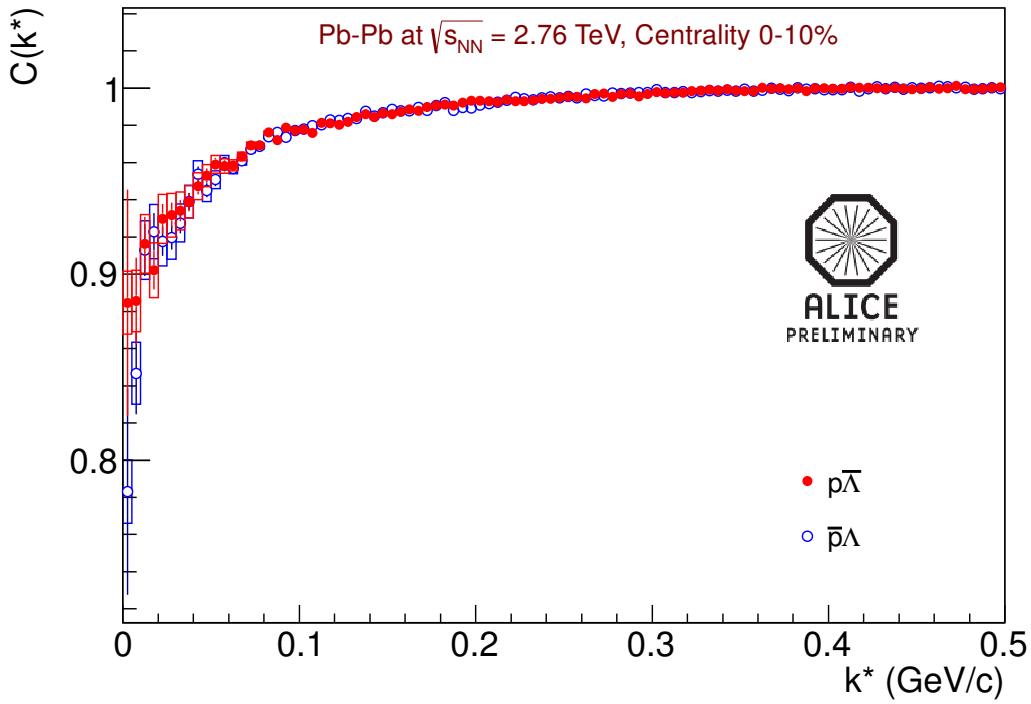

Figure 9.9: The correlation functions for $\bar{p}\Lambda$ and $p\bar{\Lambda}$ pairs for the most central events (0–10% centrality class).

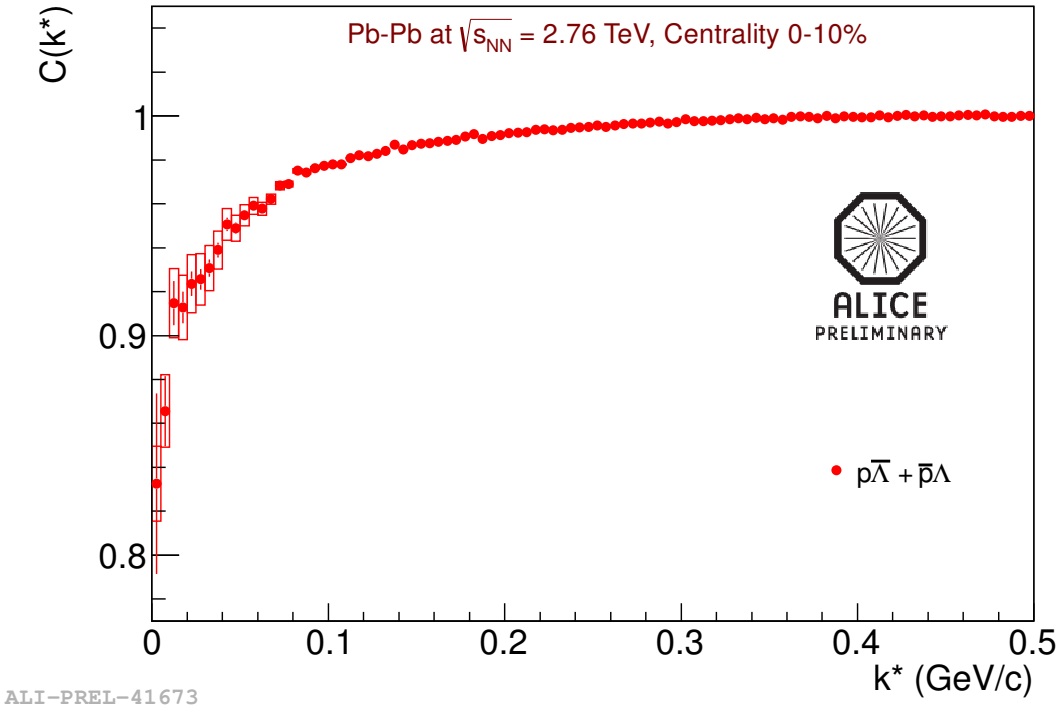

Figure 9.10: The combined $\bar{p}\Lambda$+$p\bar{\Lambda}$ correlation function plotted for the most central events (0 – 10% centrality class).

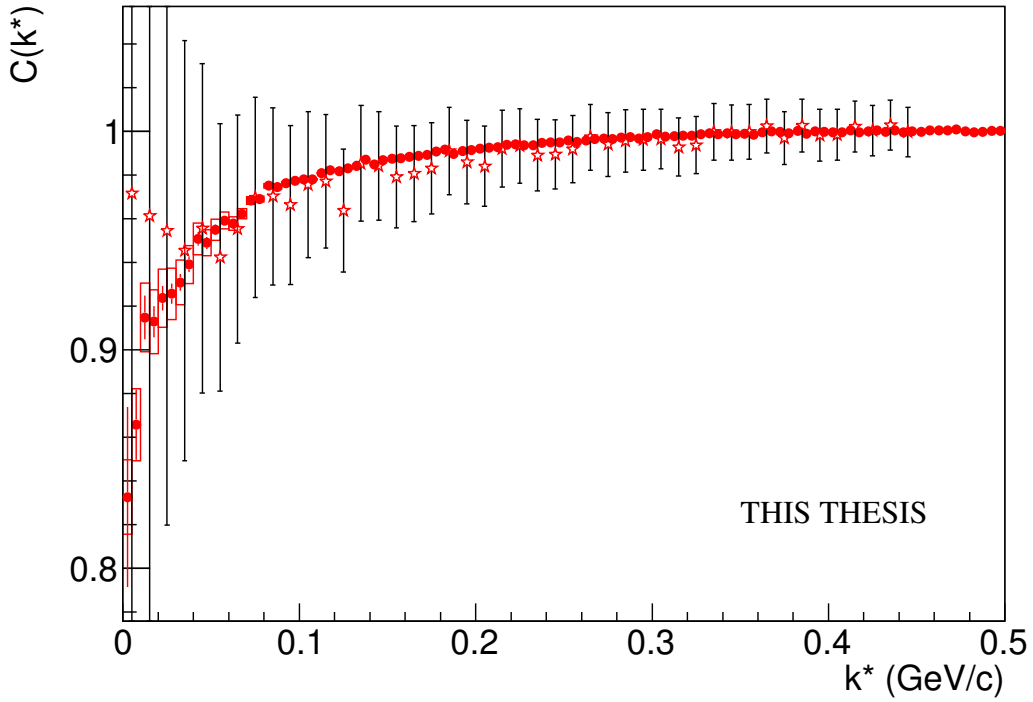

Figure 9.11: The combined $p\overline{\Lambda}+\bar{p}\Lambda$ correlation function calculated in ALICE (red full circles) from Pb–Pb collisions at $\sqrt{s_{NN}}$ = 2.76 TeV and STAR [294] (red open stars) from Au–Au collisions at $\sqrt{s_{NN}}$ = 200 GeV plotted for the 0–10% centrality range.

reverting the procedure described in Ref. [294]. Figure 9.11 shows the comparison of combined $p\overline{\Lambda}+\bar{p}\Lambda$ correlation functions from STAR (after reversing the purity correction) and ALICE for the 0–10% centrality range. The results of two experiments are qualitatively consistent with each other, except for the few first points.

9.3 Summary and outlook

The analysis of baryon-baryon ($p\Lambda$, $\bar{p}\overline{\Lambda}$) and baryon-antibaryon ($p\overline{\Lambda}$, $\bar{p}\Lambda$) systems was performed and preliminary results were obtained. The presented results exhibit clear centrality dependence of the correlation functions for all measured baryon-baryon and baryon-antibaryon systems, which is an indication of the expected increase of the source size with increasing event centrality.

We observe a significant residual correlation between primary protons contributing to the $p\Lambda$ ($\bar{p}\overline{\Lambda}$) correlation functions. The procedure to reduce such correlations was introduced and validated.

The baryon-antibaryon systems were qualitatively compared to the theoretical expectations from the Lednicky & Lyuboshitz analytital model. A wide anticorrelation effect, comparable to the one obtained from the model, was observed. This effect is consistent with the significant baryon-antibaryon annihilation process, which can be responsible for the lower baron yields observed at the LHC.

Future studies of correlations of protons with lambda hyperons are planned. First, further adjustments of the selection criteria in order to obtain more pure samples of lambdas are required. Second, the effects of splitting and merging need to be carefully studied in order to understand and remove all undesired detector influences. Third, the residual correlations from different sources must be carefully studied with the help ofthe `CorrFit` tool and the THERMINATOR 2 model. Finally, when the final correlation functions are obtained, the next step will be to apply a robust fitting method, described in details in Ref. [296], in order to extract both the source sizes and the cross sections.

Chapter 10

Summary and conclusions

Conclusions from pion femtoscopy in p–Pb

The p–Pb data presented in this thesis were delivered by the LHC and registered by the ALICE detector, first as a short pilot run in September 2012, and then in a month-long dedicated run in the beginning of 2013, just before the LHC Long Shutdown 1. Until then, the properties of the Quark-Gluon Plasma at the LHC had been assessed mainly by comparing the measurements in Pb–Pb collisions with the corresponding pp results which served as a benchmark. In general, in proton-proton collisions, where the overlapping volume of the colliding system is small, one does not expect QGP formation and essentially all created partons fragment into the vacuum. On the contrary, in central Pb–Pb collisions the large collision region is thought to provide favorable conditions for the creation of a deconfined medium, like the predicted QGP state of matter. In this case partons emerging from the primary collision traverse through the hot and dense plasma. Thus, the comparison of observables from the different collision systems allows us to draw conclusions on the properties of the QGP. The missing link in this game was: how our observables look like when particles formed in a collision of single nucleons traverse the "cold nuclear matter", i.e. a nucleus made of protons and neutrons rather than a plasma of quarks and gluons. To address such questions, p–Pb collisions are studied. The goal of this thesis is to perform femtoscopic measurements that probe the space-time evolution of the particle emitting source and its collective properties, thus providing insight into the underlying physics mechanisms.

The p–Pb collisions at the LHC (as well as p/d–Au at RHIC), initially expected to serve as another control measurement, in fact turned out to reveal surprising results which have cast doubt on this paradigm. Some measurements seem to agree with cold nuclear matter expectations. However, other observables, typically testing the hydrodynamic description of the collision system, like the behavior of the particle spectra at low momenta and the observa-

tion of long-range azimuthal correlations, show that p–Pb collisions can not be explained by an incoherent superposition of pp collisions and indicate the presence of collective effects. In addition, some of the LHC results can be also tested against models involving gluon saturation mechanism in a Color Glass Condensate framework. In fact, a CGC initial-state model, without hydrodynamic phase, predicts similar source sizes in both p–Pb and pp collisions. In contrast, the existence of a hydrodynamic phase in high-multiplicity p–Pb collisions would result in source sizes significantly larger with respect to pp at similar multiplicity. Therefore, the pion femtoscopic measurements, which are presented in this thesis, add crucial information and constraints for the understanding of the p–Pb collisions at the LHC.

The analysis of p–Pb data comprises two parts: (1) methodological, focusing on the development of a formalism to extract reliable physics information, and (2) experimental, which deals with the analysis of the collision data. The two parts can not be treated separately as the development of the formalism was motivated by the needs of the analysis of the experimental correlation functions obtained first from pp and then p–Pb collisions.

In particular, first the femtoscopic analysis of pp collisions revealed that the correlation functions are significantly affected by the presence of additional correlations, not originating from the symmetrization of the pair wave function, and hence referred to as non-femtoscopic. The same type of correlations were found in p–Pb collisions, complicating the extraction of the femtoscopic radii. In order to reliably obtain the femtoscopic information they had to be taken into account in the analysis procedure.

We studied the non-femtoscopic correlations employing the EPOS model, which is the only Monte Carlo event generator that includes these effects and also provides freeze-out coordinates, information crucial for femtoscopy. We validated a robust procedure to account for such additional correlations during the extraction of the femtoscopic radii in three dimensions. Specifically, we showed that if both, the magnitude as well as the shape of the non-femtoscopic background, are properly constrained with the help of the Monte Carlo simulation, the correct values of the radii can be extracted. We evaluated that the systematic uncertainty coming from the method itself is approximately 3-8%. The proper selection of the fitting range was also discussed. As a result of these studies, general recommendations could be drawn; in particular, it was underlined that it is important to use a range that fully includes the femtoscopic signal, together with a reasonable portion of the background-dominated region of the relative momentum. For the first time such detailed studies of the non-femtoscopic correlations, in three

dimensions, were performed. The method as well as the provided recommendations have been published and can be applied to any femtoscopic measurements where additional correlations are significant.

We then applied this procedure to extract the femtoscopic radii from the collision data. For the first time, the three-dimensional pion femtoscopic radii were measured in p–Pb collisions at $\sqrt{s_{\mathrm{NN}}}$ = 5.02 TeV, in four multiplicity and seven pair transverse momentum k_{T} ranges. The radii decrease with k_{T} in all cases, similar to the measurements in A–A and high-multiplicity pp collisions. The radii also increase with event multiplicity. At low multiplicity they are comparable to pp values, while at higher multiplicities and low k_{T} they are larger by 10–20%. However, they do not reach the values observed in A–A collisions at lower energies.

The high multiplicity p–Pb data were compared to predictions from two hydrodynamic models. They predict larger values of the R_{out} and R_{long} parameters; however, the introduction of smaller initial size of the system brings calculations closer to the experimental data. In particular, the R_{side} parameter and the slope of the k_{T} dependence of the radii are in reasonable agreement. The models are challenged by the collision data; however, it may be possible to reproduce the high multiplicity results with a careful choice of the initial conditions of the hydrodynamic evolution.

On the other hand, the models based on the Color Glass Condensate formalism, without the hydrodynamic evolution, suggest source sizes similar to those obtained in pp experimental data. However, the observed differences, of the order of 10–20%, between high multiplicity pp and p–Pb collisions do not exclude this scenario.

The unique measurement of the three-dimensional pion femtoscopy in p–Pb collisions at $\sqrt{s_{\mathrm{NN}}}$ = 5.02 TeV was performed for this thesis and will be published soon. These results are essential for the study of the interplay between initial- and final-state effects in the p–Pb system, which are crucial for our understanding of the Quark Gluon Plasma. The obtained femtoscopic radii are compared to the ones measured in the pp system and to p–Pb predictions involving hydrodynamic evolution in the final-state. They are slightly higher than pp and lower than predictions from hydrodynamics; however, the definite answer whether final-state effects manifest in p–Pb can not be drawn yet. Further refinements of hydrodynamic models and systematic comparisons with the experimental data are needed.

Conclusions from baryon femtoscopy in Pb–Pb

One of the surprising results from Pb–Pb collisions at $\sqrt{s_{\mathrm{NN}}}$ = 2.76 TeV at the LHC are the yields of protons and lambda hyperons, which are lower than predicted by extrapolations from lower energies. The most serious candidate for the explanation of this effect is the presence of a significant hadronic rescattering phase in the collision evolution process; in particular, the annihilation between different baryon-antibaryon pairs. However, this hypothesis can not be fully validated at the moment because the parameters of the strong interaction for most of the two-baryon systems are not known. The novel application of the femtoscopic formalism, applied to baryon pairs and going beyond the typical studies of the system size, allows us to measure these parameters. Moreover, these type of correlations are expected to not only characterize the hot and dense medium created in Pb–Pb collisions, but also to provide important input to astrophysics, as they are needed to understand processes that occur in the cores of neutron stars.

The reported analysis presents preliminary results of correlations of protons with lambda hyperons in Pb–Pb collisions at $\sqrt{s_{\mathrm{NN}}}$ = 2.76 TeV. The correlation functions for different systems (baryon-baryon: $\mathrm{p}\Lambda$, $\overline{\mathrm{p}}\overline{\Lambda}$, as well as baryon-antibaryon: $\mathrm{p}\overline{\Lambda}$, $\overline{\mathrm{p}}\Lambda$) have been obtained for five centrality ranges. Baryon-antibaryon correlations were compared to theoretical expectations calculated using the Lednicky & Lyuboshitz analytical model with and without the annihilation process. The qualitative comparison revealed the presence of a wide anticorrelation that can be interpreted as a significant contribution of the baryon-antibaryon annihilation process. This result is in agreement with the annihilation hypothesis that causes the lower baryon yields at the LHC and is the starting point for measurements of interaction cross sections in these systems, which will be used to explain the baryon yields at the LHC.

The ALICE detector is a unique machine, ideally suited for the study of particle correlations in all collision systems delivered by the LHC and provides further insight into the understanding of physics of matter at the elementary level. The unique femtoscopic measurements of p–Pb and Pb–Pb data presented in this thesis, address different aspects of the same fundamental question of the LHC program, the characterization of the Quark Gluon Plasma.

All the measurements of the p–Pb and Pb–Pb collisions, presented in this thesis, were delivered by the CERN LHC recorded by the ALICE detector. All the studies were performed in the frame of the ALICE Collaboration and the Femtoscopy Physics Analysis Group.

Appendices

Appendix A

Details of Monte Carlo studies

Monte Carlo models have been employed both for systematic checks of the experimental results and description of non-femtoscopic structures observed in the collision data. In the first case they were used to verify the influence of the detector setup and the reconstruction algorithms on the final result. The description of the non-femtoscopic background has been done using EPOS 3.076 and PYTHIA 6.4, tune Perugia-0, from pp collisions at $\sqrt{s}$ = 7 TeV, which has been motivated and discussed several times in previous chapters. However, this choice was based on extensive studies performed with many other Monte Carlo models available for p–Pb collisions at $\sqrt{s_{\mathrm{NN}}}$ = 5.02 TeV. Therefore, in this chapter we will focus on those Monte Carlo models which were found not to describe the non-femtoscopic correlations.

A.1 Multiplicity determination in MC

We must note, that most of the MC studies were performed during the early stage of the analysis; therefore, some selection criteria both for the correlation functions calculated from collision data and Monte Carlo models, which are shown on the plots in the following sections, may differ slightly from the ones described in Chapter 6 and the final results presented in Chapter 7. One of them is multiplicity. At the early stage of the analysis the multiplicity was defined on the basis of the combined signal of V0A and VOC detectors (such combined signal is referred to as V0M multiplicity estimator). However, as the analysis advanced a common multiplicity definition, based only on the signal from the V0A detector (located on the Pb-remnant side), for all ALICE studies in p–Pb system was introduced. Therefore, the change of the multiplicity definition from V0M to V0A was made also in the analysis presented in this thesis. We note that the difference in the correlation functions calculated with V0M and V0A multiplicity estimators is located only in the large relative momentum q region and the femtoscopic peak is unaffected.

Table A.1 presents the V0M multiplicity classes which were used prior to the V0A intervals introduced in Table 6.1.

Table A.1: Definition of the V0M event classes as fractions of the analyzed event sample and their corresponding $\mathrm{d}N/\mathrm{d}\eta$ within $|\eta| < 0.5$ as well as the mean number of charged particles within $|\eta| < 1.2$ and $p_{\mathrm{T}} > 0.5$ GeV/c. The given uncertainties are systematic as the statistical ones are negligible.

Event class	V0M range (a.u.)	$\mathrm{d}N\mathrm{d}\eta\|_{\|\eta\|<0.5}$ $p_{\mathrm{T}} >$ GeV/c	$N_{\mathrm{trk}}\|_{\|\eta\|<1.2}$ $p_{\mathrm{T}} > 0.5$ GeV/c
60–100%	< 138	6.6 ± 0.2	6.4 ± 0.2
40–60%	138–216	16.2 ± 0.4	16.9 ± 0.6
20–40%	216–318	23.7 ± 0.5	26.1 ± 0.9
0–20%	> 318	34.9 ± 0.5	42.5 ± 1.5

A.2 Detector and reconstruction inefficiencies

The effects of the detector and reconstruction process on the experimental results are usually studied using Monte Carlo models. In principle the reconstructed Monte Carlo data should reproduce the same result which is obtained from the Monte Carlo "truth" data, where only the generator-level information is available[1]. Any discrepancies between the results from those two datasets are due to detector and reconstruction effects (such as detection or identification inefficiencies). If these deviations are significant they should be corrected for using a dedicated procedure.

In the studies presented in this thesis p–Pb collisions at $\sqrt{s_{\mathrm{NN}}} = 5.02$ TeV generated with HIJING [45] model were used for this purpose. The same femtoscopic analysis was performed on MC truth and reconstructed data producing two sets of correlation functions which are shown in Fig. A.1. The observed deviations between these two results are very small and have been included as part of the systematic uncertainty on the correlation function level.

[1] Such comparison is usually referred to as *Monte Carlo closure test*.

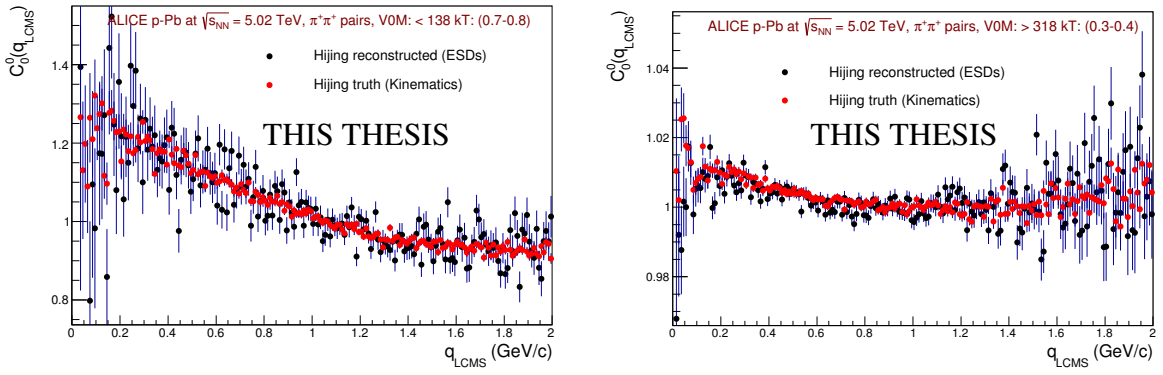

Figure A.1: C_0^0 spherical harmonic components of the correlation functions for HIJING: simulation only and reconstructed data, for two (low and high) V0M multiplicity ranges and two k_T intervals.

A.3 Non-femtoscopic correlations

The non-femtoscopic correlations were studied using several Monte Carlo models, both for p–Pb collisions at $\sqrt{s_{NN}}$ = 5.02 TeV and pp collisions at $\sqrt{s}$ = 7 TeV. The analyzed p–Pb collisions were generated by AMPT [46], HIJING [45], DPMJET [47], THERMINATOR 2 [286] (with 3+1 viscous hydrodynamics and local charge conservation [140]), EPOS 3.076 [147], and PYTHIA 6.4 [144] Perugia-2011 [145]. The pp MC data came from PYTHIA 8.1 [287] tune 4C [288], and PYTHIA 6.4 tunes Perugia-0 [145] and Z2.

The reconstructed Monte Carlo data were available only for HIJING, DPMJET, and PYTHIA Perugia-0. For all other models the generator-level information was used to calculate the correlation functions.

A complete list of all Monte Carlo models used in the analysis presented in this thesis in the studies of non-femtoscopic correlations is shown in Table 6.3.

From all these models only EPOS 3.076 and PYTHIA 6.4 Perugia-0 were able to describe the non-femtoscopic correlations observed in p–Pb experimental correlation functions and were used in the procedure of extracting the femtoscopic radii described in Chapter 5. In this section all other models are briefly discussed.

A.3.1 HIJING

A.3.1.1 Comparison with collision data

Figure A.2 shows the spherical harmonic components of the like-sign pion correlation functions which were calculated using information from the HIJING model. They were compared with the correlation functions calculated from collision data for two (low and high) multiplicity classes and k_{T} ranges. The rise of the non-femtoscopic effect in C_0^0 is visible both for collision data and HIJING; however, correlation functions from the generated data show almost flat dependence on q at low k_{T}, which means practically no correlation, and even stronger than collision data correlation at high k_{T}. The shapes of the C_2^0 and C_2^2 components also differ from the collision data. However for high multiplicity collisions no solid statement can be made due to lack of statistics.

A.3.1.2 Comparison of unlike-sign pairs

Unlike-sign correlation functions calculated from the HIJING model were also studied. Since no Bose-Einstein efffects are present in this system, direct comparison between model and collision data can be performed, which is shown in Fig. A.3.

As opposed to like-sign pairs described in Sec. A.3.1.1, the shape of the HIJING unlike-sign correlation functions quite well describes the correlations observed in the collision data. The resonance peaks in HIJING – the wide peak near 0.8 GeV/c from ρ particle and the narrow peak near 0.4 GeV/c from K_0^S, are more prominent than the ones in the collision data. The biggest difference between unlike-sign correlation functions calculated from HIJING and collision data is observed at the highest multiplicity and lowest k_{T} rages.

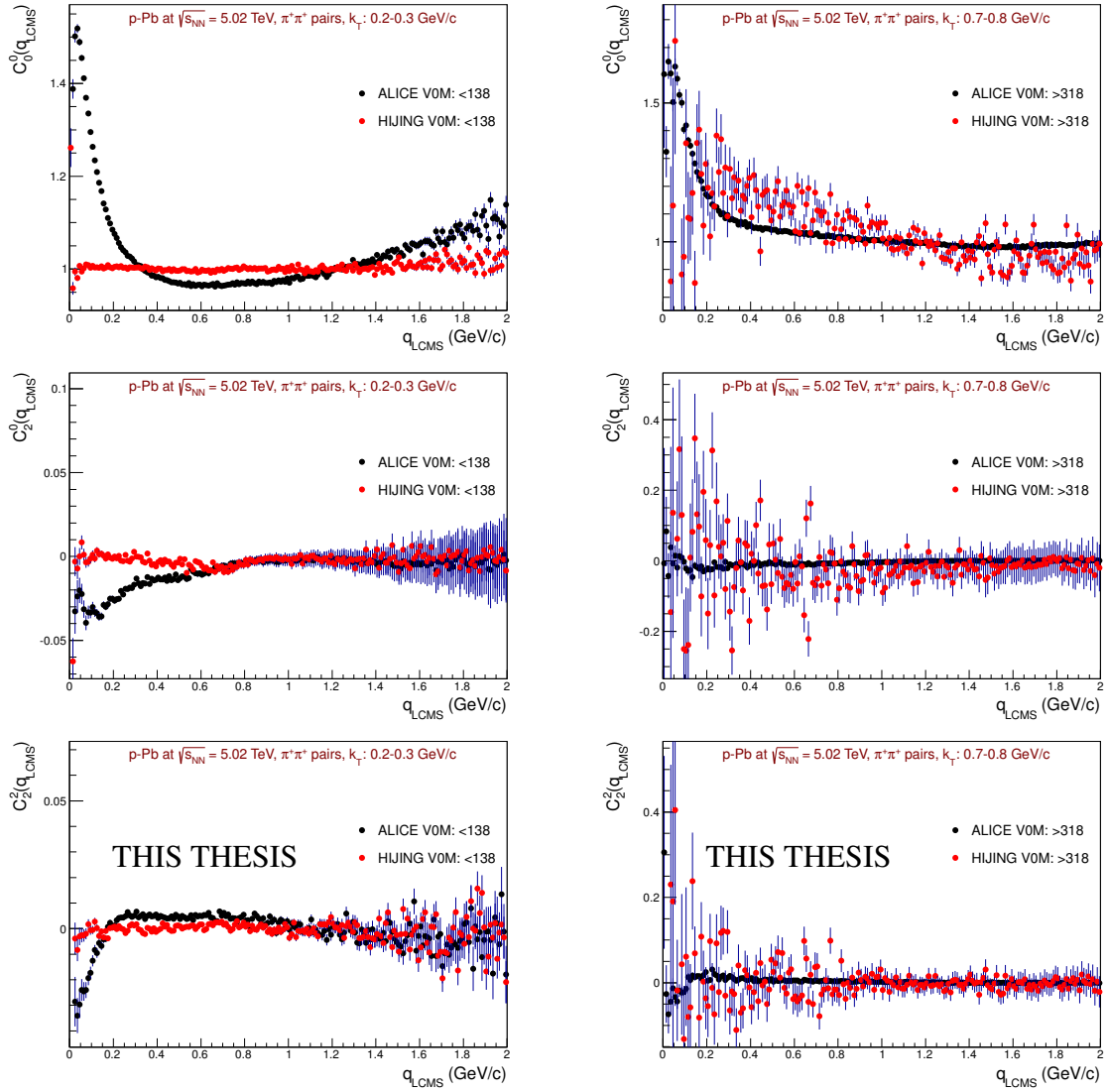

Figure A.2: Spherical harmonic components of the correlation functions calculated from HIJING compared to ALICE collision data for two (low and high) multiplicity and k_{T} ranges.

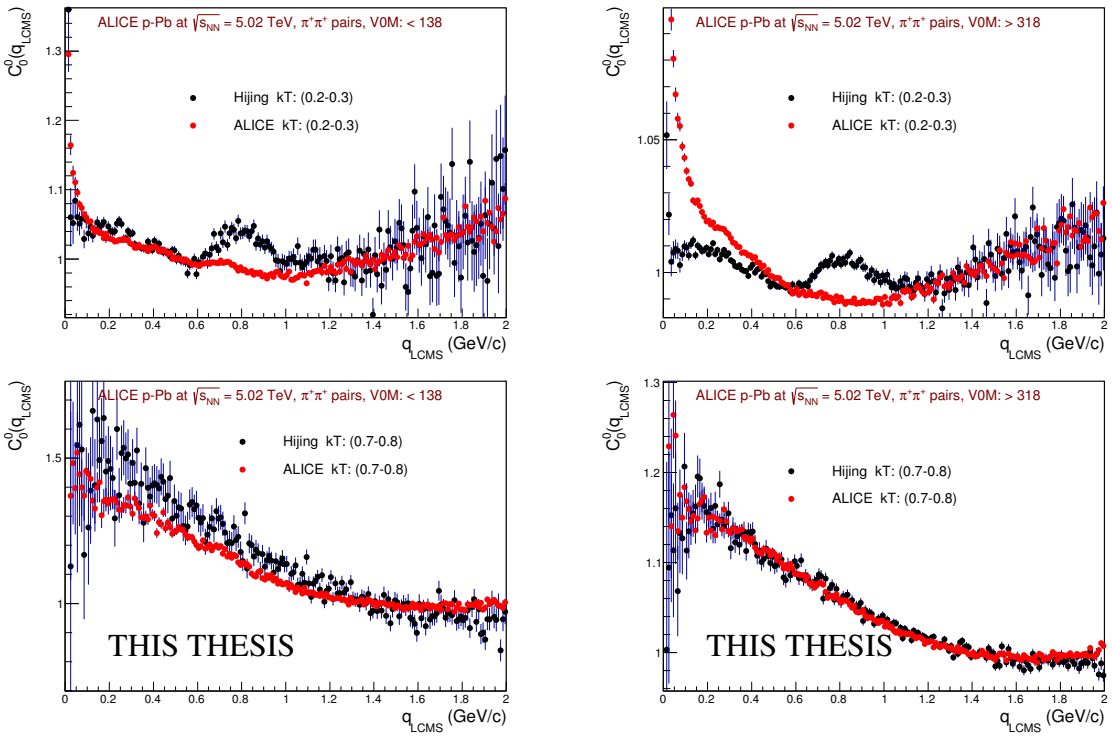

Figure A.3: C_0^0 spherical harmonic components of the unlike-sign correlation functions of pions calculated from HIJING and collision data for two (low and high) multiplicity and k_{T} ranges.

A.3.2 DPMJET

Correlation functions, both for like- and unlike-sign pairs of pions, have been also calculated from the DPMJET model. Their comparison with correlation functions obtained from collision data is shown Fig. A.4. At low k_T practically a flat dependence of the correlation function on q is observed for both like- and unlike-sign pairs. However, the correlation develops with increasing k_T. At the highest k_T range the slope of the correlation function from DPMJET is even stronger than in data.

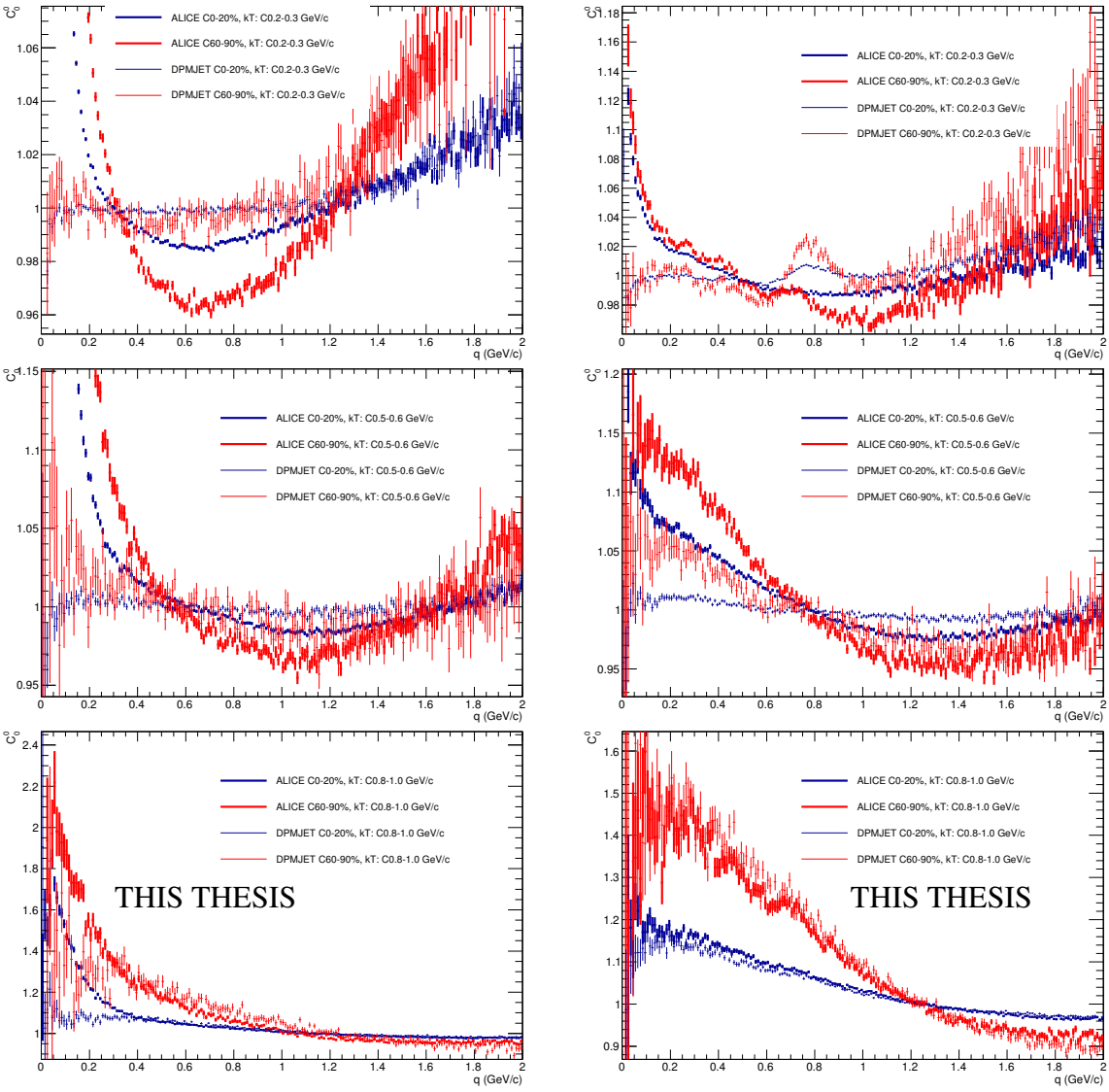

Figure A.4: C_0^0 spherical harmonic components of the correlation functions calculated from the DPMJET model (thin lines) and collision data (thick lines) for (left) like-sign and (right) unlike-sign pairs for two (low and high) multiplicity and three (low, middle, and high) k_T ranges.

A.3.3 AMPT

In the case of AMPT model only generator-level information was available. However, as it was already described in Sec. A.2, the detector effects on the correlation function are practically negligible; thus, we could proceed with the comparison of AMPT to experimental results.

A.3.3.1 Comparison with data

Figure A.5 shows the spherical harmonic components of correlation functions calculated from the AMPT model compared to correlation functions calculated from collision data at high multiplicity and two (low and high) k_{T} ranges. Similarly to previously described models, there is a correlation growing with increasing k_{T}. but the collision data are also not reproduced. In addition, the 3-dimensional shape, reflected in C_0^2 and C_2^2 components, is significantly different from the one observed in collision data.

A.3.3.2 Comparison with HIJING

In Fig. A.6 a comparison between correlation functions calculated from AMPT and HIJING models is shown. Correlation functions from both Monte Carlo models reflect similar trends and behavior as observed in the collision data (correlation growing with increasing k_{T} and decreasing with multiplicity). However, the slopes are not the same – correlation function from HIJING is higher than AMPT at high k_{T} range.

A.3.3.3 Comparison of unlike-sign pairs

Correlation functions of unlike-sign pairs pairs of pions were also calculated from AMPT model. As it can be observed in Fig. A.7, which shows the comparison with collision data, the resonance peaks in AMPT are reflected very poorly. However, the shapes of the both correlation functions tend to agree better for unlike-sign pairs.

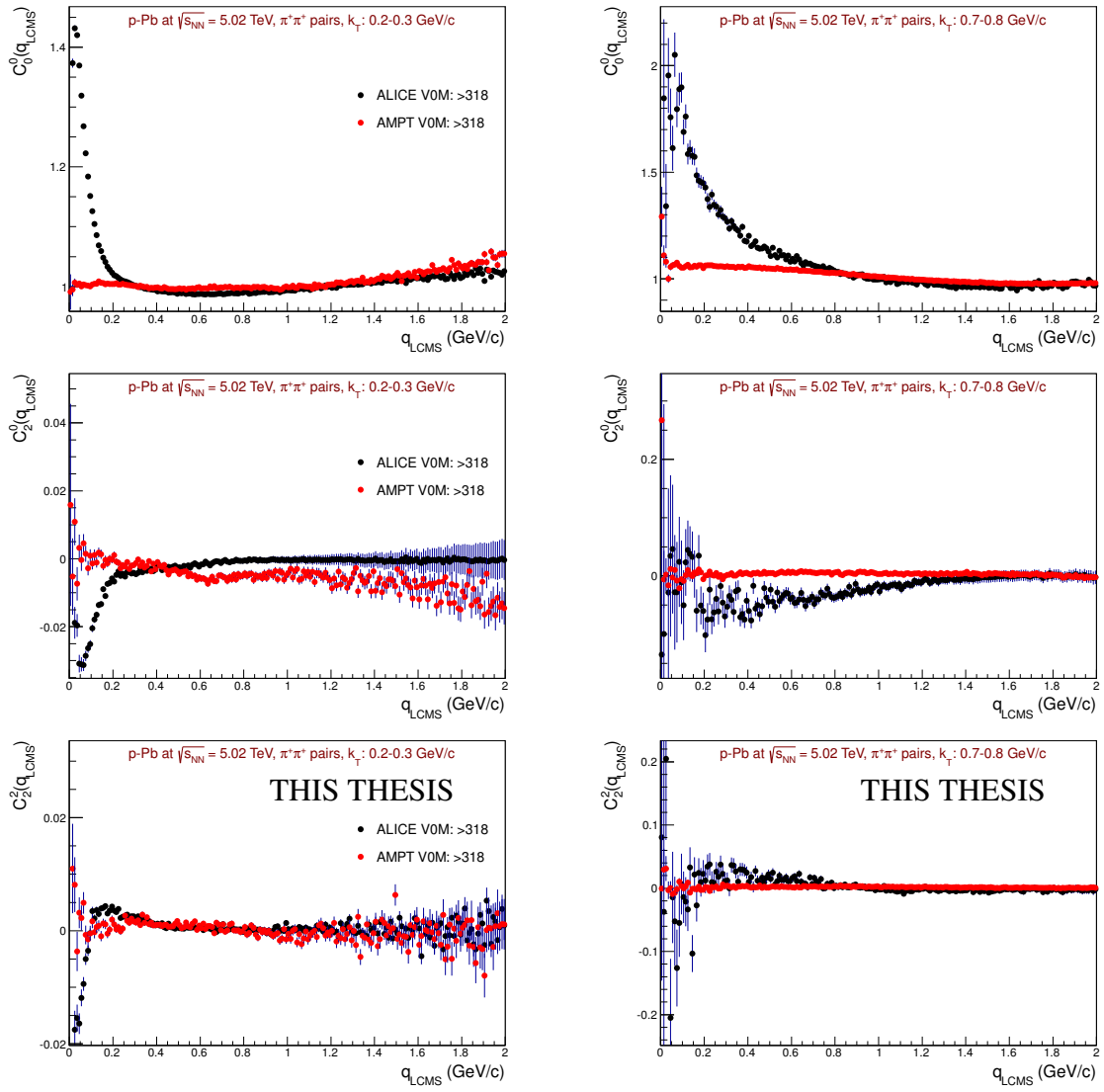

Figure A.5: Spherical harmonic components of correlation functions calculated from AMPT model compared to ALICE collision data at high multiplicity and two (low and high) k_{T} ranges.

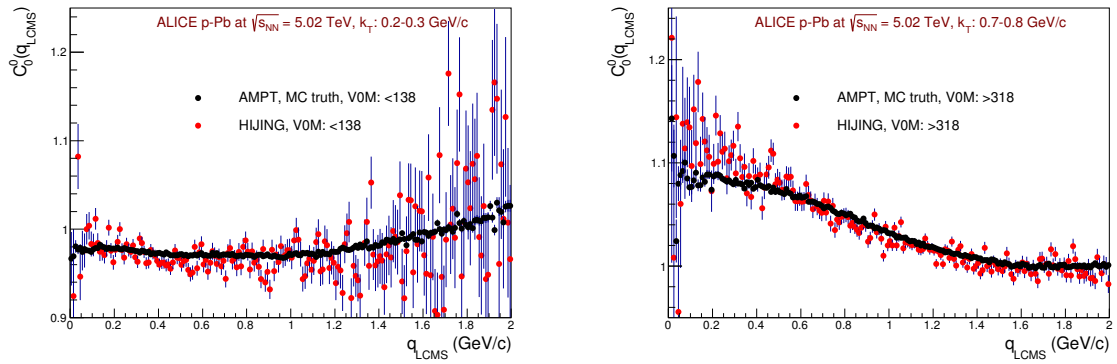

Figure A.6: C_0^0 components of the correlation functions from AMPT and HIJING models for like-sign pairs for (left) low multiplicity and low k_{T} intervals and (right) high multiplicity and high k_{T} ranges.

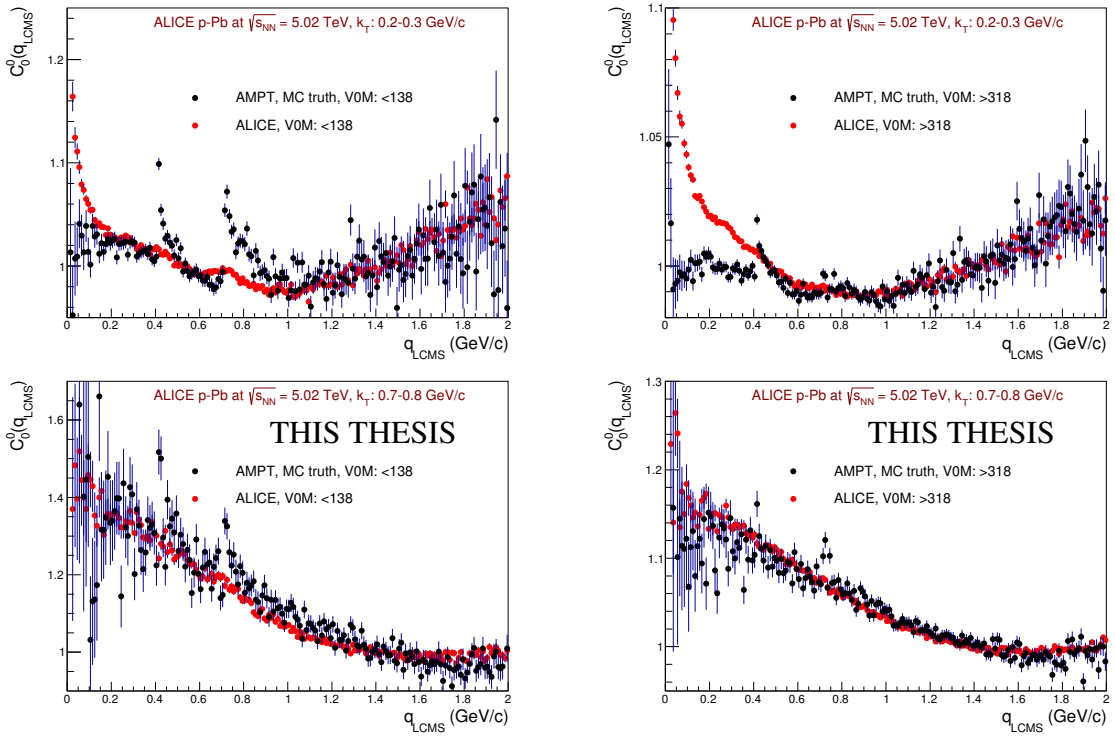

Figure A.7: C_0^0 spherical harmonic components of the unlike-sign correlation functions from AMPT compared to collision data for two (low and high) multiplicity and k_{T} intervals.

A.3.4 THERMINATOR 2

Like- and unlike-sign correlation functions were also calculated using THERMINATOR 2 model with 3+1 viscous hydrodynamics and also with charge balancing. Figure A.8 shows comparison between THERMINATOR 2, EPOS 3.076 and collision data for the highest multiplicity and different k_T intervals for both systems. There are four different versions of THERMINATOR calculations: with initial transverse size of 0.5 fm (called *s0.5* in the plots), with initial transverse size of 1.0 fm (called *s1.0* in the plots), and also with the so-called charge balancing (called *bal* in the plots). We can see that none of the THERMINATOR calculations describes the experimental data. In the case of like-sign pairs they are practically flat for both low and high k_T. On the other hand, for umlike-sign pairs there is a small slope visible at large k_T range for calculations without charge balancing. It is much stronger than calculations with charge balancing. From this comparison we can also clearly see that EPOS describes the non-femtoscopic structure observed in like-sign pairs very well.

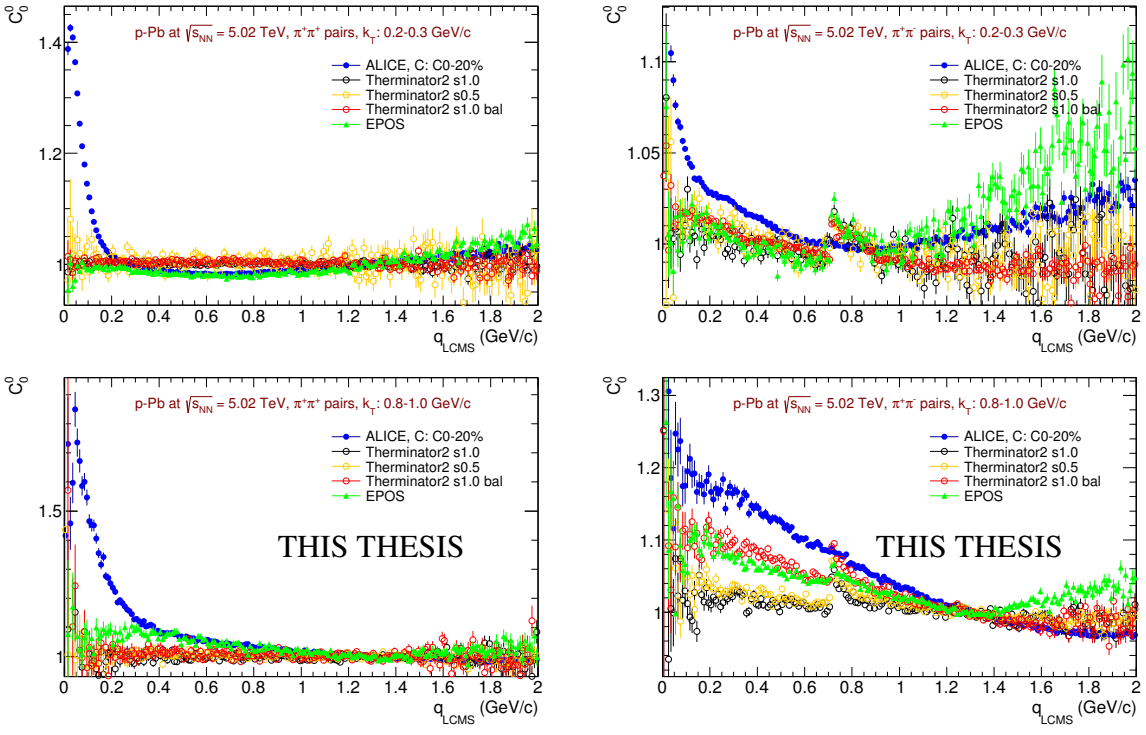

Figure A.8: C_0^0 spherical harmonic components of the correlation functions from EPOS 3.076 (green), three versions of THERMINATOR 2 (black, yellow, red), and ALICE data (blue) for like-sign pairs (left plots) and unlike-sign pairs (right plots) of pions for highest multiplicity and two (low and high) k_T ranges.

A.3.5 PYTHIA p–Pb at $\sqrt{s_{\mathrm{NN}}} = 5.02$ TeV

Figure A.9 shows comparison between PYTHIA 6.4 p–Pb data with collision data for the 40-60% V0A multiplicity class for like-sign pairs of pions for three (low, middle, and high) k_{T} ranges. We can see that the slope for PYTHIA, even for the low k_{T}, is much higher than the non-femtoscopic correlations observed in the collision data.

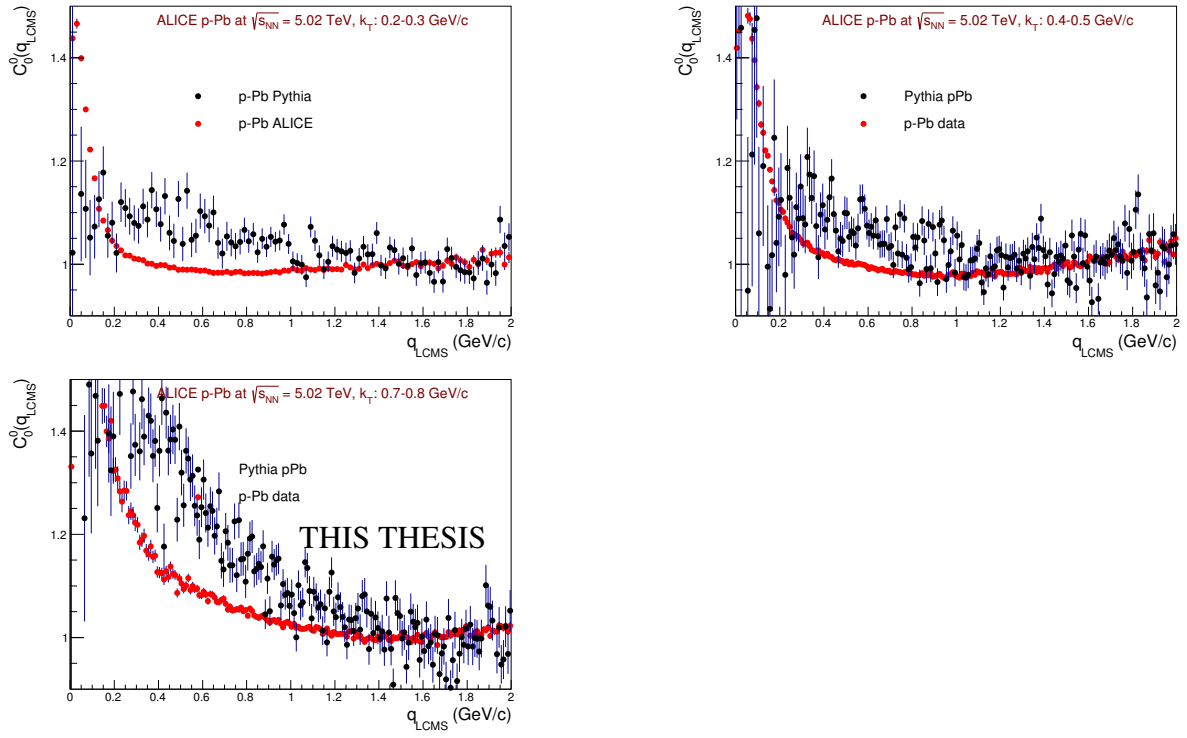

Figure A.9: The C_0^0 component of the correlation functions for PYTHIA (black) and ALICE data (red) p–Pb data for like-sign pairs for 40-60% multiplicity class and three k_{T} bins (top left: 0.2-0.3 GeV/c, top right: 0.4-0.5 GeV/c, bottom left: 0.7-0.8 GeV/c.

A.3.6 PYTHIA pp at $\sqrt{s} = 7$ TeV – Z2 and 4C tunes

In addition to Perugia-0, other tunes of PYTHIA for pp collisions at $\sqrt{s} = 7$ TeV were studied – PYTHIA 8 tune 4C and PYTHIA 6.4 tune Z2. Only generator-level information was available for both datasets. Figures A.10 and A.11 (with the y axis zoomed to better show the models) show the comparison of like-sign correlation functions from all the studied PYTHIA datasets compared to the EPOS model and collision data. We can clearly see that Z2 and 4C PYTHIA tunes do not reproduce the non-femtoscopic background well. In addition, they exhibit a significant rise of the correlation effect for large values of q. Comparisons for unlike-sign pion

pairs can be seen in Fig. A.12 – neither 4C nor Z2 PYTHIA tunes can describe the shape of the correlation function calculated from the collision data.

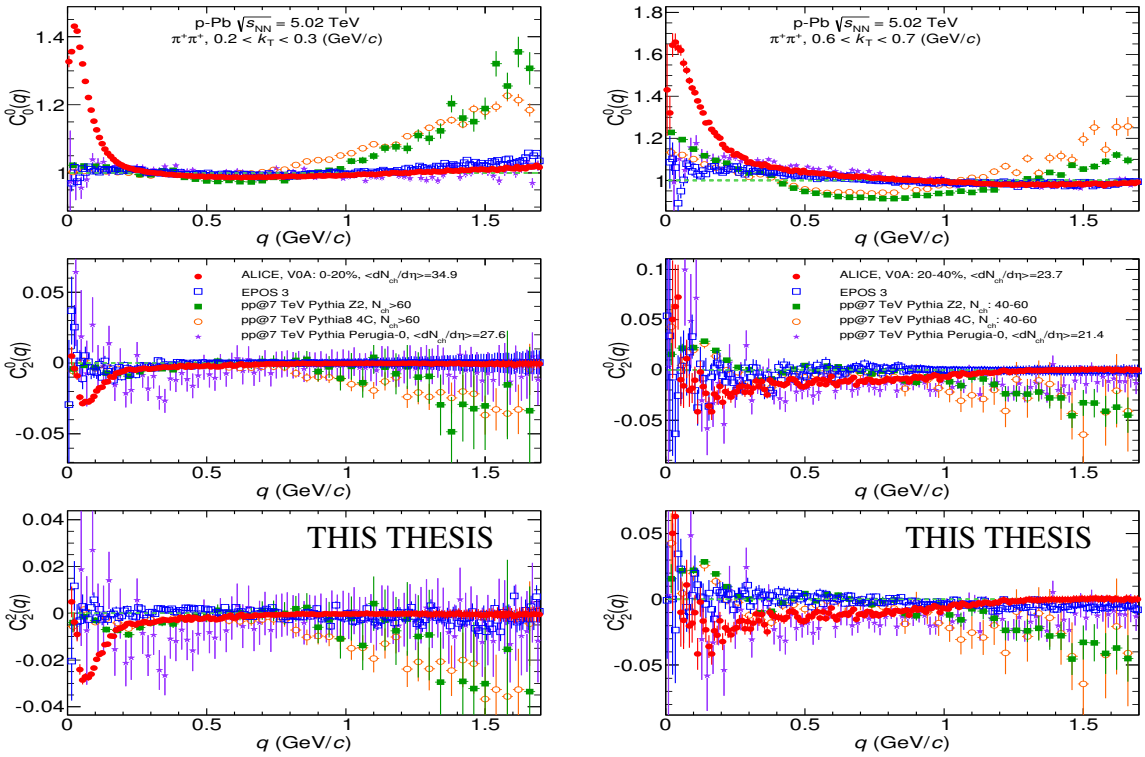

Figure A.10: Spherical harmonic components of the like-sign correlation functions from PYTHIA Perugia-0, 4C, and Z2 tunes for pp collisions at $\sqrt{s}$ = 7 TeV compared with collision data for two (low and high) k_T ranges.

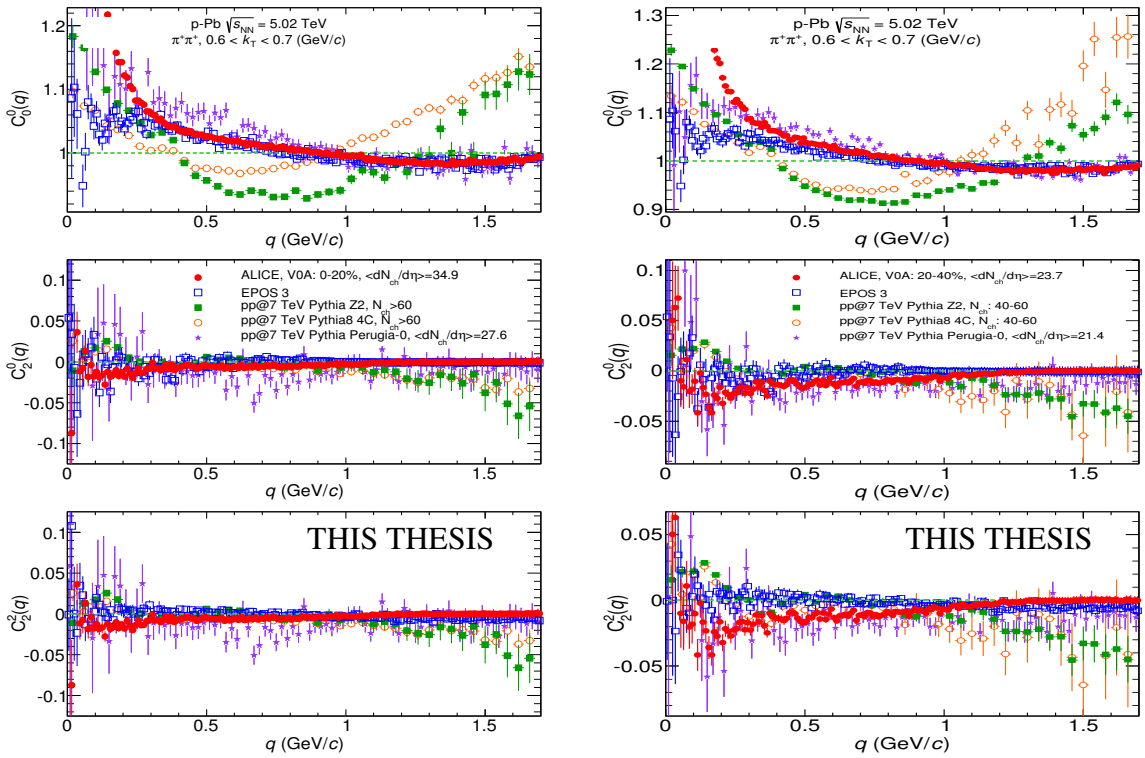

Figure A.11: Spherical harmonic components of the like-sign correlation functions from PYTHIA Perugia-0, 4C, and Z2 tunes for pp collisions at $\sqrt{s}$ = 7 TeV compared with collision data for two (low and high) k_T ranges. The y axis is of the plots is zoomed to better show the behavior of the models.

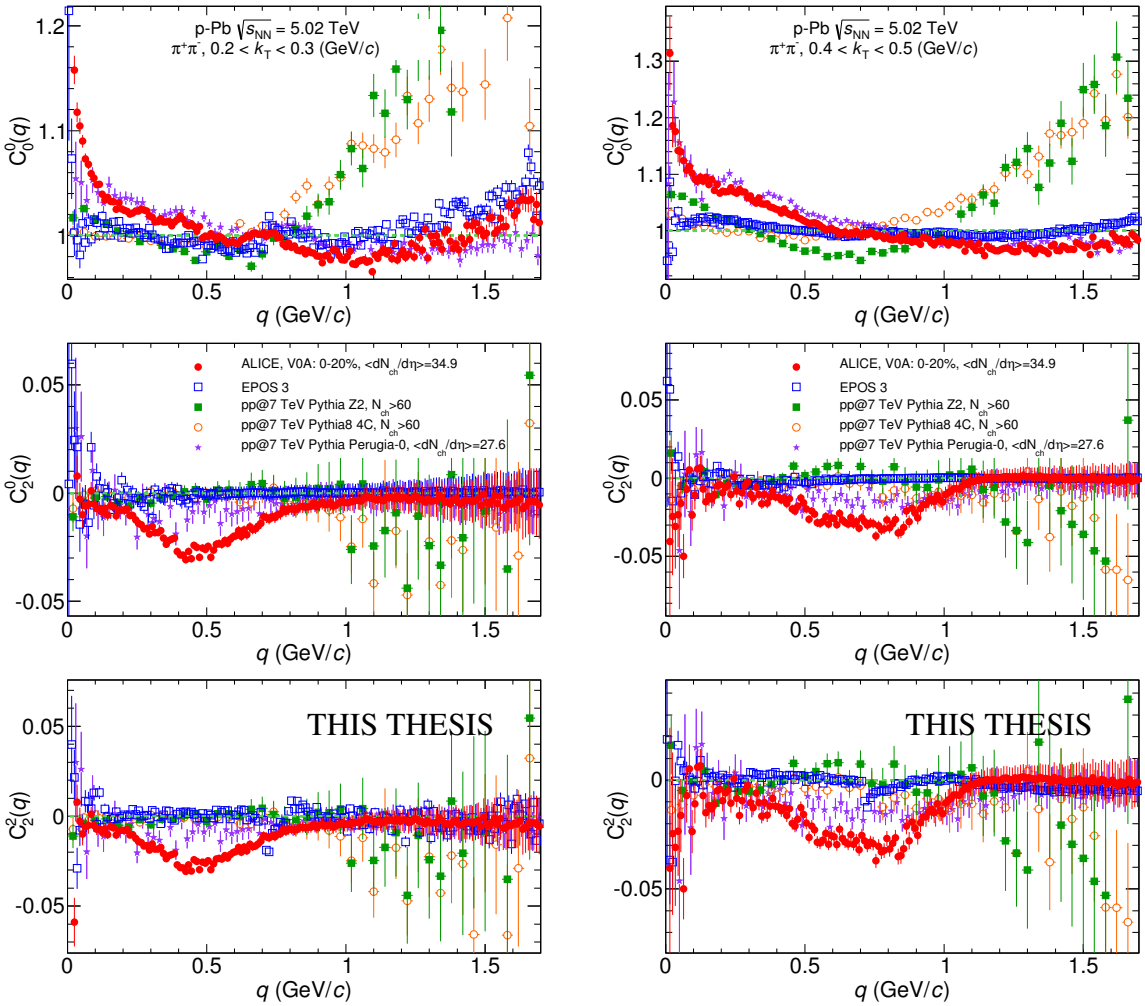

Figure A.12: Spherical harmonic components of the unlike-sign correlation functions from PYTHIA Perugia-0, 4C, and Z2 tunes for pp collisions at $\sqrt{s}$ = 7 TeV compared with collision data for two (low and high) k_T intervals.

A.3.7 Outcome of the Monte Carlo studies

As we have shown, only EPOS 3.076 and PYTHIA 6.4 Perugia-0 Monte Carlo models were able to describe the non-femtoscopic correlations observed in collision data. However, even these two models cannot describe the correlations of unlike-sign pairs. All other models, for like-sign pairs, mostly do not show any correlation at low k_{T} (flat correlation function) and develop the correlation with rising k_{T}, however the shapes are different (either the slope is too low or even higher thain in experimental data). Surprisingly, for unlike-sign pairs, the agreement with data tends to be better, however prominent resonance peaks are observed, which in some cases are not reproduced correctly.

In summary, we have decided to focus only on EPOS 3.076 and PYTHIA 6.4 Perugia-0 in the analysis of collision data, however a dedicated study of Monte Carlo models in small systems (both pp and p–A) would be of particular interest.

Appendix B

Correlations of unlike-sign pions

Pairs of unlike-sign pions by definition are not affected by Bose-Einstein quantum statistics, hence they cannot be used for the extraction of femtoscopic radii. However, the Coulomb attraction and other non-femtoscopic effects are present in unlike-sign correlations. Moreover, it is important to note that there are also additional correlations (i.e. decay of resonances) which are not present for like-sign particles.

One could try to use the correlation of unlike-sign particles to correct for the non-femtoscopic effect in the like-sign case. However, such a procedure requires the removal of the resonance peaks which can introduce additional biases. For example, decay pions misidentified as primary can modify the shape of the correlation function in a non-trivial way [297].

The measured $\pi^+\pi^-$ correlation functions for p–Pb collisions for both like- and unlike-sign pairs of pions are presented in the same plot in Fig. B.1. We can see that the non-femtoscopic part of the correlation of the like-sign pairs has clearly different shape than the one of the unlike-sign pairs. However, a qualitative analysis and comparison with unlike-sign correlations from Monte Carlo models is possible.

Figures B.2 and B.3 show the dependence of the $\pi^+\pi^-$ correlation functions on the event multiplicity (without binning in k_{T}; left panel) and pair transverse momentum for the lowest multiplicity range (right panel). We can clearly see that the width of the non-femtoscopic background is not changing with multiplicity; only the magnitude changes – increases for decreasing multiplicity and increasing pair transverse momentum k_{T}.

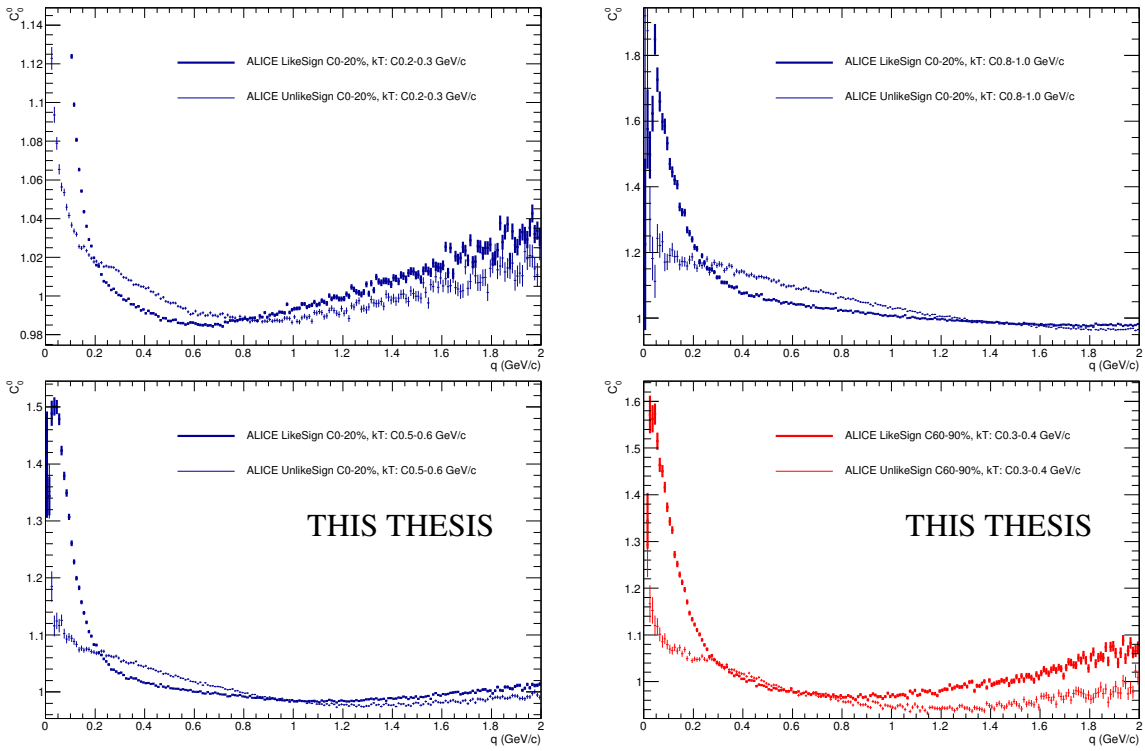

Figure B.1: C_0^0 spherical harmonic components of the correlation functions for $\pi^+\pi^+$ and $\pi^+\pi^-$ pairs in ranges of both V0A multiplicity class and k_{T}. Top left: (0-20%, 0.2 – 0.3 GeV/c), top right: (0-20%, 0.8 – 1.0 GeV/c), bottom left: (0-20%, 0.5 – 0.6 GeV/c), bottom right: (60-90%, 0.3 – 0.4 GeV/c).

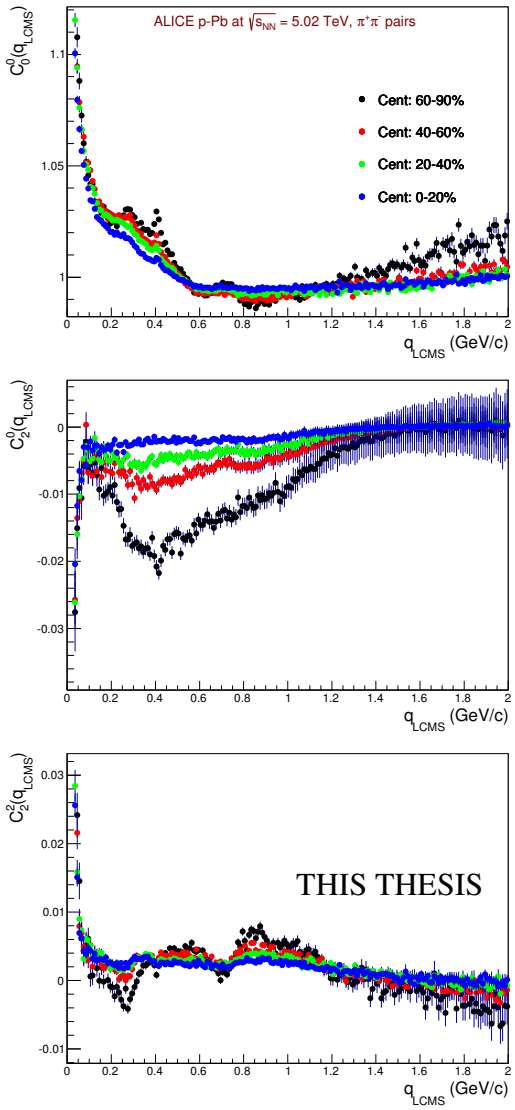

Figure B.2: Three non-vanishing spherical harmonic components of the correlation functions for $\pi^+\pi^-$ pairs for four V0A multiplicity classes.

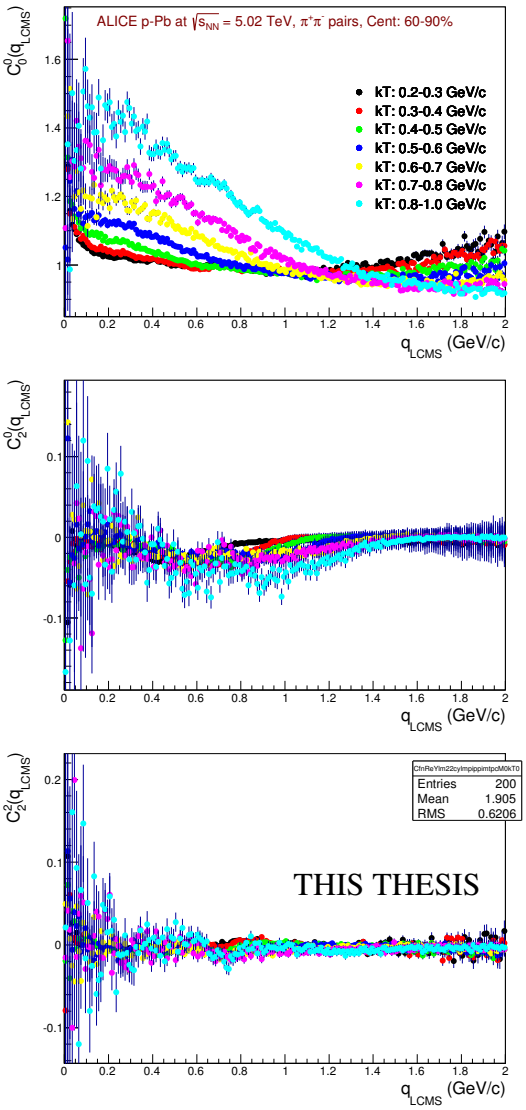

Figure B.3: Three non-vanishing spherical harmonic components of the correlation functions for $\pi^+\pi^-$ pairs for 60–80% V0A multiplicity class and seven pair transverse momentum k_T ranges.

Appendix C

Angular correlation in $\Delta\eta\Delta\varphi$ space

Another way of looking at two-particle correlations is the representation of the correlation function in relative pseudorapidity $\Delta\eta = \eta_1 - \eta_2$ and azimuthal angle $\Delta\varphi = \varphi_1 - \varphi_2$ space. The $\Delta\eta\Delta\varphi$ correlation function also commonly referred to as angular correlation. It is important to note that these type of correlations are sensitive to the same correlation sources that are present in femtoscopy, only the representation is different. Untriggered $\Delta\eta\Delta\varphi$ correlations in pp collisions at $\sqrt{s} = 7$ TeV in ALICE, for unidentified and identified particles, have been extensively studied by us, for details see Refs. [122, 123, 298, 299].

The angular correlations open up the possibility to study different physics mechanisms at the same time, i.e: minijets, elliptic flow, Bose-Einstein correlations, resonance decays etc. Each of these effects is a manifestation of a distinct correlation source and produces a unique distribution in $\Delta\eta\Delta\varphi$ space. The obtained result is a combination of all of them and the influence of all of these effects on $\Delta\eta\Delta\varphi$ correlation function can be seen in Fig. C.1. The study of untriggered non-identified particles in pp collisions has been performed in order to decompose the experimental correlation function and quantify the contribution of each of the correlation sources [122, 298]. The results of the analysis of triggered angular correlations in p–Pb collisions at $\sqrt{s_{\mathrm{NN}}} = 5.02$ TeV and Pb–Pb collisions at $\sqrt{s_{\mathrm{NN}}} = 2.76$ TeV have been reported by the ALICE Collaboration in Ref. [300] and Ref. [132]. Similar studies were also performed for pp and heavy-ion systems by other experiments at LHC and RHIC, for details see Refs. [130, 131, 133, 301–303].

The angular correlations analysis can be performed also for identified particles (pions, kaons and protons – each of them having a different quark content and flavor), where the main goal is to complement the results from the studies of non-identified particles. It is especially important because in addition to the correlation sources mentioned above, we expect also the conservation laws to play a relatively significant role in the determination of the shape of the $\Delta\eta\Delta\varphi$ correlation

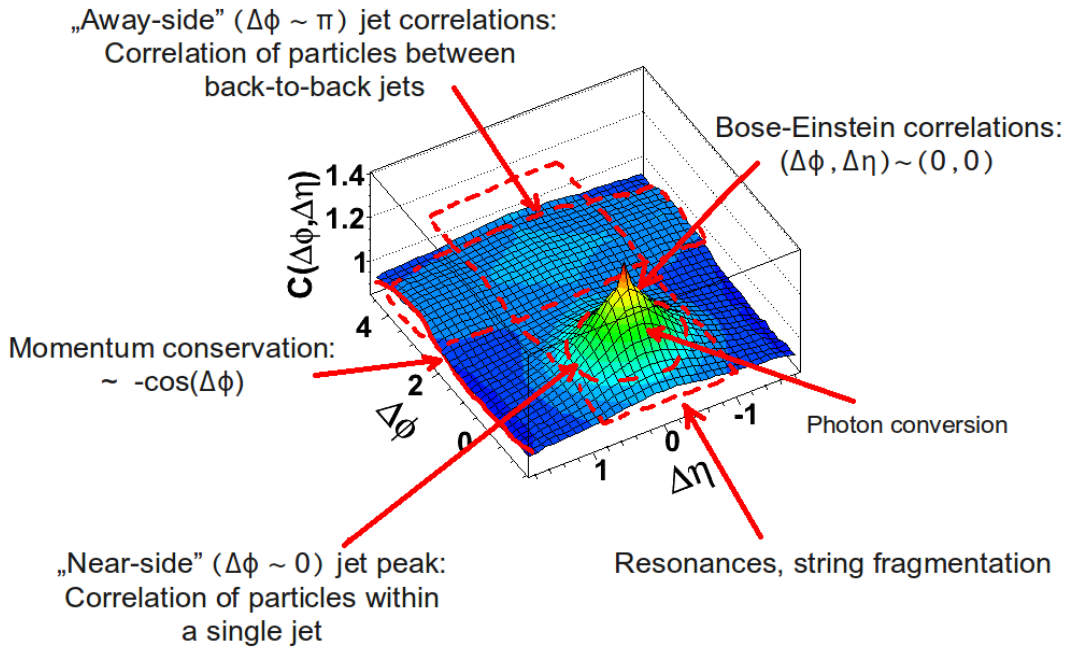

Figure C.1: Contributions from different correlation sources to the $\Delta\eta\Delta\varphi$ correlation function for like-sign particle pairs ($\sqrt{s}$ = 7 TeV pp collision data).

function. Moreover, the comparison of measured correlation functions with the ones obtained from Monte Carlo event generators can be useful for the correct implementation of conservation laws in the models. For details of the motivation and results of analysis of correlations identified particles see Ref. [123] and Ref. [299]

Figures C.2 and C.3 show $\Delta\eta\Delta\varphi$ like- and unlike-sign pion correlation functions for four analyzed V0A multiplicity classes from p–Pb collision data. We must note that these correlation function have not been corrected for purity and inefficiencies, which in the case of angular correlations have significant effect (though the lowest for pions). However, from these uncorrected correlation functions we can clearly see that the shapes both for like- and unlike-sign pairs and the decrease of the correlation with increasing multiplicity is consistent with the results obtained in pp analysis.

Studies of untriggered angular correlations in p–Pb collisions, both for unidentified and identified particles, require future work.

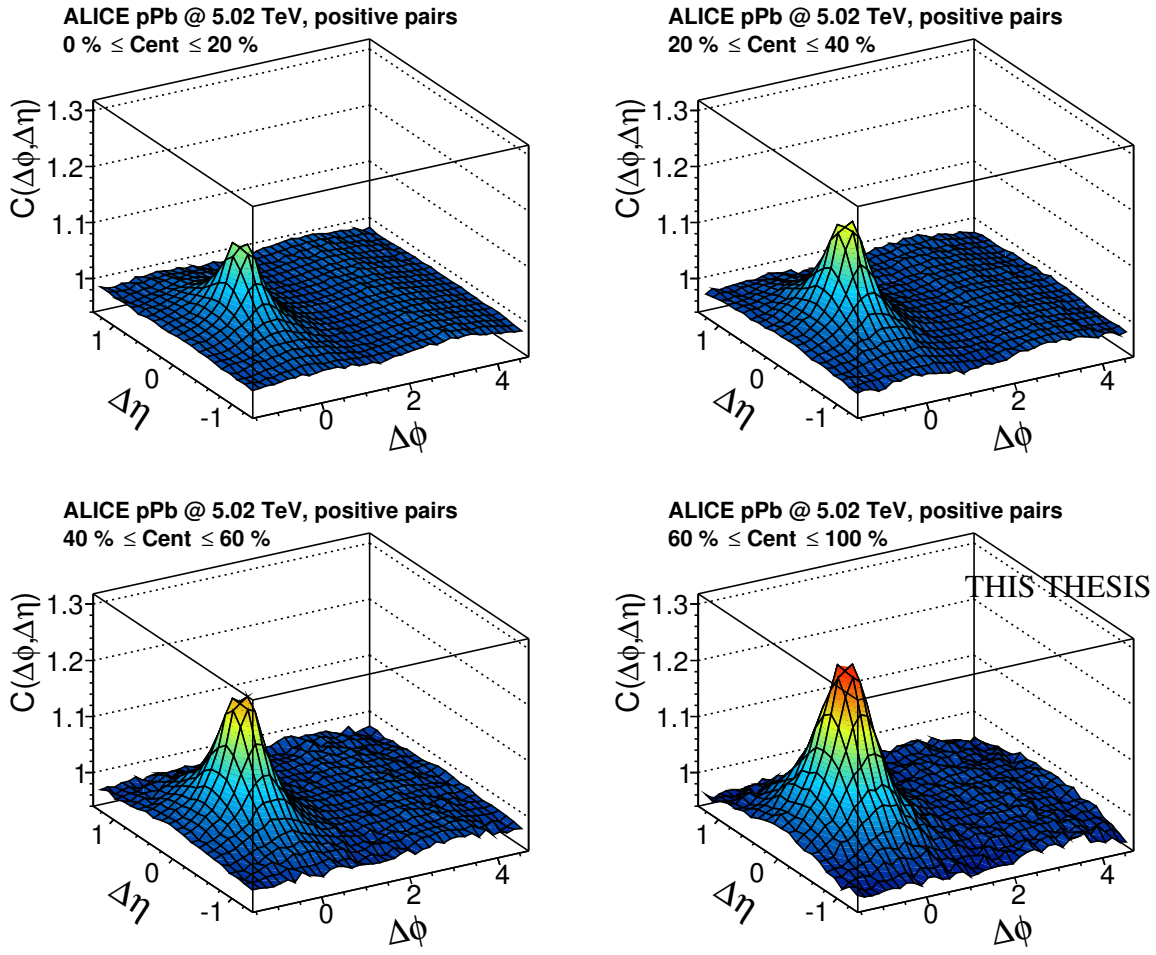

Figure C.2: $\Delta\eta\Delta\varphi$ like-sign pion correlation functions for ALICE p–Pb collision data for four V0A multiplicity classes.

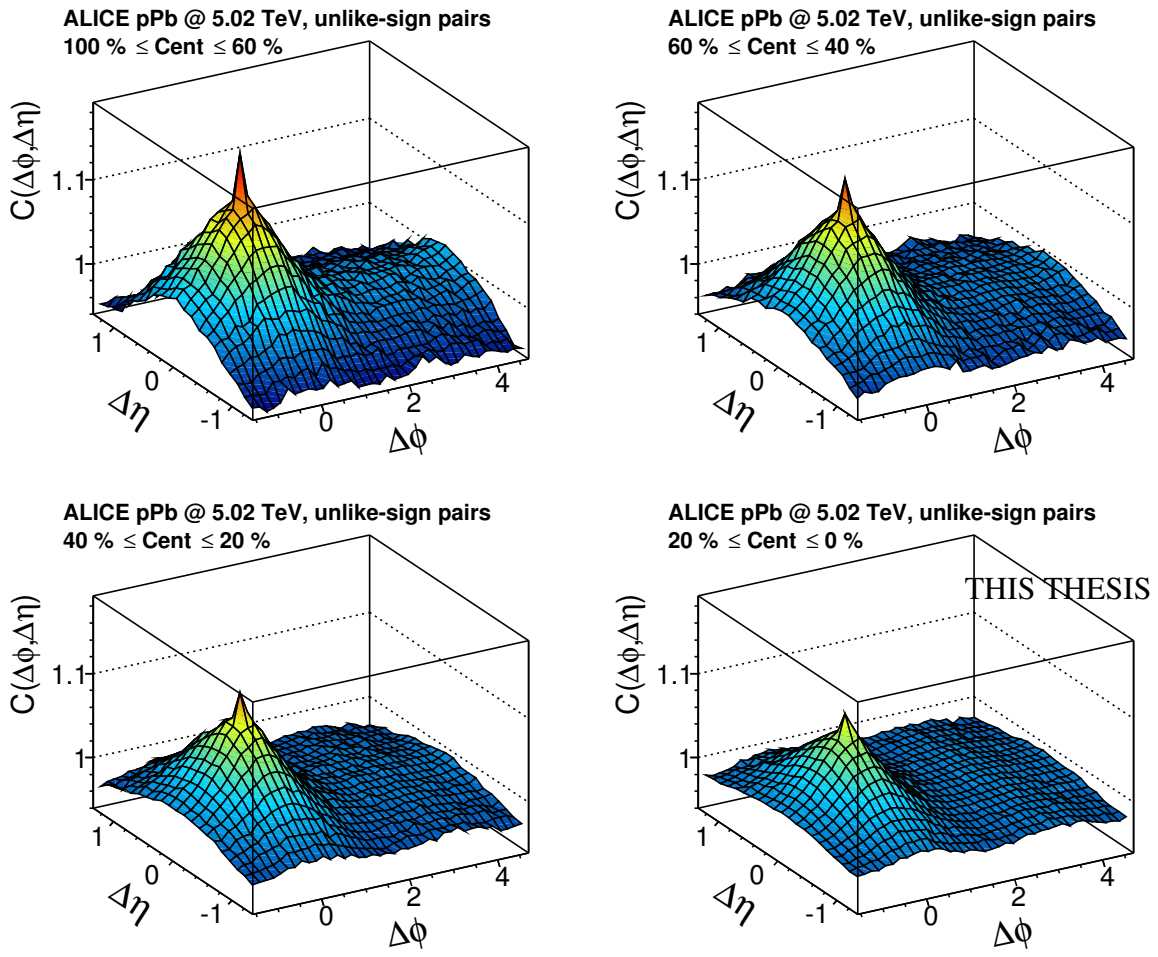

Figure C.3: $\Delta\eta\Delta\varphi$ unlike-sign pion correlation functions for ALICE p–Pb collision data for four V0A multiplicity classes.

Bibliography

[1] L. K. Graczykowski, A. Kisiel, M. A. Janik, and P. Karczmarczyk, *Extracting femtoscopic radii in the presence of significant additional correlation sources*, Acta Phys.Polon., vol. B45, pp. 1993–2009, 2014.

[2] J. Adam *et al.*, (ALICE), *Two-pion femtoscopy in p–Pb collisions at* $\sqrt{s_{\rm NN}} = 5.02$ *TeV* , Phys. Rev., vol. C91, p. 034906, 2015.

[3] L. K. Graczykowski, *Pion femtoscopy measurements in small systems with ALICE at the LHC*, poster presented at the Quark Matter 2014 conference, May 2014.

[4] D. R. Gangadharan, *Freeze-out radii extracted using two- and three-pion Bose–Einstein correlations in pp, p–Pb, and Pb–Pb collisions at the LHC*, Nucl.Phys., vol. A931, pp. 1066–1071, 2014, DOI: 10.1016/j.nuclphysa.2014.08.098.

[5] G. Aad *et al.*, (ATLAS Collaboration), *Observation of a new particle in the search for the Standard Model Higgs boson with the ATLAS detector at the LHC*, Phys.Lett., vol. B716, pp. 1–29, 2012.

[6] S. Chatrchyan *et al.*, (CMS Collaboration), *Observation of a new boson at a mass of 125 GeV with the CMS experiment at the LHC*, Phys.Lett., vol. B716, pp. 30–61, 2012.

[7] R. Aaij *et al.*, (LHCb collaboration), *Observation of the resonant character of the* $Z(4430)^-$ *state*, Phys.Rev.Lett., vol. 112, p. 222002, 2014.

[8] F. Englert and R. Brout, *Broken Symmetry and the Mass of Gauge Vector Mesons*, Phys.Rev.Lett., vol. 13, pp. 321–323, 1964.

[9] P. W. Higgs, *Broken Symmetries and the Masses of Gauge Bosons*, Phys.Rev.Lett., vol. 13, pp. 508–509, 1964.

[10] G. Guralnik, C. Hagen, and T. Kibble, *Global Conservation Laws and Massless Particles*, Phys.Rev.Lett., vol. 13, pp. 585–587, 1964.

[11] *Wikipedia - The Free Encyclopedia*, http://en.wikimedia.org.

[12] M. Gell-Mann, *A Schematic Model of Baryons and Mesons*, Phys.Lett., vol. 8, pp. 214–215, 1964.

[13] G. Zweig, *An SU(3) model for strong interaction symmetry and its breaking. Version 2*, CERN-TH-412, NP-14146, PRINT-64-170, pp. 22–101, 1964.

[14] G. Zweig, *An SU(3) model for strong interaction symmetry and its breaking. Version 1*, CERN-TH-401, 1964.

[15] O. Greenberg, *Spin and Unitary Spin Independence in a Paraquark Model of Baryons and Mesons*, Phys.Rev.Lett., vol. 13, pp. 598–602, 1964.

[16] M. Han and Y. Nambu, *Three Triplet Model with Double SU(3) Symmetry*, Phys.Rev., vol. 139, pp. B1006–B1010, 1965.

[17] W. Florkowski, *Phenomenology of Ultra-Relativistic Heavy-Ion Collisions*. World Scientific, Singapore, 2010.

[18] J. Bartke, *Introduction to relativistic heavy ion physics*. World Scientific, Singapore, 2009.

[19] C. Amsler *et al.*, (Particle Data Group), *Review of Particle Physics*, Phys.Lett., vol. B667, pp. 1–1340, 2008.

[20] D. J. Gross and F. Wilczek, *Ultraviolet Behavior of Nonabelian Gauge Theories*, Phys.Rev.Lett., vol. 30, pp. 1343–1346, 1973.

[21] H. D. Politzer, *Reliable Perturbative Results for Strong Interactions?*, Phys.Rev.Lett., vol. 30, pp. 1346–1349, 1973.

[22] G. S. Bali, *QCD forces and heavy quark bound states*, Phys.Rept., vol. 343, pp. 1–136, 2001.

[23] *Forschungszentrum Juelich*, http://www.fz-juelich.de/.

[24] K. Brinkmann, P. Gianotti, and I. Lehmann, *Exploring the mysteries of strong interactions: The PANDA experiment*, Nucl.Phys.News, vol. 16, pp. 15–18, 2006.

[25] J. M. Maldacena, *The Large N limit of superconformal field theories and supergravity*, Int.J.Theor.Phys., vol. 38, pp. 1113–1133, 1999.

[26] J. Casalderrey-Solana, H. Liu, D. Mateos, K. Rajagopal, and U. A. Wiedemann, *Gauge/String Duality, Hot QCD and Heavy Ion Collisions*. Cambridge University Press, Cambridge, 2014.

[27] Z. Merali, *String theory finds a bench mate*, Nature, vol. 478, pp. 302–304, 2011.

[28] M. Luzum and P. Romatschke, *Conformal Relativistic Viscous Hydrodynamics: Applications to RHIC results at* $\sqrt{s_{\rm NN}} = 200$ *GeV*, Phys.Rev., vol. C78, p. 034915, 2008.

[29] H. H. Dalsgaard, *Pseudorapidity Densities in p+p and Pb+Pb collisions at LHC measured with the ALICE experiment*, CERN-THESIS-2011-241.

[30] H. Satz, *Color deconfinement in nuclear collisions*, Rept.Prog.Phys., vol. 63, p. 1511, 2000.

[31] A. Andronic and P. Braun-Munzinger, *Ultrarelativistic nucleus-nucleus collisions and the quark gluon plasma*, Lect.Notes Phys., vol. 652, pp. 35–67, 2004.

[32] F. Karsch, *Lattice QCD at high temperature and density*, Lect.Notes Phys., vol. 583, pp. 209–249, 2002.

[33] F. Karsch, *Lattice results on QCD thermodynamics*, Nucl.Phys., vol. A698, pp. 199–208, 2002.

[34] E. Fermi, *High-energy nuclear events*, Prog.Theor.Phys., vol. 5, pp. 570–583, 1950.

[35] L. Landau, *On the multiparticle production in high-energy collisions*, Izv.Akad.Nauk Ser.Fiz., vol. 17, pp. 51–64, 1953.

[36] J. Bjorken, *Highly Relativistic Nucleus-Nucleus Collisions: The Central Rapidity Region*, Phys.Rev., vol. D27, pp. 140–151, 1983.

[37] M. Kliemant, R. Sahoo, T. Schuster, and R. Stock, *Global Properties of Nucleus-Nucleus Collisions*, Lect.Notes Phys., vol. 785, pp. 23–103, 2010.

[38] P. Ade *et al.*, (Planck Collaboration), *Planck 2013 results. XVI. Cosmological parameters*, Astron.Astrophys., 2014.

[39] A. A. Penzias and R. W. Wilson, *A Measurement of excess antenna temperature at 4080-Mc/s*, Astrophys.J., vol. 142, pp. 419–421, 1965.

[40] A. Bialas, M. Bleszynski, and W. Czyz, *Multiplicity Distributions in Nucleus-Nucleus Collisions at High-Energies*, Nucl.Phys., vol. B111, p. 461, 1976.

[41] A. Bialas, M. Bleszynski, and W. Czyz, *Relation Between the Glauber Model and Classical Probability Calculus*, Acta Phys.Polon., vol. B8, pp. 389–392, 1977.

[42] T. Ludlam, A. Pfoh, and A. Shor, *HIJET. A Monte Carlo event generator for p–nucleus and nucleus–nucleus collisions*, BNL-37196, 1986.

[43] A. Shor and R. S. Longacre, *Effects of Secondary Interactions in Proton – Nucleus and Nucleus-nucleus Collisions Using the Hijet Event Generator*, Phys.Lett., vol. B218, p. 100, 1989.

[44] M. L. Miller, K. Reygers, S. J. Sanders, and P. Steinberg, *Glauber modeling in high energy nuclear collisions*, Ann.Rev.Nucl.Part.Sci., vol. 57, pp. 205–243, 2007.

[45] X.-N. Wang and M. Gyulassy, *HIJING: A Monte Carlo model for multiple jet production in p p, p A and A A collisions*, Phys.Rev., vol. D44, pp. 3501–3516, 1991.

[46] Z.-W. Lin, C. M. Ko, B.-A. Li, B. Zhang, and S. Pal, *A Multi-phase transport model for relativistic heavy ion collisions*, Phys.Rev., vol. C72, p. 064901, 2005.

[47] S. Roesler, R. Engel, and J. Ranft, *The Monte Carlo event generator DPMJET-III*, SLAC-PUB-8740, pp. 1033–1038, 2000.

[48] W. Broniowski, M. Rybczynski, and P. Bozek, *GLISSANDO: Glauber initial-state simulation and more..*, Comput.Phys.Commun., vol. 180, pp. 69–83, 2009.

[49] L. D. McLerran, *The Color Glass Condensate and small x physics: Four lectures*, Lect.Notes Phys., vol. 583, pp. 291–334, 2002.

[50] M. Gyulassy and L. McLerran, *New forms of QCD matter discovered at RHIC*, Nucl.Phys., vol. A750, pp. 30–63, 2005.

[51] J. Breitweg *et al.*, (ZEUS Collaboration), *ZEUS results on the measurement and phenomenology of F(2) at low x and low* Q^2, Eur.Phys.J., vol. C7, pp. 609–630, 1999.

[52] K. Dusling and R. Venugopalan, *Comparison of the color glass condensate to dihadron correlations in proton-proton and proton-nucleus collisions*, Phys.Rev., vol. D87, no. 9, p. 094034, 2013.

[53] A. Bzdak, B. Schenke, P. Tribedy, and R. Venugopalan, *Initial state geometry and the role of hydrodynamics in proton-proton, proton-nucleus and deuteron-nucleus collisions*, Phys.Rev., vol. C87, no. 6, p. 064906, 2013.

[54] J. Adams *et al.*, (STAR Collaboration), *Experimental and theoretical challenges in the search for the quark gluon plasma: The STAR Collaboration's critical assessment of the evidence from RHIC collisions*, Nucl.Phys., vol. A757, pp. 102–183, 2005.

[55] K. Adcox *et al.*, (PHENIX Collaboration), *Formation of dense partonic matter in relativistic nucleus-nucleus collisions at RHIC: Experimental evaluation by the PHENIX collaboration*, Nucl.Phys., vol. A757, pp. 184–283, 2005.

[56] B. Back, M. Baker, M. Ballintijn, D. Barton, B. Becker, *et al.*, *The PHOBOS perspective on discoveries at RHIC*, Nucl.Phys., vol. A757, pp. 28–101, 2005.

[57] I. Arsene *et al.*, (BRAHMS Collaboration), *Quark gluon plasma and color glass condensate at RHIC? The Perspective from the BRAHMS experiment*, Nucl.Phys., vol. A757, pp. 1–27, 2005.

[58] M. Krzewicki, (ALICE Collaboration), *Elliptic and triangular flow of identified particles at ALICE*, J.Phys., vol. G38, p. 124047, 2011.

[59] K. Aamodt *et al.*, (ALICE Collaboration), *Elliptic flow of charged particles in Pb-Pb collisions at 2.76 TeV*, Phys.Rev.Lett., vol. 105, p. 252302, 2010.

[60] K. Aamodt *et al.*, (ALICE Collaboration), *Centrality dependence of the charged-particle multiplicity density at mid-rapidity in Pb–Pb collisions at* $\sqrt{s_{\mathrm{NN}}} = 2.76$ *TeV*, Phys.Rev.Lett., vol. 106, p. 032301, 2011.

[61] J.-Y. Ollitrault, *Relativistic hydrodynamics for heavy-ion collisions*, Eur.J.Phys., vol. 29, pp. 275–302, 2008.

[62] P. Romatschke, *New Developments in Relativistic Viscous Hydrodynamics*, Int.J.Mod.Phys., vol. E19, pp. 1–53, 2010.

[63] C. Gale, S. Jeon, and B. Schenke, *Hydrodynamic Modeling of Heavy-Ion Collisions*, Int.J.Mod.Phys., vol. A28, p. 1340011, 2013.

[64] N. Brambilla, S. Eidelman, P. Foka, S. Gardner, A. Kronfeld, *et al.*, *QCD and Strongly Coupled Gauge Theories: Challenges and Perspectives*, Eur.Phys.J., vol. C74, no. 10, p. 2981, 2014.

[65] C. Wong, *Introduction to high-energy heavy ion collisions*. World Scientific, Singapore, 1994.

[66] J. W. Harris and B. Muller, *The Search for the quark - gluon plasma*, Ann.Rev.Nucl.Part.Sci., vol. 46, pp. 71–107, 1996.

[67] A. Datta, B. Mukhopadhyaya, and A. Raychaudhuri, *Physics at the Large Hadron Collider*. Springer, New Delhi, 2009.

[68] K. Aamodt *et al.*, (ALICE Collaboration), *Two-pion Bose-Einstein correlations in central Pb-Pb collisions at* $\sqrt{s_{\rm NN}} = 2.76$ *TeV*, Phys.Lett., vol. B696, pp. 328–337, 2011.

[69] R. Snellings, *Elliptic Flow: A Brief Review*, New J.Phys., vol. 13, p. 055008, 2011.

[70] J.-Y. Ollitrault, *Anisotropy as a signature of transverse collective flow*, Phys.Rev., vol. D46, pp. 229–245, 1992.

[71] S. A. Voloshin, A. M. Poskanzer, and R. Snellings, *Collective phenomena in non-central nuclear collisions*, in Landolt – Boernstein, Relativistic Heavy Ion Physics, vol. 1/23. Springer-Verlag, Berlin, 2008.

[72] P. F. Kolb and U. W. Heinz, *Hydrodynamic description of ultrarelativistic heavy ion collisions*, SUNY-NTG-03-06, 2003.

[73] Y. Schutz and U. A. Wiedemann, *Quark matter. Proceedings, 22nd International Conference on Ultra-Relativistic Nucleus-Nucleus Collisions, Quark Matter 2011, Annecy, France, May 23-28, 2011*, J.Phys., vol. G38, p. 120301, 2011.

[74] G.-Y. Qin, H. Petersen, S. A. Bass, and B. Muller, *Translation of collision geometry fluctuations into momentum anisotropies in relativistic heavy-ion collisions*, Phys.Rev., vol. C82, p. 064903, 2010.

[75] J. Jia, *ATLAS v_n results*, Quark Matter 2011 plenary talk.

[76] J. Adams *et al.*, (STAR Collaboration), *Particle type dependence of azimuthal anisotropy and nuclear modification of particle production in Au + Au collisions at* $\sqrt{s} = 200$ *GeV*, Phys.Rev.Lett., vol. 92, p. 052302, 2004.

[77] B. Abelev *et al.*, (STAR Collaboration), *Mass, quark-number, and* $\sqrt{s_{NN}}$ *dependence of the second and fourth flow harmonics in ultra-relativistic nucleus-nucleus collisions*, Phys.Rev., vol. C75, p. 054906, 2007.

[78] S. Adler *et al.*, (PHENIX Collaboration), *Elliptic flow of identified hadrons in Au+Au collisions at* $\sqrt{s_{NN}} = 200$ *GeV*, Phys.Rev.Lett., vol. 91, p. 182301, 2003.

[79] S. Afanasiev *et al.*, (PHENIX Collaboration), *Elliptic flow for phi mesons and (anti)deuterons in Au + Au collisions at* $\sqrt{s_{NN}} = 200$ *GeV*, Phys.Rev.Lett., vol. 99, p. 052301, 2007.

[80] A. Adare *et al.*, (PHENIX Collaboration), *Scaling properties of azimuthal anisotropy in Au+Au and Cu+Cu collisions at* $\sqrt{s_{NN}} = 200$ *GeV*, Phys.Rev.Lett., vol. 98, p. 162301, 2007.

[81] D. Molnar and S. A. Voloshin, *Elliptic flow at large transverse momenta from quark coalescence*, Phys.Rev.Lett., vol. 91, p. 092301, 2003.

[82] V. Greco, C. Ko, and P. Levai, *Parton coalescence at RHIC*, Phys.Rev., vol. C68, p. 034904, 2003.

[83] R. Fries, B. Muller, C. Nonaka, and S. Bass, *Hadron production in heavy ion collisions: Fragmentation and recombination from a dense parton phase*, Phys.Rev., vol. C68, p. 044902, 2003.

[84] R. C. Hwa and C. Yang, *Recombination of shower partons in fragmentation processes*, Phys.Rev., vol. C70, p. 024904, 2004.

[85] B. B. Abelev *et al.*, (ALICE Collaboration), *Elliptic flow of identified hadrons in Pb-Pb collisions at* $\sqrt{s_{\mathrm{NN}}} = 2.76$ *TeV*, arXiv: 1405.4632 [nucl-ex], 2014.

[86] J. Harris, *Exploring the Quark-Gluon Plasma at RHIC and LHC - Today's Perspective*, Frascati Physics Series, vol. XLVI, 2007.

[87] A. Andronic, P. Braun-Munzinger, K. Redlich, and J. Stachel, *The thermal model on the verge of the ultimate test: particle production in Pb–Pb collisions at the LHC*, J.Phys., vol. G38, p. 124081, 2011.

[88] A. Andronic, P. Braun-Munzinger, and J. Stachel, *Thermal hadron production in relativistic nuclear collisions: The Hadron mass spectrum, the horn, and the QCD phase transition*, Phys.Lett., vol. B673, pp. 142–145, 2009.

[89] J. Cleymans and K. Redlich, *Unified description of freezeout parameters in relativistic heavy ion collisions*, Phys.Rev.Lett., vol. 81, pp. 5284–5286, 1998.

[90] A. Andronic, P. Braun-Munzinger, and J. Stachel, *Hadron production in central nucleus–nucleus collisions at chemical freeze-out*, Nucl.Phys., vol. A772, pp. 167–199, 2006.

[91] R. Rapp and E. V. Shuryak, *Resolving the anti-baryon production puzzle in high-energy heavy ion collisions*, Phys.Rev.Lett., vol. 86, pp. 2980–2983, 2001.

[92] C. Greiner and S. Leupold, *Anti-hyperon production in relativistic heavy ion collision*, J.Phys., vol. G27, pp. L95–L102, 2001.

[93] P. Braun-Munzinger, J. Stachel, and C. Wetterich, *Chemical freezeout and the QCD phase transition temperature*, Phys.Lett., vol. B596, pp. 61–69, 2004.

[94] P. Huovinen and P. Ruuskanen, *Hydrodynamic Models for Heavy Ion Collisions*, Ann.Rev.Nucl.Part.Sci., vol. 56, pp. 163–206, 2006.

[95] E. Schnedermann, J. Sollfrank, and U. W. Heinz, *Thermal phenomenology of hadrons from 200* A/GeV *S+S collisions*, Phys.Rev., vol. C48, pp. 2462–2475, 1993.

[96] U. W. Heinz, *Concepts of heavy ion physics*, CERN-2004-001-D, pp. 165–238, 2004.

[97] J. Cleymans, I. Kraus, H. Oeschler, K. Redlich, and S. Wheaton, *Statistical model predictions for particle ratios at* $\sqrt{s_{\mathrm{NN}}} = 5.5$ *TeV*, Phys.Rev., vol. C74, p. 034903, 2006.

[98] B. Abelev *et al.*, (ALICE Collaboration), *Pion, Kaon, and Proton Production in Central Pb–Pb Collisions at* $\sqrt{s_{\rm NN}}$ = 2.76 *GeV*, Phys.Rev.Lett., vol. 109, p. 252301, 2012.

[99] B. Abelev *et al.*, (STAR Collaboration), *Systematic Measurements of Identified Particle Spectra in pp, d+Au and Au+Au Collisions from STAR*, Phys.Rev., vol. C79, p. 034909, 2009.

[100] S. Adler *et al.*, (PHENIX Collaboration), *Identified charged particle spectra and yields in Au+Au collisions at* $\sqrt{s_{\rm NN}}$ = 200 *GeV*, Phys.Rev., vol. C69, p. 034909, 2004.

[101] C. Shen, U. Heinz, P. Huovinen, and H. Song, *Radial and elliptic flow in Pb+Pb collisions at the Large Hadron Collider from viscous hydrodynamic*, Phys.Rev., vol. C84, p. 044903, 2011.

[102] Y. Karpenko and Y. Sinyukov, *Femtoscopic scales in central A+A collisions at RHIC and LHC energies in hydrokinetic model*, J.Phys., vol. G38, p. 124059, 2011.

[103] I. Karpenko, Y. Sinyukov, and K. Werner, *Uniform description of bulk observables in hydrokinetic model of A+A collisions at RHIC and LHC*, Phys.Rev., vol. C87, p. 024914, 2013.

[104] S. Bass, M. Belkacem, M. Bleicher, M. Brandstetter, L. Bravina, *et al.*, *Microscopic models for ultrarelativistic heavy ion collisions*, Prog.Part.Nucl.Phys., vol. 41, pp. 255–369, 1998.

[105] M. Bleicher, E. Zabrodin, C. Spieles, S. Bass, C. Ernst, *et al.*, *Relativistic hadron hadron collisions in the ultrarelativistic quantum molecular dynamics model*, J.Phys., vol. G25, pp. 1859–1896, 1999.

[106] J. Steinheimer, J. Aichelin, and M. Bleicher, *Non-thermal* p/π *ratio at LHC as a consequence of hadronic final state interactions*, Phys.Rev.Lett., vol. 110, p. 042501, 2013.

[107] P. Bozek, *Flow and interferometry in 3+1 dimensional viscous hydrodynamics*, Phys.Rev., vol. C85, p. 034901, 2012.

[108] P. Bozek, *Hydrodynamic flow from RHIC to LHC*, Acta Phys.Polon., vol. B43, p. 689, 2012.

[109] C. Salgado, J. Alvarez-Muniz, F. Arleo, N. Armesto, M. Botje, *et al.*, *Proton-Nucleus Collisions at the LHC: Scientific Opportunities and Requirements*, J.Phys., vol. G39, p. 015010, 2012.

[110] B. Abelev *et al.*, (ALICE Collaboration), *Pseudorapidity density of charged particles p-Pb collisions at* $\sqrt{s_{\rm NN}}$ = 5.02 *TeV*, Phys.Rev.Lett., vol. 110, p. 032301, 2013.

[111] A. Dumitru, D. E. Kharzeev, E. M. Levin, and Y. Nara, *Gluon Saturation in pA Collisions at the LHC: KLN Model Predictions For Hadron Multiplicities*, Phys.Rev., vol. C85, p. 044920, 2012.

[112] G. Barnafoldi, J. Barrette, M. Gyulassy, P. Levai, and V. Topor Pop, *Predictions for p+Pb at 4.4A TeV to Test Initial State Nuclear Shadowing at energies available at the CERN Large Hadron Collider*, Phys.Rev., vol. C85, p. 024903, 2012.

[113] P. Tribedy and R. Venugopalan, *QCD saturation at the LHC: comparisons of models to p+p and A+A data and predictions for p+Pb collisions*, Phys.Lett., vol. B710, pp. 125–133, 2012.

[114] J. L. Albacete, A. Dumitru, H. Fujii, and Y. Nara, *CGC predictions for p+Pb collisions at the LHC*, Nucl.Phys., vol. A897, pp. 1–27, 2013.

[115] R. Xu, W.-T. Deng, and X.-N. Wang, *Nuclear modification of high-*$p_{\rm T}$ *hadron spectra in p+A collisions at LHC*, Phys.Rev., vol. C86, p. 051901, 2012.

[116] B. Back *et al.*, (PHOBOS Collaboration), *Pseudorapidity distribution of charged particles in d + Au collisions at* $\sqrt{s_{\rm NN}}$ = 200 *GeV*, Phys.Rev.Lett., vol. 93, p. 082301, 2004.

[117] B. Alver *et al.*, (PHOBOS Collaboration), *Phobos results on charged particle multiplicity and pseudorapidity distributions in Au+Au, Cu+Cu, d+Au, and p+p collisions at ultra-relativistic energies*, Phys.Rev., vol. C83, p. 024913, 2011.

[118] S. Chatrchyan *et al.*, (CMS Collaboration), *Study of the production of charged pions, kaons, and protons in pPb collisions at* $\sqrt{s_{\rm NN}}$ = 5.02 *TeV*, Eur.Phys.J., vol. C74, p. 2847, 2014.

[119] B. B. Abelev *et al.*, (ALICE Collaboration), *Multiplicity Dependence of Pion, Kaon, Proton and Lambda Production in p-Pb Collisions at* $\sqrt{s_{\rm NN}}$ = 5.02 *TeV*, Phys.Lett., vol. B728, pp. 25–38, 2014.

[120] T. Pierog, I. Karpenko, J. Katzy, E. Yatsenko, and K. Werner, *EPOS LHC: test of collective hadronization with LHC data*, DESY-13-125, 2013.

[121] P. Bozek, *Collective flow in p-Pb and d-Pb collisions at TeV energies*, Phys.Rev., vol. C85, p. 014911, 2012.

[122] M. Janik, *Two-particle angular correlations in pp collisions recorded with the ALICE detector at the LHC*, EPJ Web Conf., vol. 71, p. 00058, 2014.

[123] L. K. Graczykowski and M. A. Janik, *Angular correlations measured in pp collisions by ALICE at the LHC*, Nucl.Phys., vol. A926, pp. 205–212, 2014.

[124] U. Heinz and R. Snellings, *Collective flow and viscosity in relativistic heavy-ion collisions*, Ann.Rev.Nucl.Part.Sci., vol. 63, pp. 123–151, 2013.

[125] C. Andrés, A. Moscoso, and C. Pajares, *Onset of the ridge structure in AA, pA , and pp collisions*, Phys.Rev., vol. C90, no. 5, p. 054902, 2014.

[126] M. Braun, C. Pajares, and V. Vechernin, *Ridge from Strings*, arXiv: 1407.4590 [hep-ph], 2014.

[127] W. Li, *Observation of a 'Ridge' correlation structure in high multiplicity proton-proton collisions: A brief review*, Mod.Phys.Lett., vol. A27, p. 1230018, 2012.

[128] R. Venugopalan, *Long range correlations in high multiplicity hadron collisions: Building bridges with ridges*, Annals Phys., 2014.

[129] L. De Silva, $\Delta\eta$-$\Delta\varphi$ *correlations and the ridge structure in STAR*, J.Phys.Conf.Ser., vol. 389, p. 012039, 2012.

[130] V. Khachatryan *et al.*, (CMS Collaboration), *Observation of Long-Range Near-Side Angular Correlations in Proton-Proton Collisions at the LHC*, JHEP, vol. 1009, p. 091, 2010.

[131] S. Chatrchyan *et al.*, (CMS Collaboration), *Observation of long-range near-side angular correlations in proton-lead collisions at the LHC*, Phys.Lett., vol. B718, pp. 795–814, 2013.

[132] B. Abelev *et al.*, (ALICE Collaboration), *Long-range angular correlations on the near and away side in p-Pb collisions at* $\sqrt{s_{\rm NN}}$ = 5.02 *TeV*, Phys.Lett., vol. B719, pp. 29–41, 2013.

[133] G. Aad *et al.*, (ATLAS Collaboration), *Observation of Associated Near-Side and Away-Side Long-Range Correlations in* $\sqrt{s_{\rm NN}}$ = 5.02 *TeV Proton-Lead Collisions with the ATLAS Detector*, Phys.Rev.Lett., vol. 110, no. 18, p. 182302, 2013.

[134] A. Adare *et al.*, (PHENIX Collaboration), *Quadrupole Anisotropy in Dihadron Azimuthal Correlations in Central d + Au Collisions at* $\sqrt{s_{\rm NN}}$ = 200 *GeV*, Phys.Rev.Lett., vol. 111, no. 21, p. 212301, 2013.

[135] A. Bilandzic, R. Snellings, and S. Voloshin, *Flow analysis with cumulants: Direct calculations*, Phys.Rev., vol. C83, p. 044913, 2011.

[136] S. Chatrchyan *et al.*, (CMS Collaboration), *Multiplicity and transverse momentum dependence of two- and four-particle correlations in pPb and PbPb collisions*, Phys.Lett., vol. B724, pp. 213–240, 2013.

[137] G. Aad *et al.*, (ATLAS Collaboration), *Measurement with the ATLAS detector of multi-particle azimuthal correlations in p+Pb collisions at sqrt*$s_{\rm NN}$ = 5.02 *TeV*, Phys.Lett., vol. B725, pp. 60–78, 2013.

[138] K. Dusling and R. Venugopalan, *Explanation of systematics of CMS p+Pb high multiplicity di-hadron data at* $\sqrt{s_{\rm NN}}$ = 5.02 *TeV*, Phys.Rev., vol. D87, no. 5, p. 054014, 2013.

[139] P. Bozek and W. Broniowski, *Correlations from hydrodynamic flow in p-Pb collisions*, Phys.Lett., vol. B718, pp. 1557–1561, 2013.

[140] P. Bozek and W. Broniowski, *Collective dynamics in high-energy proton-nucleus collisions*, Phys.Rev., vol. C88, no. 1, p. 014903, 2013.

[141] G.-Y. Qin and B. Müller, *Elliptic and triangular flow anisotropy in deuteron-gold collisions at* $\sqrt{s_{\rm NN}} = 200$ *GeV at RHIC and in proton-lead collisions at* $\sqrt{s_{\rm NN}} = 5.02$ *TeV at the LHC*, Phys.Rev., vol. C89, no. 4, p. 044902, 2014.

[142] C. E. Coleman-Smith and B. Müller, *Mapping the proton's fluctuating size and shape*, Phys.Rev., vol. D89, no. 2, p. 025019, 2014.

[143] G. Basar and D. Teaney, *A scaling relation between pA and AA collisions*, Phys.Rev., vol. C90, p. 054903, 2014.

[144] T. Sjostrand, S. Mrenna, and P. Z. Skands, *PYTHIA 6.4 Physics and Manual*, JHEP, vol. 0605, p. 026, 2006.

[145] P. Z. Skands, *Tuning Monte Carlo Generators: The Perugia Tunes*, Phys.Rev., vol. D82, p. 074018, 2010.

[146] K. Werner, B. Guiot, I. Karpenko, and T. Pierog, *Analysing radial flow features in p–Pb and p–p collisions at several TeV by studying identified particle production in EPOS3*, Phys.Rev., vol. C89, p. 064903, 2014.

[147] K. Werner, M. Bleicher, B. Guiot, I. Karpenko, and T. Pierog, *Evidence for flow in pPb collisions at 5 TeV from v2 mass splitting*, Phys.Rev.Lett., vol. 112, p. 232301, 2014.

[148] P. Bozek and W. Broniowski, *Size of the emission source and collectivity in ultra-relativistic p–Pb collisions*, Phys.Lett., vol. B720, pp. 250–253, 2013.

[149] V. Shapoval, P. Braun-Munzinger, I. A. Karpenko, and Y. M. Sinyukov, *Femtoscopic scales in p + p and p+Pb collisions in view of the uncertainty principle*, Phys.Lett., vol. B725, pp. 139–147, 2013.

[150] L. Evans and P. Bryant, *LHC Machine*, JINST, vol. 3, p. S08001, 2008.

[151] C. Lefèvre, *The CERN accelerator complex. Complexe des accélérateurs du CERN*, http://cds.cern.ch/record/1260465, Dec 2008.

[152] K. Aamodt *et al.*, (ALICE Collaboration), *The ALICE experiment at the CERN LHC*, JINST, vol. 3, p. S08002, 2008.

[153] N. Antoniou *et al.*, (ALICE Collaboration), *Letter of Intent for A Large Ion Collider Experiment*, 1993.

[154] L. K. Graczykowski, *ALICE: the heavy-ion experiment at the CERN/LHC*, Proc. SPIE, vol. 8903, 2013.

[155] *ALICE Home Page*, http://aliceinfo.cern.ch/.

[156] G. Dellacasa *et al.*, (ALICE Collaboration), *ALICE technical design report of the inner tracking system (ITS)*, CERN-LHCC-99-12, 1999.

[157] F. Carminati *et al.*, (ALICE Collaboration), *ALICE: Physics performance report, volume I*, J.Phys., vol. G30, pp. 1517–1763, 2004.

[158] G. Dellacasa *et al.*, (ALICE Collaboration), *ALICE: Technical design report of the time projection chamber*, CERN-OPEN-2000-183, CERN-LHCC-2000-001, 2000.

[159] P. Cortese *et al.*, (ALICE Collaboration), *ALICE technical design report of the transition radiation detector (TRD)*, CERN-LHCC-2001-021, 2001.

[160] G. Dellacasa *et al.*, (ALICE Collaboration), *ALICE technical design report of the time-of-flight system (TOF)*, CERN-LHCC-2000-012, 2000.

[161] P. Cortese *et al.*, (ALICE Collaboration), *ALICE technical design report on forward detectors: FMD, T0 and V0*, CERN-LHCC-2004-025, 2004.

[162] I. Antcheva, M. Ballintijn, B. Bellenot, M. Biskup, R. Brun, *et al.*, *ROOT: A C++ framework for petabyte data storage, statistical analysis and visualization*, Comput.Phys.Commun., vol. 182, pp. 1384–1385, 2011.

[163] *Root User's Guide*, http://root.cern.ch/download/doc/ROOTUsersGuideHTML/index.html.

[164] R. Brun and F. Rademakers, *ROOT: An object oriented data analysis framework*, Nucl.Instrum.Meth., vol. A389, pp. 81–86, 1997.

[165] *ALICE code developement website*, http://aliweb.cern.ch/Offline/AliRoot/Code-Development.html.

[166] F. Carminati and A. Morsch, *Simulation in ALICE*, eConf, vol. C0303241, p. TUMT004, 2003.

[167] R. Brun *et al.*, *GEANT3 User Guide*, CERN Data Handling Division, DD/EE/84-1, 1985.

[168] S. Agostinelli *et al.*, (GEANT4), *GEANT4: A Simulation toolkit*, Nucl.Instrum.Meth., vol. A506, pp. 250–303, 2003.

[169] G. Battistoni, F. Broggi, M. Brugger, M. Campanella, M. Carboni, *et al.*, *Applications of FLUKA Monte Carlo code for nuclear and accelerator physics*, Nucl.Instrum.Meth., vol. B269, pp. 2850–2856, 2011.

[170] T. Sjostrand, *High-energy physics event generation with PYTHIA 5.7 and JETSET 7.4*, Comput.Phys.Commun., vol. 82, pp. 74–90, 1994.

[171] *AliEn website*, http://alien2.cern.ch/.

[172] *MonALISA - ALICE GRID monitoring website*, http://http://alimonitor.cern.ch/map.jsp.

[173] M. Lisa, *AliFemto - A Femtoscopic Analysis Framework for ALICE; User Guide and Reference Manual*, http://www.physics.ohio-state.edu/ lisa/AliFemtoDocumentation/UsersGuide.pdf, 2010.

[174] *AliRoot Git repository*, http://git.cern.ch/pubweb/AliRoot.git/tree.

[175] R. Hanbury Brown and R. Twiss, *A New type of interferometer for use in radio astronomy*, Phil.Mag., vol. 45, pp. 663–682, 1954.

[176] R. Hanbury Brown and R. Twiss, *A Test of a new type of stellar interferometer on Sirius*, Nature, vol. 178, pp. 1046–1048, 1956.

[177] A. Kisiel, *Studies of non-identical meson-meson correlations at low relative velocities in relativistic heavy-ion collisions registered by the STAR experiment*, Ph.D. Thesis, Warsaw University of Technology, 2003.

[178] G. Baym, *The Physics of Hanbury Brown-Twiss intensity interferometry: From stars to nuclear collisions*, Acta Phys.Polon., vol. B29, pp. 1839–1884, 1998.

[179] G. Kopylov, V. Lyuboshits, and M. Podgoretsky, *Correlations Between the Particles Which Have Small Relative Momenta*, JINR-P2-8069, 1974.

[180] R. Lednicky, *Correlation femtoscopy of multiparticle processes*, Phys.Atom.Nucl., vol. 67, pp. 72–82, 2004.

[181] A. Kisiel, *Non-identical particle femtoscopy at* $\sqrt{s_{\rm NN}} = 200$ *AGeV in hydrodynamics with statistical hadronization*, Phys.Rev., vol. C81, p. 064906, 2010.

[182] G. Goldhaber, S. Goldhaber, W.-Y. Lee, and A. Pais, *Influence of Bose-Einstein statistics on the anti-proton proton annihilation process*, Phys.Rev., vol. 120, pp. 300–312, 1960.

[183] A. Kisiel, W. Florkowski, and W. Broniowski, *Femtoscopy in hydro-inspired models with resonances*, Phys.Rev., vol. C73, p. 064902, 2006.

[184] U. A. Wiedemann and U. W. Heinz, *Particle interferometry for relativistic heavy ion collisions*, Phys.Rept., vol. 319, pp. 145–230, 1999.

[185] C. Adler *et al.*, (STAR Collaboration), *Pion interferometry of* $\sqrt{s_{\rm NN}} = 130$ *AGeV Au+Au collisions at RHIC*, Phys.Rev.Lett., vol. 87, p. 082301, 2001.

[186] J. Adams *et al.*, (STAR Collaboration), *Azimuthally sensitive HBT in Au + Au collisions at* $\sqrt{s_{\rm NN}} = 200$ *GeV*, Phys.Rev.Lett., vol. 93, p. 012301, 2004.

[187] J. Adams *et al.*, (STAR Collaboration), *Pion interferometry in Au+Au collisions at* $\sqrt{s_{\rm NN}} = 200$ *GeV*, Phys.Rev., vol. C71, p. 044906, 2005.

[188] B. Abelev *et al.*, (STAR Collaboration), *Pion Interferometry in Au+Au and Cu+Cu Collisions at RHIC*, Phys.Rev., vol. C80, p. 024905, 2009.

[189] K. Adcox *et al.*, (PHENIX Collaboration), *Transverse mass dependence of two pion correlations in Au+Au collisions at* $\sqrt{s_{\rm NN}} = 130$ *GeV*, Phys.Rev.Lett., vol. 88, p. 192302, 2002.

[190] S. Adler *et al.*, (PHENIX Collaboration), *Evidence for a long-range component in the pion emission source in Au + Au collisions at* $\sqrt{s_{\rm NN}} = 200$ *GeV*, Phys.Rev.Lett., vol. 98, p. 132301, 2007.

[191] S. Afanasiev *et al.*, (PHENIX Collaboration), *Source breakup dynamics in Au+Au Collisions at* $\sqrt{s_{\rm NN}}$ = 200 *GeV via three-dimensional two-pion source imaging*, Phys.Rev.Lett., vol. 100, p. 232301, 2008.

[192] Y. Sinyukov, *Spectra and correlations in locally equilibrium hadron and quark - gluon systems*, Nucl.Phys., vol. A566, pp. 589C–592C, 1994.

[193] K. Aamodt *et al.*, (ALICE Collaboration), *Femtoscopy of pp collisions at* $\sqrt{s}$ = 0.9 *and 7 TeV at the LHC with two-pion Bose-Einstein correlations*, Phys.Rev., vol. D84, p. 112004, 2011.

[194] L. K. Graczykowski, *Femtoscopy of proton-proton collisions at the LHC with the ALICE experiment*, PoS, vol. WPCF2011, p. 017, 2011.

[195] L. K. Graczykowski, (ALICE Collaboration), *Pion femtoscopy measurements in ALICE at the LHC*, EPJ Web Conf., vol. 71, p. 00051, 2014.

[196] R. Lednicky, *Femtoscopic correlations and final state resonance formation*, Phys.Part.Nucl.Lett., vol. 8, pp. 965–968, 2011.

[197] R. Lednicky, *Finite-size effects on two-particle production in continuous and discrete spectrum*, Phys.Part.Nucl., vol. 40, pp. 307–352, 2009.

[198] M. Bowler, *Coulomb corrections to Bose-Einstein correlations have been greatly exaggerated*, Phys.Lett., vol. B270, pp. 69–74, 1991.

[199] Y. Sinyukov, R. Lednicky, S. Akkelin, J. Pluta, and B. Erazmus, *Coulomb corrections for interferometry analysis of expanding hadron systems*, Phys.Lett., vol. B432, pp. 248–257, 1998.

[200] A. Kisiel and D. A. Brown, *Efficient and robust calculation of femtoscopic correlation functions in spherical harmonics directly from the raw pairs measured in heavy-ion collisions*, Phys.Rev., vol. C80, p. 064911, 2009.

[201] D. A. Brown and P. Danielewicz, *Optimized discretization of sources imaged in heavy ion reactions*, Phys.Rev., vol. C57, pp. 2474–2483, 1998.

[202] Z. Chajecki and M. Lisa, *Global Conservation Laws and Femtoscopy of Small Systems*, Phys.Rev., vol. C78, p. 064903, 2008.

[203] Z. Chajecki, *Femtoscopy in hadron and lepton collisions: RHIC results and world systematics*, Acta Phys.Polon., vol. B40, pp. 1119–1136, 2009.

[204] Y. Sinyukov, S. Akkelin, I. Karpenko, and V. Shapoval, *Femtoscopic and Nonfemtoscopic Two-Particle Correlations in A + A and p + p Collisions at RHIC and LHC Energies*, Adv.High Energy Phys., vol. 2013, p. 198928, 2013.

[205] W. Kittel, *Bose-Einstein correlations in Z fragmentation and other reactions*, Acta Phys.Polon., vol. B32, pp. 3927–3972, 2001.

[206] G. Alexander, *Bose-Einstein and Fermi-Dirac interferometry in particle physics*, Rept.Prog.Phys., vol. 66, pp. 481–522, 2003.

[207] M. A. Lisa, S. Pratt, R. Soltz, and U. Wiedemann, *Femtoscopy in relativistic heavy ion collisions*, Ann.Rev.Nucl.Part.Sci., vol. 55, pp. 357–402, 2005.

[208] L. Lonnblad and T. Sjostrand, *Modeling Bose-Einstein correlations at LEP-2*, Eur.Phys.J., vol. C2, pp. 165–180, 1998.

[209] D. Hardtke and S. Voloshin, *The Relationship between particle freezeout distributions and HBT radius parameters*, Phys.Rev., vol. C61, p. 024905, 2000.

[210] S. Pratt, *The Long Slow Death of the HBT Puzzle*, Nucl.Phys., vol. A830, pp. 51C–57C, 2009.

[211] N. Agababyan *et al.*, (EHS/NA22 Collaboration), *Two-dimensional and three-dimensional analysis of Bose-Einstein correlations in π^+ / K^+ p interactions at 250 GeV/c.*, Z.Phys., vol. C71, pp. 405–414, 1996.

[212] R. Ganz, (NA49 collaboration), *A Systematic study of two particle correlations from NA49 at CERN SPS*, Nucl.Phys., vol. A661, pp. 448–451, 1999.

[213] G. Abbiendi *et al.*, (OPAL Collaboration), *Bose-Einstein study of position-momentum correlations of charged pions in hadronic Z0 decays*, Eur.Phys.J., vol. C52, pp. 787–803, 2007.

[214] P. Achard *et al.*, (L3 Collaboration), *Bose-Einstein correlations of neutral and charged pions in hadronic Z decays*, Phys.Lett., vol. B524, pp. 55–64, 2002.

[215] A. Smirnova, *Bose-einstein correlations at the z0 peak*, in *Soft Multihadron Dynamics* (N. A. et al., ed.), Hackensack, USA: World Scientific, 1999.

[216] R. Adler *et al.*, (CPLEAR Collaboration), *Bose-Einstein correlations in anti-p p annihilations at rest*, Z.Phys., vol. C63, pp. 541–548, 1994.

[217] A. Angelopoulos *et al.*, (CPLEAR Collaboration), *Direct determination of two pion correlations for anti-p p -> 2 π^+ 2 π^- annihilation at rest*, Eur.Phys.J., vol. C1, pp. 139–148, 1998.

[218] M. Deutschmann *et al.*, (Aachen-Berlin-Bonn-CERN-Cracow-London-Vienna-Warsaw Collaboration), *A Study of Second Order Interference for Pions Produced in Various Hadronic Interactions*, Nucl.Phys., vol. B204, p. 333, 1982.

[219] J. Uribe *et al.*, (BNL-E766 Collaboration), *Pion-pion correlations at low relative momentum produced in pp collisions at 27.5 GeV/c*, Phys.Rev., vol. D49, pp. 4373–4393, 1994.

[220] J. Bailly *et al.*, (NA23 Collaboration, EHS-RCBC Collaboration), *Bose-Einstein Correlations for Pions Produced in pp Collisions at 360 GeV/c*, Z.Phys., vol. C43, p. 341, 1989.

[221] M. Aguilar-Benitez *et al.*, (LEBC-EHS Collaboration, NA27 Collaboration), *Bose-Einstein correlations in p p collisions at 400 GeV/c*, Z.Phys., vol. C54, pp. 21–32, 1992.

[222] T. Akesson *et al.*, (Axial Field Spectrometer Collaboration), *Bose-Einstein correlations between kaons*, Phys.Lett., vol. B155, p. 128, 1985.

[223] T. Akesson *et al.*, (Axial Field Spectrometer Collaboration), *Evidence for a Directional Dependence of Bose-Einstein Correlations at the CERN Intersecting Storage Rings*, Phys.Lett., vol. B187, p. 420, 1987.

[224] T. Akesson *et al.*, (Axial Field Spectrometer Collaboration), *Pion Interferometry in Jet Events at the CERN Intersecting Storage Rings*, Z.Phys., vol. C36, p. 517, 1987.

[225] A. Breakstone *et al.*, (Ames-Bologna-CERN-Dortmund-Heidelberg-Warsaw Collaboration), *Multiplicity Dependence of the Average Transverse Momentum and of the Particle Source Size in pp Interactions at* $\sqrt{s}$ = 62 *GeV, 44 GeV and 31 GeV*, Z.Phys., vol. C33, p. 333, 1987.

[226] C. De Marzo, M. De Palma, A. Distante, C. Favuzzi, P. Lavopa, *et al.*, *Measurement of the average transverse momentum and of the pion emission volume in proton–nucleus and anti-proton–nucleus reactions at 200 GeV*, Phys.Rev., vol. D29, pp. 363–367, 1984.

[227] Z. Chajecki, (STAR Collaboration), *Identical particle correlations in STAR*, Nucl.Phys., vol. A774, pp. 599–602, 2006.

[228] A. M. Glenn, (PHENIX Collaboration), *Recent HBT results in Au+Au and p+p collisions from PHENIX*, Nucl.Phys., vol. A830, pp. 833C–836C, 2009.

[229] V. Khachatryan *et al.*, (CMS Collaboration), *Measurement of Bose-Einstein correlations with first CMS data*, Phys.Rev.Lett., vol. 105, p. 032001, 2010.

[230] V. Khachatryan *et al.*, (CMS Collaboration), *Measurement of Bose-Einstein Correlations in pp Collisions at* $\sqrt{s}$ = 0.9 *and 7 TeV*, JHEP, vol. 1105, p. 029, 2011.

[231] K. Aamodt *et al.*, (ALICE Collaboration), *Two-pion Bose-Einstein correlations in pp collisions at* $\sqrt{s}$ = 900 *GeV*, Phys.Rev., vol. D82, p. 052001, 2010.

[232] T. Akesson *et al.*, (Axial Field Spectrometer Collaboration), *Bose-Einstein Correlations in* $\alpha\alpha$*, pp and* $p\overline{p}$ *Interactions*, Phys.Lett., vol. B129, p. 269, 1983.

[233] C. Albajar *et al.*, (UA1 Collaboration), *Bose-Einstein Correlations in* $\overline{p}p$ *Interactions at* $\sqrt{s}$ = 0.2 *TeV to 0.9 TeV*, Phys.Lett., vol. B226, p. 410, 1989.

[234] T. Alexopoulos, C. Allen, E. Anderson, V. Balamurali, S. Banerjee, *et al.*, *A Study of source size in p – anti-p collisions at* $\sqrt{s}$ = 1.8 *TeV using pion interferometry*, Phys.Rev., vol. D48, pp. 1931–1942, 1993.

[235] Z. Chajecki, T. Gutierrez, M. Lisa, and M. Lopez-Noriega, (STAR Collaboration), *AA versus PP (and dA): A Puzzling scaling in HBT at RHIC*, 2005.

[236] A. Adare *et al.*, (PHENIX Collaboration), *Comparison of the space-time extent of the emission source in d+Au and Au+Au collisions at* $\sqrt{s_{\rm NN}}$ = 200 *GeV*, arXiv: 1404.5291 [nucl-ex], 2014.

[237] B. B. Abelev *et al.*, (ALICE Collaboration), *Freeze-out radii extracted from three-pion cumulants in pp, p—Pb and Pb-–Pb collisions at the LHC*, Phys.Lett., vol. B739, pp. 139–151, 2014.

[238] N. Agababyan *et al.*, (EHS-NA22 Collaboration), *Influence of multiplicity and kinematical cuts on Bose-Einstein correlations in* π+ *p interactions at 250 GeV/c*, Z.Phys., vol. C59, pp. 195–210, 1993.

[239] I. Juricic, G. Goldhaber, G. Gidal, G. Abrams, D. Amidei, *et al.*, *Bose-Einstein Correlations in* e^+e^- *Collisions*, Phys.Rev., vol. D39, p. 1, 1989.

[240] P. Avery *et al.*, (CLEO Collaboration), *Bose-Einstein correlations in* e^+e^- *annihilations in the Upsilon region*, Phys.Rev., vol. D32, pp. 2294–2302, 1985.

[241] H. Aihara *et al.*, (TPC/Two Gamma Collaboration), *Study of Bose-Einstein correlations in* e^+e^- *annihilation at 29 GeV*, Phys.Rev., vol. D31, p. 996, 1985.

[242] M. Althoff *et al.*, (TASSO Collaboration), *Particle Correlation Observed in* e^+e^- *Annihilations Into Hadrons at c.m. Energies Between 29 GeV and 37 GeV*, Z.Phys., vol. C29, p. 347, 1985.

[243] M. Althoff *et al.*, (TASSO Collaboration), *Bose-Einstein Correlations Observed in* e^+e^- *Annihilation at a Center-of-mass Energy of 34 GeV*, Z.Phys., vol. C30, p. 355, 1986.

[244] S. Choi *et al.*, (AMY Collaboration), *A Measurement of Bose-Einstein correlations in* e^+e^- *annihilation at TRISTAN*, Phys.Lett., vol. B355, pp. 406–414, 1995.

[245] G. Abbiendi *et al.*, (OPAL Collaboration), *Bose-Einstein correlations of* π^0 *pairs from hadronic Z0 decays*, Phys.Lett., vol. B559, pp. 131–143, 2003.

[246] G. Alexander *et al.*, (OPAL Collaboration), *A First measurement of the Lambda – anti-Lambda and Lambda – Lambda (anti-Lambda – anti-Lambda) spin compositions in hadronic Z0 decays*, Phys.Lett., vol. B384, pp. 377–387, 1996.

[247] G. Abbiendi *et al.*, (OPAL Collaboration), *Bose-Einstein correlations in* K^+- K^+- *pairs from Z0 decays into two hadronic jets*, Eur.Phys.J., vol. C21, pp. 23–32, 2001.

[248] R. Akers *et al.*, (OPAL Collaboration), *The Production of neutral kaons in Z0 decays and their Bose-Einstein correlations*, Z.Phys., vol. C67, pp. 389–402, 1995.

[249] P. Abreu *et al.*, (DELPHI Collaboration), *Bose-Einstein correlations in the hadronic decays of the Z0*, Phys.Lett., vol. B286, pp. 201–210, 1992.

[250] P. Abreu *et al.*, (DELPHI Collaboration), *Invariant mass dependence of particle correlations in hadronic final states from the decay of the Z0*, Z.Phys., vol. C63, pp. 17–28, 1994.

[251] P. Abreu *et al.*, (DELPHI Collaboration), *Kaon interference in the hadronic decays of the Z0*, Phys.Lett., vol. B379, pp. 330–340, 1996.

[252] P. Abreu *et al.*, (DELPHI Collaboration), *Interference of neutral kaons in the hadronic decays of the Z0*, Phys.Lett., vol. B323, pp. 242–252, 1994.

[253] D. Decamp *et al.*, (ALEPH Collaboration), *A Study of Bose-Einstein correlations in e+ e- annihilation at 91-GeV*, Z.Phys., vol. C54, pp. 75–86, 1992.

[254] A. Heister *et al.*, (ALEPH Collaboration), *Two-dimensional analysis of Bose-Einstein correlations in hadronic Z decays at LEP*, Eur.Phys.J., vol. C36, pp. 147–159, 2004.

[255] S. Schael *et al.*, (ALEPH Collaboration), *Two-particle correlations in p-p, anti-p - anti-p and K0(S) - K0(S) pairs from hadronic Z decays*, Phys.Lett., vol. B611, pp. 66–80, 2005.

[256] R. Barate *et al.*, (ALEPH Collaboration), *Fermi-Dirac Correlations in lambda pairs in hadronic Z decays*, Phys.Lett., vol. B475, pp. 395–406, 2000.

[257] S. Chekanov *et al.*, (ZEUS Collaboration), *Bose-Einstein correlations in one and two-dimensions in deep inelastic scattering*, Phys.Lett., vol. B583, pp. 231–246, 2004.

[258] S. Chekanov *et al.*, (ZEUS Collaboration), *Bose-Einstein Correlations of Charged and Neutral Kaons in Deep Inelastic Scattering at HERA*, Phys.Lett., vol. B652, pp. 1–12, 2007.

[259] C. Adloff *et al.*, (H1 Collaboration), *Bose-Einstein correlations in deep inelastic ep scattering at HERA*, Z.Phys., vol. C75, pp. 437–451, 1997.

[260] M. Arneodo *et al.*, (European Muon Collaboration), *The Bose-Einstein correlations in deep inelastic μp interactions at 280 GeV*, Z.Phys., vol. C32, p. 1, 1986.

[261] M. Adams *et al.*, (E665 Collaboration), *An Investigation of Bose-Einstein correlations in muon – nucleon interactions at 490 GeV*, Phys.Lett., vol. B308, pp. 418–424, 1993.

[262] V. Korotkov *et al.*, (Big Bubble Chamber Neutrino Collaboration), *Bose-Einstein correlations in neutrino and anti-neutrino interactions with nucleons*, Z.Phys., vol. C60, pp. 37–52, 1993.

[263] M. Aggarwal *et al.*, (STAR Collaboration), *Pion femtoscopy in p + p collisions at* $\sqrt{s}$ = 200 *GeV*, Phys.Rev., vol. C83, p. 064905, 2011.

[264] G. Paic and P. K. Skowronski, *Effect of hard processes on momentum correlations in pp and p – anti-p collisions*, J.Phys., vol. G31, pp. 1045–1054, 2005.

[265] P. Bozek, *Observation of the collective flow in proton-proton collisions*, Acta Phys.Polon., vol. B41, p. 837, 2010.

[266] K. Werner, I. Karpenko, T. Pierog, M. Bleicher, and K. Mikhailov, *Evidence for hydrodynamic evolution in proton-proton scattering at 900 GeV*, Phys.Rev., vol. C83, p. 044915, 2011.

[267] S. Adler *et al.*, (PHENIX Collaboration), *Bose-Einstein correlations of charged pion pairs in Au + Au collisions at* $\sqrt{s_{\mathrm{NN}}}$ = 200 *GeV*, Phys.Rev.Lett., vol. 93, p. 152302, 2004.

[268] D. Adamova *et al.*, (CERES collaboration), *Beam energy and centrality dependence of two pion Bose-Einstein correlations at SPS energies*, Nucl.Phys., vol. A714, pp. 124–144, 2003.

[269] P. Bozek, M. Chojnacki, W. Florkowski, and B. Tomasik, *Hydrodynamic predictions for Pb+Pb collisions at* $\sqrt{s_{\mathrm{NN}}}$ = 2.76 *TeV*, Phys.Lett., vol. B694, pp. 238–241, 2010.

[270] B. Schenke and R. Venugopalan, *Eccentric protons? Sensitivity of flow to system size and shape in p+p, p+Pb and Pb+Pb collisions*, Phys.Rev.Lett., vol. 113, p. 102301, 2014.

[271] T. A. Rijken, M. Nagels, and Y. Yamamoto, *Baryon-baryon interactions: Nijmegen extended-soft-core models*, Prog.Theor.Phys.Suppl., vol. 185, pp. 14–71, 2010.

[272] J. Haidenbauer, *Baryon-baryon interactions from chiral effective field theory*, Nucl.Phys., vol. A914, pp. 220–230, 2013.

[273] W. Bruckner, H. Dobbeling, F. Guttner, D. von Harrach, H. Kneis, *et al.*, *Real to Imaginary Ratio of the $\overline{p}p$ Forward Elastic Scattering Amplitude in the Momentum Range Between 180 MeV/c and 590 MeV/c*, Phys.Lett., vol. B158, p. 180, 1985.

[274] D. Bugg, J. Hall, A. Clough, R. Shypit, K. Bos, *et al.*, *Anti-p p total cross-sections below 420 MeV/c*, Phys.Lett., vol. B194, pp. 563–567, 1987.

[275] W. Bruckner, B. Cujec, H. Dobbeling, K. Dworschak, H. Kneis, *et al.*, *Measurements of the anti-proton - proton elastic cross-section in the beam momentum range between 180 MeV/c and 600 MeV/c*, Z.Phys., vol. A339, pp. 367–377, 1991.

[276] J. Beringer *et al.*, (Particle Data Group), *Review of Particle Physics (RPP)*, Phys.Rev., vol. D86, p. 010001, 2012.

[277] C. Batty, *Anti-protonic hydrogen atoms*, Rept.Prog.Phys., vol. 52, pp. 1165–1216, 1989.

[278] H. Pirner, B. Kerbikov, and J. Mahalanabis, *Updating the effective range expansion of low-energy N anti-N scattering*, Z.Phys., vol. A338, pp. 111–112, 1991.

[279] I. Grach, B. Kerbikov, and Y. Simonov, *Nucleon anti-nucleon low-energy interaction in the effective range approximation*, Sov.J.Nucl.Phys., vol. 48, pp. 609–616, 1988.

[280] E. Klempt, F. Bradamante, A. Martin, and J. Richard, *Antinucleon nucleon interaction at low energy: Scattering and protonium*, Phys.Rept., vol. 368, pp. 119–316, 2002.

[281] R. Lednicky and V. Lyuboshits, *Final State Interaction Effect on Pairing Correlations Between Particles with Small Relative Momenta*, Sov.J.Nucl.Phys., vol. 35, p. 770, 1982.

[282] G. Bertsch, *Pion Interferometry as a Probe of the Plasma*, Nucl.Phys., vol. A498, pp. 173C–180C, 1989.

[283] S. Pratt, *Pion Interferometry of Quark-Gluon Plasma*, Phys.Rev., vol. D33, pp. 1314–1327, 1986.

[284] P. Z. Skands, *The Perugia Tunes*, FERMILAB-CONF-09-113-T, pp. 284–297, 2009.

[285] A. Morsch, (ALICE Collaboration), *p-Pb Results from ALICE with an Emphasis on Centrality Determination*, J.Phys.Conf.Ser., vol. 509, p. 012021, 2014.

[286] M. Chojnacki, A. Kisiel, W. Florkowski, and W. Broniowski, *THERMINATOR 2: THERMal heavy IoN generATOR 2*, Comput.Phys.Commun., vol. 183, pp. 746–773, 2012.

[287] T. Sjostrand, S. Mrenna, and P. Z. Skands, *A Brief Introduction to PYTHIA 8.1*, Comput.Phys.Commun., vol. 178, pp. 852–867, 2008.

[288] R. Corke and T. Sjostrand, *Interleaved Parton Showers and Tuning Prospects*, JHEP, vol. 1103, p. 032, 2011.

[289] N. Neumeister *et al.*, (UA1-Minimum Bias-Collaboration), *Higher order Bose-Einstein correlations in p anti-p collisions at* $\sqrt{s}$ = 630 *GeV and* 900 *GeV*, Phys.Lett., vol. B275, pp. 186–194, 1992.

[290] I. Bearden *et al.*, (NA44 Collaboration), *One-dimensional and two-dimensional analysis of 3-π correlations measured in Pb + Pb interactions*, Phys.Lett., vol. B517, pp. 25–31, 2001.

[291] B. Abelev *et al.*, (ALICE Collaboration), *Centrality determination of Pb-Pb collisions at* $\sqrt{s_{\rm NN}}$ = 2.76 *TeV with ALICE*, Phys.Rev., vol. C88, no. 4, p. 044909, 2013.

[292] M. P. Szymanski, (ALICE Collaboration), *Meson and baryon femtoscopy in heavy-ion collisions at ALICE*, Nucl.Phys., vol. A904-905, pp. 447c–450c, 2013.

[293] M. P. Szymanski, (ALICE Collaboration), *Baryon femtoscopy in heavy-ion collisions at ALICE*, EPJ Web Conf., vol. 71, p. 00130, 2014.

[294] J. Adams *et al.*, (STAR Collaboration), *Proton - lambda correlations in central Au+Au collisions at* $\sqrt{s_{\rm NN}}$ = 200 *GeV*, Phys.Rev., vol. C74, p. 064906, 2006.

[295] A. Kisiel, *CorrFit – a program to fit arbitrary correlation functions*, Nukleonika, vol. 49 (Suppl. 2), pp. 81–83, 2004.

[296] A. Kisiel, H. Zbroszczyk, and M. Szymanski, *Extracting baryon-antibaryon strong interaction potentials from $p\overline{\Lambda}$ femtoscopic correlation function*, Phys.Rev., vol. C89, p. 054916, 2014.

[297] Z. Chajecki, *Global conservation laws and femtoscopy at RHIC*, Ph.D. Thesis, Ohio State University, 2009.

[298] M. Janik, *$\Delta\eta\Delta\varphi$ angular correlations in pp collisions at the LHC registered by the ALICE experiment*, PoS, vol. WPCF2011, p. 026, 2011.

[299] M. Janik, *Two-particle correlations as a function of relative azimuthal angle and pseudorapidity in proton-proton collisions registered by the ALICE experiment*, Ph.D. Thesis, Warsaw University of Technology, 2014.

[300] K. Aamodt *et al.*, (ALICE Collaboration), *Harmonic decomposition of two-particle angular correlations in Pb-Pb collisions at $\sqrt{s_{\rm NN}}$ = 2.76 TeV*, Phys.Lett., vol. B708, pp. 249–264, 2012.

[301] G. Aad *et al.*, (ATLAS Collaboration), *Measurement of inclusive two-particle angular correlations in pp collisions with the ATLAS detector at the LHC*, JHEP, vol. 1205, p. 157, 2012.

[302] R. Porter and T. Trainor, (STAR Collaboration), *Correlation structures from soft and semi-hard components in p - p collisions at $\sqrt{s_{\rm NN}}$ = 200 GeV*, Acta Phys.Polon., vol. B36, pp. 353–359, 2005.

[303] B. Alver *et al.*, (PHOBOS Collaboration), *Cluster properties from two-particle angular correlations in p + p collisions at $\sqrt{s_{\rm NN}}$ = 200 GeV and 410 GeV*, Phys.Rev., vol. C75, p. 054913, 2007.